공학박사학위논문

수소 및 메탄 연료로 운전되는 중온 평판형 고체 산화물 연료전지의 마이크로/매크로 시뮬레이션

Micro/Macroscale Simulations of Planar Intermediate-Temperature Solid Oxide Fuel Cells operated with Hydrogen and Methane Fuels

2013 년 8 월

서울대학교 대학원

기계항공공학부

백 승 만

수소 및 메탄 연료로 운전되는 중온 평판형 고체 산화물 연료전지의 마이크로/매크로 시뮬레이션

Micro/Macroscale Simulations of Planar Intermediate-Temperature Solid Oxide Fuel Cells operated with Hydrogen and Methane Fuels

지도교수 김 찬 중

이 논문을 공학박사 학위논문으로 제출함

2013 년 4 월

서울대학교 대학원

기계항공공학부

백 승 만

백승만의 공학박사 학위논문을 인준함

2013 년 7 월

위 원 장 : _____ 인

부위원장 : _____ 인

위 원 : _____ 인

위 원 : _____ 인

위 원 : _____ 인

Abstract

Micro/Macroscale Simulations of Planar Intermediate-Temperature Solid Oxide Fuel Cells operated with Hydrogen and Methane Fuels

Seung Man Baek
School of Mechanical and Aerospace Engineering
The Graduate School
Seoul National University

The intermediate temperature solid oxide fuel cells (IT-SOFCs) are promising SOFC technologies that can solve many problems of high temperature SOFCs (HT-SOFCs), such as stringent restriction on material selection, accelerated degradation of electrode microstructure, limitation in thermal cycling, requirement for longer startup times, etc. Most of these constraints and limitations are originated from the operating temperature of HT-SOFCs around 1000°C. Since IT-SOFCs are operated at relatively lower temperatures ranging from 600~800°C, less expensive materials can be used with better long-term stabilities. In addition, the advantages of the SOFC technologies are largely retained, such as the use of non-precious metal catalyst, the direct internal reforming of hydrocarbon fuels, the production of quality waste heat, etc.

Therefore, this dissertation presents the development of comprehensive three-dimensional micro/macroscale models for simulating, designing, and optimizing planar, anode-supported IT-SOFCs operated with hydrogen and methane fuels. The micro/macroscale models are constructed with many constitutive models, including the models for electrode microstructure characterization based on random binary packing theories, the models for electrode processes with detailed consideration on the electrochemical reactions at TPBs, the models for heat and mass transport in three-dimensional interconnect plate/gas channel geometries with fully-developed laminar flow assumption, and the models for direct internal reforming in the anode consisting of the steam reforming, water-gas shift reaction, and reverse methanation reactions. These simulations are performed with the properties of standard materials

for IT-SOFCs, such as nickel, YSZ, LSM, and stainless steel. In addition, accurate thermodynamic properties are used for air (O_2 and N_2) and fuels (H_2, H_2O, CH_4, CO, and CO_2).

The three-dimensional micro/macroscale model is utilized to investigate the performance and operating characteristics of planar, anode-supported IT-SOFCs with co- and counter-flow configurations, when they are fueled with wet hydrogen or partially reformed methane fuel. The current–voltage performance curves are presented along with the contribution of activation, concentration, ohmic and contact overpotentials to total potential loss. In addition, the spatial distribution of temperature, current density, and concentrations is also investigated in detail. The simulation results indicate that hydrogen-fueled IT-SOFCs with the counter-flow configuration result in higher cell efficiencies than the co-flow configuration. However, the co-flow configuration is found to have more uniform distribution of temperature and current density compared with the counter-flow configuration. Thus, the co-flow configuration is concluded to be more advantageous for long-term stability of cell performance as well as mechanical durability of IT-SOFCs. Extensive parametric study is also performed to clarify the effects of operational, microstructural, and dimensional parameters. The simulation results also point out that the counter-flow configuration leads to higher efficiencies and more uniform distribution of temperature for methane-fueled IT-SOFCs. This is identified as caused by the endothermic steam methane reforming reactions.

The results presented in this dissertation clearly demonstrate the capabilities of the present three-dimensional micro/macroscale models as an accurate and efficient design tool for optimizing the operating conditions, electrode microstructures, and cell geometries of planar, anode-supported IT-SOFCs as well as for quantitatively investigating the detailed chemical, electrochemical, and transport processes.

Keywords: Solid oxide fuel cell (SOFC); Intermediate-temperature SOFC; anode-supported SOFC; Direct internal reforming (DIR); Steam methane reforming (SMR); Co-flow and counter-flow; Microscale model; Macroscale model; Electrode microstructure; Interconnect plate; Flow channel; Ni/YSZ; LSM/YSZ; SUS 430
Student Number: 2008-30856

Contents

List of Tables

List of Figures

Nomenclatures

A	area, m^2
c_i	molar concentration of species i, mol/m^3
c_p	molar specific heat, J/mol-K
d	neck diameter of contact particles, m or mean particle diameter, m
d_h	hydraulic diameter of the channel, m
D_{ij}	binary diffusivity of species i and j, m^2/s
D_{iK}	Knudsen diffusivity of species i, m^2/s
F	Faraday constant, 96,487 C/mol
Δg	Gibbs free energy, J/ mol
$h(T)$	molar sensible enthalpy, J/mol
ΔH	adsorption enthalpy, J/mol
$\mathbf{i}$	current vector
i	current density, A/m^2
K	flow permeability, m^2, or adsorption constant
K_{eq}	equilibrium constant
k	thermal conductivity, W/m-K or reaction rate constant
L	thickness or length
L_e	hydraulic entrance length, m
M	molecular mass, kg/mol
$\mathbf{n}$	molar flux vector, mol/m^2-s
n	number fraction
$n_{x,tot}$	total axial molar flux, , mol/m^2-s
N_t	number density of all particles, $\#/m^3$
$N_{x,tot}$	total molar flow rate in channel, mol/s
P	percolation probability
p	pressure, Pa
$\dot{q}$	volumetric heat generation, W/m^3
Re	Reynolds number
R	universal gas constnt, 8.314 J/mol-K or electrical resistance, Ω
r	area-specific resistance, Ω-m^2 or reaction rate, mol/m^2_{cat}-s

T	temperature, K
$\mathbf{u}$	bulk velocity in porous media, m/s
u	fluid velocity, m/s
V	volume, m^3
V_i	diffusion volume for species i.
x, y, z	coordinate, m
x_i	mole fraction of species, i
Z	coordination number
W	width

Greek letters

α	mean diameter ratio, $\alpha \equiv d_{io} / d_{el}$ or channel aspect ratio, $\alpha \equiv b / a$
μ	dynamic viscosity, Pa-s
ε	porosity
ϕ	particle volume fraction
η	overpotential, V or nickel surface efficiency, η_{Ni}^{eff}
φ	potential, V
λ	area- or volume-specific TPBL or volumetric Ni surface area, m^2/m^3
θ_c	neck contact angle, $^\circ$
σ	electrical conductivity, S/m
τ	tortuosity or $\tau = T/1000$
ζ	fuel and air utilization factor

Subscripts and superscripts

A	anode or area-specific
AFL	anode functional layer
ASL	anode substrate layer
act	activation
air	air or air channel
asr	contact resistance
C	cathode

c	contact
CFL	cathode functional layer
CCCL	cathode current collector layer
CH	channel
cell	cell
conc	concentration
d	diffusive
EL	electrolyte
eff	effective
el	electronic phase
ex	exchange current
fuel	fuel or fuel channel
gen	generation
INT	interconnect plate
io	ionic phase
lim	limiting current
m	mean
max	maximum
o	inlet or intrinsic value
ohm	ohmic
PEN	posivtie/electrolyte/nagative
ref	reference
rib	channel rib
sf	solid/fluid
t	total
tpb	three-phase boundary
tr	transfer current
V	volume-specific
v	viscous
x	axial direction

CHAPTER 1

INTRODUCTION

1.1 Solid Oxide Fuel Cell

Solid oxide fuel cell (SOFC) is one of the most promising fuel cell systems that can convert the chemical energy of fuels to electrical energy and heat through the electrochemical reactions of fuel and oxidant gases (Minh, 1993; Larminie and Dicks, 2000). While hydrogen is the primary fuel for any fuel cell system, SOFCs are able to operate with a wide range of fuels, including methane (natural gas), gasoline, diesel, coal gas, etc (Achenbach and Riensche, 1994; Su et al., 2011; Liu et al., 2008; Ma et al.,2006). In addition, its clean operation and high efficiency makes the SOFC as a promising candidate for the next-generation power sources. Many of these advantages are the results of high operating temperature of SOFCs at about 500~1000°C. In fact, high operating temperature of SOFCs also allows the use of non-precious metal catalysts for electrochemical reactions.

The operating principle of the SOFC is presented in Fig. 1.1, where the basic configuration composed of an anode, an electrolyte, a cathode, and fuel and oxidant channels is also shown. In general, the electrodes are made by sintering the mixture of electronic and ionic particles of small diameters and thus have porosity as well as

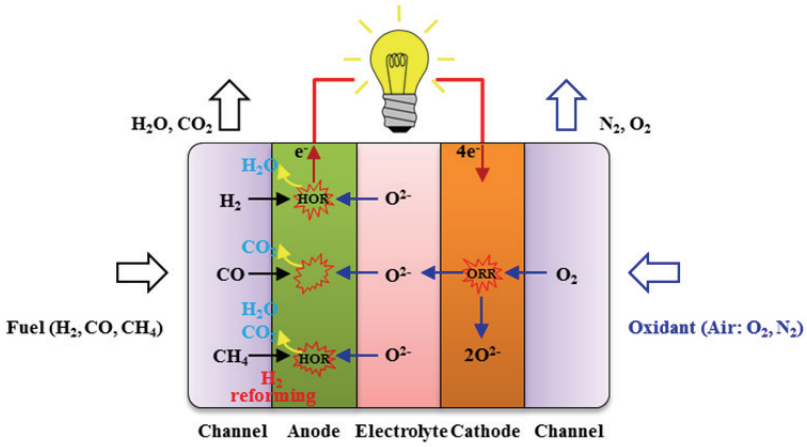

Fig. 1.1 The operating principle of SOFC.

electronic and ionic conductivities. The electrochemical reactions are completed with gas molecules, electrons, and ions that are transferred through the electrodes by diffusion and conduction. Hydrogen oxidation reaction (HOR) mainly occurs in the anode and the oxygen reduction (ORR) occurs in the cathode. The electrolyte is a thin solid ceramic membrane which can transfer oxygen ion from the cathode to the anode.

By using hydrogen as fuel, SOFCs can operate at much higher efficiencies while producing only water vapor (H_2O) as emissions. However, SOFCs are still able to operate with other hydrocarbon fuels less expensive than hydrogen. When hydrocarbon fuels such as methane are supplied, the reforming reactions occur inside the porous cathode and convert the hydrocarbon fuels into hydrogen. This process is the so-called direct internal reforming which is possible due to high operating temperature of SOFCs. Fig. 1.1 illustrates that the carbon monoxide produced during the reforming reactions also participates in the electrochemical reactions. The carbon monoxide (CO) is electrochemically converted into carbon dioxide (CO_2) while producing electricity and heat.

1.1.1 Planar SOFC

Historically, several different design concepts have been proposed and tested for SOFCs. According to their overall system design, SOFCs can be divided into the tubular or planar types. The tubular designs are the most advanced SOFC technologies, with commercial systems available in the market. In tubular SOFCs, air (or fuel gas) is forced to flow through a long ceramic tube while fuel gas (or air) is forced to flow outside the tube. Thus, electricity is produced by the electrochemical reactions that occur across the tube wall. Sealing is not generally required thanks to the tubular positive electrode/electrolyte/negative electrode (PEN) geometry. The tubular SOFCs are believed to be suitable for large-scale production of electricity and heat, such as SOFC/gas turbine (GT) hybrid systems (Minh, 2003).

Planar SOFCs are composed of flat-plate PENs and another flat-plate interconnects with embedded gas distribution channels. The fabrication cost for ceramic plates (planar PENs) is lower than that for ceramic tubes (tubular PENs). In

addition, planar SOFCs offer other advantages such as compact design, higher power density, and good scaling capability. Because a planar SOFC is made by stacking many single cells, the capacity of a SOFC can be easily modified by changing the number of stacked single cell.

1.1.2 Anode-supported SOFC

The SOFCs are also categorized as the anode-supported, cathode-supported, or electrolyte-supported, based on the supporting layer for PENs. The electrolyte-supported structure can provide good mechanical strength to PENs but tend to increase the ohmic potential loss. Thus, the electrolyte-supported structure is generally adopted in SOFCs operated at high temperatures. The cathode-supported structure has been generally used for tubular SOFCs because this structure helps reduce the activation potential loss (Minh, 2003). For planar SOFCs, the anode-supported structure is extensively used these days due to several reasons. Because the anode layers support the whole PEN structure, the thickness of the electrolyte can be significantly reduced to decrease the ohmic overpotential. In addition, the thick anode layers also contribute to the reforming of hydrocarbon fuels in the SOFC.

Note that the electrodes of SOFCs are generally designed to have functionally-graded multiple layers in these days. For example, a double-layer electrode is composed of two different layers: a thin porous layer of fine electronic and ionic particles (smaller than 0.5 μm) near the electrolyte, and a porous layer of coarse electronic (and ionic) particles (larger than 1 μm) near the gas channel or interconnect plate. The primary role of the fine particle layer is to enhancing the electrochemical reactions by increasing the three-phase boundaries (TPBs) where electrons, ions, and gas molecules co-exists. Likewise, the primary role of the coarse particle layer is to enhance the mass transport (and electron conduction) by providing more porous and less tortuous paths (Zhao and Virkar, 2005; Haanappel et al., 2005).

1.1.3 Intermediate temperature SOFC

According to their operating temperature, SOFCs are categorized as low temperature (LT)-SOFCs operating below 600°C, intermediate temperature (IT)-SOFCs operating at about 600~800°C, and high temperature (HT)-SOFCs operating above 800°C. The high operating temperature of HT-SOFCs is undisputedly helpful to achieve high efficiency by enhancing the ionic conductivity and electrochemical reaction activity. However, careful selection of materials is required for interconnect, sealing, and other structural components in order to resist harsh environments. In addition, these materials are generally expensive increasing the fabrication cost of SOFCs.

In recent years, the research focus on the SOFC technology has shifted from HT-SOFCs to IT-SOFCs, and then to LT-SOFCs. Lowering the operating temperature of SOFCs has significant implication from the viewpoint of material selection and degradation. At the intermediate temperature range, less expensive materials such as stainless steel can be used for interconnect plates and for other structural and sealing components. In addition, the long-term stability of the performance can be greatly improved by suppressing the degradation of electrode materials by operational sintering (Oremrod, 2003). However, ohmic potential loss in the electrolyte tends to increase at the intermediate temperatures, and this problem may be solved by using thin film electrolytes in anode-supported structures.

It is believed that the operating temperature of LT-SOFCs will guarantee the long-term stability of performance as well as the durability of materials. However, the electrochemical activity of catalyst materials and the ionic conductivity of electrolyte materials seem to be very low in LT-SOFCs. Thus, developing materials should be conducted first currently for such low temperature operation of SOFCs.

At this point, it should be clearly stated that the present study is focused on the planar, anode-supported, IT-SOFCs with two-layer electrodes. Micro/macroscale models are developed to simulate the operation of these SOFCs with hydrogen or methane fuel. In addition, these models fully consider the three-dimensional (3D) geometrical effects including the temperature and concentration variation along the channel and the blockage of mass transport due to interconnect ribs. Thus, it is believed that the present model can be a useful analysis tool for the characteristic

performance of the IT-SOFCs as well as the effects of various parameters influencing the performance.

1.1.4 Materials

In planar, anode-supported IT-SOFCs with two-layer electrodes, a PEN structure is composed of a two-layer anode, an electrolyte, and a two-layer cathode. The term functional layer is used for the thin layers of fine particles in the anode (anode functional layer, AFL) and in the cathode (cathode functional layer, CFL) because the main role of the functional layers is to enhancing the electrochemical reactions. The coarse particle layer in the anode is called the anode substrate layer (ASL) while that in the cathode is called the cathode current collector layer (CCCL). The role of these layers is to efficiently transport gas molecules and electrons, and thus may be called as the transport layer. These PEN structures are placed in between the interconnect plates whose role is to conduct electrons and distribute the fuel and gas flow. The standard materials considered in this study are briefly explained as follows.

Electrolyte – The solid electrolyte is generally made of Yttria-stabilized zirconia (YSZ) because it is good oxygen ion conductor at elevated temperatures (Singhal and Kendall, 2003). In addition, YSZ has good chemical and mechanical stability that can contribute to the integrity of SOFC. In general, the electrolytes in IT-SOFCs are made to be very thin (~10 μm) to reduce the ohmic potential loss.

ASL – The ASL is the thickest layer (~1 mm) and thus serves as the mechanical support for the PEN in anode-supported SOFCs. In general, ASL is made as the binary mixture of coarse nickel (Ni) and YSZ particles. Then, YSZ particles in the ASL are related with supporting role while the Ni particles are related with electron conducting role of the ASL. When methane is used as fuel instead of hydrogen, the Ni particles in the ASL provides rich catalytic surface area for steam reforming reactions.

AFL – The AFL is the thin reaction layer (~20 μm) where the hydrogen oxidation reaction (HOR) occurs. Made by sintering the binary mixture of fine Ni and YSZ particles, the AFL provides a large number of TPB sites to enhance the

efficiency of the electrochemical reactions. Thus, the role of YSZ particles in the AFL is to extend the reaction sites from the electrode/electrolyte interface towards the electrode volume. However, the thickness of the AFL should be small because low porosity and fine particle diameter tends to increase the mass transport resistance.

CFL – The CFL is the thin reaction layer (~20 μm) for the oxygen reduction reaction (ORR). The CFL is also made by sintering the binary mixture of fine particles of YSZ and lanthanum-strontium-manganite (LSM) which is an electronic conductor. Likewise, the CFL also provides a large number of active TPB sites for the electrochemical reactions (Kenjo and Nishiya, 1992).

CCCL – The CCCL is generally composed of coarse LSM particles, which facilitates the electron conduction as well as oxygen diffusion in the in-plane direction. The thickness of the CCCL is about 50~100 μm. Note that LSM is widely used as the cathode material for it has a thermal expansion coefficient very similar to that of YSZ (Fergus, 2007).

Interconnector plate – The relatively low operating temperature of IT-SOFCs allows to use less expensive metal for interconnect plates (Steele, 2000). The stainless steel 430 (SUS430) has been extensively studied for use as the metallic interconnect plates for IT-SOFCs, due to its good machinability and oxidation resistance (Fergus, 2005). Additional oxide coatings are routinely applied to the metallic interconnect to further increase the corrosion resistance, such as LSM-coated SUS430.

1.2 Motivation and Objectives

The motivation of this dissertation is to provide better understanding of the fuel cell processes in the IT-SOFCs, including the electrochemical reactions and the transport processes for electrons, ions, mass, and heat. Thus, this study aims to elucidate how various microstructural, operational, and dimensional parameters influences the operation characteristics and performance of IT-SOFCs.

Previous microscale models were focused merely on finding the correlation between the microstructure of the electrodes and their electrochemical efficiencies

(Costamagna et al., 1998: Chan and Xia, 2001; Chen et al., 2004; Janardhanan et al.,2008; Chen et al., 2009; Hussain et al., 2009). However, this study attempted to extend these microscale models toward a complete 3D micro/macroscale model that can both considers the microscale processes inside the electrodes as well as the macroscale processes due to the channel flow and interconnect plate geometries. Note that the microscale processes primarily denote the charge transport and electrochemical reactions in the electrodes, whereas the macroscale processes denote the mass and heat transfer in the PEN, gas channels, and interconnect plate including contact resistances at the interface of the PEN and the interconnect rib.

Thus, the micro/macroscale model is constructed to consider the complete 3D calculation domain of IT-SOFCs, comprising of a PEN, two interconnect plates, and two gas channels. The macroscale transport in the gas channels is formulated by assuming the fully-developed laminar flow. As will be discussed in the next chapter, this assumption is valid without significant error for ordinary operation of IT-SOFCs having straight gas channels of rectangular cross-section. An advantage of this approach is that complex fluid dynamics calculation can be avoided by directly prescribing the axial molar flux in the gas channels. Although the computational efforts related with the fluid dynamics calculation can be saved, the present model can still consider the 3D mass blocking effect caused by interconnect ribs, not to mention the temperature and concentration variation along the channel.

According to the motivation of this study, the micro/macroscale model is further extended to consider the operation of IT-SOFCs with methane fuel. Three-step reaction models are taken into account, which consists of the steam reforming reaction, water-gas shift reaction, and reverse methanation reaction. The reaction kinetics suggested by Xu and Froment (1989a, 1989b) is reformulated based on the catalytic surface area of Ni particles in the anode. In addition, mass transport calculation is modified to consider the multicomponent anode gas mixtures (CH_4, H_2O, H_2, CO, and CO_2), and the volumetric heat sources due to the reforming reactions are also included in the heat transfer calculation.

With all these efforts, the 3D micro/macroscale model developed in this study is expected to be useful for understanding the multi-physics, multi-scale processes

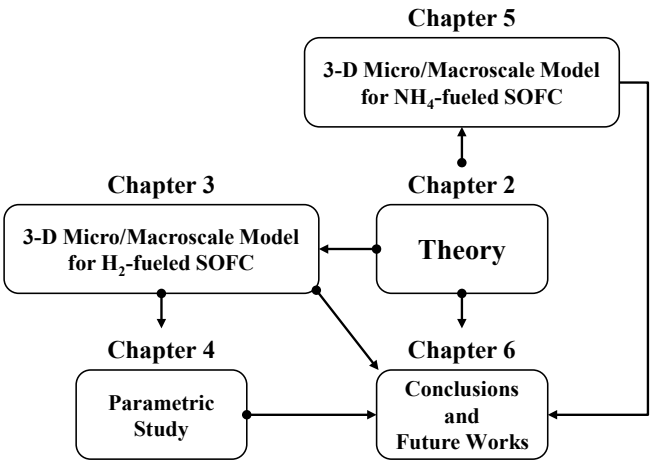

Fig. 1.2 The structure of this dissertation.

occurring inside the IT-SOFCs operated with hydrogen or methane. In addition, the present model can also be used as a design and optimization tool for predicting the performance of a certain cell design or for assessing the effects of the design or operational parameter change.

1.3 Outline

This dissertation is organized as six chapters as shown in Fig. 1.2. First, in chapter 2, the fundamental concepts and theories underlying the present 3D micro/macroscale model is explained in the context of planar, anode-supported IT-SOFCs operated with hydrogen fuel. Models for characterizing the electrode microstructures are explained first, followed by the continuum electrode model for calculating charge transport and electrochemical reactions in the PEN. Then, models for mass transfer in the porous electrode and gas channels are described, and finally, models for heat transfer calculation along with heat source terms are fully explained. In addition, the validity of the present model is also checked at the end of chapter 2.

The micro/macroscale model described in chapter 2 is directly utilized to investigate the basic performance and operating characteristics of IT-SOFCs fueled with hydrogen. The current–voltage performance curves of IT-SOFCs with the co-

flow and counter-flow configuration is investigated, along with a detailed analysis of activation, concentration, and ohmic overpotentials. In addition, the spatial distribution of temperature, gas concentration, and current density along the flow direction is also studied in detail. The temperature gradient in the AFL, electrolyte, and CFL is investigated since it is closely related with the thermal stress.

In chapter 4, extensive parametric studies are conducted on the basis of the theories and the results presented in chapter 2 and 3. The effects of the operating conditions such as temperature and pressure are studied first, followed by the parametric investigation on the effects of the electrode microstructural parameters such as particle diameter and porosity. Then, the effects of the geometrical parameters such as electrode thickness and channel dimension are investigated parametrically. The sensitivity analysis is performed to evaluate the influence of each parameter on the Nernst potential as well as the activation, concentration, and ohmic polarizations.

The chapter 5 begins with the brief explanation for the extension of the model described in chapter 2 towards the micro/macroscale model for IT-SOFCs operated with methane fuel. First, three-step reaction kinetics for considering the steam methane reforming in the anode is explained, followed by the mass transfer calculation considering the multicomponent diffusion as well as the additional heat sources due to reforming reactions. Then, the basic performance and operating characteristics of IT-SOFCs operated with methane fuel are investigated through simulations. Finally, the conclusion of the present study and suggestions about future works are presented in chapter 6.

CHAPTER 2

THEORY

In this chapter, fundamental theories are summarized which underlying the present three-dimensional (3D) micro/macroscale model for predicting the performance and detailed operation characteristics of intermediate-temperature solid oxide fuel cells (IT-SOFCs). The micro/macroscale model is formulated first for IT-SOFCs operated with hydrogen and air. The extension of this model towards methane-fueled IT-SOFCs will be explained in chapter 5, with detailed description of relevant models for multicomponent mass diffusion and direct internal reforming.

It should be noted that the present micro/macroscale model is composed of many sub-models for physical phenomena related with the operation of SOFC. Those includes the models for microstructural characterization of porous electrodes, the models for charge transport and electrochemical reactions, and the models for heat and mass transport in electrodes, gas channels, and interconnects.

The microstructural model determines the important geometrical parameters for the electrochemical performance of electrode, which are the three-phase boundary length (TPBL) and the ionic and electronic conductivities. The cermet anodes and composite cathodes in SOFCs are ideally modeled as a mixture of randomly packed spherical particles of ionic and electronic materials (called the binary particle mixture) (Suzuki and Oshima, 1983; Bouvard and Lange, 1991; Kuo and Gupta, 1995). Based on the statistical percolation theory and coordination number theory, the formation of percolated particle clusters of ionic and electronic phase and the resulting electrochemically active sites between them are determined (Kirkpatrick, 1973; Bouvard and Lange, 1991).

Then, the microscale electrode model predicts the rate of electrochemical reactions (or equally the electricity generation) inside the electrodes. Based on the parameters determined by the preceding microstructural model, the continuum conservation equations are formulated to consider the ionic and electronic charge transport (ohmic loss), the mass diffusion (concentration loss), and the

electrochemical reactions at TPBs (activation loss) in porous electrodes. The non-negligible contact resistance between an electrode and an interconnector is also considered in the model.

The present micro/macroscale model also considers the macroscale transport phenomena caused by the presence of long flow channel. That is, the concentration and temperature significantly vary along the flow channel due to the consumption of fuel and oxidant and the generation of reaction heat. Based on the fully-developed laminar velocity profiles, heat and mass convection in gas channels can be considered accurately without complicated fluid dynamics calculation. In addition, the 3D effects on heat and mass transport due to the presence of interconnect is also fully considered. Finally, the validity of the micro/macroscale model is checked at the end of this chapter.

2.1 Model Description

High-temperature (HT) operation of SOFCs at around 1000°C is known to improve the cell performance because the ionic conductivity of solid electrolytes and the electrochemical activity of electrode (catalyst) materials is high at those temperatures. However, higher cell temperature generally increases the possibility of mechanical failure of SOFCs, including electrode delamination, crack formation, and fracture. In addition, the sintering or coarsening of electrode particles is accelerated as the operating temperature increases, leading to more noticeable long-term performance degradation.

As an alternative to such HT-SOFC technologies, intermediate-temperature (IT) SOFCs with lower operating temperature ranging about 600~800°C have received much research attention these days. The lower operating temperature of IT-SOFCs is believed to solve many problems of HT-SOFCs while also enables more flexible selection of interconnect and sealing materials. However, IT-SOFCs inevitably suffer from reduced electrochemical activity at lower temperatures, and this problem is solved by adopting the planar cell structures with two-layer electrodes to achieve higher current densities. A two-layer electrode is composed of a thin functional layer and a relatively thick bulk transport layer, where their role is to

enhance the electrochemical reactions and to enhance mass transport and current conduction, respectively (Zhao and Virkar, 2005; Haanappel et. al., 2005).

Thin functional layers located near the electrolyte are made with ionic and electronic particles of very small diameters (less than 0.5 μm). Thus, they provide rich TPBs for electrochemical reactions, resulting in sufficiently high current density at lower operating temperature ranges of IT-SOFCs . On the contrary, bulk transport layers are primarily composed of electronic particles of larger diameters (larger than 1 μm), and thus improve mass transport. Ionic (ceramic) particles are often added to the bulk transport layers in order to reduce the operational sintering and consequent pore closure. The thickness of the functional layers is around 10~20 μm, while that of the transport layers varies as higher than 500 μm in anodes (for reforming of hydrocarbon fuels) or around 50 μm in cathodes.

As the IT-SOFC technologies advances, the need for reliable numerical tools for analysis and prediction of IT-SOFCs is steadily growing. Previous microscale models generally take into account the transport and reaction in a single positive electrode/electrolyte/negative electrolyte (PEN) structure as in one-dimensional (1D) models (Costamagna et al., 1998; Nam and Jeon, 2006; Jeon et al., 2006; Ni et al., 2007; Zhu and Kee, 2008), or parallel PEN structures connected across or along the flow channel as in two-dimensional (2D) models (Sohn et al., 2010). However, accurate prediction of the operation characteristics of IT-SOFCs requires consideration of the 3D channel and interconnect geometry. The performance of SOFCs is affected by the presence of the interconnect structure as well as the temperature and concentration variation along the flow channel.

Therefore, the present micro/macroscale model is developed by extending the previous 2D micro/macroscale model to include the 3D channel/interconnect geometry effects. Then, the present model can take into account both the effect of electrode microstructures and those of flow field and interconnect geometries, not to mention the effect of operating conditions. Planar, anode-supported, IT-SOFCs with two-layer electrodes is the main objective of the 3D micro/macroscale model.

2.1.1 Structure of IT-SOFC

The physical processes occurring in an anode-supported IT-SOFC with two-layer electrodes are described in Fig. 2.1, where the IT-SOFC is depicted to be operated with hydrogen and air. At the center of the cell is a thin solid electrolyte of about 10 μm thickness, which is supported by a much thicker anode (support layer) of about 500~1000 μm. A cathode is located on top of the electrolyte and has a thickness of about 100 μm. These three layers (with an overall thickness of around 600~1100 μm) comprises the PEN structure of the IT-SOFC, where most of the fuel cell processes take place. The anode-supported cell structure is believed to be viable option for IT-SOFCs by significantly reducing the electrolyte thickness.

The standard materials for the PEN are yttria-stabilized zirconia (YSZ) for the solid electrolyte, cermet mixture of nickel (Ni) and YSZ for the anode layers, and composite mixture of lanthanum strontium manganite (LSM) and YSZ for the cathode layers. YSZ is a ceramic material based on zirconium oxide and has high oxygen ion conductivity at high temperature. In addition, YSZ is widely used for thermal barrier coating due to its good chemical and mechanical stability at elevated temperatures. In the Ni/YSZ cermet anode, Ni provides electron conduction paths

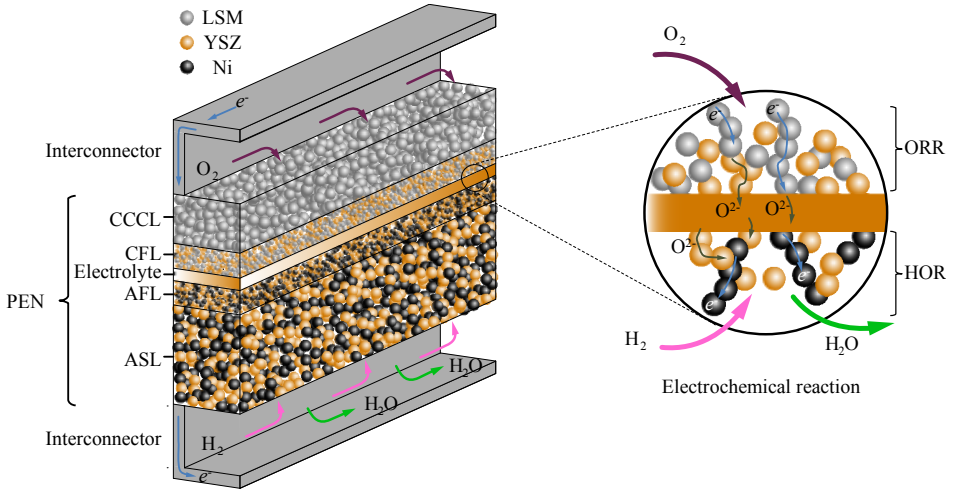

Fig. 2.1 Physical process in an anode-supported IT-SOFC with two-layer electrodes, operated with hydrogen and air.

and catalytic activity for hydrogen oxidation reaction (HOR), while YSZ provides ion conduction paths which greatly increase the TPBL inside the electrode. Similarly, in the LSM/YSZ composite cathode, LSM provides electron conduction paths and catalytic activity for oxygen reduction reaction (ORR). The inclusion of YSZ in the electrodes also increases their mechanical integrity as well as decreases the thermal expansion mismatch in the PEN structure.

In Fig. 2.1, the anode comprises of a thin anode functional layer (AFL) of about 20 μm thickness and a thick anode substrate layer (ASL) of about 500~1000 μm. Likewise, the cathode consists of a thin cathode functional layer (CFL) of about 20 μm thickness and another thin cathode current collector layer (CCCL) of about 50 μm. These functional layers are located near the electrolyte and made to have very fine particle sizes less than 0.5 μm. This increases the number of active TPB sites in the AFL and the CFL, thereby enhancing the efficiencies of the electrochemical reactions. Note that the core electrochemical processes in IT-SOFCs generally occur inside this 50 μm thin AFL/electrolyte/CFL structure.

The role of the ASL is to support all the other thin layers of the PEN on top of it and also to serve as the electron conduction and mass diffusion pathway. Likewise, the role of the CCCL is to conduct electrons and to transport oxygen molecules. Thus, both the ASL and the CCCL are made with larger electronic particles of diameters larger than 1 μm to improve the mass diffusion. To provide mechanical support, the ASL is generally made from cermet Ni/YSZ powder mixtures while the CCCL is made only with LSM particles. Thus, the electrodes in the PEN should provide proper electronic conductivity, ionic conductivity, and mass diffusivity, by carefully adjusting electronic phase (Ni and LSM), ionic phase (YSZ), and void phase (pore). Note that the solid electrolyte should be gas tight to reduce the efficiency loss due to fuel and oxidant crossover.

Placed between two PENs, an interconnect plate (or the so-called bipolar plate) are serve as a flow distributor for fuel and air gas and also an electronic conductor for connection of the PENs in series. It is also believed that the interconnect plate serves as an effective heat distributor which enables more uniform temperature distribution. In IT-SOFCs, metallic interconnect materials can be used thanks to the

relatively low operating temperatures. Thus, oxide-coated stainless steel alloys (SUS430) are extensively used for interconnect plates due to their good machinability and resistance to highly oxidizing environment (cathode side).

2.1.2 Fuel cell process

In Fig. 2.1, the basic fuel cell processes during the operation of the IT-SOFC with hydrogen and air are described. While air flows through the cathode flow channel, oxygen molecules (O_2) diffuse into the CCCL and finally reach the active TPBs in the CFL. On the other hand, electrons (e^-) flow from the interconnect plate to the CCCL and finally to the active TPBs. At the cathode TPBs, these oxygen molecules and electrons are combined to produce oxygen ions (O^{2-}), according to the ORR in Eq. (2.1), which are then transported towards the anode through the solid electrolyte. At the anode, hydrogen molecules (H_2) diffuse from the anode flow channel to the active TPBs in the AFL where these hydrogen molecules and oxygen ions are combined to produce water vapor (H_2O), according to the HOR in Eq. (2.2). The electrons separated from the oxygen ions move out of the anode along the electron conducting phase in the AFL and ASL and finally flow to the interconnect plate. The overall chemical reaction can be written as Eq. (2.3).

Cathode reaction: $$\frac{1}{2}O_2 + 2e^- \rightarrow O^{2-} \tag{2.1}$$

Anode reaction: $$H_2 + O^{2-} \rightarrow H_2O + 2e^- \tag{2.2}$$

Overall reaction: $$H_2 + \frac{1}{2}O_2 \rightarrow H_2O + (\text{Power}) + (\text{Heat}) \tag{2.3}$$

The overall fuel cell reaction of Eq. (2.3) is exothermic, i.e., heat is generated during the operation of SOFCs. When a SOFC is operated at the maximum thermodynamic efficiency, the reaction heat becomes lowest as the difference between the enthalpy of formation of water vapor and the Gibb's free energy. However, the maximum efficiency operation is only achievable when the cell voltage equals to the Nernst potential and thus the cell current approaches zero.

When the SOFC is operated at a finite current density, additional voltage loss is inevitable and the reaction heat increases accordingly. In IT-SOFCs fueled with hydrogen, this reaction heat is generally exhausted by the air stream that flows in the cathode interconnect.

2.1.3 Model configuration

The present 3D micro/macroscale model is developed by combining the microscale models for detailed electrode processes including microstructural characterization and the macroscale models for heat and mass transfer in electrodes, flow channels, and interconnect plates. Fig. 2.2 summarizes the components of the micro/macroscale model, including the electrode microstructure characterization, the continuum electrode model, and heat and mass transfer models. The electrode microstructure characterization offers the relationship between the electrochemical performance and the microstructure of electrodes, on the basis of the statistical percolation theory and coordination number theory for random binary mixtures of ionic and electronic particles. Then, effective phase conductivities and volume-specific TPBL of the electrodes are determined from the microstructural parameters including as porosity, phase composition, and particle sizes. This characterization is

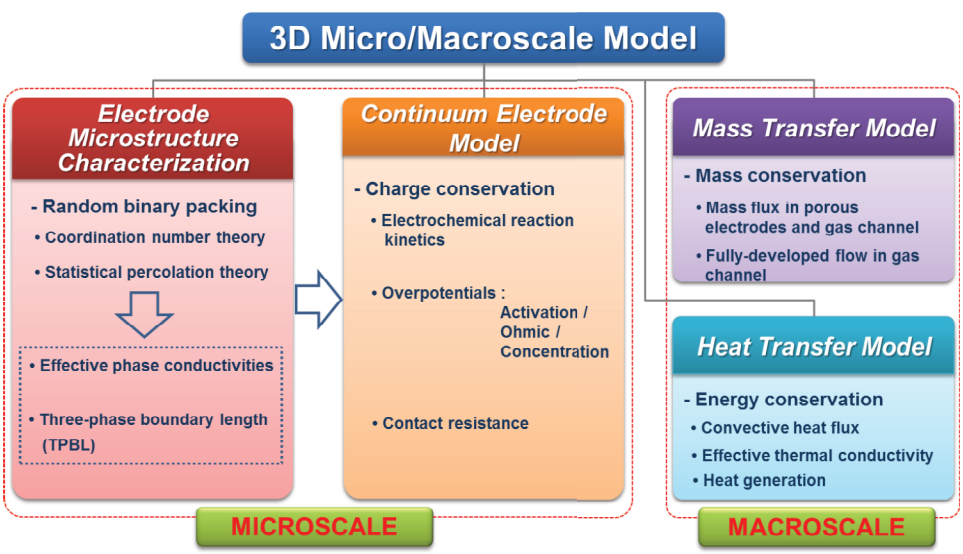

Fig. 2.2 Overall configuration of the present 3D micro/macroscale model.

an essential element for investigating the effects of the electrode microstructure on the performance of SOFCs.

The continuum electrode models, combined with the statistical microstructure characterization, have been widely used for detailed investigation of the transport phenomena and electrochemical reactions occurring inside the electrodes. The continuum electrode model solves the charge conservation equations in the electrodes, the electrolyte, and the interconnect plates, as required. The electronic potential is solved in the AFL, the ASL, the CFL, the CCCL, and the interconnect plates considering the contact resistance, whereas the ionic potential is solved in the AFL, the CFL, and the electrolyte. The electrochemical reactions at TPBs in the AFL and the CFL govern the consumption or generation of electrons and ions, which is included as the source or sink for electronic and ionic potential calculations. Thus, the continuum electrode model predicts the potential and resulting current distributions inside the SOFC by fully considering the activation, concentration, and ohmic overpotentials.

Recent studies demonstrated the possibility of direct fuel cell simulation based on actual phase distribution in electrodes measured by tomography technique. This approach is promising for characterizing a single electrode performance. However, this approach is not suitable for the objective of this study to investigate the performance of SOFCs with flow channel and interconnect geometry due to its high computational cost. Thus, the continuum electrode model in combination with the statistical microstructure characterization is a better choice for 3D micro/macroscale simulations.

Final elements of the present model are the heat and mass transfer models that can consider the macroscale flow channel effects. During the ordinary operation of planar IT-SOFCs, flow in straight gas channels readily converges to fully-developed laminar flow due to low flow rates and small channel dimensions. Assuming the fully-developed laminar velocity profiles, the convective heat and mass transport in gas channels can be easily determined without significant loss of accuracy. This simplification also enhances the solution efficiency by avoiding complicated fluid dynamics calculation for channel flow. The mass transport inside the porous

electrodes is calculated by the dusty-gas model (DGM) which considers the binary diffusion, Knudsen diffusion, and viscous flow.

The heat transfer model solves the energy conservation equation in the whole calculation domain. That is, heat transfer by conduction is considered in the solid electrolyte and the interconnect plates, while heat transfer by simultaneous conduction and convection is considered in the electrodes and the flow channels. The present model fully considered the heat generation by electrochemical reactions and Joule heating (including contact resistance), and thus achieved 0.0001% error in the energy balance in sensible and total enthalpies. Note that radiative heat transfer is not considered in the present model.

2.2 Electrode Microstructure Characterization

The electrodes in SOFCs are generally fabricated by mixing, compacting and sintering ceramic powders at high temperatures (around 1500°C). Thus, the microstructure of these electrodes has been successfully modeled as binary mixtures of electronic and ionic particles (with pores), such as Ni and YSZ particle mixtures for cermet anodes and LSM and YSZ particle mixtures for composite cathodes. The scanning electron microscope (SEM) images are used to investigate the electrode microstructures, from which the particle size and shape, pore size, and phase composition can be determined. These microstructural parameters are input to the present electrode characterization based on the coordination number theory. The average number of contacts (coordination number) between randomly packed binary spherical particles is estimated, from which the percolation probability for a phase to form globally connected clusters is calculated. The coordination number and phase percolation probability are essential to determine the effective phase conductivity and volume-specific TPBL inside the electrodes.

Several recent studies reported the direct reconstruction of 3D electrode microstructures using X-ray tomography or focused ion beam (FIB) SEM techniques. This approach allows in-depth investigation of actual phase distribution inside the electrodes. The reconstructed 3D structures enable accurate determination of the volume-specific TBPL by summing up the interfacial perimeter of the

electronic phase and ionic phase (open to pores). In addition, the effective phase conductivity is also accurately calculated through simple conduction analysis. This approach is promising but still subject to the errors related with the resolution of imaging techniques. It should be noted that the properties (phase conductivity and TPBL) determined by these reconstruction techniques can be properly used in the present micro/macroscale model.

2.2.1 Random packing of binary mixtures

When spherical particles of electronic and ionic phase are randomly packed, the average number of contacts (or the coordinate number) is dependent on the particle size and phase composition. The average number of contacts for electronic particles, Z_{el}, is calculated as (Bouvard and Lange, 1991)

$$Z_{\mathrm{el}} = 3 + \frac{Z-3}{n_{\mathrm{el}} + (1-n_{\mathrm{el}})\alpha^2}, \tag{2.4}$$

and that for ionic particles, Z_{io}, is also calculated as

$$Z_{\mathrm{io}} = 3 + \frac{(Z-3)\alpha^2}{n_{\mathrm{el}} + (1-n_{\mathrm{el}})\alpha^2}. \tag{2.5}$$

Here, Z denotes the average coordination number for all particles, which equals to six ($Z = 6$) for randomly packed spherical particles. In the above equations, α is the ratio of the ionic particle diameter to the electronic particle diameter ($\alpha \equiv d_{\mathrm{io}} / d_{\mathrm{el}}$). And n_{el} is the number fraction of electronic particles which is determined from the volume fraction of electronic phase, ϕ_{el}, and the particle size ratio, α, as

$$n_{\mathrm{el}} = \frac{\alpha^3 \phi_{\mathrm{el}}}{1 - \phi_{\mathrm{el}} + \alpha^3 \phi_{\mathrm{el}}}. \tag{2.6}$$

The number fraction of ionic particles is simply

$$n_{\mathrm{io}} = 1 - n_{\mathrm{el}}. \tag{2.7}$$

The average coordination number for i-phase particles to contact with j-phase particles is determined as

$$Z_{\mathrm{i-j}} = n_{\mathrm{j}} \frac{Z_{\mathrm{i}} Z_{\mathrm{j}}}{Z}. \tag{2.8}$$

The coordination number for the electronic-electronic contact pair, $Z_{\mathrm{el-el}}$, for the ionic-ionic contact pair, $Z_{\mathrm{io-io}}$, and for the electronic-ionic contact pair, $Z_{\mathrm{el-io}}$, can be calculated.

The percolation or the formation of globally connected particle network is closely related with the coordination number. For an electronic particle to work as a transport path for current, it should contact with at least two electronic particles. Studies showed that the percolation threshold for $Z_{\mathrm{i-i}}$ is about 1.764 for random packing of uniform size spheres. In this study, the percolation probability of the phase i particles, P_{i}, is calculated as (Bouvard and Lange, 1991)

$$P_{\mathrm{i}} = \left[1 - \left(\frac{4.236 - Z_{\mathrm{i-i}}}{2.472} \right)^{2.5} \right]^{0.4}, \tag{2.9}$$

where $Z_{\mathrm{el-el}}$ is used for the electronic phase and $Z_{\mathrm{io-io}}$ is for the ionic phase.

2.2.2 Effective conductivity

The effective electronic and ionic conductivities in porous electrodes are estimated as (Chen et. al., 2004)

$$\sigma_{\mathrm{i}}^{\mathrm{eff}} = \sigma_{\mathrm{i}}^{\mathrm{o}} \left[(1-\varepsilon)\phi_{\mathrm{i}} P_{\mathrm{i}} \right]^{m}, \tag{2.10}$$

where $\sigma_{\mathrm{i}}^{\mathrm{o}}$ is the intrinsic conductivity for i-phase materials, ε is the porosity of the electrode, ϕ_{i} is the volume fraction, P_{i} is the percolation probability form, m is the Bruggeman exponent (set as 1.5 in this study). Note that the $(1-\varepsilon)\phi_{\mathrm{i}} P_{\mathrm{i}}$ term is equal to the volume of i-phase particles that belong to the percolated clusters and the Bruggeman exponent is needed to consider the constriction effect at the particle contacts.

The intrinsic conductivities $\sigma_{\mathrm{i}}^{\mathrm{o}}$ for YSZ, Ni, and LSM are given as a function of temperature, T, as (Ferguson et al., 1996; Anselmi-Tamburini et al., 1996; Kiatkittpong et al., 2005)

$$\sigma_{\mathrm{YSZ}}^{\mathrm{o}} = 3.34 \times 10^{4} \exp\left(-\frac{10300}{T} \right), \tag{2.11}$$

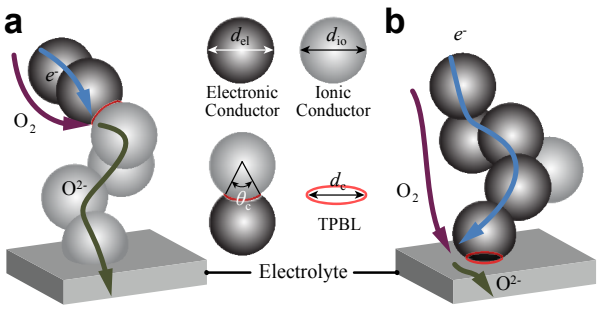

Fig. 2.3 The formation of TPBs (a) inside the electrode (volume-specific TPBL) and (b) at the electrode/electrolyte interface (area-specific TPBL).

$$\sigma^{o}_{Ni} = 3.27\times10^{6} - 1065.3T\,, \tag{2.12}$$

$$\sigma^{o}_{LSM} = \frac{8.855\times10^{7}}{T}\exp\left(-\frac{1082.5}{T}\right). \tag{2.13}$$

Note that the intrinsic conductivity for YSZ, σ^{o}_{YSZ}, is also used for the ionic conductivity of the electrolyte. In addition, the electronic conductivity of the interconnect plate (SUS 430) is given as (Chu and Ho, 1978)

$$\sigma^{\circ}_{SUS430} = 2.30\times10^{6} - 2591\,T + 1.15T^{2}\,, \tag{2.14}$$

where the range of the temperature is 300 to1200 K.

2.2.3 Three-phase boundary length

The three-phase boundary (TPB) denotes the interfacial line formed by the electronic phase, ionic phase, and pore phase. The electrochemical reactions are believed to occur at TPBs because all the elements (electrons, ions, and gas molecules) participating the electrochemical reactions coexist there. Fig. 2.3 shows two different TPBs formed in the electrode, inside the electrode volume and at the electrolyte/electrolyte interface area. In this study, the three-phase boundary length (TPBL) is determined utilizing the coordination number and the percolation probability presented above (Bounvard and Lange, 1991).

The TPBL formed inside the electrode is termed as the volume-specific TPBL, λ^{V}_{tpb}, and calculated as (Costamagna et al., 1998; Sunde, 2000)

$$\lambda_{\mathrm{tpb}}^{\mathrm{V}} = \pi d_{\mathrm{c}}^{\mathrm{V}} N_{\mathrm{t}} n_{\mathrm{io}} n_{\mathrm{el}} \frac{Z_{\mathrm{io}} Z_{\mathrm{el}}}{Z} P_{\mathrm{io}} P_{\mathrm{el}}, \tag{2.15}$$

where the number density (#/m^3) of all particles, N_{t}, is given as

$$N_{\mathrm{t}} = \frac{1-\varepsilon}{\frac{\pi}{6} d_{\mathrm{el}}^3 \left[n_{\mathrm{el}} + (1-n_{\mathrm{el}})\alpha^3 \right]}, \tag{2.16}$$

and the neck diameter, $d_{\mathrm{c}}^{\mathrm{V}}$, formed by the contact of electronic-ionic particle pairs is determined as

$$d_{\mathrm{c}}^{\mathrm{V}} = \sin\left(\frac{\theta_{\mathrm{c}}}{2}\right) \min(d_{\mathrm{io}}, d_{\mathrm{el}}). \tag{2.17}$$

Here, the contact angle of the particle contact, θ_{c} (shown in Fig. 2.3) is assumed to be 30° (Costamagna et al., 1998).

The TPBL formed at the electrode/electrolyte interface is termed as the area-specific TPBL, $\lambda_{\mathrm{tpb}}^{\mathrm{A}}$, which is calculated as (Nam and Jeon, 2006; Jeon et al., 2006)

$$\lambda_{\mathrm{tpb}}^{\mathrm{A}} = \pi d_{\mathrm{c}}^{\mathrm{A}} N_{\mathrm{t}} d_{\mathrm{el}} n_{\mathrm{el}} P_{\mathrm{el}}. \tag{2.18}$$

The $N_{\mathrm{t}} d_{\mathrm{el}} n_{\mathrm{el}} P_{\mathrm{el}}$ term is equal to the number of percolated electronic particles in the thickness of d_{el}. The neck diameter, $d_{\mathrm{c}}^{\mathrm{A}}$, formed by the contact of electronic particles to the electrolyte is determined as

$$d_{\mathrm{c}}^{\mathrm{A}} = \sin\left(\frac{\theta_{\mathrm{c}}}{2}\right) d_{\mathrm{el}}. \tag{2.19}$$

Note that the area-specific TPBL is much more active for electrochemical reactions than the volume-specific TPBL (Nam and Jeon, 2006; Jeon et al., 2006). This is because the oxygen ion conduction through ionic particles in the electrodes is relatively slow compared to the electron conduction through electronic particles. Thus, it is believed to be important to consider the area-specific TPBL accurately.

2.3 Continuum Electrode Model

From the viewpoint of the continuum mechanics, governing equations for the conservation of electrons and ions are derived. The electrochemical reaction kinetics are formulated based on the experimental data obtained using patterned Ni anodes and patterned LSM cathode on YSZ electrolytes. The variation of activation,

concentration, and ohmic overpotentials due to temperature and concentration change is fully taken into account in this model. In addition, the contact resistance at the interface of the electrode and the interconnect plate is also considered.

2.3.1 Charge conservation equations

The electronic and ionic charge conservation is described as

$$\nabla \cdot \mathbf{i}_{\mathrm{el}} \equiv \nabla \cdot \left(-\sigma_{\mathrm{el}}^{\mathrm{eff}} \nabla \varphi_{\mathrm{el}} \right) = +i_{\mathrm{tr}} \equiv +i_{\mathrm{tpb}} \lambda_{\mathrm{tpb}} , \tag{2.20}$$

$$\nabla \cdot \mathbf{i}_{\mathrm{io}} \equiv \nabla \cdot \left(-\sigma_{\mathrm{io}}^{\mathrm{eff}} \nabla \varphi_{\mathrm{io}} \right) = -i_{\mathrm{tr}} \equiv -i_{\mathrm{tpb}} \lambda_{\mathrm{tpb}} , \tag{2.21}$$

where $\mathbf{i}$ denotes the current vector, σ^{eff} denotes the effective electrical conductivity, φ denotes the electrical potential (electronic or ionic), i_{tr} is the volumetric transfer current density, i_{tpb} is the TPBL-specific transfer current density, and λ_{tpb} is the TPBL. Note that i_{tpb} is defined positive when electronic current is generated. In the numerical calculation, $\lambda_{\mathrm{tpb}}^{\mathrm{V}}$ is used for the volume cells inside the AFL or the CFL, and thus multiplying i_{tpb} (A/m) and $\lambda_{\mathrm{tpb}}^{\mathrm{V}}$ (m/m^3) results in the volumetric transfer current i_{tr} (A/m^3) for electronic potential. For the area cells at the AFL/electrolyte or CFL/electrolyte interfaces, $\lambda_{\mathrm{tpb}}^{\mathrm{A}}$ will be used and $i_{\mathrm{tr}} \equiv i_{\mathrm{tpb}} \lambda_{\mathrm{tpb}}^{\mathrm{A}}$ comes to have a unit of A/m^2.

2.3.2 Electrochemical reaction kinetics

The rate of an electrochemical reaction, the same as the transfer current i_{tpb}, is primarily dependent on the activation overpotential, η^{act}, and this is described by the fundamental relationship called the Butler-Volmer equation. Based on the experimental data for Ni pattern anodes formed on top of YSZ electrolytes (Bieberle et al., 2001), the TPBL-specific transfer current density for hydrogen oxidation reaction (HOR), $i_{\mathrm{tpb,A}}$, is formulated as

$$i_{\mathrm{tpb,A}} = i_{\mathrm{tpb,A}}^{\mathrm{ex}} \left[\exp\left(\frac{F}{RT} \eta_{\mathrm{A}}^{\mathrm{act}} \right) - \exp\left(-\frac{F}{RT} \eta_{\mathrm{A}}^{\mathrm{act}} \right) \right] , \tag{2.22}$$

where $i_{\mathrm{tpb,A}}^{\mathrm{ex}}$ is the anodic exchange current, $\eta_{\mathrm{A}}^{\mathrm{act}}$ is the activation overpotential, F is the Faraday constant (96485 C/mole), and R is the universal gas constant (8.314 J/mol-K).

The exchange current density, $i_{\mathrm{tpb,A}}^{\mathrm{ex}}$, is determined as (Nam and Jeon, 2006; Jeon et al., 2006)

$$\begin{cases} i_{\mathrm{tpb,A}}^{\mathrm{ex}} = \dfrac{RT}{2F}\dfrac{1}{r_{\mathrm{tpb,A}}} = \dfrac{RT}{2F}\dfrac{1}{1.645 p_{\mathrm{H_2}}^{-0.11} p_{\mathrm{H_2O}}^{-0.67} \exp\left(\dfrac{10212}{T}\right)}, & p_{\mathrm{H_2O}} \le 14{,}000 \\ i_{\mathrm{tpb,A}}^{\mathrm{ex}} = \dfrac{RT}{2F}\dfrac{1}{1.645 p_{\mathrm{H_2}}^{-0.11} 14{,}000^{-0.67} \exp\left(\dfrac{10212}{T}\right)}, & p_{\mathrm{H_2O}} > 14{,}000 \end{cases} \tag{2.23}$$

where p_{k} denotes the partial pressures of species k. In Eq. (2.23), and $r_{\mathrm{tpb,A}}$ corresponds to the linear charge transfer resistance at zero activation overpotential. Note that the exchange current density is a complex function of gas concentration and temperature.

The TPBL-specific transfer current density for oxygen reduction reaction (ORR), $i_{\mathrm{tpb,C}}$, is formulated as

$$i_{\mathrm{tpb,C}} = i_{\mathrm{tpb,C}}^{\mathrm{ex}}\left[\exp\left(\frac{2F}{RT}\eta_{\mathrm{C}}^{\mathrm{act}}\right) - \exp\left(-\frac{2F}{RT}\eta_{\mathrm{C}}^{\mathrm{act}}\right)\right], \tag{2.24}$$

and the exchange current density, $i_{\mathrm{tpb,C}}^{\mathrm{ex}}$, is determined as

$$i_{\mathrm{tpb,C}}^{\mathrm{ex}} = \frac{RT}{4F}\frac{1}{r_{\mathrm{tpb,C}}} = \frac{RT}{4F}\frac{1}{0.00136 p_{\mathrm{O_2}}^{-0.25} \exp\left(\dfrac{17401}{T}\right)}. \tag{2.25}$$

These equations are derived from the experimental data for LSM pattern cathodes formed on top of YSZ electrolytes (Radhakrishnan et al., 2005). Again $r_{\mathrm{tpb,C}}$ is the linear charge transfer resistance at negligible overpotential and current.

2.3.3 Overpotentials

The output voltage of SOFCs, φ^{cell}, is calculated by subtracting various overpotentials (potential loss) from the reversible potential, φ^{o}, as

$$\varphi^{\mathrm{cell}} = \varphi^{\mathrm{o}} - \eta^{\mathrm{act}} - \eta^{\mathrm{ohm}} - \eta^{\mathrm{conc}}, \tag{2.26}$$

where η^{act} is the activation overpotential, η^{ohm} is the ohmic overpotential, and η^{conc} is the concentration overpotential. The activation potential loss is originated from the activation energy barriers of electrochemical reactions. Secondly, the

concentration overpotential arises because the fuel gas concentration decreases at the reaction sites due to mass diffusion resistance as well as continuous consumption. Finally, the ohmic potential loss is due to the resistance for electron and ion conduction in the electrodes, electrolyte, and interconnect plates including the contact resistance.

The Nernst potential for the H_2-HO system is given as

$$\varphi^{\mathrm{o}} = -\frac{\Delta g_{\mathrm{f,H_2O}}(T)}{2F} + \frac{RT}{2F}\left[\frac{p^{\mathrm{o}}_{\mathrm{H_2}}}{p^{\mathrm{o}}_{\mathrm{H_2O}}} \cdot \left(\frac{p^{\mathrm{o}}_{\mathrm{O_2}}}{100{,}000}\right)^{1/2}\right], \tag{2.27}$$

where $\Delta g_{\mathrm{f,H_2O}}(T)$ is the Gibbs free energy of formation at the temperature T when the reactants and products are 1 bar in pressure. And the superscript o of partial pressures denotes the reference condition such as the inlet condition. In this study, the Gibbs free energy of formation for water vapor is calculated as

$$\Delta g_{\mathrm{f,H_2O}}(T) = 54.85T - 247340\,. \tag{2.28}$$

The concentration overpotential, η^{conc}, is dependent on the reduction of fuel and oxidant concentrations and the increase of product concentration. For the cathode, this is calculated as a function of oxygen partial pressure at the reaction sites as

$$\eta^{\mathrm{conc}}_{\mathrm{C}} = -\frac{RT}{4F}\ln\left(\frac{p_{\mathrm{O_2}}}{p^{\mathrm{o}}_{\mathrm{O_2}}}\right). \tag{2.29}$$

At the anode, the consumption of hydrogen and the production of water occurs simultaneously at the reaction site, and thus the anodic concentration overpotential is expressed as

$$\eta^{\mathrm{conc}}_{\mathrm{A}} = -\frac{RT}{2F}\ln\left(\frac{p_{\mathrm{H_2}}}{p^{\mathrm{o}}_{\mathrm{H_2}}} \cdot \frac{p^{\mathrm{o}}_{\mathrm{H_2O}}}{p_{\mathrm{H_2O}}}\right). \tag{2.30}$$

The activation overpotential is voltage loss due to the slow electrochemical reactions at TPBs in the AFL and the CFL. In this study, the activation overpotentials are defined as

$$\eta^{\mathrm{act}}_{\mathrm{A}} = \varphi_{\mathrm{el}} - \varphi_{\mathrm{io}} - \eta^{\mathrm{conc}}_{\mathrm{A}}, \tag{2.31}$$

$$\eta_{\mathrm{C}}^{\mathrm{act}} = \varphi_{\mathrm{io}} - \varphi_{\mathrm{el}} - \eta_{\mathrm{C}}^{\mathrm{conc}}, \tag{2.32}$$

where φ_{el} and φ_{io} denote the electronic potential and ionic phase potential, respectively. Then, these activation overpotentials are used to obtain the TPBL-specific transfer current density through the Butler-Volmer equations described in Eq. (2.22) and (2.24).

The ohmic overpotential is mainly caused by the electrolyte due to low oxygen ion conductivity. However, other cell components also contribute to the ohmic potential loss while conducting electrons or ions. In this study, the ohmic overpotential is implicitly calculated by solving the charge conservation equations in Eq. (2.20) and (2.21). Another important ohmic overpotential is originated from the contact resistance between the electrodes and the interconnect plates, which is believed to be considerable (Jiang et al., 2003). The metal interconnect plates are generally coated with thin protective films to resist the corrosion in highly oxidizing environment, which results in considerable contact resistance. From the measured data for LSM-coated SUS 430 substrates (Kim et al., 2004), the area-specific contact resistance r_{asr} (Ω-m^2) is derived as

$$r_{\mathrm{asr}} = 4.0 \times 10^{-13} T \exp\left(\frac{0.8F}{RT}\right). \tag{2.33}$$

Thus, the contact resistance, R_{c}, at an electrode/interconnect interface of area A is determined as

$$R_{\mathrm{c}} = \frac{r_{\mathrm{asr}}}{A}, \tag{2.34}$$

and included in the electron conservation calculation. Note that the contact resistance increases as the area increases.

2.4 Mass Transfer Model

The governing equations for the participating gas species are derived considering the ordinary diffusion, Knudsen diffusion, and Darcy permeation in the porous electrodes based on the dusty-gas model (DGM). In addition, the fully-developed laminar flow and ordinary diffusion in the gas channels are also considered using the prescribed velocity profiles for fully-developed laminar

channel flow. These calculations for the electrodes and the gas channels are matched on the basis of continuity of partial pressures and mass flux. The production and consumption of gas species due to the electrochemical reactions are included as the source terms.

2.4.1 Mass conservation equations

The mass conservation of gas species i is expressed as

$$\nabla \cdot \mathbf{n}_{\mathrm{i}} = \nabla \cdot (\mathbf{n}_{\mathrm{i}}^{\mathrm{v}} + \mathbf{n}_{\mathrm{i}}^{\mathrm{d}}) = i_{\mathrm{tpb}} \lambda_{\mathrm{tpb}} \beta_{\mathrm{i}}, \tag{2.35}$$

where $\mathbf{n}_{\mathrm{i}}$ denotes the molar flux (mol/m^2-s) of species i, $\mathbf{n}_{\mathrm{i}}^{\mathrm{v}}$ denotes the viscous convective flux, and $\mathbf{n}_{\mathrm{i}}^{\mathrm{d}}$ denotes the diffusive flux. The right-hand side (RHS) term, $i_{\mathrm{tpb}} \lambda_{\mathrm{tpb}} \beta_{\mathrm{i}}$, is the mass source for species i in the AFL and the CFL, which is the molar production/consumption rate due to the electrochemical relations at TPBs. Table 2.1 summarizes the variable β_{i} for the AFC and CFL. Note that β_{i} is zero in all the other regions.

Table 2.1 The mass production/consumption variable β_{i} for functional layers.

Regions	CFL		AFL	
Species	O_2	N_2	H_2	H_2O
β_{i}	$-\frac{1}{4F}$	0	$\frac{1}{2F}$	$-\frac{1}{2F}$

2.4.2 Mass flux in porous electrodes

The DGM is employed to predict the molar fluxes through porous electrodes considering parallel transport mechanisms of the ordinary diffusion, Knudsen diffusion, and viscous flow (Mason and Malinauskas, 1983; Krishna et al., 1997). The total molar flux in porous media is expressed as

$$\mathbf{n}_{\mathrm{i}} = \mathbf{n}_{\mathrm{i}}^{\mathrm{d}} + \mathbf{n}_{\mathrm{i}}^{\mathrm{v}}, \tag{2.36}$$

where $\mathbf{n}_{\mathrm{i}}^{\mathrm{d}}$ and $\mathbf{n}_{\mathrm{i}}^{\mathrm{v}}$ is the diffusive and viscous molar flux, respectively. The diffusion flux in the multicomponent system is described by the Maxwell-Stefan

equation written as (Krishna et al., 1997)

$$-\frac{1}{RT}\nabla p_{\mathrm{i}} = \frac{\mathbf{n}_{\mathrm{i}}^{\mathrm{d}}}{D_{\mathrm{iK}}^{\mathrm{eff}}} + \sum_{\mathrm{j}=1,\mathrm{j}\neq 1}^{n} \frac{x_{\mathrm{j}}\mathbf{n}_{\mathrm{i}}^{\mathrm{d}} - x_{\mathrm{i}}\mathbf{n}_{\mathrm{j}}^{\mathrm{d}}}{D_{\mathrm{ij}}^{\mathrm{eff}}}, \tag{2.37}$$

where p_{i} is the partial pressure of species i, x_{i} is the mole fraction, $D_{\mathrm{iK}}^{\mathrm{eff}}$ is the effective Knudsen diffusivity, and $D_{\mathrm{ij}}^{\mathrm{eff}}$ is the effective binary diffusivity for the i-j species pair. Note that the partial pressure, p_{i}, can is the product of mole fraction x_{i} and total pressure p_{t}. In Eq. (2.37), the LHS term accounts for the driving force for the diffusion of species i, while the RHS term account for the drag force acting on species i by porous structures and other gas molecules: the first term is for the Knudsen diffusion and the second term is for ordinary diffusion. The diffusive molar flux $\mathbf{n}_{\mathrm{i}}^{\mathrm{d}}$ is determined by rearranging this Maxwell-Stefan equation.

The effective Knudsen diffusivity for species i within the porous media is was determined as (Bird et al., 2002)

$$D_{\mathrm{iK}}^{\mathrm{eff}} = \left(\frac{\varepsilon}{\tau}\right) D_{\mathrm{iK}} = \frac{\varepsilon}{\tau}\frac{97}{2} d_{\mathrm{p}} \sqrt{\frac{T}{M_{\mathrm{i}}}}, \tag{2.38}$$

where ε is the porosity, τ is the tortuosity factor, M_{i} is the molecular mass (kg/kmol) for species i. And d_{p} is the mean pore diameter calculated as (assumed the same as the hydraulic diameter)

$$d_{\mathrm{p}} = \frac{4\varepsilon}{(1-\varepsilon)A_0}. \tag{2.39}$$

Here A_0 is the solid/fluid interfacial area per unit solid volume ($A_0 \equiv A_{\mathrm{sf}} / V_{\mathrm{s}}$), and calculated as

$$A_0 = \frac{6}{d_{\mathrm{el}}} \frac{n_{\mathrm{el}} + (1-n_{\mathrm{el}})\alpha^2}{n_{\mathrm{el}} + (1-n_{\mathrm{el}})\alpha^3}. \tag{2.40}$$

The binary diffusivity is determined from empirical correlation as (Fuller et al., 1966)

$$D_{\mathrm{ij}} = \frac{0.0143 T^{1.75}}{p_{\mathrm{t}} M_{\mathrm{ij}}^{1/2} \left(V_{\mathrm{i}}^{1/3} + V_{\mathrm{j}}^{1/3}\right)^2}, \tag{2.41}$$

where M_{ij} is the mean molar mass, defined as

$$M_{\mathrm{ij}} = 2\left(\frac{1}{M_{\mathrm{i}}} + \frac{1}{M_{\mathrm{j}}}\right)^{-1}, \tag{2.42}$$

and, V_{i} is the diffusion volume for species i. The relevant properties for gases are listed in Table 2.2. The effective diffusivity in porous material is then determined by using the porosity ε and tortuosity τ as (Williford et al., 2003)

$$D_{\mathrm{ij}}^{\mathrm{eff}} = \left(\frac{\varepsilon}{\tau}\right) D_{\mathrm{ij}}. \tag{2.43}$$

The viscous flux in porous media is determined by the Darcy law as (Karviany, 1999)

$$\mathbf{n}_{\mathrm{i}}^{\mathrm{v}} = -\frac{p_{\mathrm{i}}}{RT}\frac{K}{\mu}\nabla p_{\mathrm{t}} = c_{\mathrm{i}}\mathbf{u}_{\mathrm{i}}^{\mathrm{v}}, \tag{2.44}$$

where K is the permeability, μ is the dynamic viscosity of the gas mixture, c_{i} is the molar concentration of species i ($c = n/V$, $pV = nRT$) and $\mathbf{u}_{\mathrm{i}}^{\mathrm{v}}$ is the bulk velocity due to the viscous flow in porous media. The Kozeny-Carman correlation is used to determine the permeability, K, as as (Karviany, 1999)

$$K = \frac{\varepsilon^3}{k_{\mathrm{K}}(1-\varepsilon)^2 A_0^2} = \frac{\varepsilon^3}{5(1-\varepsilon)^2 A_0^2}. \tag{2.45}$$

Table 2.2 Diffusion volumes of gas molecules (Fuller et al., 1966).

Species	Molar mass (kg/kmol)	Diffusion volume
O_2	32	16.3
N_2	28.01	18.5
H_2	2.02	6.12
H_2O	18.02	13.1

2.4.3 Fully-developed laminar flow

The present micro/macroscale model assumes that the flow in the rectangular gas channels is close to the fully-developed and laminar. In addition, the viscous pressure drop (and accelerating and decelerating pressure drop) is assumed to be negligible and thus the total pressure inside the gas channel is constant. With this

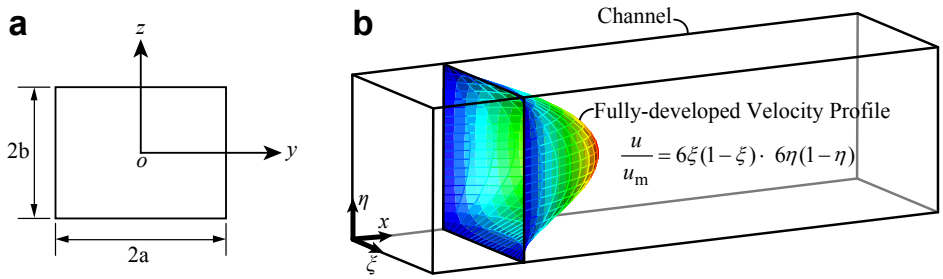

Fig. 2.4 Fully-developed laminar velocity profile: (a) coordinate system for flow channels with rectangular cross-sections, and (b) an exemplary velocity profile in a square flow channel.

assumption, complex fluid dynamics calculation for solving the continuity and Navier-Stokes equations can be put aside. The validity of this assumption can be checked by calculating the Reynolds number for gas channels, written as

$$\mathrm{Re}_{d_\mathrm{h}} = \frac{\rho u_\mathrm{m} d_\mathrm{h}}{\mu}. \tag{2.46}$$

Here u_m is the average flow speed, μ is the viscosity, and d_h is the hydraulic diameter of the channel ($d_\mathrm{h} = 4A/P$).

At temperature around 1000 K, the viscosity and the density of air (21% oxygen and 79% nitrogen) at 1 bar are estimated to be 4.32×10^{-5} Pa-s and 0.347 kg/m^3 (ideal gas law). For a square channel of 1 mm × 1 mm cross-section, the hydraulic diameter, d_h, is 1 mm. Then, the Reynolds number is estimated to be about 40 for the cathode channel flow with $u_\mathrm{m} = 5$ m/s. Note that the $u_\mathrm{m} = 5$ m/s at 1000 K roughly corresponds to the air flow rate that is required to produce the current density of 2.5 A/cm^2 in 10 cm long planar SOFCs (active area width is 2 mm).

The hydraulic entrance length, L_e, for laminar flow inside a channel can be estimated as

$$\frac{L_\mathrm{e}}{d_\mathrm{h}} \approx 0.06\,\mathrm{Re}_{d_\mathrm{h}}. \tag{2.47}$$

By substituting the Reynolds number, it is found that the hydraulic entrance length is very small and the whole channel flow can be assumed to be fully-developed. The

Reynolds number for fuel flow is always smaller than the air flow because of high fuel utilization factor in use as well as very small density and relatively high viscosity of hydrogen.

For a square duct with the edge length of H, a double parabolic velocity profile can be used as

$$\frac{u}{u_{\mathrm{m}}} = 6\xi(1-\xi)\cdot 6\eta(1-\eta),\ \ \xi = y/H,\ \ \eta = z/H, \tag{2.48}$$

where u_{m} is the mean fluid velocity in the duct. This profile is an approximation to the exact series expansion solution but has an error level of about 2~3%. Note that the origin of the coordinate is located at a vertex in Fig. 2.4(b).

A rectangular duct with $2a$ width and $2b$ height is shown in Fig. 2.2(a), where the origin of the coordinate is located at the center of the duct. Purday (1949) suggested an approximate velocity profile for fully-developed laminar flow across such rectangular ducts as

$$\frac{u}{u_{\max}} = (1-\xi^{s})(1-\eta^{r}),\ \ \xi = y/a,\ \ \eta = z/b, \tag{2.49}$$

where $u_{\max}$ is the maximum velocity at the center of the duct. This approximate profile is valid for the aspect ratio α_{ch} ($\alpha_{\mathrm{ch}} \equiv b/a$) less than unity. Nataragjan and Lakchmanan (1972) solved the momentum equation to determine the exponents s and r using the finite difference method and matched the obtained velocity profile to the empirical Eq. (2.49). The resulting relationships between the aspect ratio and the exponents are written as

$$s = 1.7 + 0.5\alpha_{\mathrm{ch}}^{-1.4}, \tag{2.50}$$

$$r = \begin{cases} 2 & \text{for } \alpha_{\mathrm{ch}} \le 1/3 \\ 2 + 0.3(\alpha_{\mathrm{ch}} - 1/3) & \text{for } \alpha_{\mathrm{ch}} > 1/3 \end{cases}. \tag{2.51}$$

Note that the Eq. (2.49) approximates the exact laminar velocity profile with an error of a few percent. By integrating Eq. (2.49) over the cross-sectional area of the duct, the mean velocity is calculated as

$$\frac{u_{\max}}{u_{\mathrm{m}}} = \left(\frac{s+1}{s}\right)\left(\frac{r+1}{r}\right). \tag{2.52}$$

Then, Eq. (2.33) can be rearranged as

$$\frac{u}{u_{\mathrm{m}}}=\left(\frac{s+1}{s}\right)\left(\frac{r+1}{r}\right)\left(1-|\xi|^{s}\right)\left(1-|\eta|^{r}\right),\quad \xi=y/a,\quad \eta=z/b\,. \tag{2.53}$$

2.4.4 Mass flux in gas channels

As explained above, this model assumes the fully-developed laminar flow in gas channels and an approximate laminar velocity profile is used instead of calculating the flow field in the channels. Then, the molar flux of species k in the axial direction (x-direction), $n_{\mathrm{x,k}}$, can be calculated as

$$n_{\mathrm{x,k}}=c_{\mathrm{k}}u=\frac{p_{\mathrm{k}}}{RT}u=x_{\mathrm{k}}c_{\mathrm{t}}u\,, \tag{2.54}$$

where c_{k} is the molar concentration of species k, x_{k} is the mole fraction, c_{t} is the total molar concentration ($c_{\mathrm{t}}=p_{\mathrm{t}}/RT$), and u is the prescribed fluid velocity in the axial direction.

The molar flux of species k in the transverse direction (y- and z-direction) is determined by considering the ordinary diffusion and viscous flow through the channel volume. Thus, the molar flux vector for species k, $\mathbf{n}_{\mathrm{k}}$, can be expressed by combining the axial and the transversal molar flux as

$$\mathbf{n}_{\mathrm{k}}=\mathbf{n}_{\mathrm{k}}^{\mathrm{d}}+\mathbf{n}_{\mathrm{k}}^{\mathrm{v}}=-\frac{1}{RT}D_{\mathrm{m,k}}\nabla^{\mathrm{yz}}p_{\mathrm{k}}-\frac{p_{\mathrm{k}}}{RT}\frac{K_{\mathrm{CH}}}{\mu}\nabla^{\mathrm{yz}}p_{\mathrm{t}}+\frac{p_{\mathrm{k}}}{RT}u\,\vec{\mathbf{e}}_{\mathrm{x}}\,, \tag{2.55}$$

where $D_{\mathrm{m,k}}$ is the effective diffusivity of species k (binary diffusivity for binary gases), K_{CH} is the permeability of the flow channel, ∇^{yz} is the horizontal del operator in the yz-plane, and $\vec{\mathbf{e}}_{\mathrm{x}}$ is the unit vector in the axial direction (x-direction). Note that K_{CH} acts as a constraint to make the total pressure in the channels close to the operating pressure, $p_{\mathrm{fuel}}^{\mathrm{o}}$ or $p_{\mathrm{air}}^{\mathrm{o}}$. In this study, K_{CH} is set to $200D_{\mathrm{m,k}}/p_{\mathrm{t}}$ considering the solution convergence.

If we add up the molar flux, $n_{\mathrm{x,k}}$, in Eq. (2.54) for all gas species, the total axial molar flux, $n_{\mathrm{x,tot}}$, is calculated as

$$n_{\mathrm{x,tot}}=\sum_{k}\left(x_{\mathrm{k}}\right)c_{\mathrm{t}}u=c_{\mathrm{t}}u\,, \tag{2.56}$$

which results in $n_{\mathrm{x,k}}=x_{\mathrm{k}}n_{\mathrm{x,tot}}$. Then, the total molar flow rate in the axial direction

through the channel, $N_{\mathrm{x,tot}}$, is obtained by integrating $n_{\mathrm{x,tot}}$ for the cross-sectional area, dA_{CH}, as

$$N_{\mathrm{x,tot}} = \int n_{\mathrm{x,tot}} dA_{\mathrm{CH}} \ . \tag{2.57}$$

In addition, $N_{\mathrm{x,tot}}$ can also be determined from the inlet to the outlet by considering the consumption and generation of gas species

Provided that molar flow rate at a cross-section i, $N^{\mathrm{i}}_{\mathrm{x,tot}}$, is known, the molar flow rate at the next cross-section $\mathrm{i}+1$, $N^{\mathrm{i+1}}_{\mathrm{x,tot}}$, is calculated as

$$N^{\mathrm{i+1}}_{\mathrm{x,\,tot}} = N^{\mathrm{i+1}}_{\mathrm{x,\,tot}} - \sum_{k} N^{\mathrm{i\sim i+1}}_{\mathrm{k,CH\rightarrow PEN}} \ . \tag{2.58}$$

Here, $N^{\mathrm{i\sim i+1}}_{\mathrm{k,CH\rightarrow PEN}}$ denotes the molar flow rate of species k that enters the PEN from the channel while gas flows from the cross-section i to $\mathrm{i}+1$. Thus, $N^{\mathrm{i}}_{\mathrm{x,tot}}$ for each cross-section i can be determined using the values of $N^{\mathrm{i\sim i+1}}_{\mathrm{k,CH\rightarrow PEN}}$ obtained during the previous iterative calculation.

Now consider a small cross-sectional area, dA_{j}, inside the channel cross-sectional area, dA_{CH}. Then, the axial flow rate through this small area, $N^{\mathrm{j}}_{\mathrm{x,tot}}$, can be calculated as

$$N^{\mathrm{j}}_{\mathrm{x,tot}} = \int n_{\mathrm{x,tot}} dA_{\mathrm{j}} = \frac{\int u dA_{\mathrm{j}}}{\int u dA_{\mathrm{CH}}} N_{\mathrm{x,tot}} = f_{\mathrm{j}} N_{\mathrm{x,tot}} \ , \tag{2.59}$$

where f_{j} is the fraction of volume flow rate through dA_{j} in the channel. Note that u is prescribed by Eq. (2.49) or (2.53) according to the fully-developed laminar flow assumption. Thus, f_{j} is calculated by integrating the prescribed velocity u over dA_{j} and dA_{CH}, and this calculation is needed to be conducted only once at the beginning of the calculation.

2.5 Heat Transfer Model

The governing equations for energy conservation should be solved for all calculation domains of IT-SOFCs. In solid domains such as the electrolyte and interconnect plates, conduction heat transfer is considered, whereas convection heat transfer due to mass diffusion is also considered for porous domains such as the anode and cathode. In the gas channels, conduction heat transfer through gas phase

Table 2.3 Molar specific heat of gas species.

Species	Specific heat [J/mol-K]
O_2	$c_{\mathrm{p,O_2}} = 34.850 - 57.975\tau + 203.68\tau^2 - 300.37\tau^3 + 231.72\tau^4 - 91.821\tau^5 + 14.776\tau^6$
N_2	$c_{\mathrm{p,N_2}} = 29.027 + 4.8987\tau - 38.040\tau^2 + 105.17\tau^3 - 13.56\tau^4 + 55.554\tau^5 - 10.350\tau^6$
H_2	$c_{\mathrm{p,H_2}} = 21.157 + 56.036\tau - 150.55\tau^2 + 199.29\tau^3 - 136.15\tau^4 + 46.903\tau^5 - 6.4725\tau^6$
H_2O	$c_{\mathrm{p,H_2O}} = 37.373 - 41.205\tau + 146.01\tau^2 - 217.08\tau^3 + 181.54\tau^4 - 79.409\tau^5 + 14.015\tau^6$

$\tau = T/1000$

and convection due to mass diffusion should be considered for transverse directions (y- and z-directions), while only convection heat transfer due to prescribed velocity profile is considered for axial direction (x-direction). The generation of heat due to the electrochemical reactions and Joule heating is fully taken into account. In addition, the contact resistance for heat transfer at the electrode/interconnect interfaces are also considered, including the resulting Joule heating sources.

2.5.1 Energy conservation equation

The governing equation for the energy conservation is expressed as

$$\nabla \cdot \left(\sum_{\mathrm{i}} \mathbf{n}_{\mathrm{i}} h_{\mathrm{i}}(T) - k_{\mathrm{eff}} \nabla T \right) = \dot{q}_{\mathrm{gen}}, \tag{2.60}$$

where $\mathbf{n}_{\mathrm{i}}$ is the molar mass flux, $h_{\mathrm{i}}(T)$ is the molar sensible enthalpy of species i, k_{eff} is the effective thermal conductivity, and $\dot{q}_{\mathrm{gen}}$ is the volumetric heat generation source of the related domain. Note that the term inside the parentheses on the LHS of Eq. (2.60) is the total heat flux q due to convection and conduction. The convective heat flux is calculated by summing up all the molar sensible heats of

gas species, while the conductive heat flux is calculated by the effective conductivity and temperature gradient.

The molar sensible enthalpy $h_{\mathrm{i}}(T)$ of species i is obtained by integrating the molar specific heat, $c_{\mathrm{p,i}}(T)$, as

$$h_{\mathrm{i}}(T) = \int_{T_{\mathrm{ref}}}^{T} c_{\mathrm{p,i}}(T^*)\, dT^* , \tag{2.61}$$

where T_{ref} is the reference temperature for the integration. In order to reduce the error associated with the integration, T_{ref} is set equal to the lower values between the fuel an air inlet temperatures. Note that inlet temperature is generally the lowest temperature observed inside the IT-SOFC. Table 2.3 summarizes the molar specific heat of gas species (Todd and Young, 2002; Hernandez-Pacheco and Mann, 2004).

2.5.2 Convective heat flux

In porous electrodes, the convective heat flux is easily calculated after the molar mass flux of gas species is determined. In general, this convective flux is much smaller than conductive heat flux because mass flux is low while thermal conductivity is high in porous electrodes. In numerical solution procedure, the convective heat flux in electrodes is generally treated as a source term in the resulting algebraic equation.

However, in gas channels, the convective heat flux in the axial direction, $q_{\mathrm{x,conv}}$, is dominant while those in the transverse directions are small. Thus, an solution approach different from that for the porous electrodes is required. From the fully-developed velocity profiles, the molar mass flux at the axial direction, $n_{\mathrm{x,tot}}$, is determined before. Using this $n_{\mathrm{x,tot}}$, the convective heat flux can be expressed as

$$q_{\mathrm{x,conv}} = n_{\mathrm{x,tot}} \bar{c}_{\mathrm{p,mix}} (T - T_{\mathrm{ref}}) , \tag{2.62}$$

Where $\bar{c}_{\mathrm{p,mix}}$ is the average specific heat of gas mixtures, defined as

$$\bar{c}_{\mathrm{p,mix}} = \frac{\sum_{\mathrm{i}} x_{\mathrm{i}} h_{\mathrm{i}}(T)}{T - T_{\mathrm{ref}}} . \tag{2.63}$$

Then, using the upwind numerical scheme, the $n_{\mathrm{x,tot}} \bar{c}_{\mathrm{p,mix}}$ term is retained on the coefficient matrix of the resulting algebraic equation. This makes the coefficient

matrix to be diagonally dominant assuring the convergence.

2.5.3 Effective thermal conductivity

The effective thermal conductivities of the porous and solid domains are summarized in Table 2.4. These values are compiled from literatures (Iwata et al., 2000; Iora et al., 2005). Note that the thermal contact resistance at the electrode/interconnect interfaces are also considered in this study.

Table 2.4 Effective thermal conductivity for porous and solid domains.

Material	Thermal conductivity [W/m-K]
Anode	6.0
Electrolyte	2.7
Cathode	11
Interconnect plate	25
Electrode/interconnect contact	0.1 [a]

[a] The thermal contact layer is assumed to have a spacing of 1 μm. Then area-specific thermal resistance amounts to 10^{-5} m^2-K/W.

Table 2.5 Thermal conductivity of gas species.

Species	Thermal conductivity [W/m-K]
O_2	$k_{O_2} = 0.01\times(-0.1857 + 11.118\tau - 7.3734\tau^2 + 6.7130\tau^3 - 4.1797\tau^4 + 1.4910\tau^5 - 0.2278\tau^6)$ [a]
N_2	$k_{N_2} = 0.01\times(-0.3216 + 14.810\tau - 25.473\tau^2 + 38.837\tau^3 - 32.133\tau^4 + 13.493\tau^5 - 2.2741\tau^6)$
H_2	$k_{H_2} = 0.01\times(1.5040 + 62.892\tau - 47.190\tau^2 + 47.763\tau^3 - 31.939\tau^4 + 11.972\tau^5 - 1.8954\tau^6)$
H_2O	$k_{H_2O} = 0.01\times(2.0103 - 7.9139\tau + 35.922\tau^2 - 41.390\tau^3 + 35.993\tau^4 - 18.974\tau^5 + 4.1531\tau^6)$

[a] $\tau = T/1000$

The effective thermal conductivity in the flow channels can be determined by molar averaging each gas species in the mixture as

$$k_{\mathrm{eff}} = \sum_{\mathrm{i}} x_{\mathrm{i}} k_{\mathrm{i}} \ , \tag{2.64}$$

where x_{i} is the mole fraction of gas species i and k_{i} is the thermal conductivity. Table 2.5 provides the correlations for the thermal conductivities of fuel cell gases, which are valid over the temperature range 273~1473K at ambient pressure (Todd and Young, 2002).

2.5.4 Heat generation

In IT-SOFCs, heat is generated by the electrochemical reaction and Joule heating due to electronic conduction, ionic conduction, and contact resistance. The total chemical energy in the fuel that is not converted into electric energy eventually released as heat and this increases the temperature of IT-SOFCs. The volumetric heat sources considered in this study are summarized in Table 2.6, where the reaction heat, $\dot{q}_{\mathrm{re}}$, and Joule heat, $\dot{q}_{\mathrm{joule}}$, are separately presented. The reaction heat is present only in the functional layers where the electrochemical reactions occur. In Table 2.4, $\Delta h_{\mathrm{f,H_2O}}(T_{\mathrm{ref}})$ is the enthalpy of formation of H_2O at the reference temperature, T_{ref}, and calculated as

$$\Delta h_{\mathrm{f,H_2O}}(T_{\mathrm{ref}}) = 10^{-3} \times \frac{-238.0392 - 0.07369004\, T_{\mathrm{ref}} - 2.072838 \times 10^{-6}\, T_{\mathrm{ref}}^{2}}{1 + 0.0002495145\, T_{\mathrm{ref}}} \ . \tag{2.65}$$

Thus, the term $\Delta h_{\mathrm{f,H_2O}}(T_{\mathrm{ref}})/2F$ is an imaginary potential if all the chemical energy of hydrogen at T_{ref} is completely converted into electricity, which is about 1.284 V at 1000 K.

Then, the reaction heat is calculated for the AFL by multiplying the volumetric transfer current density, i_{tr}, and the potential drop from $-\Delta h_{\mathrm{f,H_2O}}(T_{\mathrm{ref}})/2F + \varphi_{\mathrm{el}}$ to φ_{io}. Note that in the AFL, i_{tr} has negative values in general by definition. The reaction heat at CFL is also determined similarly as $+i_{\mathrm{tr}}(\varphi_{\mathrm{io}} - \varphi_{\mathrm{el}})$, which is the product of i_{tr} and the potential drop, $(\varphi_{\mathrm{io}} - \varphi_{\mathrm{el}})$. Besides the reaction heat, the Joule heat due to the conduction of ionic current and electronic current as well as the contact resistance is fully considered as provided in Table 2.6.

Table 2.6 Heat sources for calculation domains.

Region	Reaction heat $\dot{q}_{\mathrm{re}}$	Joule heat $\dot{q}_{\mathrm{joule}}$
Interconnect plate		$i_{\mathrm{el}}^2 r_{\mathrm{el}}$ [a]
ASL/Interconnect		$i_{\mathrm{el}}^2 r_{\mathrm{asr}}$ [b]
ASL		$i_{\mathrm{el}}^2 r_{\mathrm{el}}$
AFL	$-i_{\mathrm{tr}}(-\frac{\Delta h_{\mathrm{f,H_2O}}(T_{\mathrm{ref}})}{2F}+\varphi_{\mathrm{el}}-\varphi_{\mathrm{io}})$	$i_{\mathrm{el}}^2 r_{\mathrm{el}}+i_{\mathrm{io}}^2 r_{\mathrm{io}}$
Electrolyte		$i_{\mathrm{io}}^2 r_{\mathrm{io}}$
CFL	$+i_{\mathrm{tr}}(\varphi_{\mathrm{io}}-\varphi_{\mathrm{el}})$	$i_{\mathrm{el}}^2 r_{\mathrm{el}}+i_{\mathrm{io}}^2 r_{\mathrm{io}}$
CCCL		$i_{\mathrm{el}}^2 r_{\mathrm{el}}$
CCCL/Interconnect		$i_{\mathrm{el}}^2 r_{\mathrm{asr}}$

[a] For volume domains, the current density i [A/m^2] multiplied by $r=1/\sigma$ [Ω-m] results in volumetric heat source $i^2 r$ [W/m^3].

[b] For interface domains, the current density i [A/m^2] multiplied by r_{asr} [Ω-m^2] results in area heat source $i^2 r_{\mathrm{asl}}$ [W/m^2].

2.6 Computational Domain

A planar IT-SOFC is constructed by stacking many unit cells repeatedly to obtain a proper level of output power as shown in Fig. 2.5(a). In general, the output voltage of a unit cell in IT-SOFCs is around 0.7 V and this requires 100 unit cells connected in serial to attain 70 V. A repeating unit cell is shown in Fig. 2.5(a), which comprises of a PEN structure sandwiched by two interconnect plate. Gas channels are engraved in the both sides of the interconnect plates, through which the fuel and oxidant gases are transported. The interconnect ribs (or lands) are in contact with the PENs structure to complete the electrical circuit among the

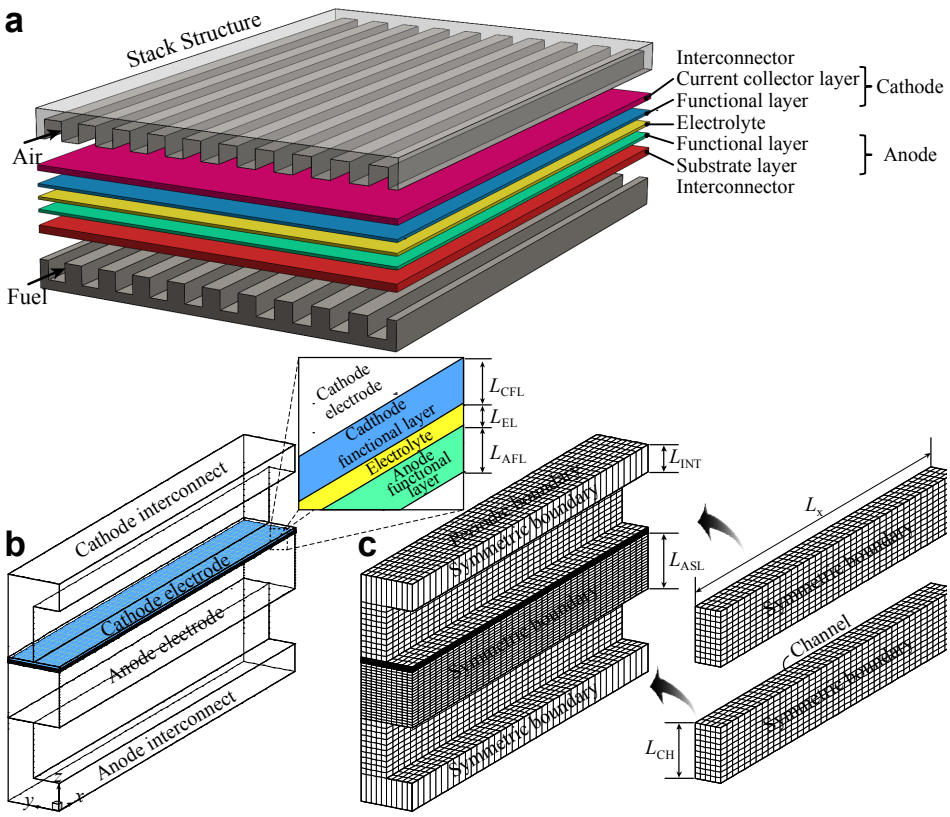

Fig. 2.5 The structure of an IT-SOFC with two layer electrodes: (a) repeating unit, (b) computational domain (half domain), and (c) grid structure.

repeated PENs.

In Fig. 2.5(a), the PEN is composed of an ASL, a AFL, a solid electrolyte layer, a CFL, and a CCCL. The ASL acts a thick support structure for the PEN, while it also transports electrons and gases. In addition, the ASL allows internal reforming when hydrocarbon fuels are used. The AFL and CFL are the main reaction layers where the electrochemical reactions occur, and the electrolyte transports oxygen ions from the cathode to the anode. The primary role of the CCCL is to delivering electrons and gases to the CFL from the interconnect plate and the gas channel.

The computational domain in the present micro/macroscale model is shown in Fig. 2.5(b), where only half channel/interconnect rib domain is considered. Note

Table 2.7 Standard microstructural and geometrical parameters.

Parameters	Values
Anode substrate layer: porous Ni/YSZ cermet	
Layer thickness, L_{ASL}	1 mm
Porosity, $\varepsilon_{\mathrm{ASL}}$	0.5
Tortuosity, $\tau_{\mathrm{ASL}} (= \tau_{\mathrm{AFL}} = \tau_{\mathrm{CFL}} = \tau_{\mathrm{CCCL}})$	3.0
Particle diameter, $d_{\mathrm{io,ASL}} (= d_{\mathrm{el,ASL}})$	1.0 μm
Electronic phase fraction, $\phi_{\mathrm{el,ASL}}$	0.5
Anode functional layer: porous Ni/YSZ cermet	
Layer thickness, L_{AFL}	20 μm
Porosity, $\varepsilon_{\mathrm{AFL}}$	0.25
Particle diameter, $d_{\mathrm{io,AFL}} (= d_{\mathrm{el,AFL}})$	0.5 μm
Electronic phase fraction, $\phi_{\mathrm{el,AFL}}$	0.5
Electrolyte: dense YSZ	
Layer thickness, L_{EL}	10 μm
Cathode functional layer: porous LSM/YSZ composite	
Layer thickness, L_{CFL}	20 μm
Porosity, $\varepsilon_{\mathrm{CFL}}$	0.25
Particle diameter, $d_{\mathrm{io,CFL}} (= d_{\mathrm{el,CFL}})$	0.5 μm
Electronic phase fraction, $\phi_{\mathrm{el,CFL}}$	0.5
Cathode current collector layer: porous LSM	
Layer thickness, L_{CCCL}	50 μm
Porosity, $\varepsilon_{\mathrm{CCCL}}$	0.5
Particle diameter, $d_{\mathrm{io,CCCL}} (= d_{\mathrm{el,CCCL}})$	1.0 μm
Electronic phase fraction, $\phi_{\mathrm{el,CCCL}}$	1.0
Gas channel	
Length, L_{x}	10 cm
Width, W_{CH}	1 mm
Height, L_{CH}	1 mm
Interconnect plate	
Half thickness above the channel, L_{INT}	0.5 mm
Rib width, W_{Rib}	1 mm

that this computational domain is sufficient to obtain the characteristics of IT-SOFC operations because of the symmetry (in the y- direction) and repeatedness (in the z- direction) of the stack structure. Thus, the symmetry conditions are imposed on the side boundaries of the domain for potential, mass, and energy calculation. In addition, equipotential conditions ($\varphi_{\mathrm{el}} = 0$ at the bottom boundary and $\varphi_{\mathrm{el}} = \varphi^{\mathrm{cell}}$ at the top boundary) are used for potential calculation and a periodic condition connecting the top and bottom boundaries is applied for energy calculation to simulate the repeated stack structure.

The detailed geometrical parameters for the computational domain are summarized in Table 2.7 (Zhao and Virkar, 2005; Jeon and Nam, 2006). The grid structure used for the calculation is illustrated in Fig. 2.5(c), where the grids for the porous and solid domains and those for the channel domains are separately presented. Note that an orthogonal structured grid is used. A typical grid has 40 cells in the x-direction, and 10 cells in the y-direction, like 5 cell under the channel and 5 cells under the interconnect rib. About 100 volume or interface cells are placed in the z-direction, including one for the electrolyte, 20 for the AFL and the CFL, 20 for the ASL, 10 for the CCCL, and 10 for each gas channel, and so on.

2.7 Operating and Boundary Conditions

To investigate the performance and operational characteristics of the anode-supported IT-SOFC, the simulations are conducted with the standard operating conditions given in Table 2.8. The standard inlet temperature, T^{o}, and pressure, p^{o}, is set to 700°C and 1 bar for both the fuel and air streams. However, in the parametric study, these are varied as from 600°C to 800°C or 1 bar to 3 bar according to the operating temperature ranges of IT-SOFCs. The standard fuel composition is set to 70% hydrogen and 30% water vapor, and the flow rate equivalent to 1.0 A/cm^2 in the active cell area is used. The standard current density is set to 0.65 A/cm^2, and thus the fuel gas utilization factor, ζ_{fuel}, amounts to 65%. Likewise, air composition of 21% oxygen and 79% nitrogen the flow rate equivalent to 4 A/cm^2 are used as the standard conditions. Thus, the air utilization factor, ζ_{air}, is 16.25%.

Table 2.8 Standard operating conditions.

Parameters	Values
Anode Fuel: H_2/H_2O mixture (0.7/0.3)	
Inlet temperature, $T_{\text{fuel}}^{\text{o}}$	700°C
Pressure, $p_{\text{fuel}}^{\text{o}}$	1 atm
Flow rate (limiting current density), $i_{\text{fuel}}^{\text{lim}}$	1.0 A/cm^2 equivalent
Fuel utilization, ζ_{fuel}	65%
Cathode Air: O_2/N_2 mixture (0.21/0.79)	
Inlet temperature, $T_{\text{air}}^{\text{o}}$	700°C
Pressure, $p_{\text{air}}^{\text{o}}$	1 atm
Flow rate (limiting current density), $i_{\text{air}}^{\text{lim}}$	4.0 A/cm^2 equivalent
Fuel utilization, ζ_{air}	16.25%

The boundary conditions for the momentum, energy and species conservation at the side and the top boundaries are explained previously and illustrated in Fig. 2.5(c). The mass flow rate and temperature conditions in Table 2.8 are imposed on the inlets of the fuel and air flow channels for the solution of mass and energy conservation. The standard outlet conditions are used for the outlet of the channels.

2.8 Model Validation

In order to validate the reliability of the developed model, the experiments for anode-supported IT-SOFCs with two-layer electrodes conducted by Zhao and Virkar (2006) are simulated. The simulation conditions are provided in Table 2.9, where all the properties except for the particle diameters are the measured values from the experiments. The tortuosity factor is assumed to be 3 for all the porous layers of the ASL, AFL, CFL, and CCCL. It should be noted Zhao and Virkar (2006) conducted the experiments using the single cells with mesh current collector. That is, there were no fuel or air channels in the experimented cells and thus cells are exposed to relatively uniform gas composition provided in Table 2.9. Thus, one-dimensional (1D) simulation model is prepared to consider the electrochemical reactions and transport processes only inside the PEN structure.

Table 2.9 Parameters used for model validation, from Zhao and Virkar (2006).

Parameters	Values
Anode substrate layer: porous Ni/YSZ cermet	
Layer thickness, L_{ASL}	1 mm
Porosity, $\varepsilon_{\mathrm{ASL}}$	0.48
Particle diameter, $d_{\mathrm{io,ASL}}(=d_{\mathrm{el,ASL}})$	1.0 μm[a]
Electronic phase fraction, $\phi_{\mathrm{el,ASL}}$	0.55
Anode functional layer: porous Ni/YSZ cermet	
Layer thickness, L_{AFL}	20 μm
Porosity, $\varepsilon_{\mathrm{AFL}}$	0.23
Particle diameter, $d_{\mathrm{io,AFL}}(=d_{\mathrm{el,AFL}})$	0.5 μm [a]
Electronic phase fraction, $\phi_{\mathrm{el,AFL}}$	0.55
Electrolyte: dense YSZ	
Layer thickness, L_{EL}	8 μm
Cathode functional layer: porous LSM/YSZ composite	
Layer thickness, L_{CFL}	20 μm
Porosity, $\varepsilon_{\mathrm{CFL}}$	0.26
Particle diameter, $d_{\mathrm{io,CFL}}(=d_{\mathrm{el,CFL}})$	0.5 μm [a]
Electronic phase fraction, $\phi_{\mathrm{el,CFL}}$	0.475
Cathode current collector layer: porous LSM	
Layer thickness, L_{CCCL}	50 μm
Porosity, $\varepsilon_{\mathrm{CCCL}}$	0.45
Particle diameter, $d_{\mathrm{io,CCCL}}(=d_{\mathrm{el,CCCL}})$	1.0 μm [a]
Electronic phase fraction, $\phi_{\mathrm{el,CCCL}}$	1.0
Operating conditions	
Mole fraction of hydrogen and fuel pressure, $x^{\circ}_{\mathrm{H_2}}$, $p^{\circ}_{\mathrm{fuel}}$	0.97, 1 bar
Mole fraction of oxygen and air pressure inlet, $x^{\circ}_{\mathrm{O_2}}$, $p^{\circ}_{\mathrm{O_2}}$	0.21, 1 bar

[a] Estimated values

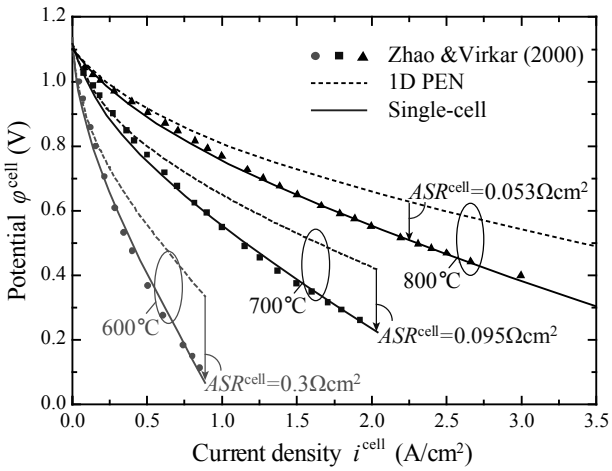

Fig. 2.6 Validation of the micro/macroscale SOFC model

Fig. 2.6 compares the current–voltage ($I-V$) curves experimentally measured by Zhao and Virkar (2006) and those obtained by the present 1D simulation model. In Fig. 2.6, symbols denote the experimental points while dashed lines denote the numerically determined $I-V$ curves of the PEN structure. The single cell current–voltage curves are then calculated (shown as solid lines) by considering the additional voltage loss due to the contact resistance at the current collector meshes. The area-specific contact resistance, ASR^{cell}, of 0.053 Ω-cm^2 for 800°C and 0.095 Ω-cm^2 for 700°C is the actual values suggested by Zhao and Virkar (2006), while 0.3 Ω-cm^2 for 600°C is the estimated value to fit the performance curves. The coefficient of determination, R^2, is also calculated, which is found to be 0.998 for 800°C, 0.994 for 700°C, and 0.993 for 600°C. These values are believed to be very high to assure the validity and accuracy of the present model.

2.9 Model Comparison (Two- vs. Three-dimensionality)

Previously, Sohn et al. (2010) developed a two-dimensional (2D) micro/macroscale model and utilized it to study the current–voltage performance characteristics of hydrogen-fueled IT-SOFCs, as shown in Fig. 2.7. As mentioned earlier, the 3D micro/macroscale models presented in this dissertation are the direct extension of the 2D model by Sohn et al. (2010) to consider the 3D channel and interconnect plate geometries. The simulation results obtained by the 2D

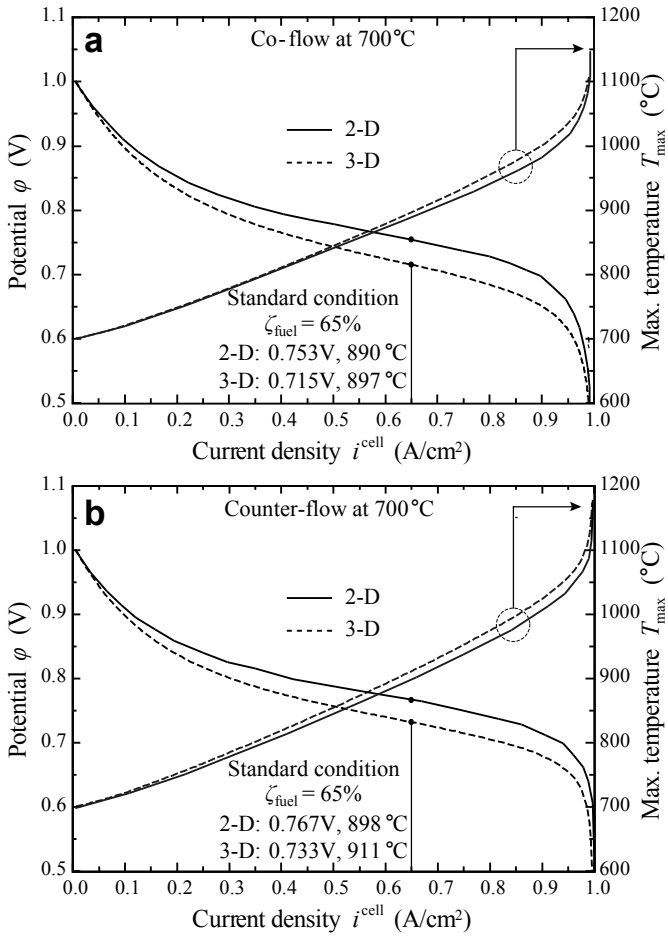

Fig. 2.7 The comparison of the current–voltage performance curves for IT-SOFCs predicted by the previous 2D micro/macroscale model and the present 3D model: (a) co-flow configuration and (b) counter-flow configuration

micro/macroscale model were very useful to investigate the effects of fuel and air flow on the overall performance characteristics. However, those results were only accepted as qualitative results since the 3D geometries of planar IT-SOFCs could not be considered properly in the 2D framework.

The present 3D micro/macroscale models resolve such dimensional limitation, while the accuracy and detailedness of the previous 1D microscale and 2D micro/macroscale models is preserved. Fig. 2.7 compares the current–voltage performance curves obtained by the 2D micro/macroscale model from Sohn et al. (2010) and the 3D model of the present study. In general, the 2D model is found to

overestimate the cell potential compared the 3D model, which is believed to be the result of ignoring the 3D geometries of the interconnect plates and flow channels in planar IT-SOFCs. The interconnect rib geometry hinders the oxygen transport toward the under-rib regions of the CFL, causing higher concentration polarization and lower current generation there. In addition, the contact resistance at the contact area of the PEN and interconnect plate ribs cannot be properly considered in the 2D model.

Another dimensional limitation of the 2D micro/macroscale model is that heat transfer cannot be properly taken into account. The maximum temperature inside the IT-SOFCs is shown in Fig. 2.7, where the temperature predicted by the 2D model is lower than that by the 3D model. In the 2D model, the PEN is assumed to directly face the flow channel because the consideration of the interconnect rib geometry is not possible. Then, the cooling effects due to the fuel and air flow in the channels are essentially exaggerated, resulting in lower values for the maximum temperature. Considering the important of temperature distribution for the fuel cell processes, the development of the 3D micro/macroscale model in this study is duly justifiable.

However, the 2D micro/macroscale model is observed to still well grasp the qualitative trend for the performance of IT-SOFCs as indicated in Fig. 2.7. Thus, the 2D model can also be used to investigate the effects of certain parameters on the cell performance with much lower computational cost than the 3D model.

CHAPTER 3
HYDROGEN-FUELED IT-SOFC

In this chapter, the micro/macroscale model explained in the previous chapter is used to simulate the steady operation of planar, anode-supported, intermediate-temperature solid oxide fuel cells (IT-SOFCs) working with hydrogen and air. The geometrical model for IT-SOFCs is constructed based on the actual shapes and dimensions as a PEN structure sandwiched by two (half) interconnect plates with flow channels and contact ribs. The cell length is set to 10 cm, and the square channel width (or equally the channel height) is set to 1 mm, and the rib width is set to 1 mm. The gas channels are assumed to be straight in the axial flow direction. Then, the size of the computational domain becomes 10 cm (cell length) in the axial x-direction, 1 mm (half channel width, 0.5 mm, and half rib width, 0.5 mm) in the transverse y-direction, and 4.1 mm (PEN thickness, 1.1 mm, and interconnect plate thickness, 3 mm) in the transverse z-direction.

The properties needed for calculation are derived from the observed microstructural parameters from previous experimental researches. The electrode microstructure characterization uses these parameters to determine the effective phase conductivities, volume-specific three-phase boundary length (TPBL), and the mean pore diameters of the porous electrodes. The continuum electrode models solves the charge conservation inside the PEN as well as in the interconnect plates. The electrochemical reaction rates at the TPBs are determined by using the experimental reaction kinetics data for Ni pattern anodes and LSM pattern cathodes. The macroscale heat and mass transport processes are also fully considered by directly prescribing the fully-developed laminar velocity profiles in gas channels.

The simulations are performed for the base case operating condition at 700°C and 1 bar to investigate the effects of co- and counter-flow configuration for fuel and air. The overall current–voltage curves as well as activation, concentration, and ohmic potential losses are studied. In addition, the local distribution of temperature, concentration, and current production is also investigated in detail. In general, the capability of the present 3D micro/macroscale model in predicting the performance

and operational characteristics of IT-SOFCs is fully demonstrated.

3.1 Introduction

The electrochemical reactions inside IT-SOFCs are completed by the oxygen reduction reaction (ORR) at the cathode and the hydrogen oxidation reaction (HOR) at the anode. The ORR occurs at the three phase boundaries (TPBs) of LSM/YSZ particles inside the cathode functional layer (CFL). As a result of the ORR, oxygen ions (O^{2-}) are produced. These oxygen ions move towards the anode through the solid electrolyte of ion conducting YSZ. The HOR occurs at the TPBs inside the anode functional layer (AFL) made of Ni/YSZ particles. During the HOR, oxygen ions combine with hydrogen molecules to produce water vapor. The overall fuel cell reaction can be expressed simply as

$$H_2 + \frac{1}{2}O_2 \rightarrow H_2O + (\text{Power}) + (\text{Heat}), \tag{3.1}$$

where electric power and heat is generated due to the reaction.

The major advantages of SOFCs include fuel flexibility; a wide variety of hydrocarbon fuels such as methane, gasoline, diesel, ethanol, etc. can be direct used (Singhal, 2000; Atkinson, 2004). However, these hydrocarbon fuels should generally be prepared in fuel processing units such as pre-reformers before supplied to fuel cell stacks. Hydrogen is still an attractive option for the small-scale application because hydrogen-fueled SOFCs have higher efficiency, cleaner emission, and simpler system configuration. In this chapter, the performance and operating characteristics of hydrogen-fueled IT-SOFCs are investigated in detail using the 3D micro/macroscale model. The extension of the model towards methane-fueled IT-SOFCs will be explained in chapter 5 along with the calculation results.

3.2 Model Description

In this chapter, the 3D micro/macroscale model is used for predicting the performance of the H_2-fueled IT-SOFC. This model has been successfully validated by comparison with the available experimental results in chapter 2. As described

previously, the 3D micro/macroscale consists of the electrode microstructure characterization, the continuum electrode model for charge transport and electrochemical reactions in the PEN, the mass transfer model for gas diffusion and flow in the electrodes and gas channels, and the heat transfer model for conductive and convective transport of reaction heat (including Joule heat). Thus, the model solves coupled governing equations for the conservation of electrons, ions, gas species, and energy, with aid of constitutive models for effective transport properties and source terms dependent on the electrochemical reactions at TPBs.

3.2.1 Computational model

The computational model of planar IT-SOFCs is shown in Fig. 3.1. The model considers a repeating unit cell in stack structure composed of a PEN and two half interconnect plates with gas channels and ribs. Note that only half channel and half

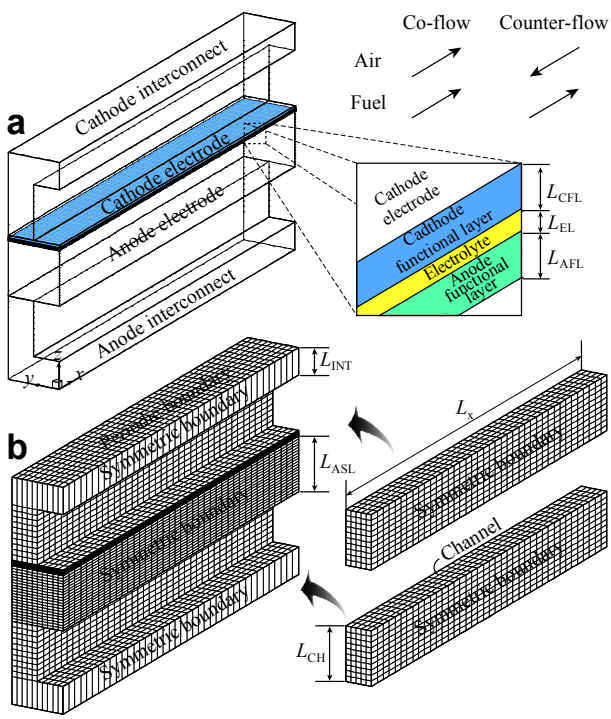

Fig. 3.1 The computational model: (a) an IT-SOFC with two layer electrodes, and (b) its grid structure.

rib regions are considered, by imposing the symmetric conditions on the side boundaries. In Fig. 3.1, the domain is divided into several regions: the anode supported layer (ASL), anode functional layer (AFL), electrolyte, cathode functional layer (CFL), cathode current collector layer (CCCL), gas channels (GCs), and interconnect plates. The detailed geometric parameters for the SOFC are summarized in Table 2.6.

The grid structure used in the calculation is also shown in Fig. 3.1(b), where each volume cell in the grid is generated to be orthogonal and structured. Uniform-sized 40 volume cells are placed in the axial direction (x-direction), whereas 10 volume cells are placed (five cells under the GC and five cells under interconnect rib) in the transverse direction (y-direction). Across the thickness of the PEN (z-direction), many volume and interface cells are generated to consider the different physical characteristics of the layers. Thus, the number of volume cells in the z-direction is 10 for the GCs (or equally for ribs), 20 for the ASL, 20 for the AFL, 1 for the electrolyte, 20 for the CFL, 10 for the CCCL, and 1 for the interconnect plate region above the channel). Then, the number of volume cells in the computational grid becomes 37200, excluding the number of interface cells. Note that periodic condition for temperature continuity is used for the top and bottom boundaries.

3.2.2 Governing equations

The governing equations and related constitutive models for the conservation of heat, mass, and charges are fully explained in the previous chapter. Here, governing equations will be presented in the discretized forms according to the finite volume method.

The discretized equation for the conservation of electronic charge for a cell i can be written as

$$\sum_{\mathrm{j=ewnstb}} I_{\mathrm{el,i\rightarrow j}} = +I_{\mathrm{tr,i}}, \tag{3.2}$$

where $I_{\mathrm{el,i\rightarrow j}}$ denotes the electronic current (A≡C/s) from the cell i to a cell j, and $I_{\mathrm{tr,i}}$ denote the transfer current due to electrochemical reaction (from ionic current to electronic current) in the cell i. The electronic current can be expressed

as

$$I_{\mathrm{el,i\to j}} = \sigma_{\mathrm{el}}^{\mathrm{eff}} \frac{\varphi_{\mathrm{el,i}} - \varphi_{\mathrm{el,j}}}{l_{\mathrm{ij}}} A_{\mathrm{ij}}, \tag{3.3}$$

where $\sigma_{\mathrm{el}}^{\mathrm{eff}}$ is the effective electronic conductivity, $\varphi_{\mathrm{el,i}}$ and $\varphi_{\mathrm{el,j}}$ are the electronic potential at the cell i and j, l_{ij} is the conduction length between the cell i and j, and A_{ij} is the conduction area. Likewise, the transfer current is also expressed as

$$I_{\mathrm{tr}} = i_{\mathrm{tpb,i}} \lambda_{\mathrm{tpb,i}} \Delta V_{\mathrm{i}}, \tag{3.4}$$

where ΔV_{i} is the volume of the cell i. Then, governing equations for charge conservation can be discretized as

$$\sum_{\mathrm{j=ewnstb}} \sigma_{\mathrm{el}}^{\mathrm{eff}} \frac{\varphi_{\mathrm{el,i}} - \varphi_{\mathrm{el,j}}}{l_{\mathrm{ij}}} A_{\mathrm{ij}} = +i_{\mathrm{tpb,i}} \lambda_{\mathrm{tpb,i}} \Delta V_{\mathrm{i}}, \tag{3.5}$$

$$\sum_{\mathrm{j=ewnstb}} \sigma_{\mathrm{io}}^{\mathrm{eff}} \frac{\varphi_{\mathrm{io,i}} - \varphi_{\mathrm{io,j}}}{l_{\mathrm{ij}}} A_{\mathrm{ij}} = -i_{\mathrm{tpb,i}} \lambda_{\mathrm{tpb,i}} \Delta V_{\mathrm{i}}. \tag{3.6}$$

Note that $i_{\mathrm{tpb,i}}$ is a function of activation overpotential, η^{act}, as well as the temperature and concentration in the cell i.

The mass conservation of gas species k in the cell i is written as

$$\sum_{\mathrm{j=ewnstb}} N_{\mathrm{k,i\to j}} = +\beta_{\mathrm{k}} I_{\mathrm{tr,i}}, \tag{3.7}$$

where $N_{\mathrm{k,i\to j}}$ denotes the molar flow rate (mol/s) of species k from the cell i to j, and β_{k} denote a modifying constant convert the transfer current to molar mass source. β_{k} has different values depending on the domain such as $1/2F$ for hydrogen and $-1/2F$ for water vapor in the AFL, and $-1/4F$ for oxygen and zero for nitrogen in the CFL. The calculation of $N_{\mathrm{k,i\to j}}$ is done by considering the ordinary and Knudsen diffusion and Darcy permeation in the electrodes, or the ordinary diffusion and prescribed velocity profiles in the GCs.

The energy conservation equation is also discretized as

$$\sum_{\mathrm{j=ewnstb}} Q_{\mathrm{i\to j}} = \dot{Q}_{\mathrm{gen,i}}, \tag{3.8}$$

where $Q_{\mathrm{i}\to\mathrm{j}}$ denotes the heat flow (W) from the cell i to j, and $\dot{Q}_{\mathrm{gen,i}}$ denote the heat source in the cell i due to reaction heat and Joule heat. The heat flow can be expressed as

$$Q_{\mathrm{i}\to\mathrm{j}} = k_{\mathrm{eff}} \frac{T_{\mathrm{i}} - T_{\mathrm{j}}}{l_{\mathrm{ij}}} A_{\mathrm{ij}} + \sum_{\mathrm{k}} h_{\mathrm{k}}(T_{\mathrm{ij}}) N_{\mathrm{k,i}\to\mathrm{j}} \,, \tag{3.9}$$

where k_{eff} is the effective thermal conductivity, T_{i} and T_{j} are the temperature at the cell i and j, and $h_{\mathrm{k}}(T_{\mathrm{ij}})$ is the sensible enthalpy of gas species k at the cell interface temperature T_{ij}. The average temperature is used for T_{ij} for the electrode as $T_{\mathrm{ij}} = (T_{\mathrm{j}} + T_{\mathrm{j}})/2$, whereas the upwind temperature is sued for the GCs.

3.2.3 Operating and boundary conditions

The operating conditions considered in the 3D micro/macroscale simulations are summarized in Table 3.1. Note that these conditions are selected by referring to the normal operating conditions for planar IT-SOFC fueled with hydrogen. In Table 3.1, the inlet conditions for hydrogen in the anode and air for the cathode are fixed at 700°C in temperature and 1 bar in pressure. The concentration of hydrogen in the fuel gas stream is set to 70% (with 30% H_2O concentration) and that of oxygen in the air stream is set to 21% (with 79% N_2 concentration). The flow rate for the fuel gas is set equivalent to the limiting current density of 1 A/cm^2 for the active area, while that for the air is set to 4 A/cm^2. Then, at the standard operating current density of 0.65 A/cm^2, the fuel utilization factor amounts to 65% while air utilization factor is only around 16%.

The boundary conditions have been briefly explained with Fig. 3.1, which are summarized in Table 3.2. The side boundaries normal to the y-coordinate are treated as the symmetric planes for the charge, mass, and energy conservation. The operating temperature, pressure, and concentration in Table 3.1 are prescribed as the inlet conditions for the fuel and air channels. The equipotential conditions are imposed for the electronic potential calculation as $\varphi_{\mathrm{el}} = 0$ for the bottom boundary and $\varphi_{\mathrm{el}} = \varphi^{\mathrm{cell}}$ for the top boundary. These top and bottom boundaries are logically connected in the grid structure to apply periodic boundary conditions for energy conservation equations.

Table 3.1 Standard operating conditions.

Parameters	Values
Air: O_2/N_2 mixture	
Inlet temperature, T^{o}_{air}	700°C
Pressure, p^{o}_{air}	1 atm
Oxygen mole fraction, $x^{o}_{O_2}$	0.21
Flow rate (limiting current density), i^{lim}_{air}	4 A/cm^2 equivalent
Fuel utilization, ζ_{air}, at 0.65 A/cm^2	16.25 %
Fuel: H_2/H_2O mixture	
Inlet temperature, T^{o}_{fuel}	700°C
Pressure, p^{o}_{fuel}	1 atm
Hydrogen mole fraction , $x^{o}_{H_2}$	0.70
Flow rate (limiting current density), i^{lim}_{fuel}	1 A/cm^2 equivalent
Fuel utilization, ζ_{fuel}, at 0.65 A/cm^2	65 %

Table 3.2 Standard boundary conditions.

Boundary	Location	Condition
Side	$y = 0$ & $(W_{CH} + W_{RIB})/2$	Symmetric BC: $d(\bullet)/dy = 0$
Inlet	$x = 0$ in GC region	Inlet BC: T^{o}, p^{o}, x^{o}, $N^{o}_{x,tot}$ prescribed
Outlet	$x = L_{cell}$ in GC region	Outlet BC: $d(\bullet)/dx = 0$
Bottom	$z = 0$	$\varphi_{el} = 0$ for electronic potential, φ_{el} Periodic BC for temperature, T
Top	$z = H_{cell}$	$\varphi_{el} = \varphi^{cell}$ for electronic potential, φ_{el} Periodic BC for temperature, T

3.3 Results and Discussions

3.3.1 Current–voltage characteristics

Fig. 3.2 shows the simulated current–voltage characteristics ($I-V$ curves) for the IT-SOFCs with co-flow and counter-flow configuration operated at 700°C. In Fig. 3.2, the maximum temperature generally observed in the electrolyte near the air outlet is also presented. The contribution of each overpotential to the total potential loss from the Nernst potential, φ°, to the cell potential, φ^{cell}, can be identified. It should be noted that φ° is defined inside the AFL as a function of local temperature, T, and inlet concentration, $p^{\text{o}}_{\text{H}_2}$, $p^{\text{o}}_{\text{H}_2\text{O}}$, and $p^{\text{o}}_{\text{O}_2}$, as

$$\varphi^{\text{o}} = -\frac{\Delta g_{\text{f,H}_2\text{O}}(T)}{2F} + \frac{RT}{2F}\left[\frac{p^{\text{o}}_{\text{H}_2}}{p^{\text{o}}_{\text{H}_2\text{O}}}\cdot\left(\frac{p^{\text{o}}_{\text{O}_2}}{100{,}000}\right)^{1/2}\right]. \tag{3.10}$$

However, φ° shown in Fig. 3.2 is an representative value obtained by averaging φ° at the anode/electrolyte interface throughout the reaction area. In Figs. 3.2(a) and (b), φ° is observed to decrease with respect to the cell current density, i^{cell}. This is because the Gibb's free energy, $\Delta g_{\text{f,H}_2\text{O}}(T)$, decreases as the cell temperature increases according to i^{cell}.

In Fig. 3.2, the subscripts A, C, and E attached to the overpotential, η, denote the anode, the cathode, and the electrolyte, respectively, whereas the superscripts asr, act, and conc denote the electrode/interconnect contact, the activation polarization, and the concentration polarization. The cell potential curves clearly exhibit the performance characteristics of IT-SOFCs, consisting of initial steep potential drop at low current densities (the activation loss dominant region), final steep potential drop near the liming current density (the concentration loss dominant region), and rather linear potential drop in between those two regions. Fig 3.2 indicates that the concentration overpotential in the anode, $\eta_{\text{A}}^{\text{conc}}$, is dominant potential loss at current densities, i^{cell}, higher than 0.7 A/cm^2. On the contrary, the sum of the activation and ohmic overpotentials in the cathode, calculated as $\eta_{\text{C}} - \eta_{\text{C}}^{\text{conc}}$, is dominant when the current density is lower than 0.4 A/cm^2. Note that the feed rate of fuel gas in the anode is set equivalent to 1 A/cm^2 current density, while that of air in the cathode is set equivalent to 4 A/cm^2. Thus, the limiting current behavior is

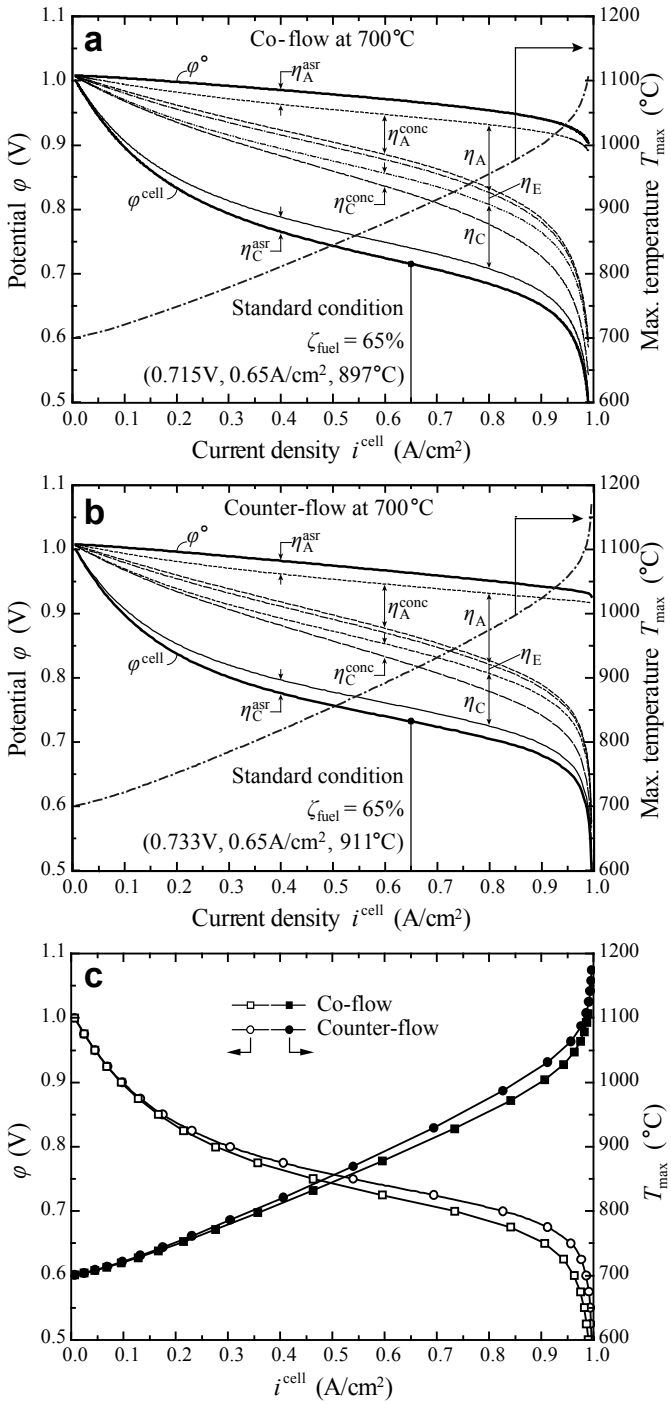

Fig. 3.2 The current–voltage ($I-V$) performance characteristics of IT-SOFCs for (a) co-flow configuration and (b) counter-flow configuration, and (c) the comparison of the co- and counter-flow configurations.

observed near the current density of 1 A/cm^2.

The current–voltage performance curves of IT-SOFCs are compared in Fig. 3.2 for the co-flow and counter-flow configurations. The flow directions for fuel and air are same in the co-flow configuration, while they are opposite in the counter-flow configuration. Fig. 3.2 indicates that the cell potential, φ^{cell}, and the maximum temperature, $T_{\max}$, are 0.715 V and 897°C for the co-flow configuration and 0.733 V and 911°C for the counter-flow configuration, at the standard operating condition: 0.65 A/cm^2 current density, 65% fuel utilization ($\zeta_{\text{fuel}} = 0.65$) and 16.25% air utilization ($\zeta_{\text{air}} = 0.1625$). Thus, the counter-flow configuration results in better performance in terms of cell potential by about 2.5% compared with the co-flow configuration. The enhanced cell potential can be explained by the higher $T_{\max}$ in the counter-flow configuration in that the activation and ohmic potential losses are strongly decreasing functions of temperature.

In Fig. 3.2(c), φ^{cell} and $T_{\max}$ for the co-flow and counter-flow configurations are compared side by side. At low current densities below 0.2 A/cm^2, the difference of φ^{cell} and $T_{\max}$ between the two flow configurations is small. However, this difference becomes larger as the current density increases. More detailed investigation will follow later in the chapter to clarify the cause for this observed performance difference.

3.3.2 Overpotentials

The contribution of each overpotential, η, to the total potential loss is approximately presented in Fig. 3.2. For easier comparison, these overpotentials along with the maximum temperature, $T_{\max}$, are separately plotted in Fig. 3.3. First, we will inspect $\eta_{\text{A}}^{\text{asr}}$ and $\eta_{\text{C}}^{\text{asr}}$ which are the electronic potential loss due to the contact resistance at the interface between the electrodes and the interconnect plate ribs. The contact resistance in SOFCs is primarily caused by the corrosion-resistant thin film coated on the interconnect plates. In Figs. 3.2 and 3.3, $\eta_{\text{A}}^{\text{asr}}$ and $\eta_{\text{C}}^{\text{asr}}$ increase with respect to i^{cell} for $i^{\text{cell}} < 0.3$ A/cm^2, remain rather constant around 0.02~0.025 V, and then decrease for $i^{\text{cell}} > 0.7$ A/cm^2. This is because the area-specific contact resistance, r^{asr}, is a decreasing function of temperature. Note that

the magnitude and behavior of $\eta_{\mathrm{A}}^{\mathrm{asr}}$ and $\eta_{\mathrm{C}}^{\mathrm{asr}}$ are almost the same according to the same interconnect plate geometry (1 mm rib width an 1 mm channel width) in the anode and the cathode side. The total potential loss due contact resistance is found to be considerable as about 0.04~0.05 V and thus should not be neglected for accurate prediction of the performance.

The η^{conc} denotes the concentration overpotential, defined as

$$\eta_{\mathrm{A}}^{\mathrm{conc}} = -\frac{RT}{2F}\ln\left(\frac{p_{\mathrm{H_2}}}{p_{\mathrm{H_2}}^{\mathrm{o}}}\cdot\frac{p_{\mathrm{H_2O}}^{\mathrm{o}}}{p_{\mathrm{H_2O}}}\right) \text{ and } \eta_{\mathrm{C}}^{\mathrm{conc}} = -\frac{RT}{4F}\ln\left(\frac{p_{\mathrm{O_2}}}{p_{\mathrm{O_2}}^{\mathrm{o}}}\right), \tag{3.11}$$

where the minus sign is added to make these values positive. Note that the $\eta_{\mathrm{A}}^{\mathrm{conc}}$ and $\eta_{\mathrm{C}}^{\mathrm{conc}}$ shown in Figs. 3.2 and 3.3 are calculated for presentation purpose, by entering the pressures at the electrode/electrolyte interfaces in Eq. (3.11). In actual calculation, the concentration overpotential is determined using the local pressures and temperature inside the AFL or the CFL. In Fig. 3.2, $\eta_{\mathrm{A}}^{\mathrm{conc}}$ is dominant loss among the potential loss in the anode, η_{A}, and this is caused by the consumption of hydrogen and the production of water vapor. In fact, Fig. 3.3 indicates that $\eta_{\mathrm{A}}^{\mathrm{conc}}$ increases rather linearly at low current densities, becomes the largest potential loss as i^{cell} passes about 0.6~0.7 A/cm^2, and then exponentially increases to infinity near $i^{\mathrm{cell}} = 1$ A/cm^2. Note that the current density of 1 A/cm^2 corresponds to 100% fuel utilization ($\zeta_{\mathrm{fuel}} = 1$). The concentration overpotential at the cathode, $\eta_{\mathrm{C}}^{\mathrm{conc}}$, is found to steadily increase with i^{cell} reaching about 0.07~0.09 V at $i^{\mathrm{cell}} = 1$ A/cm^2. The $\eta_{\mathrm{C}}^{\mathrm{conc}}$ is much smaller than $\eta_{\mathrm{A}}^{\mathrm{conc}}$ due to the larger supply of air equivalent to 4 A/cm^2 limiting current. However, the magnitude of $\eta_{\mathrm{C}}^{\mathrm{conc}}$ is still considerable, which is primarily due to the in-plane mass diffusion resistance towards the under-rib regions of the cathode (mass blocking effect of the interconnect rib).

By subtracting the concentration overpotentials, $\eta_{\mathrm{A}}^{\mathrm{conc}}$ or $\eta_{\mathrm{C}}^{\mathrm{conc}}$, from the electrode overpotentials, η_{A} or η_{C}, the sum of activation and ohmic potential losses can be determined as $\eta_{\mathrm{A}}^{\mathrm{act}} \equiv \eta_{\mathrm{A}} - \eta_{\mathrm{A}}^{\mathrm{conc}}$ for the anode and $\eta_{\mathrm{C}}^{\mathrm{act}} \equiv \eta_{\mathrm{C}} - \eta_{\mathrm{C}}^{\mathrm{conc}}$ for the cathode. In general, the activation overpotential and the ohmic overpotential in an electrode cannot be separated in the continuum electrode model frameworks. From now on, the sum of the activation and ohmic overpotentials will be termed simply as the activation overpotential, $\eta_{\mathrm{A}}^{\mathrm{act}}$ and $\eta_{\mathrm{C}}^{\mathrm{act}}$, for easier presentation. Figs

3.2 and 3.3 clearly show that the activation (and ohmic) overpotential in the cathode, $\eta_{\mathrm{C}}^{\mathrm{act}}$, is dominant potential loss (as large as 0.08~0.09 V) when the current density is lower than 0.6 A/cm^2. This is partially due to the low cell temperature at these low current densities as well as the slow electrochemical reaction in the cathode compared to that in the anode. In Fig. 3.3, $\eta_{\mathrm{C}}^{\mathrm{act}}$ is observed to increase rapidly with i^{cell} for $i^{\mathrm{cell}} < 0.2$ A/cm^2 and then slowly decreases afterwards. This behavior can be explained by the fact that increased cell temperature at high current densities greatly improves the activity of TPBs for the electrochemical reactions. The activation (and ohmic) overpotential in the anode, $\eta_{\mathrm{A}}^{\mathrm{act}}$, is found to remain rather small below 0.01 V.

The ohmic potential loss in the solid electrolyte, η_{E}, is caused by the charge conduction resistance on oxygen ions. Since the ionic conductivity of the electrolyte is an increasing function of temperature, η_{E} increases with i^{cell} for $i^{\mathrm{cell}} < 0.3$ A/cm^2, remains rather constant around 0.02 V, and then decreases for $i^{\mathrm{cell}} > 0.7$ A/cm^2. The behavior of η_{E} is quite similar to those of $\eta_{\mathrm{A}}^{\mathrm{asr}}$ and $\eta_{\mathrm{C}}^{\mathrm{asr}}$, which points out that the same mechanism (electrical conduction) works for these ohmic overpotentials.

Fig. 3.3(c) compares the major potential losses, $\eta_{\mathrm{C}}^{\mathrm{act}}$, $\eta_{\mathrm{C}}^{\mathrm{conc}}$, and $\eta_{\mathrm{A}}^{\mathrm{conc}}$, with respect to i^{cell} obtained for the co-flow and counter-flow configurations. The concentration overpotential at the cathode, $\eta_{\mathrm{C}}^{\mathrm{conc}}$, is almost same for both flow configurations when i^{cell} is lower than 0.7 A/cm^2. Then, $\eta_{\mathrm{C}}^{\mathrm{conc}}$ for the co-flow configuration begin to be higher than that for the counter-flow configuration for $i^{\mathrm{cell}} > 0.7$ A/cm^2. Fig. 3.3(c) indicates that the concentration overpotential at the anode, $\eta_{\mathrm{A}}^{\mathrm{conc}}$, is even higher for the counter-flow configuration than for the co-flow configurations at current densities lower than 0.9 A/cm^2. Thus, the improved performance of IT-SOFCs with the counter-flow configuration cannot be attributed to the variation in the concentration potential losses. The activation overpotential at the cathode, $\eta_{\mathrm{C}}^{\mathrm{act}}$, is observed to show larger differences between the co-flow and counter-flow configurations. The $\eta_{\mathrm{C}}^{\mathrm{act}}$ for both configurations show similar behaviors at low current density below 0.1 A/cm^2, but $\eta_{\mathrm{C}}^{\mathrm{act}}$ for the co-flow configuration becomes larger than that for the counter-flow configuration by as

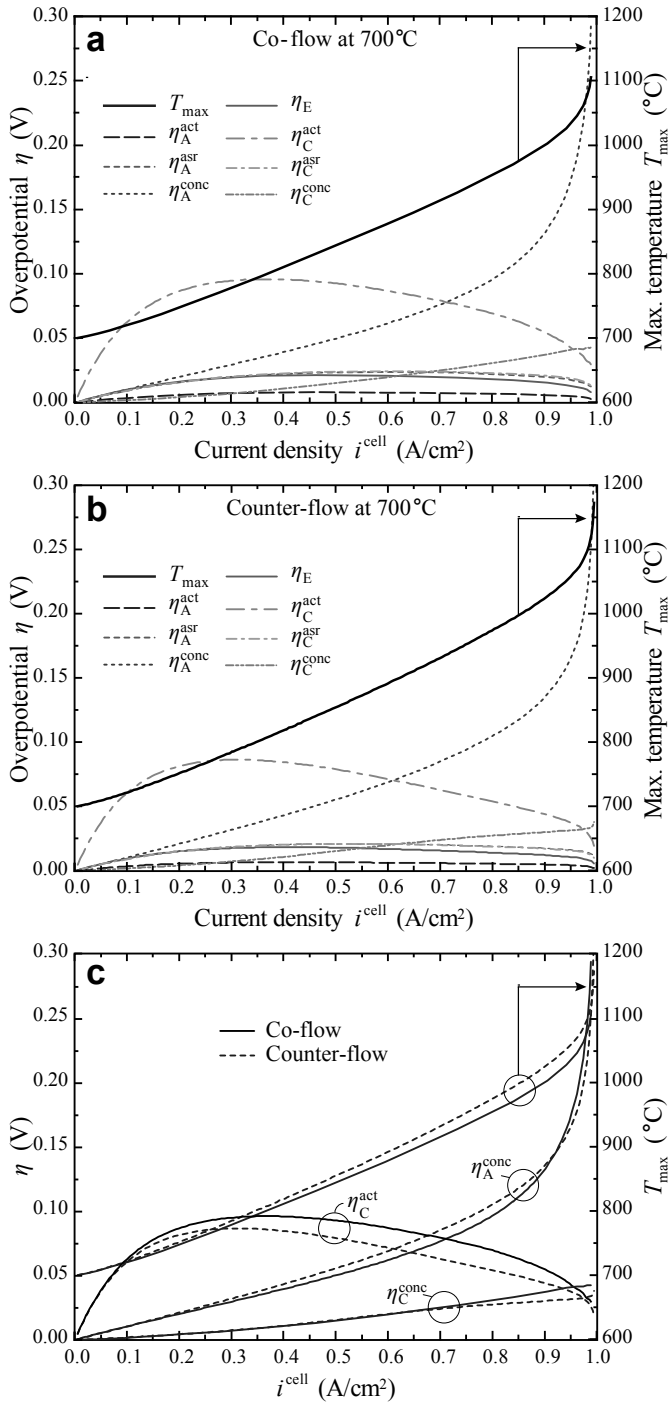

Fig. 3.3 The decomposition of overpotentials in IT-SOFCs for (a) co-flow configuration and (b) counter-flow configuration, and (c) the comparison of the co- and counter-flow configurations.

large as 0.02 V. Therefore, the reduced $\eta_{\mathrm{C}}^{\mathrm{act}}$ is found to be the main reason for the improved performance of IT-SOFCs with the counter-flow configuration. It should be noted that the concentration potential losses are generally less influenced by the cell temperature as in Eq. (3.11), compared with the activation potential losses as in Eq. (2.22) and (2.24).

The spatial distribution of electrical potentials, φ_{avg}, and electrolyte temperature, T_{avg}, along the flow channel (x-direction) of 10 cm length are shown in Fig. 3.4, where the flow directions for air and fuel are also provided for the co-flow and counter-flow configurations. The results shown in Fig. 3.4 are obtained with the standard fuel utilization of 65% ($\zeta_{\mathrm{fuel}} = 0.65$) that corresponds to $i^{\mathrm{cell}} = 0.65$ A/cm^2 (the points in Fig. 3.2 denoted as standard condition). Note that due to the 3D nature of the calculation domain, φ_{avg} and T_{avg} are obtained by averaging the potentials at relevant locations and the electrolyte temperature in the transverse y-direction. Then, Fig. 3.4 clearly presents various potential losses such as activation, concentration, ohmic overpotentials between the Nernst potential, $\varphi°$, and the cell potential, φ^{cell}.

In Fig. 3.4, the cell temperature with the co-flow configuration increases along the x-direction while the cell temperature with the counter-flow configuration decreases. This discrepancy is attributed to the cooling effect of air flow in hydrogen-fueled IT-SOFCs, which makes the cell temperature to increase along the direction of air flow. Then, the cell temperature generally increases along the direction of fuel flow in the co-flow configuration but it decreases along the direction of fuel flow in the counter-flow configuration. Fig. 3.4 shows that the Nernst potential, $\varphi°$, gradually decreases along the flow direction of air as the cell temperature increases.

In Fig. 3.4(a) for the co-flow configuration, the activation overpotential at the cathode, $\eta_{\mathrm{C}}^{\mathrm{act}}$, is dominant near the fuel inlet ($x = 0$ m) due to low cell temperature while the concentration overpotential at the anode, $\eta_{\mathrm{A}}^{\mathrm{conc}}$, is dominant near the fuel outlet ($x = 0.1$ m) due to low hydrogen and oxygen concentration. The ohmic overpotentials including η_{E}, $\eta_{\mathrm{A}}^{\mathrm{asr}}$, and $\eta_{\mathrm{C}}^{\mathrm{asr}}$ take up large portion in the potential loss (especially the contact potential loss) and they decreases along the flow

direction as the cell temperature increases. The activation overpotential at the anode, η_A^{act}, is small and slightly decreases along the flow direction as the cell temperature increases. Similarly, the concentration overpotential at the cathode, η_C^{conc}, is considerable and slightly increases along the flow direction as the oxygen concentration decreases. It should be noted that the local overpotentials are dependent on the local current density and thus should be carefully compared by referring to the current density. As will be presented in Fig. 3.5, the local current density is relatively uniform for the co-flow configuration and high overpotentials

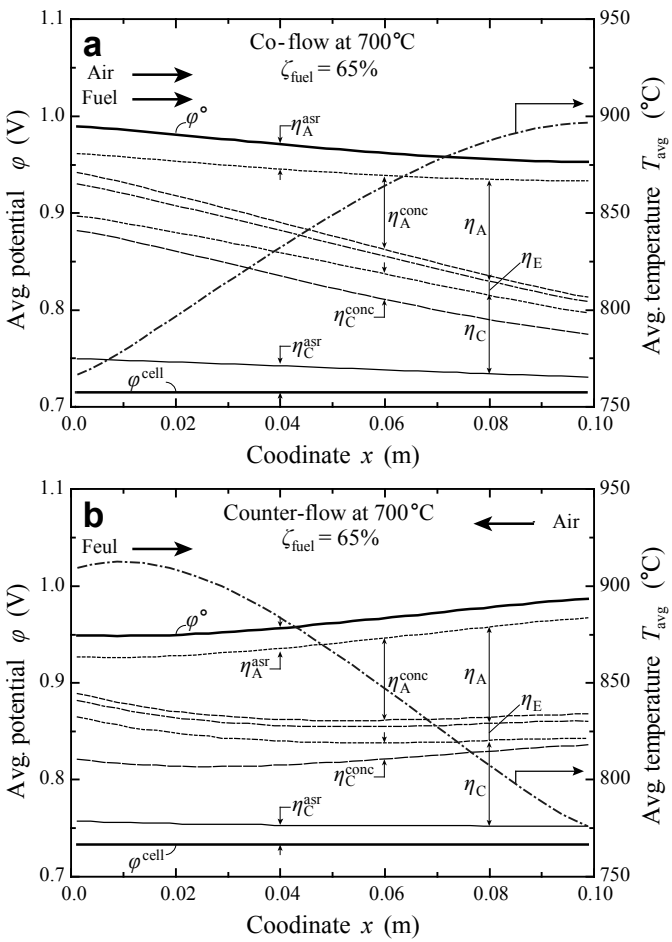

Fig. 3.4 The distribution of potential and temperature along the flow direction (x-direction) of IT-SOFCs with (a) co-flow configuration and (b) counter-flow configuration.

direct indicate high resistances.

In Fig. 3.4(b) for the counter-flow configuration, $\eta_{\mathrm{A}}^{\mathrm{conc}}$ and $\eta_{\mathrm{C}}^{\mathrm{act}}$ are dominant near the fuel inlet ($x = 0$ m) despite high cell temperature as well as high hydrogen concentrations there. This result can be explained by high current density in this inlet region as will be presented in Fig. 3.5. Because of the high local current density, theses overpotentials become very large in spite of low resistances associated with the relevant processes. The cathode concentration overpotential, $\eta_{\mathrm{C}}^{\mathrm{conc}}$, is also considerably large near the inlet due to low oxygen concentration. Near the fuel outlet ($x = 0.1$ m), the anode concentration overpotential, $\eta_{\mathrm{A}}^{\mathrm{conc}}$, and the cathode activation overpotential, $\eta_{\mathrm{C}}^{\mathrm{act}}$, are dominant due to low hydrogen concentration and low temperature, respectively. Similar to the results of the co-flow configuration, the ohmic overpotentials take up large portion in the total potential loss and especially the contact potential loss, $\eta_{\mathrm{A}}^{\mathrm{asr}}$ and $\eta_{\mathrm{C}}^{\mathrm{asr}}$, are considerable.

3.3.3 Current density distribution

Fig. 3.5 shows the local current density and temperature along the axial flow direction (x-direction) inside the IT-SOFCs with the co-flow and counter-flow configurations. The local current density and temperature data are obtained by averaging the current density and temperature for the electrolyte in the transverse y-direction. Four different fuel utilization factors, ζ_{fuel}, of 80%, 65%, 50%, and 0.35% are considered which corresponds to the cell current density, i^{cell}, of 0.8 A/cm^2, 0.65 A/cm^2, 0.5 A/cm^2, and 0.35 A/cm^2.

Fig. 3.5(a) indicates that the average local current density, i_{x}, for the co-flow configuration generally has a local maximum and this location moves towards the inlet as the fuel utilization factor, ζ_{fuel}, increase. As a result, the local current density, i_{x}, tends to more non-uniform at higher fuel utilization factor. The difference between the maximum and minimum i_{x} is observed to be about 0.06 A/cm^2 for $\zeta_{\mathrm{fuel}} = 0.35$, about 0.12 A/cm^2 for $\zeta_{\mathrm{fuel}} = 0.5$, about 0.16 A/cm^2 for $\zeta_{\mathrm{fuel}} = 0.65$, and about 0.4 A/cm^2 for $\zeta_{\mathrm{fuel}} = 0.80$. The average local temperature, T_{x}, for the co-flow configuration is shown in Fig. 3.5(b), where the temperature is

observed to increase along the flow direction (x-direction). The degree of temperature increase is larger for higher fuel utilization factor in Fig. 3.5(b), which is because the reaction heat and Joule heating are the main source for the temperature increase.

The presence of local maximum i_x in IT-SOFCs with the co-flow configuration may be explained as follows. Near the fuel inlet ($x = 0$ m), the hydrogen and oxygen concentrations are highest but the temperature is still low for fast electrochemical reactions to occur. Thus, the local current density, i_x, increases along the flow direction as the local temperature, T_x, increases. However, the reactant concentrations steadily decrease along the flow direction due to the consumption of hydrogen and oxygen by the electrochemical reactions. Then, after some distance from the inlet, the concentration overpotential becomes significant and thus the local current density, i_x, starts to decrease. Note that concentration overpotential is the major potential loss near the fuel outlet ($x = 0.1$ m), as shown in Fig. 3.4(a).

The average local current density, i_x, and the local temperature, T_x, for the counter-flow configuration is shown in Figs. 3.5(c) and (d). The distributions of i_x and T_x for the counter-flow configuration are considerably different from those for the co-flow configuration. Unlike the co-flow configuration, the local current density, i_x, with the counter-flow configuration monotonically decreases along the direction of fuel flow, resulting in the highest i_x near the fuel inlet ($x = 0$ m) and the lowest i_x ($x = 0.1$ m). The temperature is also decreasing along with the fuel flow (x-direction), primarily due to the cooling effect of air that flows opposite to the fuel. Thus, IT-SOFCs with the counter-flow configuration experience the highest hydrogen and oxygen concentrations as well as the highest temperature near the fuel inlet ($x = 0$ m). With these favorable conditions, the current density has the highest values near the fuel inlet and then decreases rapidly towards the fuel outlet, as shown in Fig. 3.5(c).

The spatial non-uniformity of the local current density, i_x, for the counter-flow configuration is much higher than that for the co-flow configuration. The difference between the maximum and minimum i_x for the counter-flow

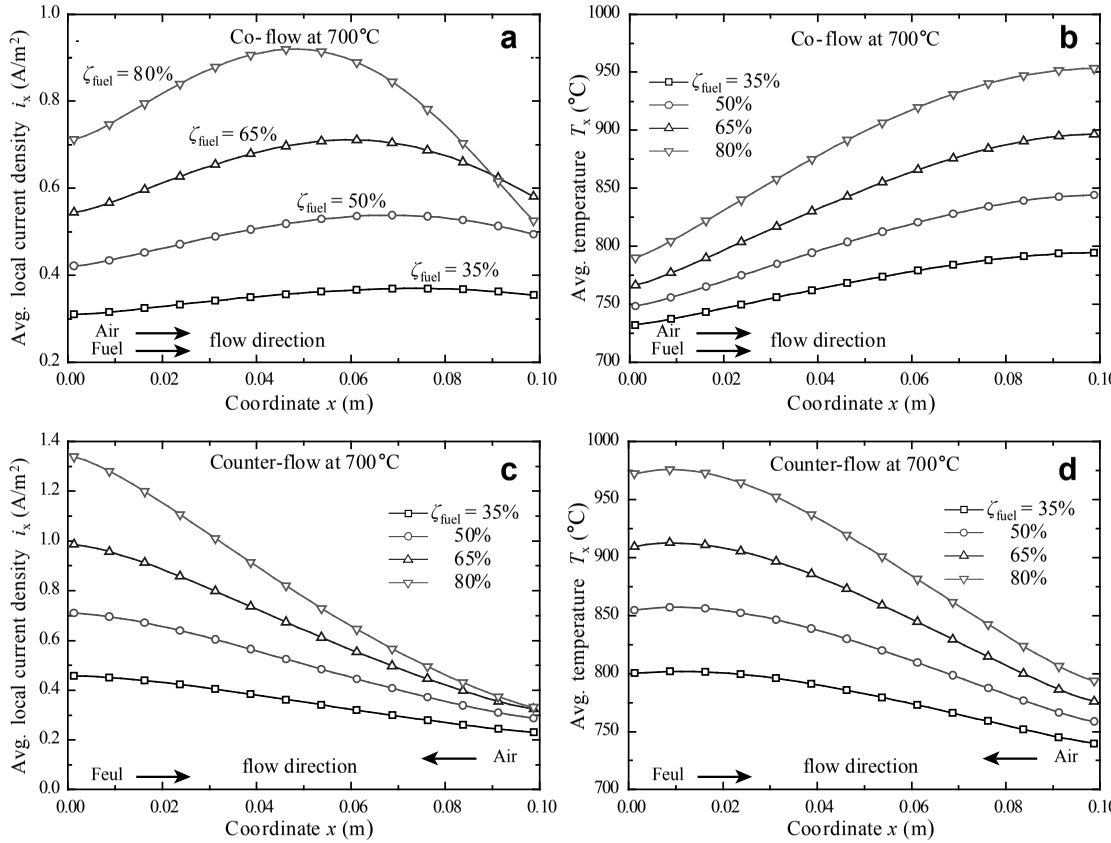

Fig. 3.5 The spatial distribution of variables along the x-coordinate in IT-SOFCs: (a) average local current density and (b) local temperature for the co-flow configuration; (c) average local current density and (d) local temperature for the counter-flow configuration.

configuration amounts to about 0.22 A/cm^2 for $\zeta_{\text{fuel}} = 0.35$, about 0.41 A/cm^2 for $\zeta_{\text{fuel}} = 0.5$, about 0.67 A/cm^2 for $\zeta_{\text{fuel}} = 0.65$, and about 1.02 A/cm^2 for $\zeta_{\text{fuel}} = 0.80$. In addition, the non-uniformity of the local temperature, T_{x}, for the counter-flow configuration is also higher than that for the co-flow configuration. Although the cell potential is higher for the counter-flow configuration than the co-flow configuration, higher non-uniformity in the temperature and current density distribution are believed to unfavorable from the viewpoint of the long-term stable performance.

More detailed inspection of the local current density is conducted with Figs.

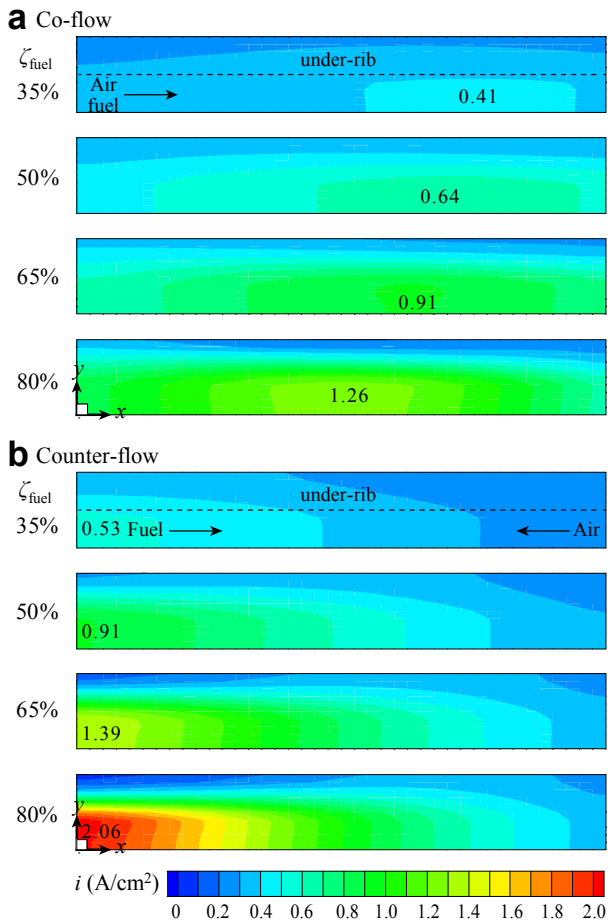

Fig. 3.6 The distribution of local current density in IT-SOFCs with (a) co-flow configuration and (b) counter-flow configuration.

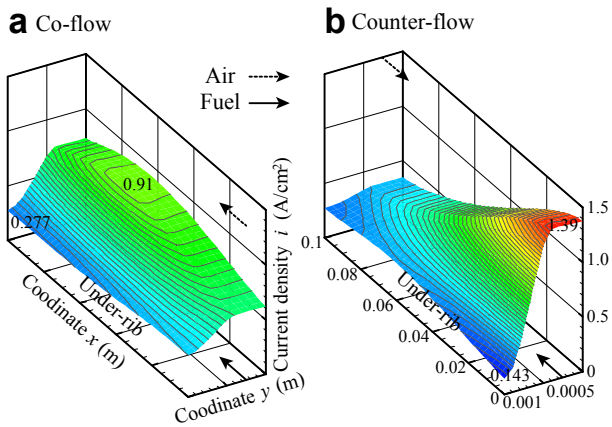

Fig. 3.7 The 3D plots of the local current density distribution for 65% fuel utilization with (a) co-flow configuration and (b) counter-flow configuration.

3.6 and 3.7, where the current density that flows through the thin electrolyte is plotted for the active area (xy-plane). Due to the interconnect rib and channel geometries, the current density shows significant variation in the transverse y-direction in addition to the variation in the axial flow direction (x-direction). In Figs. 3.6 and 3.7, the region under the interconnect rib is denoted as the under-rib region. The current density in the under-rib region is generally lower than that in the under-channel region due to the mass blocking effect of the interconnect plates. Thus, the maximum current density is generally observed in the under-channel regions where the reactant concentration is higher.

The comparison of the co-flow and counter-flow configurations indicates that the current density is more uniform with the co-flow configuration. The maximum values for the local current density, provided in Figs. 3.6 and 3.7, are always higher in the counter-flow than the co-flow configuration. The 3D plot for $\zeta_{\text{fuel}} = 0.65$ shown in Fig. 3.7 shows more clearly the difference in the current density distribution between the two flow configurations. In Fig. 3.7(a) for the con-flow configuration, the current density is distributed rather uniformly throughout the active area with a current range of 0.227 A/cm^2 to 0.91 A/cm^2. However, in Fig. 3.7(b) for the counter-flow configuration, the current density distribution is highly non-uniform with a current range of 0.143 A/cm^2 to 1.39 A/cm^2.

3.3.4 Temperature distribution

The operating temperature IT-SOFCs ranges from 600 to 800°C. At this temperature range, many problems due to high operating temperature of SOFCs (~1000°C) can be alleviated. The temperature distribution in IT-SOFCs is closely related with the mechanical failure of the PEN due to large thermal stress and the long-term performance loss of the electrode materials due to physical and chemical degradation. Thus, the temperature distribution is one of the most important objectives of the prediction models for the design and optimization of IT-SOFCs.

Fig. 3.8 shows the temperature distribution inside the calculation domain of IT-SOFCs with the co-flow and counter-flow configurations. The results are for standard operating conditions with the fuel utilization factor of 65% and the inlet temperature of 700°C. In Fig. 3.8, the cell temperature increases along the direction

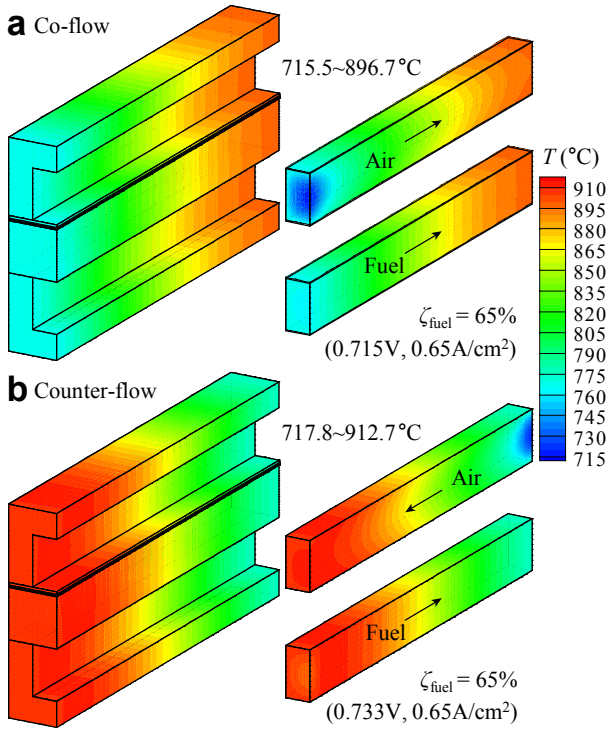

Fig. 3.8 The temperature distribution inside IT-SOFCs with (a) co-flow configuration and (b) counter-flow configuration, operated at fuel utilization factor of 65% ($\zeta_{fuel} = 0.65$).

of air due to the cooling effect of the air flow. Thus, the maximum temperature is found near the air outlet. Note that the flow rate of air is set to a large value equivalent to the current density of 4 A/cm^2. This large air flow rate supplies sufficient oxygen molecules for the cathode as well as helps to reduce the temperature of IT-SOFCs. The range of the temperature distribution in the counter-flow configuration is from 717.8 to 912.7°C, compared to that in the co-flow configuration from 715.5 to 896.7°C. The previously observed higher performance with the counter-flow configuration is due to this temperature difference that influences the electrochemical reactions.

The temperature distribution in the PEN and the interconnect plates is observed to be rather uniform in the planes (yz -plane) perpendicular to the axial direction (x -direction). The temperature distributions inside the gas channels are non-uniform as higher in the core but lower near the channel wall surfaces. It is interesting to note that the temperature inside the fuel channel is very close to the temperature of the PEN and the interconnect plate. Although the fuel gas temperature at the inlet is 700°C, fuel gas quickly approaches to the temperature of the PEN due to the low velocity and high thermal conductivity of fuel gas as well as the small dimension of the channel.

The electrolyte in planar, anode-supported IT-SOFC is fabricated to be an extremely thin YSZ layer to reduce the ohmic polarization due to relatively low ionic conduction of YSZ at lower operating temperatures. Thus, it is particularly important to inspect the temperature distribution in the electrolyte. The calculated temperature distributions inside the electrolyte is presented in Fig. 3.9, where the observed temperature ranges and the total temperature difference, ΔT_{total}, are provided for reference. In Fig. 3.9, the temperature in the electrolyte increases along the direction of air flow while the temperature distribution in the y-direction is rather uniform. Slightly lower temperature is observed under the channel due to the cooling effect of the air flow. The total temperature difference, ΔT_{total}, increases with the fuel utilization factor, ζ_{fuel}, with a linear relationship of $\Delta T_{\text{total}} \sim \zeta_{\text{fuel}}$. Fig. 3.9 also indicates that ΔT_{total} is higher for the counter-flow configuration than for the co-flow configuration.

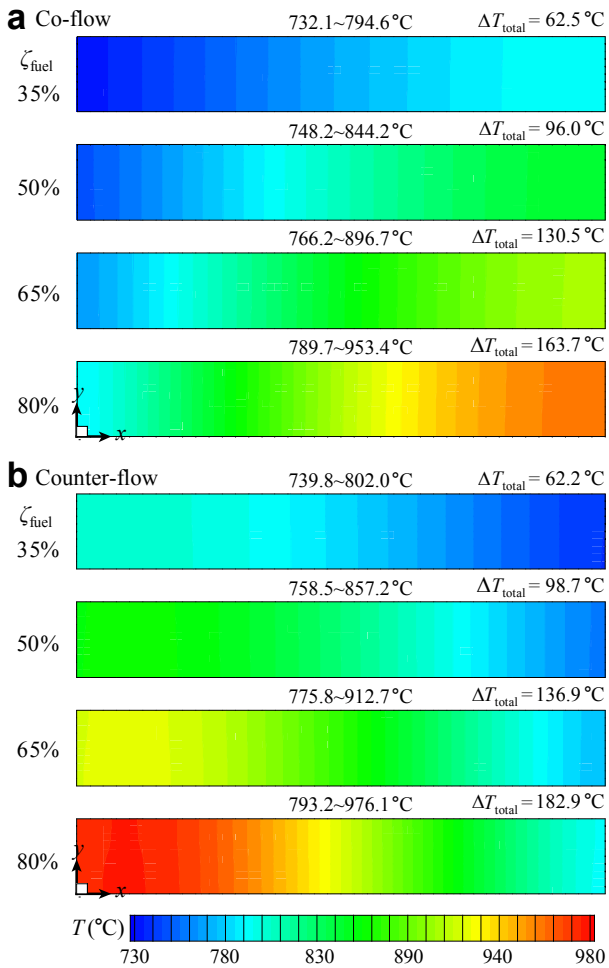

Fig. 3.9 The distribution of local temperature at the electrolyte in IT- SOFCs with (a) co-flow configuration and (b) counter- configuration.

3.3.5 Concentration distribution

The distribution of the reactant and product concentrations is closely related with the concentration polarization. In planar IT-SOFCs, fuel and air are injected through inlets, transported through gas channels, and then exhausted through outlets. While flowing in the channels, hydrogen and oxygen gas molecules enter the electrodes, diffuse through the porous structures, and finally consumed by the electrochemical reactions. The product molecules diffuse back through the anode and join the fuel gas stream in the channel. Thus, the reactant concentrations at the

TPB reaction sites are generally lower than those in the bulk gas streams in the channels due to the mass transport resistances associated with the diffusion and convection processes. In addition, the reactant concentrations in the gas channels also decrease along the channels of planar IT-FOFCs due to the consumption of reactant by electrochemical reactions.

Fig. 10 shows the distribution of reactant concentrations inside IT-SOFCs with the co-flow and counter-flow configurations. The standard operating conditions listed in Table 3.1 is used for the calculation. The partial pressure of hydrogen, p_{H_2}, is set to 70 kPa at the fuel inlet and the partial pressure of oxygen, p_{O_2}, is set to 21 kPa at the air inlet. In Fig. 3.10, p_{O_2} is observed to decrease by about 3~4 kPa while flowing through the cathode channel from the air inlet and the outlet. The exact value is calculated to be 3.4 kPa by multiplying the inlet partial pressure, $p_{\mathrm{O}_2}^{\mathrm{o}} = 2.1\,\mathrm{kPa}$, and the air utilization factor, $\zeta_{\mathrm{air}} = 0.1625$. Since air flow rate is much higher than required (4.0 A/cm^2 equivalent), the oxygen concentration remains rather constant in the air channels. However, p_{H_2} seems to decrease by about 45~50 kPa in Fig. 3.10 while flowing through the anode channel. The exact drop is calculated to be 45.5 kPa by multiplying the inlet partial pressure, $p_{\mathrm{H}_2}^{\mathrm{o}} = 70$ kPa, and the fuel utilization factor, $\zeta_{\mathrm{fuel}} = 0.65$. The high fuel utilization factor is necessary to spare the valuable hydrogen fuel.

The 3D effects on the concentration distribution are clearly observed in Fig. 3.10. The oxygen concentration is observed to be much lower in the CFL under the rib, compared with under the channel. On the contrary, the hydrogen concentration has rather uniformly distribution in the AFL, regardless of the interconnect rib and channel geometries. Oxygen molecules should diffuse through the thin cathode (70 μm total thickness) to reach the active TPBs in the under-rib region. Thus, high in-plane mass transport resistance greatly reduces the oxygen concentration, resulting in spatially non-uniform distribution. However, hydrogen molecules diffuse through the relatively thick anode (1020 μm total thickness), which makes the hydrogen concentration in the AFL (and at the anode/electrolyte interface) more uniform. Higher diffusivity of hydrogen than the diffusivity of oxygen also contributes to the more uniform distribution of hydrogen concentration in the reaction sites.

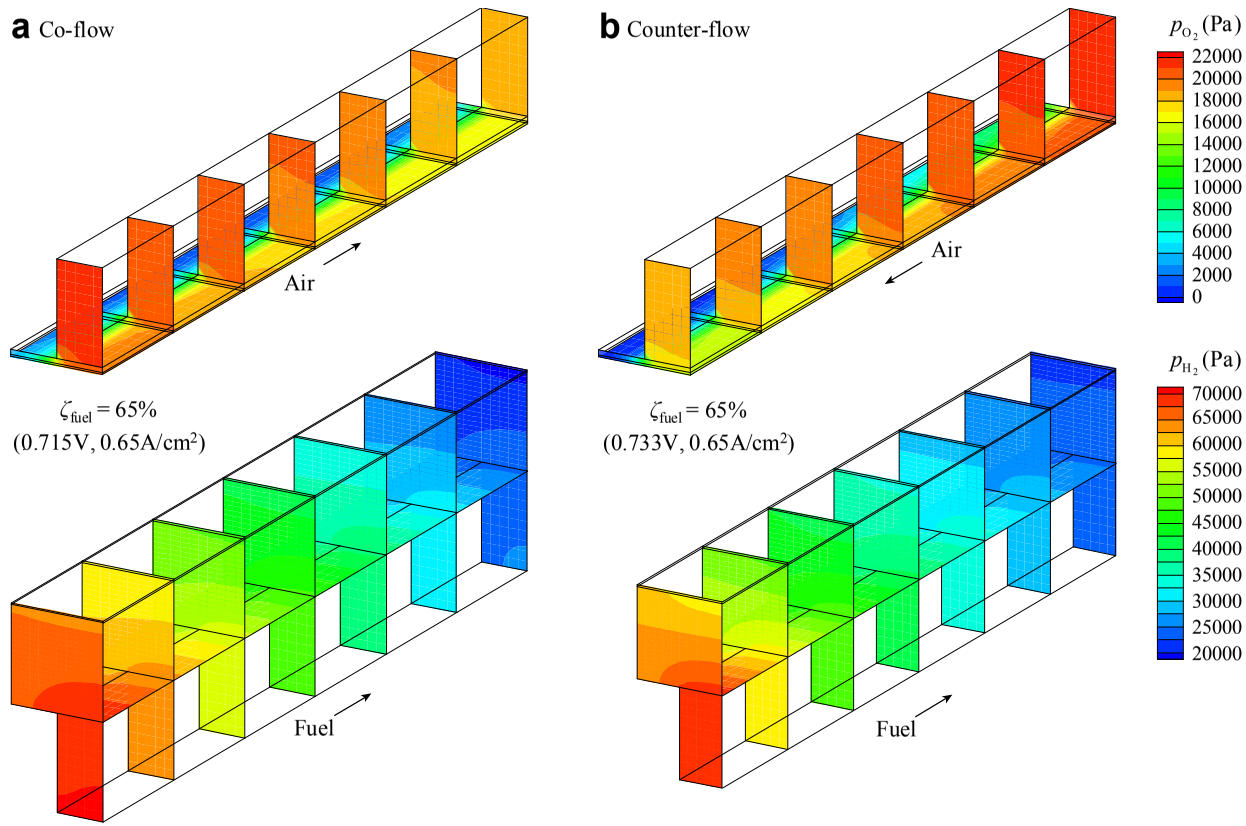

Fig. 3.10 The distribution of reactant concentrations in IT-SOFCs with (a) co-flow configuration and (b) counter-flow configuration, operated at fuel utilization factor of 65% ($\zeta_{fuel} = 0.65$).

In Fig. 3.10 (b) for the counter-flow configuration, the hydrogen concentration at the anode/electrolyte interface is lower in the under-channel region than that in the under-rib region. This result is counter-intuitive for the mass transport resistance for the under-channel region is smaller than that for the under-rib region. If we recall the current density distribution shown in Fig. 3.7(b), this result can be explained as being caused by the high current density and resultant high hydrogen consumption in the under-channel region.

In Fig. 3.11, the distribution of the oxygen and hydrogen partial pressures at the electrode/electrolyte interfaces is presented. In general, the concentration of oxygen and hydrogen gradually decreases along the flow direction and the degree of concentration reduction grows as the fuel utilization factor increases. At higher utilization factor, reactant molecules are consumed more rapidly, leading to quicker decreases of reactant concentration along the flow channel. Accordingly, the reactant concentration at the electrode/electrolyte interface decreases.

In Fig. 3.11(a), the oxygen concentration in the under-rib region is noticeably lower than that in the under-channel region. As discussed previously with the Fig. 3.10, the in-plane mass transport resistance in the cathode is high because of the small electrode thickness as well as the small oxygen diffusion coefficient. Thus, the oxygen concentration in the under-rib region becomes much lower, resulting in higher concentration potential loss there. In fact, the concentration overpotential in the cathode, $\eta_{\mathrm{C}}^{\mathrm{conc}}$, is the primary reason for the non-uniformity of local current density in transverse y-direction shown in Figs. 3.6 and 3.7. The oxygen concentration difference between the under-rib and the under-channel regions increases as the air utilization increases, which is directly connect to the difference in the local current density between the under-rib and the under-channel regions observed in Fig. 3.6.

In 3.11(b), the hydrogen concentration in the under-rib region is rather similar to that in the under-channel region, different from the oxygen concentration distribution in Fig. 3.11(a). Thus, the concentration overpotential in the anode, $\eta_{\mathrm{A}}^{\mathrm{conc}}$, does not induce the non-uniform current density in transverse y-direction. However, the hydrogen concentration decreases significantly along the direction of

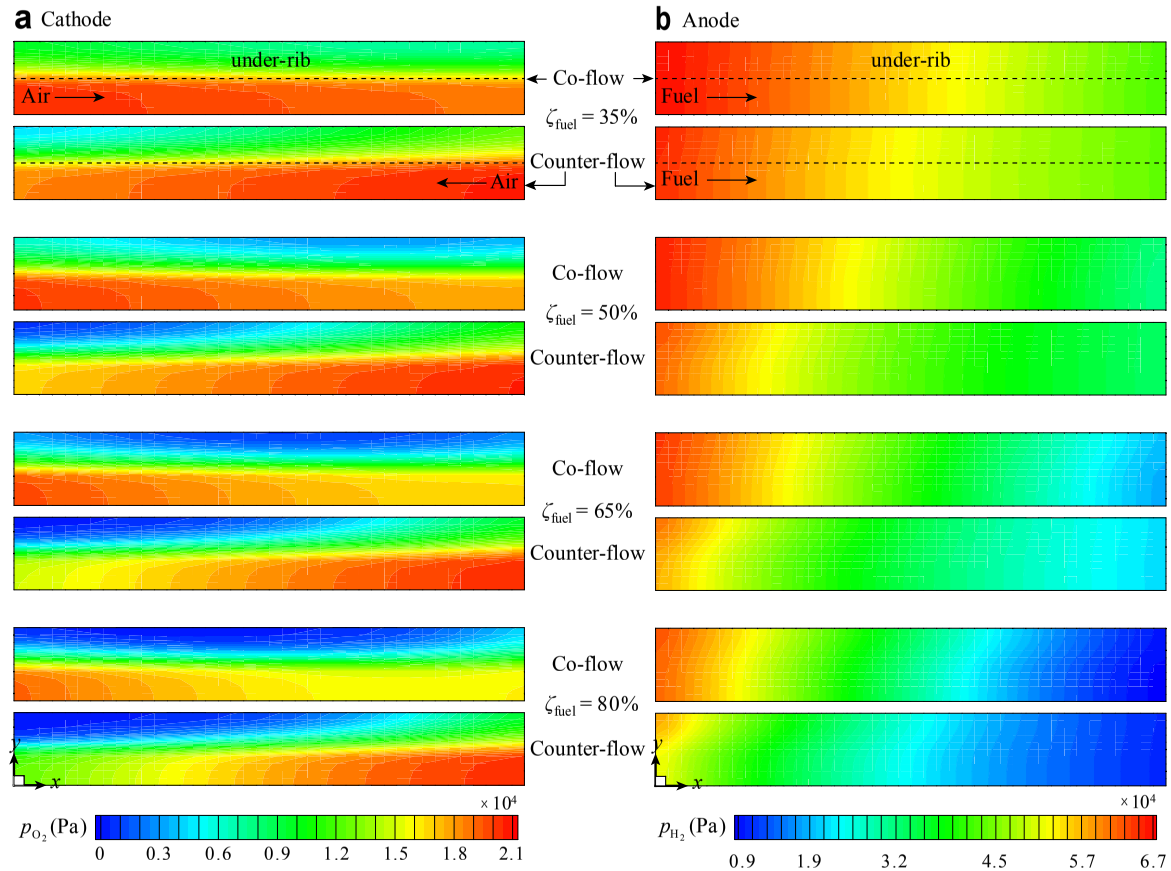

Fig. 3.11 The distribution of reactant concentration in IT-SOFCs with co-flow and counter-flow configurations, at (a) cathode /electrolyte interface and (b) anode/electrolyte interface.

fuel gas as the fuel utilization increases. Therefore, $\eta_{\mathrm{A}}^{\mathrm{conc}}$ acts as the major source for the total potential loss in IT-SOFCs operated at high fuel utilization factors.

3.3.6 Temperature gradient

High temperature has favorable effects on the performance of IT-SOFCs by enhancing the electrochemical reactions as well as the diffusion of reactants and products. However, the operating temperature of IT-SOFCs has an upper bound called the maximum allowable temperature which is generally determined by the interconnect material. In addition, the temperature gradient in the PEN results in the

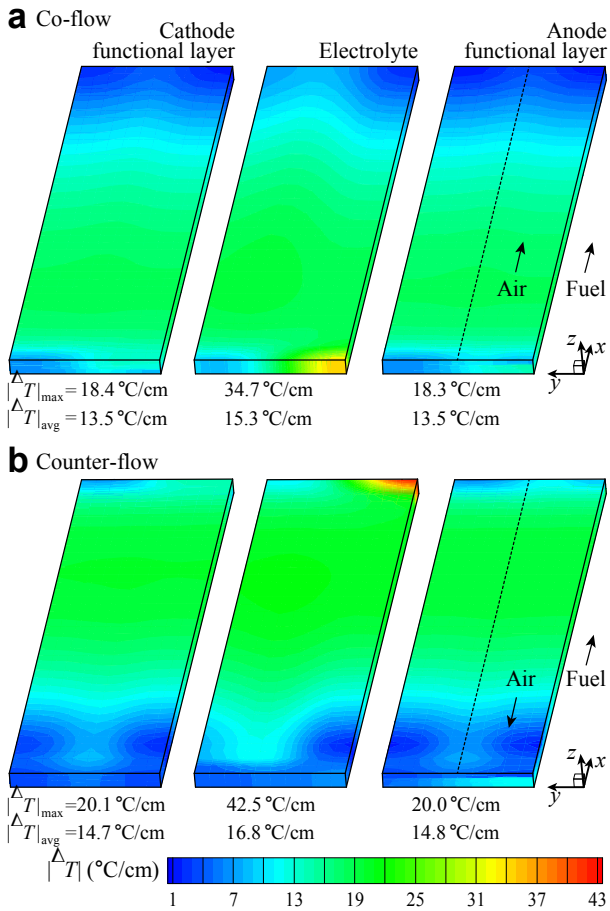

Fig. 3.12 The temperature gradient inside the electrolyte and functional layers of IT-SOFCs with (a) co-flow configuration and (b) counter-flow configuration, operated at fuel utilization factor of 65% ($\zeta_{\mathrm{fuel}} = 0.65$).

Table 3.3 Mechanical properties of the PEN (Nakajo et al., 2006).

Parameters	Cathode (LSM)	Electrolyte (YSZ)	Anode (Ni/YSZ)
Young's modulus (GPa)	35	183	57
Poisson's ratio	0.25	0.313	0.28
Thermal expansion coefficient (K^{-1})	11.7×10^{-6}	10.8×10^{-6}	12.2×10^{-6}

thermal stress build-up due to the mismatch in thermal expansion coefficients (see Table 3.3). Thus, high temperature gradient can lead to mechanical failure of the PEN such as delamination and fracture. The previous studies suggested that the maximum allowable temperature gradient for YSZ is around 10°C/cm. This temperature gradient is generally used as a constraint in planning the transient start-up schedules as well as in optimizing the steady operation conditions.

Fig. 3.12 shows the temperature gradient in the AFL, the CFL, and the electrolyte of IT-SOFCs with the co-flow and counter flow configurations. The fuel utilization factor is set to 65%. The maximum temperature gradient, $|\nabla T|_{\max}$, is generally observed in the electrolyte, under the channel and near the air inlet. This maximum gradient is thought to be caused by the sudden exposure of the PEN to the relatively cold air stream at the inlet (thermal shock). The contribution of the electrochemical reaction heat to the temperature gradient is believed to be small. As shown in Fig. 3.12(b), the fuel inlet for the counter-flow configuration (the region of the highest current density) exhibits relatively small temperature gradient. It should be noted that the predicted high temperature gradient near the air inlet may be an overestimated result caused by ignoring flow distribution manifold ahead of the gas channels. In general, the interconnect plates in planar IT-SOFCs are made to have inlet and outlet distribution manifolds connected to many gas channels. Thus, the temperature of air at the inlet increases to the temperature of the PEN while air is flowing through the inlet manifold.

In Fig. 3.12, the average temperature gradient, $|\nabla T|_{\text{avg}}$, in the electrolyte is observed to be about 15.3°C/cm for the co-flow configuration and 16.8°C/cm for the counter-flow configuration. This shows that the co-flow configuration is a better

option for mechanical stability of the electrolyte than the counter-flow configuration. However, the average temperature gradient in the electrolyte is still higher than the maximum allowable temperature gradient of 10°C/cm which is generally accepted (Aguiar et al., 2005). One way to reduce the temperature gradient is to use lower fuel utilization factors, by which the reaction heat can be reduced. Another way is to use higher air flow rate, by which the air cooling can be enhanced. Note that both methods also decrease the maximum temperature inside IT-SOFCs. In Fig. 3.12, the temperature gradient in the functional layers is generally lower than the electrolyte, and thus not considered.

3.3.7 Flow velocity

The average flow velocity at the inlet, $u_{\mathrm{m}}^{\mathrm{o}}$, is determined as

$$u_{\mathrm{m,air}}^{\mathrm{o}} = \frac{N_{\mathrm{x,tot,C}} R T_{\mathrm{air}}^{\mathrm{o}}}{p_{\mathrm{air}}^{\mathrm{o}} L_{\mathrm{ch}} W_{\mathrm{ch}}}, \tag{3.12}$$

$$u_{\mathrm{m,fuel}}^{\mathrm{o}} = \frac{N_{\mathrm{x,tot,A}} R T_{\mathrm{fuel}}^{\mathrm{o}}}{p_{\mathrm{fuel}}^{\mathrm{o}} L_{\mathrm{ch}} W_{\mathrm{ch}}}, \tag{3.13}$$

where the subscript A and C denote the anode and the cathode, respectively. T^{o} is the inlet temperatures, p^{o} is the inlet pressures, R is universal gas constant (8.314 J/mol-K), and $L_{\mathrm{ch}} W_{\mathrm{ch}}$ is the cross-sectional area of the channel (1 mm^2 in this study). The total molar flow rate, $N_{\mathrm{x,tot}}$, that flows through the channel cross-section is calculated as

$$N_{\mathrm{x,tot,C}} = 2 L_{\mathrm{x}} L_{\mathrm{y}} 10000 \frac{i_{\mathrm{air}}^{\mathrm{lim}}}{4 F x_{\mathrm{O_2}}^{\circ}}, \tag{3.14}$$

$$N_{\mathrm{x,tot,A}} = 2 L_{\mathrm{x}} L_{\mathrm{y}} 10000 \frac{i_{\mathrm{fuel}}^{\mathrm{lim}}}{2 F x_{\mathrm{H_2}}^{\circ}}. \tag{3.15}$$

Here, L_{x} and L_{y} are the length of the calculation domain, i^{lim} is the limiting current density equivalent to the gas supply rate, x^{o} is the inlet mole fraction, and F is the Faraday number. Note that $2 L_{\mathrm{x}} L_{\mathrm{y}}$ becomes the reaction area composed of one channel and one rib width (L_{x} and L_{y} are set to 0.1 m and 0.001 m in this study.) and 10000 is added to convert the unit of i^{lim} from A/cm^2 to A/m^2.

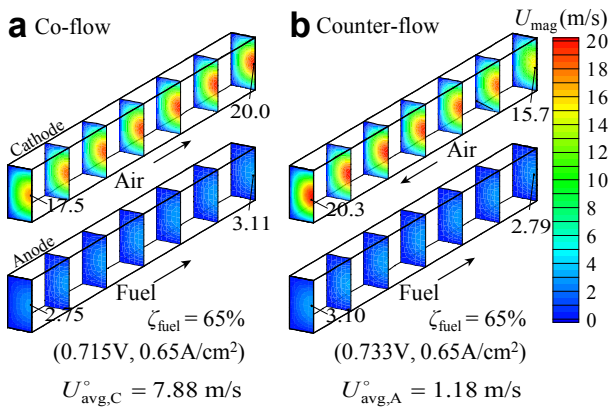

Fig. 3.13 The distribution of flow velocity in the channels of IT-SOFCs with (a) co-flow configuration and (b) counter-flow configuration, operated at fuel utilization factor of 65% ($\zeta_{\text{fuel}} = 0.65$).

Using the standard conditions in table 3.1, the average flow velocity is estimated to be 7.99 m/s at the air inlet of the cathode channel and 1.20 m/s at the fuel inlet of the cathode channel. The flow velocity is much larger in the cathode channel than the anode channel, due to the difference in the flow rate ($i_{\text{air}}^{\text{lim}} = 4$ A/cm^2 for air supply and $i_{\text{fuel}}^{\text{lim}} = 1$ A/cm^2 for fuel supply) and the concentration ($x_{\text{O}_2}^{\text{o}} = 0.21$ for air and $x_{\text{H}_2}^{\text{o}} = 0.7$ for fuel gas).

Fig. 3.13 shows the velocity distribution inside the channels of IT-SOFCs operated at $\zeta_{\text{fuel}} = 0.65$. The velocity of air in the cathode channel increases along the direction of air flow. The total molar flow rate in the cathode channel, $N_{\text{x,tot,C}}$, decreases along the direction of air flow due to the consumption of oxygen but the reduction of $N_{\text{x,tot,C}}$ is generally small. On the contrary, the cell temperature increases along the direction of air flow. According to the ideal gas law, the molar density of gas, c (mol/m^3), is calculated as

$$c = \frac{p}{RT}, \tag{3.16}$$

which means that higher temperature leads to lower density at constant pressure. Therefore, the air velocity increases along the direction of air flow, primarily due to increased cell temperature. The flow velocity of fuel gas in the anode channel is also observed to increase along the direction of air flow.

In Fig. 3.13, the highest flow velocity is found at the center of the channel while the lowest or zero velocity is obtained at the channel walls. The highest flow velocity at the inlet is roughly two times larger than The average flow velocity at the inlet, $u_{\mathrm{m}}^{\mathrm{o}}$. The distribution of flow velocity in the channel cross-section is the direct results of the laminar velocity profiles assumed in the micro/macroscale model. Thus, the present model can is believed to properly consider the effects of flow velocity distribution though the fluid dynamics calculation is not conducted.

3.4 Summary

Using a validated micro/macroscale model, this study numerically investigates the performance and operational characteristics of hydrogen-fueled IT-SOFCs with the co-flow and counter-flow configurations in detail. The calculation is conducted for the standard operating condition at 65% fuel utilization (0.65 A/cm^2) with fuel flow rate equivalent to 1 A/cm^2 and air flow rate equivalent to 4 A/cm^2. The current–voltage performance curves of the IT-SOFCs are analyzed to identify the contribution of the activation, concentration, ohmic overpotentials to the total potential loss. The behavior of each overpotential is fully explained by detailed inspection of the spatial distribution of current density, temperature, and reactant concentrations. In addition, we also investigate the thermal stress distribution in the electrolyte and the functional layers as well as the flow velocity distribution in the channels.

The calculation results point out that the counter-flow configuration results in better performance of IT-SOFCs compared to the co-flow configuration, but the performance enhancement is less noticeable when the current density is small. It is also found that the counter-flow configuration results in non-uniform distribution of current density and temperature inside the IT-SOFCs compared with the co-flow configuration. The results also indicate that higher thermal stress is expected in the IT-SOFCs when the counter-flow configurations are employed. Therefore, the co-flow configuration is believed to be a better option for long-term stable operation of IT-SOFC, considering more uniform distribution of current density and temperature as well as smaller temperature gradient and thermal stress.

CHAPTER 4
PARAMETRIC STUDY

In this chapter, we investigate the effects of various parameters, such as the operating conditions, the electrode microstructures, and the geometrical dimensions, on the performance of planar, anode-supported IT-SOFCs fueled with hydrogen. Large numbers of simulations are required to evaluate the effect of each parameter variation, and these simulations are performed fast and efficiently using the 3D micro/macroscale model described in chapter 2. The co-flow configuration is considered as the flow configuration since this leads to better uniformity inside the IT-SOFCs operated with hydrogen than the counter-flow configuration in chapter 3. Also, the number of simulation cases required to be conducted is reduced by half considering only the co-flow configuration.

From the micro/macroscale simulations of IT-SOFCs, the current–voltage performance curves are mainly examined along with the variation of the activation, concentration, ohmic potential losses. In addition, the spatial distribution of temperature and current density are also inspected for key parameters which result in significant performance variation. The parameters considered in this chapter can be divided into three categories, such as the operating conditions (inlet temperature and pressure), the electrode microstructures (particle size and porosity in electrodes), and the geometrical dimensions (electrode layer thickness, channel/ rib dimension, and cell length).

4.1 Introduction

The performance of IT-SOFCs is influenced by many factors: the electrical, physical, and electrochemical properties of materials, the microstructures of porous electrodes, the designs of PENs, gas channels, and interconnect plates, and the operating strategies. This study considers the IT-SOFCs with rather standard materials (such as Ni/YSZ cermet for the anode, dense YSZ for the electrolyte, LSM/YSZ composite for the cathode, and SUS 430 for the interconnect plate) and thus the material properties are unchanged. However, IT-SOFCs can still perform

differently with these standard material properties depending on the operational, microstructural, and dimensional parameter variations.

High operating temperatures of SOFCs are known to enhance the ionic conduction in the electrolyte as well as the electrochemical reactions in the electrodes. However, mechanical failure of the PEN structures and the physical/chemical degradation of the electrodes materials may be accelerated at such high operating temperatures (Selcuk, 2001; Radovic and Lara-Curzio, 2004). As a solution to these problems, IT-SOFCs operating at 600~800°C have been developed (Minh, 1993), which utilizes an extremely thin electrolyte (5~10 μm) to reduce the ohmic overpotential. Thus, the effects of operating conditions including inlet temperature and pressure on the performance curves are investigated first through the parametric study. Note that optimized operating conditions can result in higher efficiency and more stable operation for a given IT-SOFC.

Secondly, the properties of PENs are significantly affected by the electrode microstructures such as the particle size, porosity, electronic phase composition, etc. This means that electrodes fabricated with the same materials can have different electrical and electrochemical properties. Multi-layer electrode structures are generally adopted in IT-SOFCs, which tend to enhance different fuel cell processes in different layers. For example, the two-layer electrodes considered in this study improve the electrochemical reactions in the functional layers (AFL and CFL) and the electron conduction and mass diffusion in the bulk transport layers (ASL and CCCL). Bearing the particular roles of each layer in the two-layer electrodes in mind, the effects of the particle size and porosity on the performance of IT-SOFCs are investigated through the parametric study. Note that the particle size and porosity directly influence the density of TPBL in the electrode as well as the mass and electron transport properties.

During the operation of IT-SOFCs, heat released from the electrochemical reactions and Joule heating leads to spatially non-uniform temperature distribution inside the PEN. This non-uniformity induces thermal stresses in the PEN due to the discrepancy of thermal expansion coefficients between the anode, electrolyte, and the cathode. In planar, anode-supported IT-SOFCs, the reaction heat is generally

exhausted by the air flow in the gas channel. That is, the cell temperature is generally controlled by the convective heat transfer of air flow in planar IT-SOFCs. Thus, the effects of the channel and cell dimensions are investigated, such as the channel width and cell length. In addition, the thickness of each layer in the two-layer anode and cathode is also investigated through the parametric study.

The performance of hydrogen-fueled IT-SOFCs due to the change in the operational, microstructural, and dimensional parameters is quantitatively evaluated in terms of the current–voltage curve, maximum cell temperature, Nernst potential, as well as the activation, concentration, and ohmic potential losses (including the contact overpotential). And the sensitivity of the output potential to each parametric variation is also evaluated at the standard fuel utilization factor of 65% (0.65 A/cm^2).

4.2 Model Description

The parametric study is performed using the 3D micro/macroscale for H_2-fueled IT-SOFCs described in chapter 2 and chapter 3, thus the model explanation is not repeated here.

4.3 Results

4.3.1 Effects of operating conditions

The operating condition is important in that the performance of IT-SOFCs can be maximized when they are operated at optimized conditions. In addition, the optimized conditions can also lead to more stable performance as well as better durability of IT-SOFCs in the long term. To investigate the effects of the operating temperature, the inlet temperature of fuel and air streams is varied as 600, 700, and 800°C. Similarly, to investigate the effects of the operating pressure, the gas pressure of fuel and air streams is also varied as 1, 2, and 3 atm. Note that the present micro/macroscale model does not consider the pressure variation inside the flow channel. In other words, uniform pressure is assumed inside the gas channel. The operational parameters considered in this parametric study are listed in Table 4.1, where the values with an under bar denote the standard condition.

Table 4.1 Operational parameters.

Parameter	Values
Temperature, T	600, <u>700</u>, 800°C
Pressure, p	<u>1</u>, 2, 3 atm

* Values with under bar denote the standard conditions

4.3.1.1 Operating temperature

Fig. 4.1 presents the effects of the operating temperature, $T^{\mathrm{o}}_{\mathrm{air/fuel}}$, on the performance of hydrogen-fueled IT-SOFCs with the con-flow configuration. The current–voltage ($I-V$) characteristics of IT-SOFCs and the maximum cell temperature are plotted in Fig. 4.1(a). It is found that the performance is highly sensitive to the cell temperature over the whole range of the cell current density, i^{cell}. In fact, the operating temperature is the single most important parameter among those considered in this study. As the inlet temperature increases, electrochemical reactions are improved while various internal resistances are reduced, resulting in much higher performances. Then, the contribution of the Nernst potential and each potential loss are inspected from Figs. 4.1(c) to 4.1(g). In Fig. 4.1(c), the Nernst potential, φ°, at $i^{\mathrm{cell}}=0$ A/cm^2 decreases by about 0.02 V as the operating temperature increases by about 100°C. This is because the Gibb's free energy of formation for water vapor, $\Delta g_{\mathrm{f,H_2O}}(T)$, decreases with temperature, T. The Nernst potential continuously decreases with i^{cell}, which is also due to higher cell temperature at higher current density shown in Fig. 4.1(a).

The effects of the operating temperature on the concentration overpotentials, η^{conc}, are plotted in Fig. 4.1(d), where the anode concentration overpotential becomes the dominant potential loss as i^{cell} approaches the limiting current density of 1.0 A/cm^2. In general, the anode concentration overpotential is much higher than the cathode concentration overpotential according to the difference in the limiting current for fuel and air supplies (1 A/cm^2 for fuel supply and 4 A/cm^2 for air supply). In Fig. 4.1(d), the anode concentration overpotential is found to increase with the

operating temperature, which is the result of $RT/2F$ term in the concentration overpotential equation (see Eq. (2.30)). Because the hydrogen diffusivity is sufficiently high at 600°C, the partial pressure of hydrogen at the reaction sites does not changed much though the gas diffusivity is enhanced at higher temperatures. On the contrary, the cathode concentration overpotential becomes smaller at higher operating temperatures, primarily due to the enhanced oxygen diffusivity.

In Fig. 4.1(e), higher operating temperatures are observed to significantly reduce the activation overpotentials, η^{act}, which is because the electrochemical reactions are greatly enhanced at higher temperatures. Fig. 4.1(e) indicates that the cathode activation overpotential is the dominant potential loss at low current density, while the anode activation overpotential is much smaller. The decreasing behavior of the activation overpotentials at high i^{cell} is the result of the increased cell temperature. The effects of the operating temperature on the ohmic overpotential η_{E} in the electrolyte are presented in Fig. 4.1(f). Note that the ohmic overpotential depends on the ionic conductivity, σ_{E}, and the thickness, l_{E}, of the electrolyte as

$$\eta_{\mathrm{E}} = i \times r = i^{\mathrm{cell}} \times l_{\mathrm{E}} / \sigma_{\mathrm{E}} . \tag{4.1}$$

The ionic conductivity of the electrolyte is a function of temperature following the Arrhenius exponential behavior. Thus, the difference of the ohmic potential loss also decreases with the operating temperature. And, at high current densities, ohmic overpotential decreases because the cell temperature increases due to the reaction and Joule heat.

Fig. 4.1(e) shows the effects of the operating temperature on the potential loss at the region of the electrode and the interconnect plate contact, η^{asr}. The contact overpotential also strongly depends on the cell temperature, whose magnitude is comparable to that of the ohmic overpotential in the electrolyte. Thus, the contact overpotentials at the anode and cathode make significant contribution to the overall potential loss. Finally, Fig. 4.1(h) presents the sensitivity of the output potential at 65% fuel utilization ($\zeta_{\mathrm{fuel}} = 0.65$, or equally $i^{\mathrm{cell}} = 0.65$ A/cm^2) to the inlet gas temperature. The cell potential is found to increase by about 4.2% (from 0.715 V to 0.745 V) when the operating temperature is increased from 700°C to 750°C.

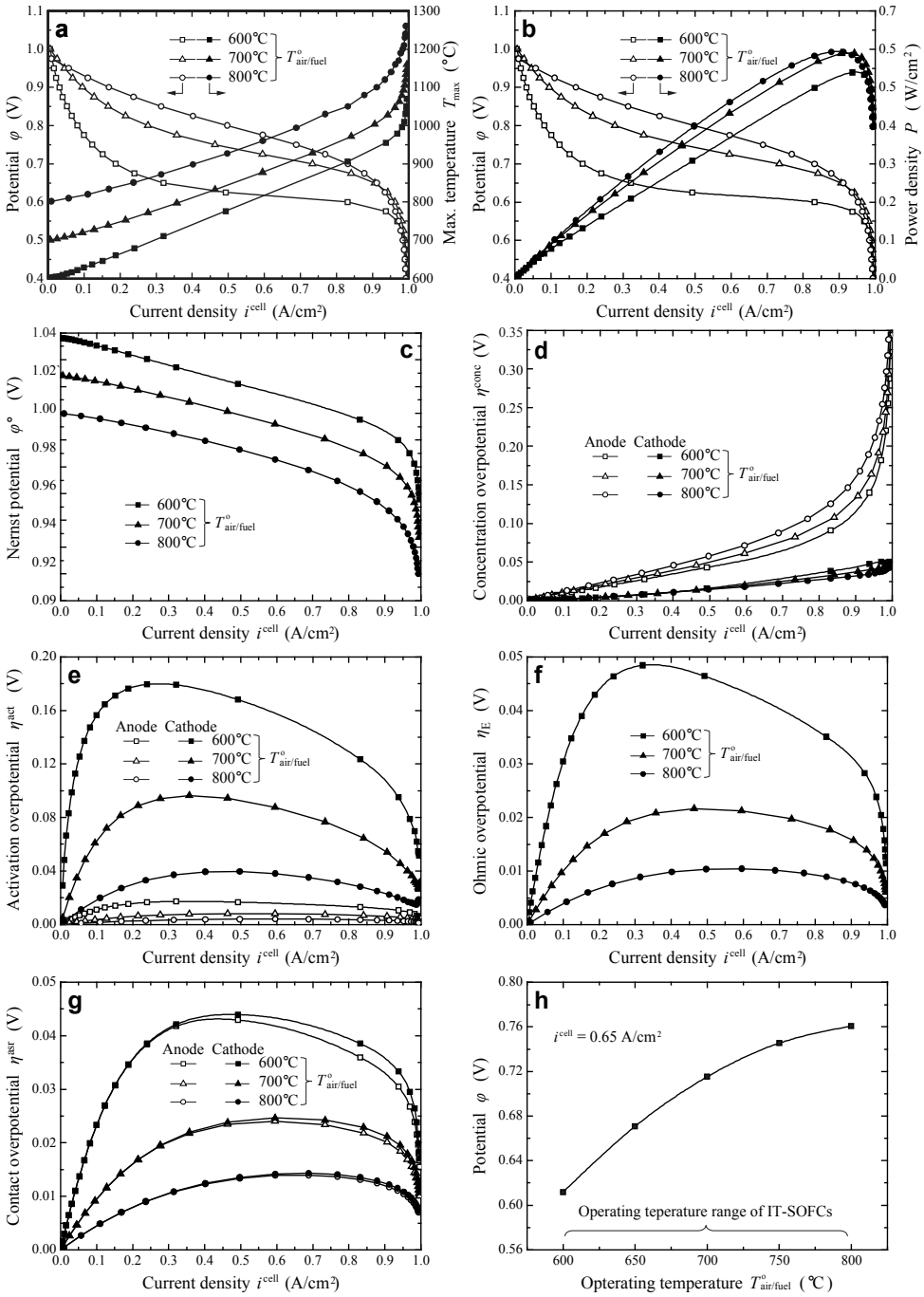

Fig. 4.1 Effect of operating temperature on (a) $I-V$ characteristics, (b) power density, (c) Nernst potential, (d) concentration overpotential, (e) activation overpotential, (f) ohmic overpotential, (g) contact overpotential, and (h) cell potential at 0.65 A/cm^2.

4.3.1.2 Operating pressure

Fig. 4.2 shows the effects of the operating pressure, $p^{\mathrm{o}}_{\mathrm{air/fuel}}$, on the performance of hydrogen-fueled IT-SOFCs with the con-flow configuration. The cell potential is observed to be considerably affected by the operating pressure over the whole range of the current density, i^{cell} in Figs. 4.2(a) and 4.2(b). The Nernst potential is found to increase with higher operating pressure in Fig. 4.2(c), which can be easily explained by referring to the Nernst potential equation given in Eq. (2.27). Higher operating pressure results in higher molar density of oxygen molecules near the cathode reaction sites, which in turn increases the Nernst potential. However, the increased operating pressure in the anode has little effect on the Nernst potential since partial pressures of hydrogen and water vapor are canceled out. Note that increasing the operating pressure of IT-SOFCs may require additional power consumption for compressor work.

The effects of the operating pressure on the concentration overpotential, η^{conc}, are presented in Fig. 4.1(d), where η^{conc} is found to generally decrease with the operating pressure. This result implies that increasing gas pressure enhances the mass transport in the porous electrodes and gas channels. When the operating pressure increases, the binary diffusivity decreases inversely proportional to the pressure while the molar density increases proportional to the pressure. Thus, the diffusion is believed to be less influenced by the operation pressure. However, the viscous flow is enhanced by the higher molar density, and this leads to faster mass transport at higher operating pressure.

The effects of the operating pressure on the activation, ohmic and contact overpotentials are plotted from Figs. 4.2(e) to 4.2(g). The cathode activation overpotential is found to decrease slightly due to higher oxygen partial pressure near the reaction sites, but other overpotentials show much smaller variations (note the scale). Thus, the operating pressure is believed to mainly alter the Nernst potential and concentration overpotential. Finally, the sensitivity of the output potential to the operating pressure is shown in Fig. 4.2(h) at the fuel utilization factor of 65%. The cell potential is found to increase by about 4.4% (from 0.715 V to 0.747 V) when the operating pressure is increased from 1 atm to 2 atm.

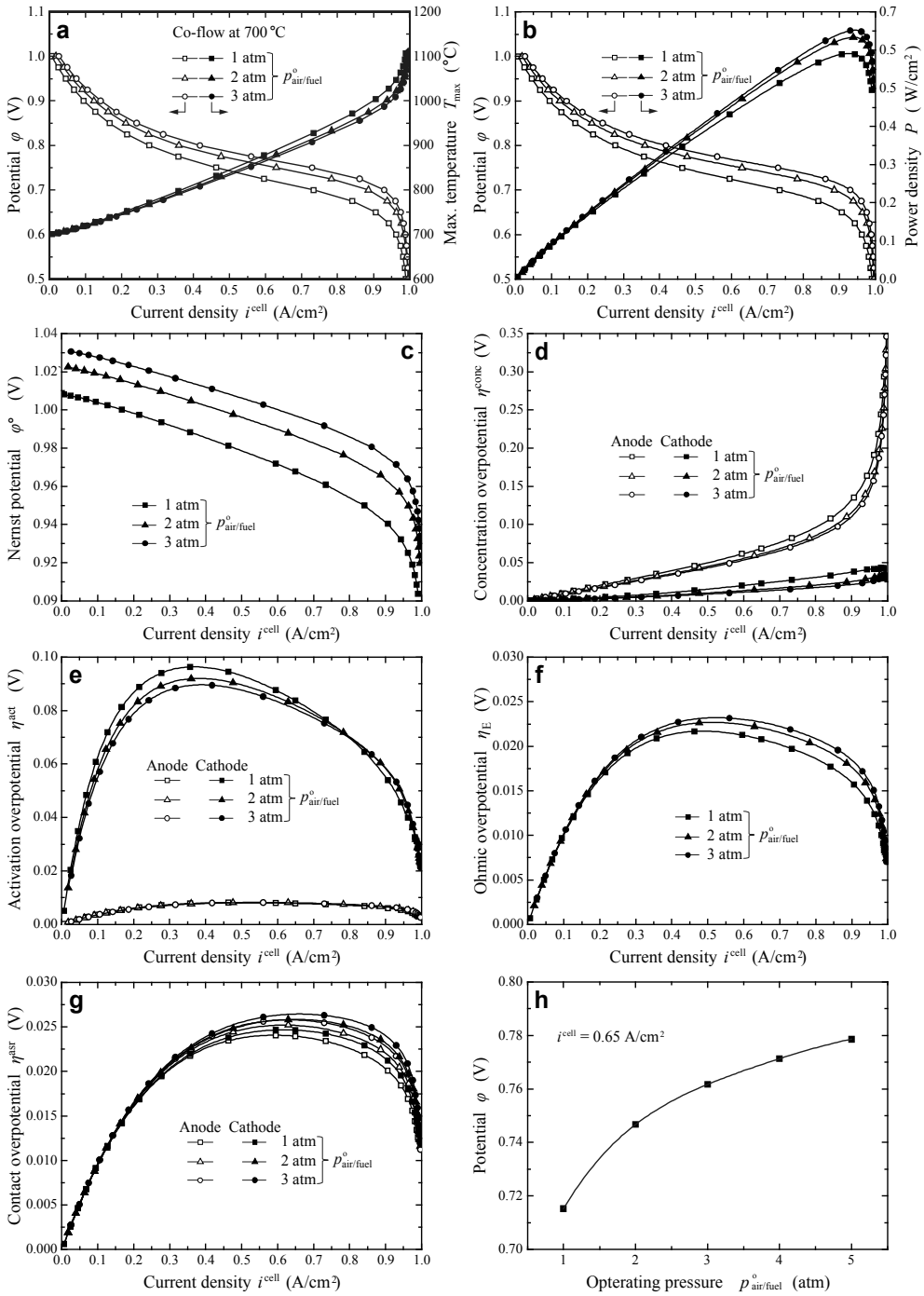

Fig. 4.2 Effect of operating pressure on (a) $I-V$ characteristics, (b) power density, (c) Nernst potential, (d) concentration overpotential, (e) activation overpotential, (f) ohmic overpotential, (g) contact overpotential, and (h) cell potential at 0.65 A/cm^2.

4.3.2 Effects of electrode microstructures

The primary role of the electrodes in IT-SOFCs is to provide active reaction sites for electrochemical reactions, which is generally taken up by the functional layers (AFL and CFL) located near the electrolyte. For this reason, the functional layers are generally made by mixing fine electronic and ionic particles to maximize the three-phase boundary length (TPBL) inside the layer. In addition, the functional layers are made to have relatively small porosity around 0.2~0.3 to further increase the TPBL. Then, the electrochemical activity of the electrodes is governed by the particle size and porosity, and also by the electronic/ionic phase composition.

The second role of the electrodes is to transport gas molecules between the reaction sites and the gas channels, not to mention to conduct electrons to and from the interconnect plates. This role is generally taken up by the bulk transport layers (ASL and CCCL) which are composed of coarse particles with higher porosity around 0.5. The transport of gas molecules in the bulk transport layers are done by the processes of ordinary diffusion, Knudsen diffusion and viscous permeation. These processes strongly depend on the microstructural parameters, such as the paricle size, porosity, and tortuosity. In summary, the electrochemical and transport properties of porous electrodes of IT-SOFCs are directly governed by the microstructural parameters.

Table 4.2 Microstructural parameters.

Parameters	Regions	Values
Particle size (diameter) $d_{io} = d_{el}$	CCCL	1, 2, 4 μm
	ASL	1, 2, 4 μm
	CFL	0.5, 1, 1.5 μm
	AFL	0.5, 1, 1.5 μm
Porosity, ε	CCCL	0.4, 0.5, 0.6
	ASL	0.4, 0.5, 0.6

* Values with under bar denote the standard conditions

In this study, the effects of the particle size and porosity on the performance of

IT-SOFCs are investigated according to the microstructural parameters listed in Table 4.2. The particle diameter is varied as 1, 2, and 4 μm for the bulk transport layers (ASL and CCCL) and 0.5, 1, and 1.5 μm for the functional layers (AFL and CFL). Note that the diameter for electronic particles is assumed equal to that for ionic particles. Similarly, the porosity is varied as 0.4, 0.5, and 0.6 for the bulk transport layers (ASL and CCCL).

4.3.2.1 Particle diameter

The effects of particle diameter, d_{el} $(=d_{\mathrm{io}})$, in the bulk transport layers (ASL and CCCL) on the performance of hydrogen-fueled IT-SOFCs are investigated in Figs. 4.3 and 4.4. The ASL is assumed to be composed of equal-sized electronic and ionic particles (Ni/YSZ), while the CCCL is assumed to be composed of solely electronic particles (LSM). Note that the current micro/macroscale model does not consider the variation of effective electronic conductivity in the bulk transport layers due to the change in the particle size. This is because the effective electronic conductivities are much larger than the ionic conductivities and thus have less impact on the overall potential loss.

The role of the CCCL is to transport electrons and oxygen molecules towards the CFL where the electrochemical reactions occur. Fig. 4.3 indicates that the effects of the particle diameter in the CCCL on the cell performance are marginal. The cell performance is observed to be slightly enhanced with larger particle diameters, which is only noticeable at higher current densities ($i^{\mathrm{cell}} > 0.5$ A/cm^2). The slight improved cell performance with larger particle diameter in the CCCL is the direct result of the reduced cathode concentration overpotential shown in Fig. 4.3(d). The particle diameter is closely related with the pore size that governs the Knudsen diffusivity and flow permeability. Thus, increasing particle size enhances the mass transport in the bulk transport layers.

Fig. 4.3(h) indicates that the cell potential at the fuel utilization factor of 65% (at 0.65 A/cm^2) is improved by about 0.7% (from 0.715 V to 0.721 V) when the particle diameter of the CCCL is increased from 1 μm to 2 μm. Considering the relatively small thickness of the CCCL (about 50~100 μm), too large particle

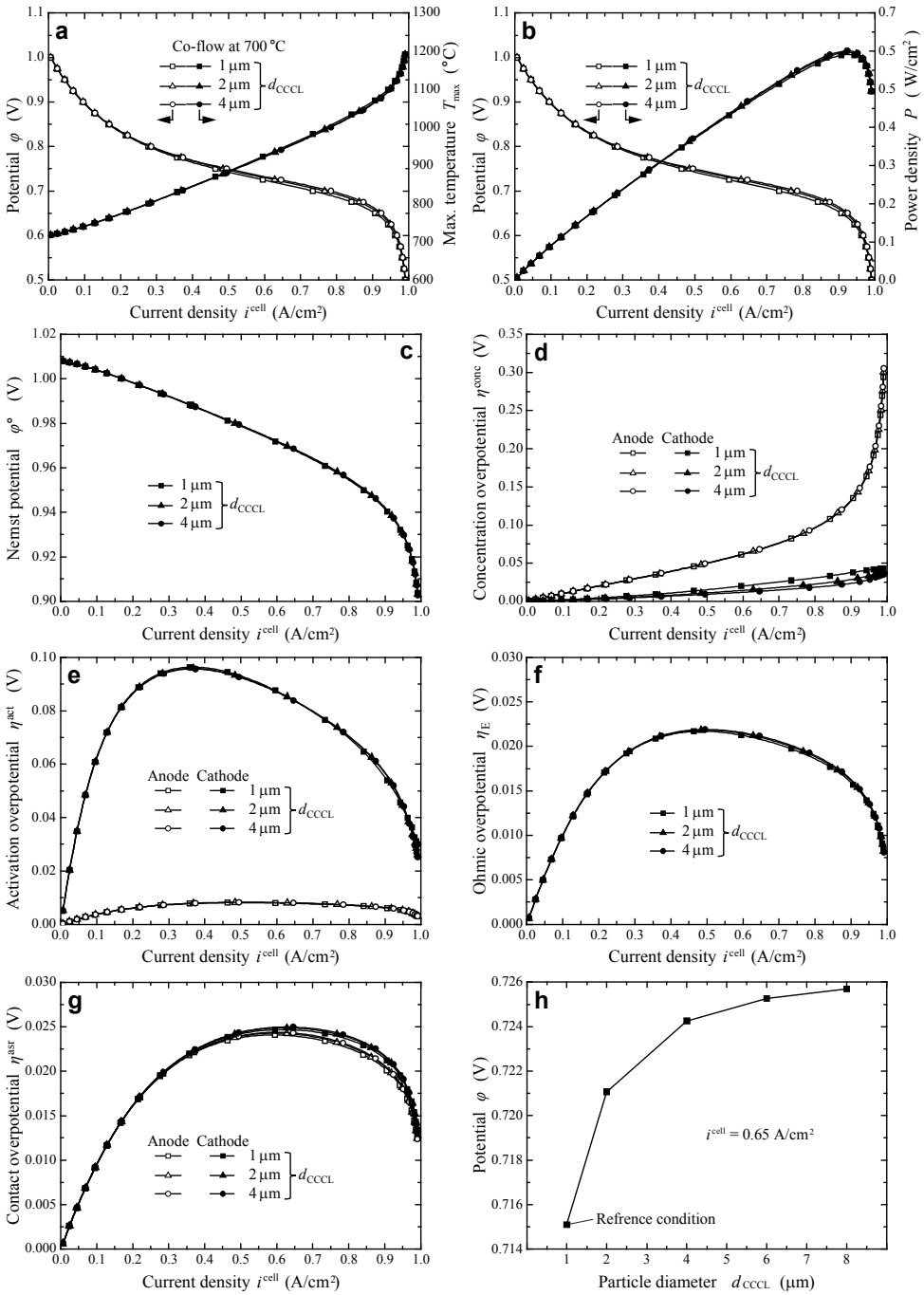

Fig. 4.3 Effect of particle diameter in CCCL on (a) $I-V$ characteristics, (b) power density, (c) Nernst potential, (d) concentration overpotential, (e) activation overpotential, (f) ohmic overpotential, (g) contact overpotential, and (h) cell potential at 0.65 A/cm^2.

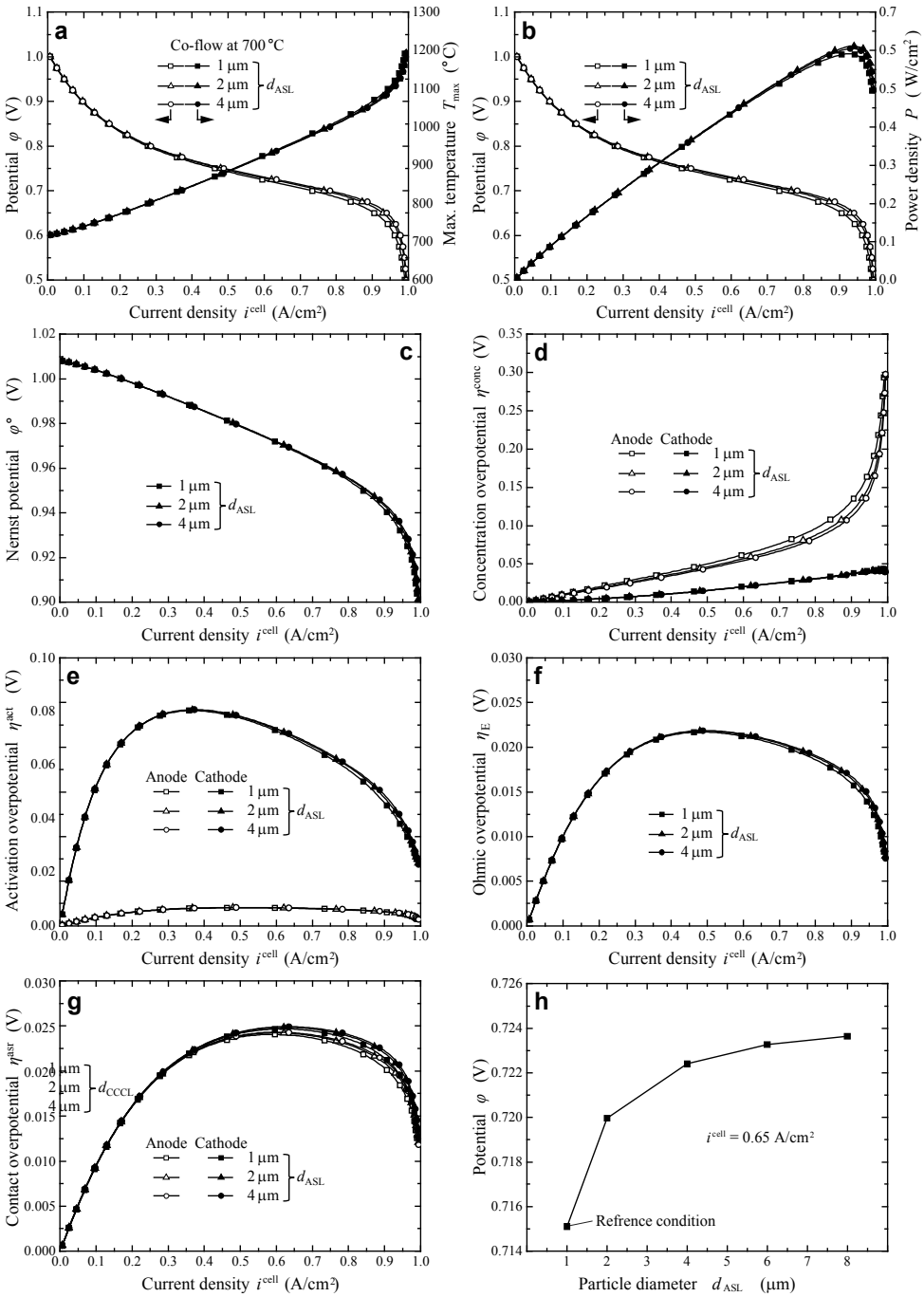

Fig. 4.4 Effect of particle diameter in ASL on (a) $I-V$ characteristics, (b) power density, (c) Nernst potential, (d) concentration overpotential, (e) activation overpotential, (f) ohmic overpotential, (g) contact overpotential, and (h) cell potential at 0.65 A/cm^2.

diameter is not believed to be desirable.

The effects of the particle diameter in the ASL on the cell performance are also presented in Fig. 4.4, where the current–voltage curves similar to those in Fig. 4.3 are observed. The role of the ASL is to conduct electrons as well as to transport hydrogen and water molecules between the AFL and the gas channel. By increasing the particle diameter in the ASL, the mass transport can be enhanced as evidenced by the lower anode concentration overpotential shown in Fig. 4.4(d). However, other overpotentials are practically unchanged with the variation in the particle diameter in Fig. 4.4, and this behavior is the same as that in Fig. 4.3.

In Fig. 4.4(h), the cell potential at 0.65 A/cm^2 is found to increase by about 0.8 % (from 0.715 V to 0.720 V) while the particle diameter of the ASL is increased from 1 μm to 2 μm. Fig. 4.4(h) also indicates that the cell potential can be improved as high as 1.5% by using larger particle diameter for the ASL. However, this enhancement is not significant, and thus the particle diameter in the ASL should be selected based on other requirements.

The effects of particle diameter, d_{el} $(=d_{\mathrm{io}})$, in the functional layers (AFL and CFL) on the performance of hydrogen-fueled IT-SOFCs are investigated in Figs. 4.5 and 4.6. The AFL is assumed to be composed of equal-sized electronic and ionic particles (Ni/YSZ), and so is the CFL (LSM/YSZ). In general, the functional layers have smaller particle diameter and have lower porosity compared with the bulk transport layers to maximize the TPBL for electrochemical reactions. Note that the electronic phase composition (the ratio of electronic phase volume to solid volume) is assumed to be 0.5 ($\phi_{\mathrm{el}} = 1 - \phi_{\mathrm{io}} = 0.5$) because this leads to largest TPBs in the functional layers.

Fig. 4.5 presents the effects of the particle diameter in the CFL on the cell potential of the H_2-fed IT-SOFCs with the co-flow configuration. The simulation points out that the particle diameter in the CFL is a key parameter that drastically alters the cell performance in the whole current density ranges. Smaller particle diameter significantly increases the number of particles and thus the number of TPBs formed between electronic and ionic particles. For example, reducing the diameter in the functional layer by half will result in eight times more TPB contacts

therein. Then, the cathode activation overpotential is reduced when the particle diameter in the CFL decreases due to the increased TPBL, which is clearly observed in Fig. 4.5(e). The maximum temperature in the PEN is found to increase as the particle diameter increases in Fig. 4.5(a), which is the result of the increased reaction heat due to the efficiency reduction. The variation of other overpotentials, which is relatively small in magnitude, is believed to be caused by the temperature variation.

In Fig. 4.5(h), the cell potential at the standard condition (0.65 A/cm^2) is observed to increase by about 4.1% (from 0.715 V to 0.745 V) as the particle diameter in the CFL is reduced from 0.5 μm to 0.25 μm. This result clearly indicates that smaller particle diameter is beneficial in improving the cell performance. However, it should be noted that too small particles in the functional layers tend to degrade faster at high temperatures.

The effects of the particle diameter in the AFL on the current–voltage curves of IT-SOFCs are plotted in Fig. 4.6. Note that the AFL is the binary mixtures of Ni particles for electronic conduction and YSZ particles for ionic conduction, along with the pore space for gas diffusion. It is observed that the effects of the particle diameter in the AFL are less noticeable compared with the effects of the particle diameter in the CFL. The anode activation overpotential is reduced when the particle diameter in the AFL decreases as shown in Fig. 4.6(e). However, the contribution of the anode activation overpotential to the total potential loss is relatively small due to its small magnitude. This result is partially due to the fast hydrogen oxidation reaction (HOR) in the TPBs of Ni and YSZ particle contacts. Note that other overpotentials are almost unchanged in Fig. 4.6.

The improvement of the cell potential at 0.65 A/cm^2 is less than 0.2% (from 0.715V to 0.717V) during the reduction of the particle diameter in the AFL from 0.5 μm to 0.25 μm. This clearly indicates that the particle diameter of 0.5 μm is sufficiently small to provide rich TPBL for the electrochemical reactions in the AFL. Instead, larger particle diameter may be sought to enhance the microstructural stability and to reduce the long-term performance loss.

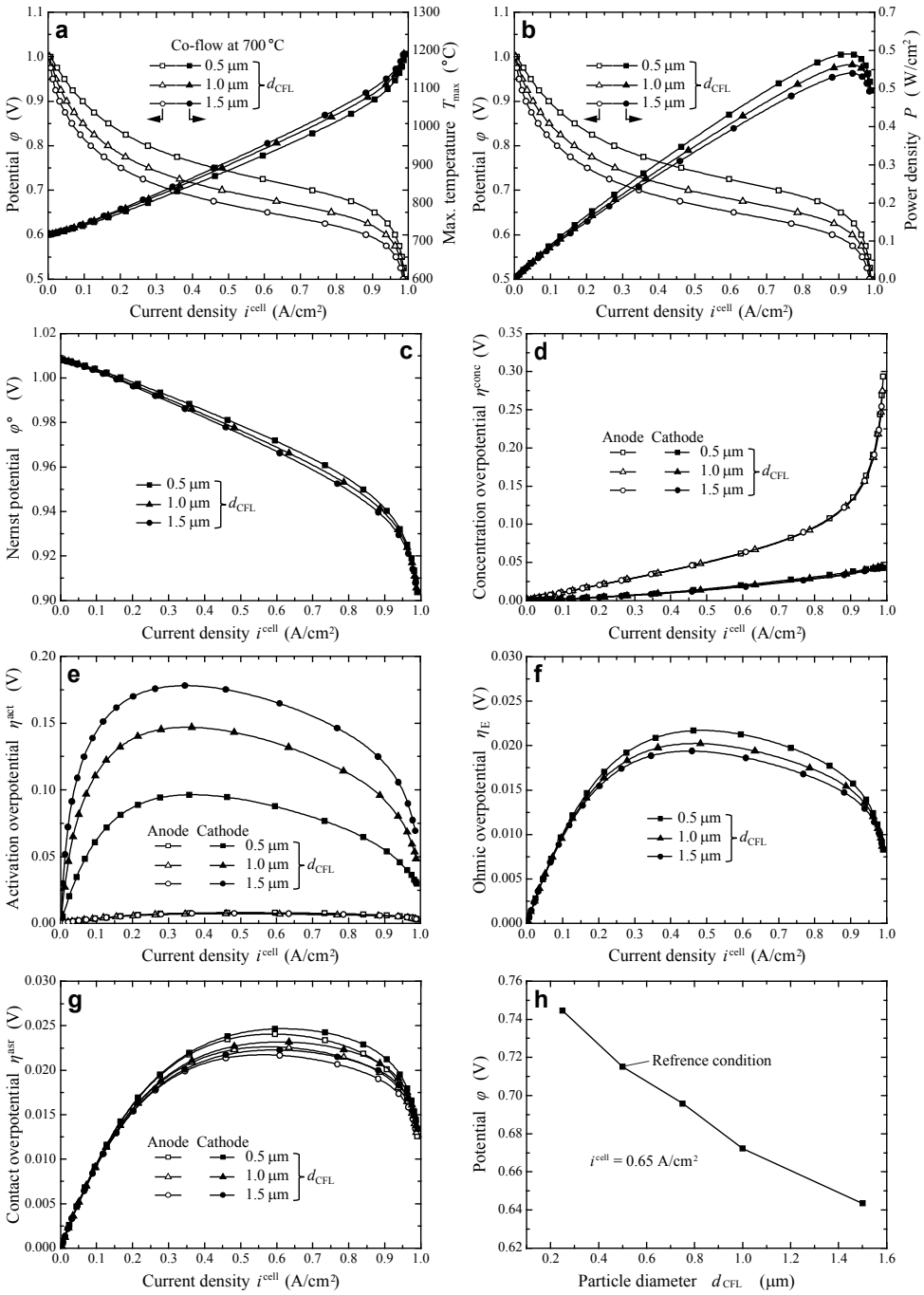

Fig. 4.5 Effect of particle diameter in CFL on (a) $I-V$ characteristics, (b) power density, (c) Nernst potential, (d) concentration overpotential, (e) activation overpotential, (f) ohmic overpotential, (g) contact overpotential, and (h) cell potential at 0.65 A/cm^2.

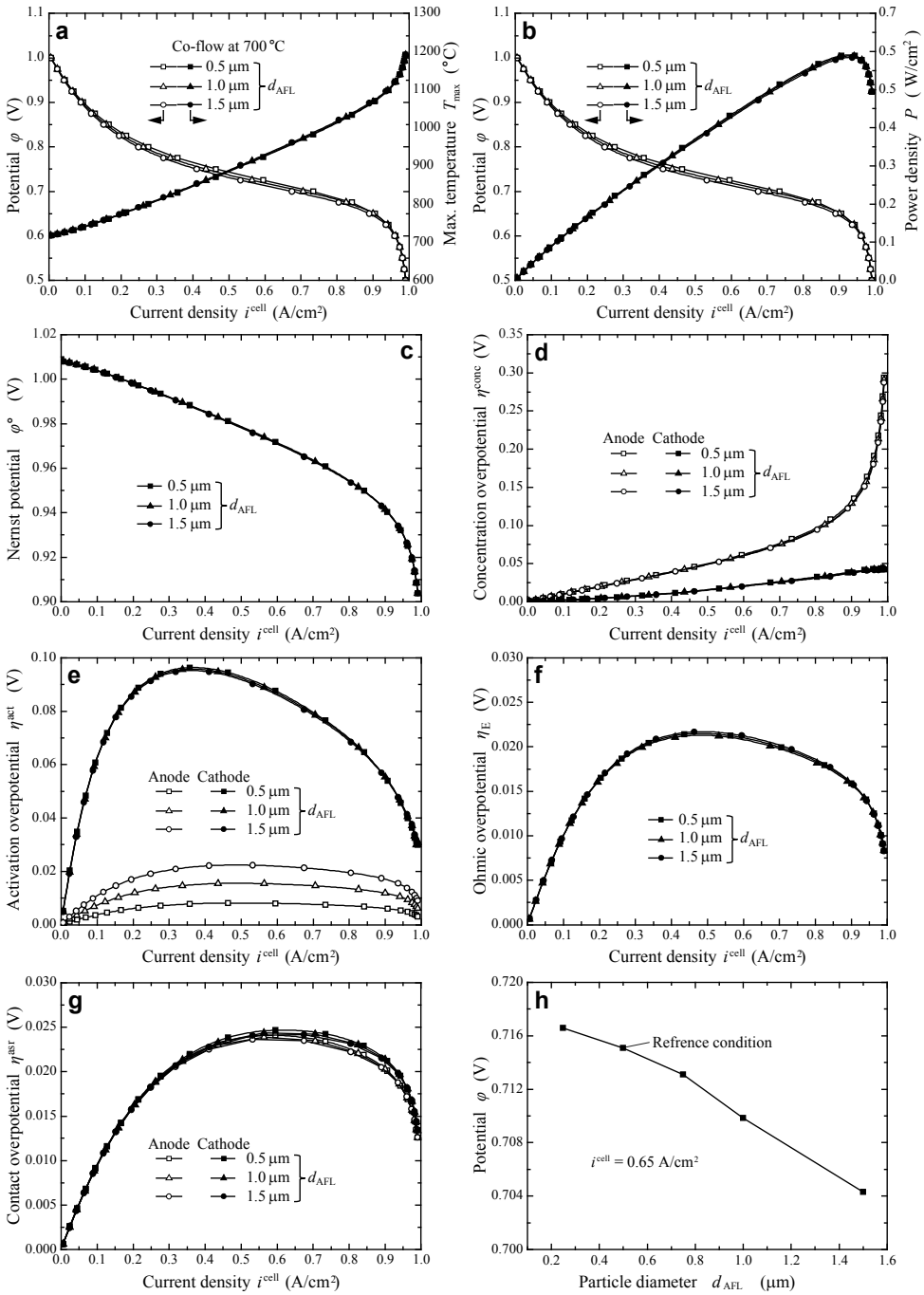

Fig. 4.6 Effect of particle diameter in AFL on (a) $I-V$ characteristics, (b) power density, (c) Nernst potential, (d) concentration overpotential, (e) activation overpotential, (f) ohmic overpotential, (g) contact overpotential, and (h) cell potential at 0.65 A/cm^2.

4.3.2.2 Porosity

The effects of porosity, ε, in the bulk transport layers (ASL and CCCL) on the performance of IT-SOFCs are investigated in Figs. 4.7 and 4.8. The porosity of the bulk transport layers changes the mass transport properties as well as the effective electronic conductivities. That is, higher porosity increases the mass transport rate but also decreases the electron conduction rate. However, the effective electronic conductivities are believed to be sufficiently higher at porosity around 0.3~0.7 as discussed above. Thus, the effects of porosity variation will be more likely to show in the concentration overpotential.

The effects of porosity in the CCCL on the performance of the H_2-fed IT-SOFCs are presented in Fig. 4.7, where higher porosity results in better performance especially at high current density range ($i^{cell} > 0.4$ A/cm^2). This behavior is easily explained by the cathode concentration overpotentials shown in Fig. 4.7(b). With higher porosity in the CCCL, the effective mass diffusivity and flow permeability increase, and this leads to higher oxygen partial pressure in the CFL. In addition, in the 3D channel/interconnect plate geometries, the region of the CFL under the interconnect rib experiences lower oxygen concentration. By increasing the porosity of the CCCL, the oxygen concentration can become more uniform under the channel and under the rib. This also partly explains the enhanced cell performance with higher porosity of the CCCL. In Fig. 4.7, potential losses other than the cathode concentration overpotential seem to rather insensitive to the porosity of the CCCL.

Finally, the sensitivity of the output potential to porosity of the CCCL is shown in Fig. 4.7(h) for the fuel utilization factor of 65%. The cell potential is found to increase by about 0.9% (from 0.715V to 0.721V) during the porosity is increased from 0.5 to 0.6. Since higher porosity tends to exhibit lower mechanical strength, too high porosity should be avoided.

Fig. 4.8 shows the effects of porosity in the ASL on the current–voltage performance of IT-SOFCs with the co-flow configuration. Fig. 4.8(a) points out that the porosity of the ASL mainly influences the cell potential at high current density ranges. The anode concentration overpotential shown in Fig. 4.8(d) explains the

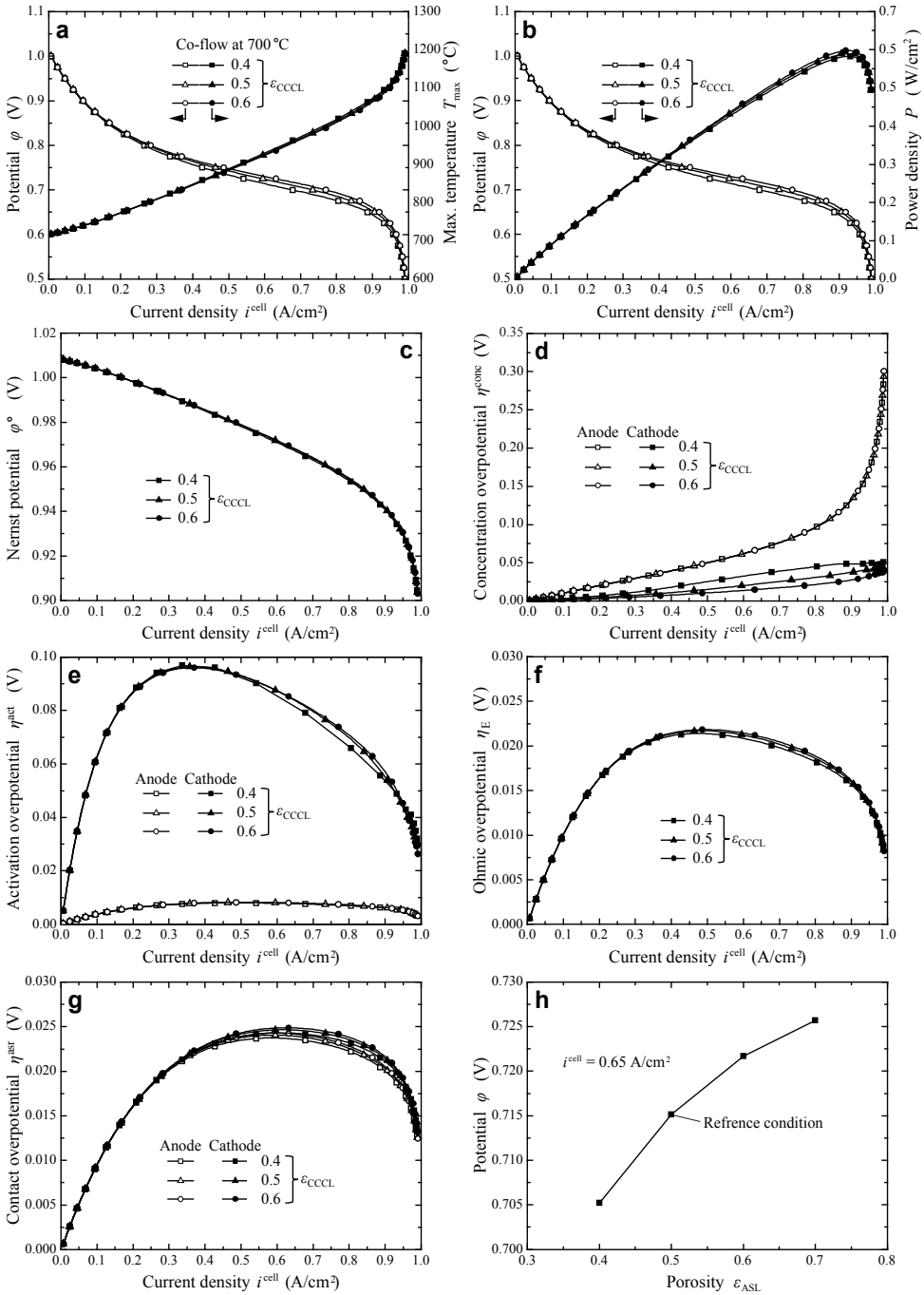

Fig. 4.7 Effect of porosity in CCCL on (a) $I-V$ characteristics, (b) power density, (c) Nernst potential, (d) concentration overpotential, (e) activation overpotential, (f) ohmic overpotential, (g) contact overpotential, and (h) cell potential at 0.65 A/cm^2.

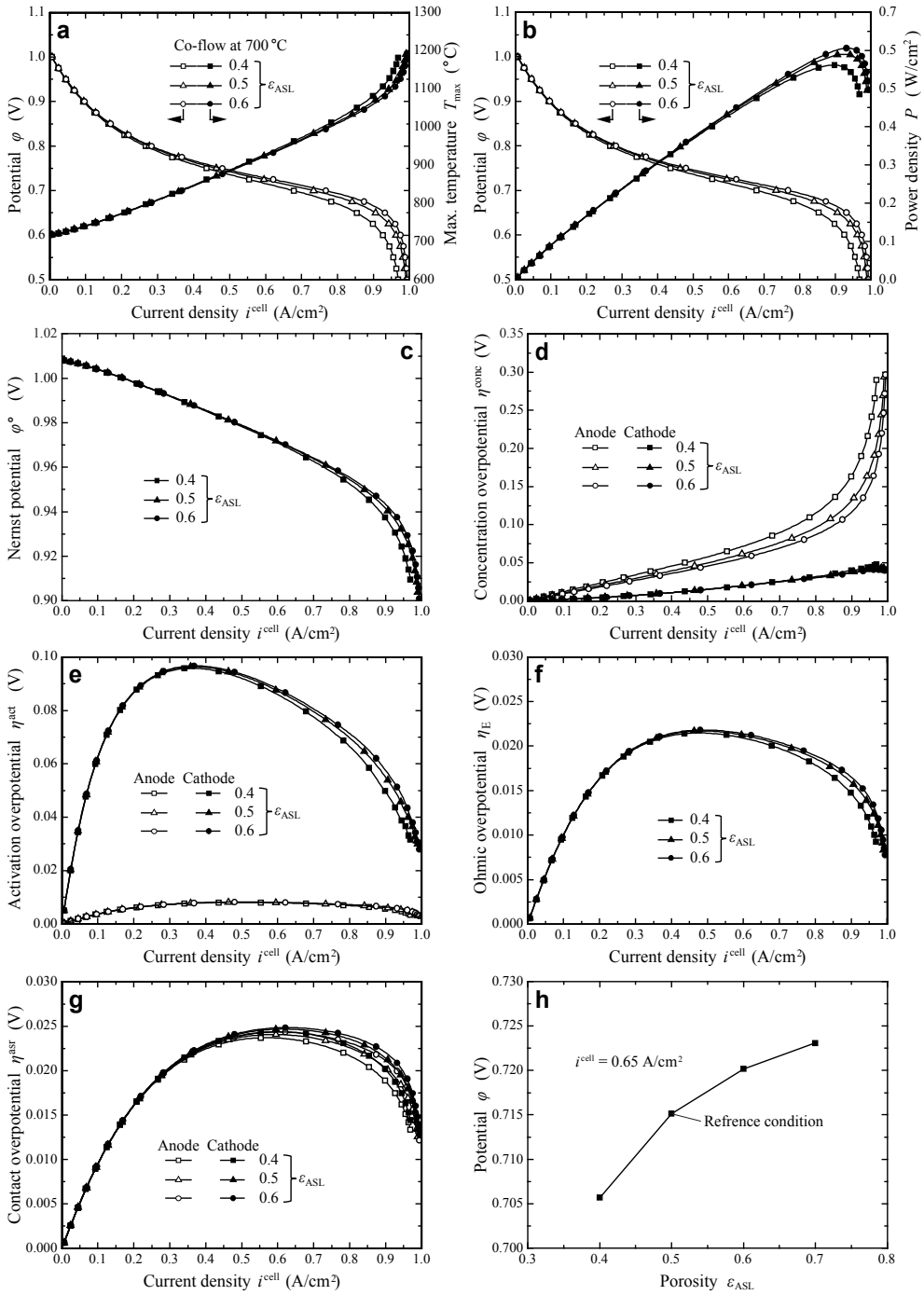

Fig. 4.8 Effect of porosity in ASL on (a) $I-V$ characteristics, (b) power density, (c) Nernst potential, (d) concentration overpotential, (e) activation overpotential, (f) ohmic overpotential, (g) contact overpotential, and (h) cell potential at 0.65 A/cm^2.

observed behavior of the cell potential. The mass transport in the ASL is facilitated as the porosity increases, which becomes more noticeable near the limiting current condition (1 A/cm^2). Thus, the anode concentration overpotential can be reduced by increasing the porosity of the ASL. Again, potential losses other than the anode concentration overpotential are found to be rather insensitive to the porosity of the ASL.

Fig. 4.8(h) indicates that the cell potential at 0.65 A/cm^2 is enhance by about 0.7% (from 0.715V to 0.720V) when the porosity of the ASL is increased from 0.5 to 0.6.

4.3.3 Effects of cell dimensions

In this section, we investigated the effects of the geometrical dimension of IT-SOFCs on the cell performance, including the thickness of each layer in the PEN, the width of the flow channel, and the overall cell length. The role of the bulk transport layers (ASL and CCCL) is mass transport and current collection and the role of the functional layers (AFL and CFL) is electrochemical reaction. Since these processes are dependent on the geometrical extent, there is an optimal thickness for achieving the particular role of each layer. However, other requirements should also be considered. For example, the ASL should provide mechanical support for the thin electrolyte and other thin layers in the PEN.

The interconnect plate with flow channels plays a role in transporting the reactant and product gas molecules, exhausting the reaction heat, and collecting and conducting electric current. The performance of IT-SOFCs is thus dependent on the channel/interconnect rib dimensions and overall cell length. In general, larger channel width is expected to be beneficial for reactant transport and thermal management. More uniform reactant concentration is expected in the reaction zones. In addition, smaller cell length is also favorable for the mechanical integrity of the PEN and for the uniform distribution of temperature.

In this study, the effects of the thickness of each layer in the PEN on the performance of IT-SOFCs are investigated first, according to the dimensional parameters summarized in Table 4.3. The layer thickness is varied as 0.25, 0.5, 1

mm for the ASL (l_{ASL}), as 50, 75, and 100 μm for the CCCL (l_{CCCL}), and 10, 20, 30 μm for the functional layers (AFL, l_{AFL}, and CFL, l_{CFL}). In order to investigate the effects of the channel/interconnect plate design, the overall cell length, L_{x}, is varied as 5, 10, and 15 cm and the channel width, W_{CH}, is varied as 1, 1.4, and 1.8 mm. The interconnect plate geometries with different channel widths are shown in Fig. 4.9, where the channel height, H_{CH}, and the interconnect rib width, W_{CH}, are fixed at 1 mm. Note that both the anode and cathode gas channels are assumed to have the same geometry.

Table 4.3 Dimensional parameters.

Parameters	Regions	Values
Electrode thickness	CCCL	50, 75, 100 μm
	ASL	250, 500, 1000 μm
	CFL	10, 20, 30 μm
	AFL	10, 20, 30 μm
Interconnect/ Channel	Channel width	1.0, 1.4, 1.8 mm
	Cell length	5, 10, 15 cm

* Values with under bar denote the standard conditions

Then, as illustrated in Fig. 4.9, the length of the calculation domain in the y-direction, L_{y}, is 1, 1.2, and 1.4 mm for $W_{\mathrm{CH}} = 1$, 1.4, and 1.8 mm, respectively. According to the variation in the channel dimension, the total axial molar flow rate at the inlet cross-section, $N^{\mathrm{o}}_{\mathrm{x,tot}}$, is calculates as

$$N^{\mathrm{o}}_{\mathrm{x,tot,C}} = 2L_{\mathrm{x}}L_{\mathrm{y}}10000\frac{i^{\mathrm{lim}}_{\mathrm{air}}}{4F\,x^{\mathrm{o}}_{\mathrm{O_2}}}, \tag{4.2}$$

$$N^{\mathrm{o}}_{\mathrm{x,tot,A}} = 2L_{\mathrm{x}}L_{\mathrm{y}}10000\frac{i^{\mathrm{lim}}_{\mathrm{fuel}}}{2F\,x^{\mathrm{o}}_{\mathrm{H_2}}}. \tag{4.3}$$

Here, $2L_{\mathrm{x}}L_{\mathrm{y}}$ denotes the double the calculation domain area, which corresponds to the reaction area that that a full channel supply the reactants. In Eq. (4.2) and (4.3), i^{lim} denotes the limiting current density of fuel and air supply, $x^{\mathrm{o}}_{\mathrm{i}}$ denotes the

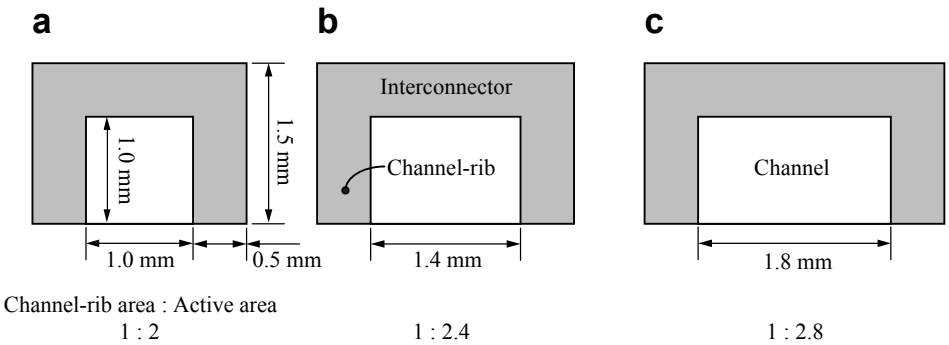

Fig. 4.9 Interconnect plate geometries with the channel width of (a) 1.0 mm, (b) 1.4 mm, and (c) 1.8 mm.

inlet mole fraction of species i and F denotes the Faraday number.

4.3.3.1 Electrode thickness

The effects of the thickness of bulk transport layers (ASL and CCCL) on the performance of hydrogen-fueled IT-SOFCs are investigated in Figs. 4.10 and 4.11. The thickness of the ASL, l_{ASL}, should be sufficiently large in order to support the whole PEN structure. In addition, the ASL also provides rich catalyst area reforming reactions when methane is used as fuel in the IT-SOFCs. However, for IT-SOFCS operated with hydrogen, l_{ASL} can be reduced until the structural requirement is satisfied. The thickness of CCCL, l_{CCCL}, is generally fabricated to be between 50 μm to 100 μm.

Fig. 4.10 points out that increasing the thickness of the CCCL, l_{CCCL}, slightly enhance the cell potential, especially at high current densities ($i^{\mathrm{cell}} > 0.5$ A/cm^2) when mass transport limitation becomes important. Except for the cathode concentration overpotential shown in Fig. 4.10(d), the Nernst potential and all the other potential losses are unchanged. It is known that the oxygen transport towards the CFL region under the interconnect rib is difficult due to the small thickness of the CCCL. Thus, increasing l_{CCCL} facilitates this in-plane (y-direction in the present calculation domain) oxygen diffusion towards the under-rib region of the CFL, which in turn leads to more uniform oxygen concentration and more uniform current generation.

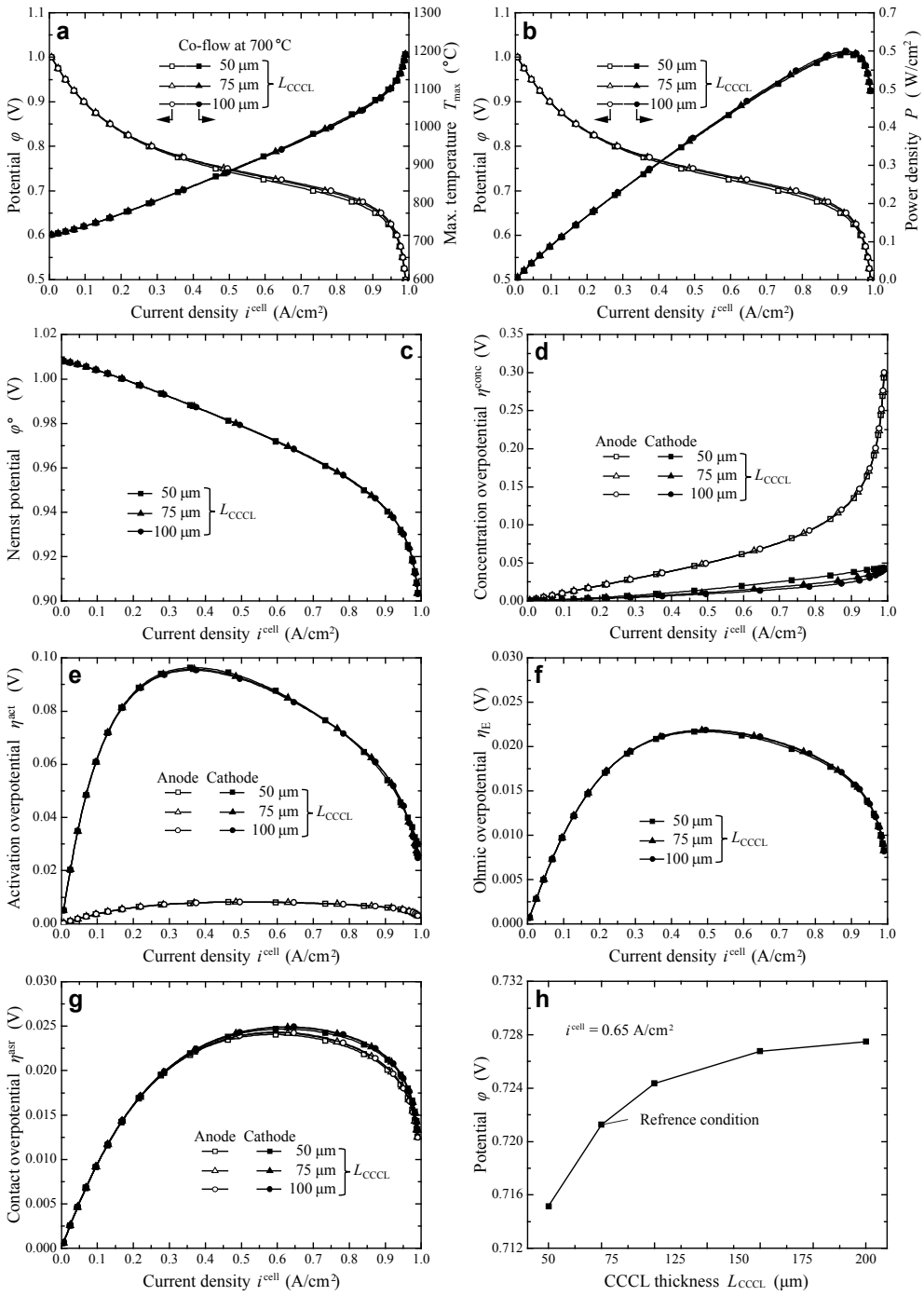

Fig. 4.10 Effect of CCCL thickness on (a) $I-V$ characteristics, (b) power density, (c) Nernst potential, (d) concentration overpotential, (e) activation overpotential, (f) ohmic overpotential, (g) contact overpotential, and (h) cell potential at 0.65 A/cm^2.

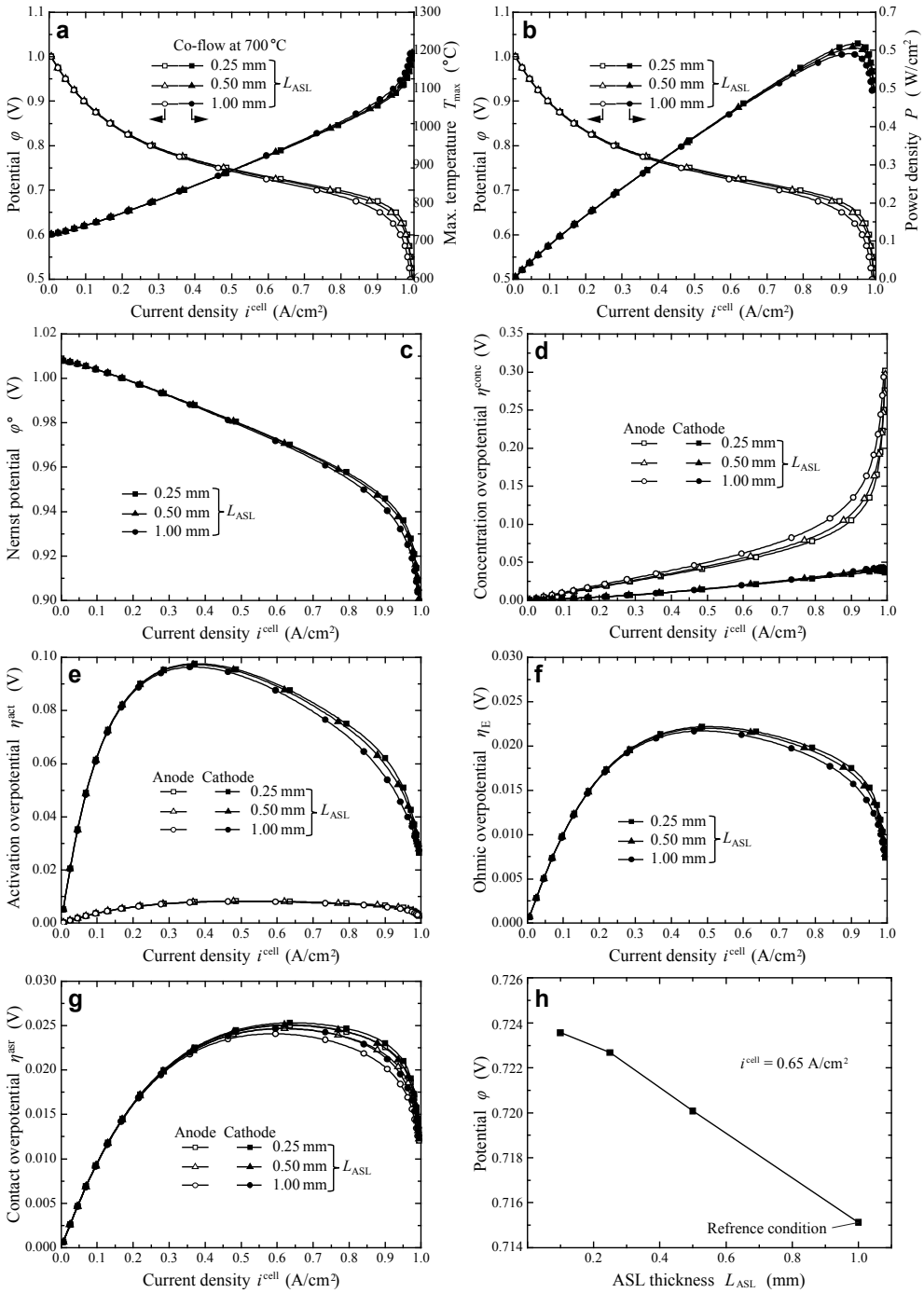

Fig. 4.11 Effect of ASL thickness on (a) $I-V$ characteristics, (b) power density, (c) Nernst potential, (d) concentration overpotential, (e) activation overpotential, (f) ohmic overpotential, (g) contact overpotential, and (h) cell potential at 0.65 A/cm^2.

In Fig. 4.10(h), the cell potential at the fuel utilization factor of 65% is improved by about 1.0% (from 0.715V to 0.721V) when the thickness of the CCCL, l_{CCCL}, is increased from 50 μm to 75 μm. Fig. 4.10(h) also points out that l_{CCCL} larger than 150 μm will result in negligible enhancement of the cell potential.

The effects on the thickness of the CCCL, l_{ASL}, on the performance of IT-SOFCs are shown in Fig. 4.11, where smaller l_{ASL} is observed to result in higher cell potential at high current densities ($i^{\mathrm{cell}} > 0.5$ A/cm^2). At high current density, the mass transport limitation becomes important and thus enhancing mass transport directly lead to better performance. The effects of l_{ASL} are mainly observed in the anode concentration overpotential, shown in Fig. 4.11(d). In the ASL, cross-plane (z-direction in the present calculation domain) diffusion is the main transport process. Thus, reducing the thickness of the ASL directly reduces the mass transport resistance, resulting in higher hydrogen concentration (and lower water vapor concentration) in the AFL. The variation of other overpotentials shown in Fig. 4.11 is largely due to the slightly different temperature at high current densities.

In addition, reducing l_{ASL} also decreases heat conduction resistance in the ASL, thereby resulting in lower temperature in the AFL, the electrolyte, and the CFL. This behavior is easily observed by the higher Nernst potential in Fig. 4.11(c), higher activation overpotentials in Fig. 4.11(e), and higher ohmic and contact overpotentials in Figs. 4.11(f) and 4.11(g) for smaller l_{ASL}.

Fig. 4.11(h) shows that the cell potential is rather linearly enhanced by decreasing the thickness of the ASL, l_{ASL}, from 1 mm to 100 μm. The cell potential is improved by about 0.7% (from 0.715V to 0.720V) when l_{ASL} is reduced from 1.0 mm to 0.5 mm. However, the thickness of the ASL should be carefully designed since the ASL acts as the mechanical support layer for the whole PEN structure.

Figs. 4.12 and 4.13 show the effects of the thickness of functional layers (AFL and CFL) on the performance of hydrogen-fueled IT-SOFCs. The thickness of the AFL, l_{AFL}, is directly related with the total length of the TPBs for hydrogen oxidation reaction (HOR). Similarly, the thickness the CFL, l_{CFL}, is related with the active TPBs for oxygen reduction reaction (ORR). Thus, the total reaction sites can be increased by employing larger l_{AFL} or l_{CFL} in designing IT-SOFCs.

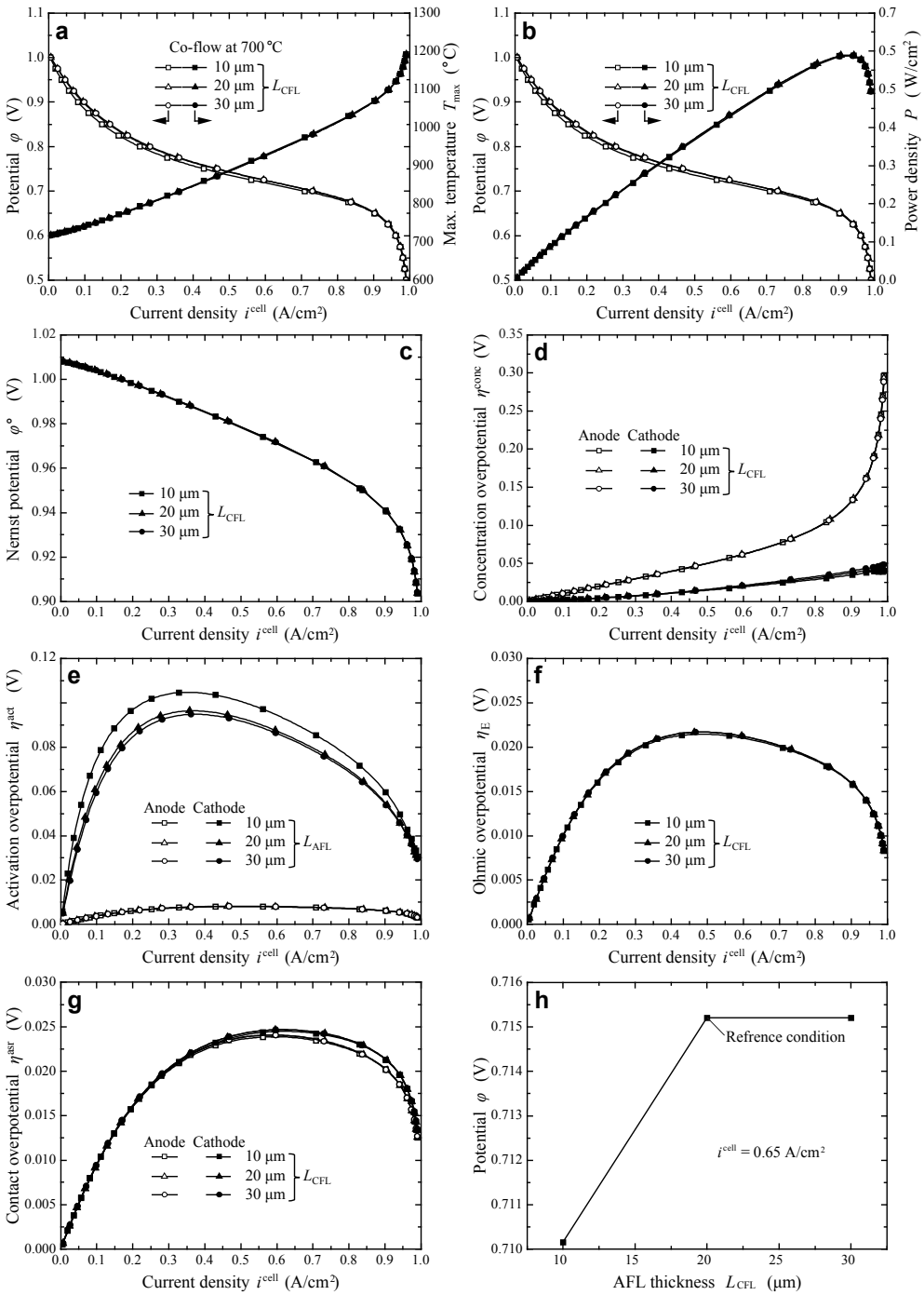

Fig. 4.12 Effect of CFL thickness on (a) $I-V$ characteristics, (b) power density, (c) Nernst potential, (d) concentration overpotential, (e) activation overpotential, (f) ohmic overpotential, (g) contact overpotential, and (h) cell potential at 0.65 A/cm^2.

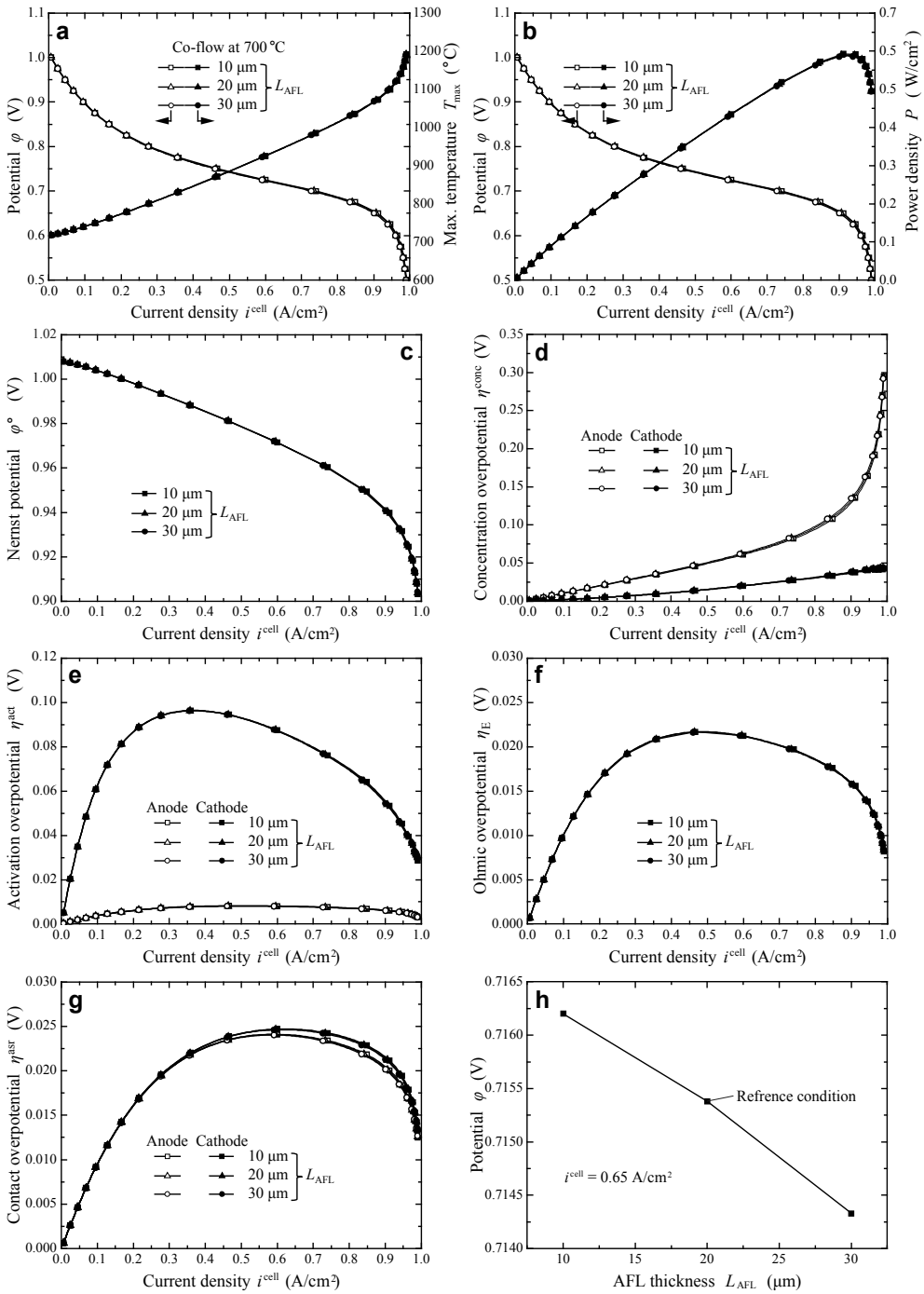

Fig. 4.13 Effect of AFL thickness on (a) $I-V$ characteristics, (b) power density, (c) Nernst potential, (d) concentration overpotential, (e) activation overpotential, (f) ohmic overpotential, (g) contact overpotential, and (h) cell potential at 0.65 A/cm^2.

However, the activity of these newly added TPBs is believed to be low because they are located far from the electrolyte. In general, the functional layers are fabricated to have around 20 μm thickness for both l_{AFL} and l_{CFL}.

In Fig. 4.12, larger thickness of the CFL, l_{CFL}, enhances the cell potential, especially at low current densities ($i^{\mathrm{cell}} < 0.5$ A/cm^2). The total potential loss at low current densities is mainly caused by the cathode activation overpotential due to its intrinsically high charge transfer resistance for the ORR. Thus, increasing l_{CFL} provides more TPBs that can be used for the ORR at low current densities, thereby reducing the cathode activation overpotential as shown in Fig. 4.12(e). However, at higher current densities, the ORR follows the Tafel equation and thus only the TPBs near the electrolyte are primarily used. Then, the cell potentials with different l_{CFL} become indiscernible.

In Fig. 4.12(h), the cell potential at 0.65 A/cm^2 is observed to increase by about 0.7% (from 0.710V to 0.715V) when the thickness of the CFL, l_{CFL}, is varied from 10 μm to 20 μm. Fig. 4.12(h) also points out that l_{CFL} larger than 20 μm result in no noticeable enhancement of the cell potential at 0.65 A/cm^2.

Fig. 4.13 shows that the thickness of the AFL, l_{AFL}, has practically no effects on the cell potential, for the 10~30 μm range of l_{AFL} considered in this study. This result can be attributed to the sufficiently fast HOR in the AFL. No noticeable differences are observed in Fig. 4.13 for the Nernst potential, all the overpotentials, and temperature. Fig. 4.13(h) indicates small potential enhancement of 0.1% at 0.65 A/cm2, during the increase of l_{AFL} from 10 to 20 μm. However, this is a negligible enhancement, smaller than the effect of any other parameters considered in this study.

4.3.3.2 Cell dimension

The effects of the channel width, W_{CH}, on the current–voltage characteristics of hydrogen-fueled IT-SOFCs are investigated in Figs. 4.14. The flow channels are inscribed in the interconnect plate and act as the passage for the fuel and air streams. The interconnect rib between two channels is also an important structure to complete the electrical connection between PENs. The channel width, W_{CH}, and

the rib width, W_{Rib}, are set to 1 mm in the standard case. Note that Larger W_{CH} and W_{Rib} may be favorable for fabricating the interconnect plates as well as reducing their manufacturing costs.

Fig. 4.14(a) indicates that increasing the channel width, W_{CH}, with fixed the rib width, W_{Rib}, decreases the overall cell performance. The reactant concentrations in the functional layers are expected to be higher as W_{CH} increases. On the contrary, temperature in the functional layers becomes lower due to the enhanced cooling effects with larger W_{CH}. Thus, the concentration overpotentials decrease with W_{CH} as observed in Fig. 4.14(d), whereas the activation overpotentials increase as shown in Fig. 4.14(e). However, the most important effect of the channel width is that it governs the contact overpotentials as shown in Fig 4.14(g). This is because increasing the channel width directly increases the contact resistance at a fixed rib width of 1 mm. Note that the ratio of the contact area between the PEN and the interconnect plates to the total active area decreases by increasing the channel width according to $\mathrm{Ratio} = W_{\mathrm{Rib}} / (W_{\mathrm{CH}} + W_{\mathrm{Rib}})$.

In Fig. 4.14(h), the cell potential at $\zeta_{\mathrm{fuel}} = 0.65$ ($i^{\mathrm{cell}} = 0.65$ A/cm^2) is degraded by about 0.8% (from 0.715V to 0.710V) when the channel width, W_{CH}, is increased from 1 mm to 2 mm. Fig. 4.10(h) also shows rather linearly decreasing behavior of the cell potential with respect to W_{CH}.

Figs. 4.15 shows the effects of the cell length, L_{x}, on the performance of IT-SOFCs fueled with hydrogen. The cell length determined the axial (x-direction) dimension of the flow channel and also the overall dimension of the stack. Larger L_{x} is desirable from the manufacturing point of view in order to reduce the costs. However, longer channel length directly induces higher non-uniformity of conditions along the flow channel. In addition, the possibility of mechanical failure in the PEN also increases as the cell length increases

It is clearly observed in Fig. 4.15(a) that higher cell potential is attained as the cell length, L_{x}, decreases from 15 cm to 5 cm. Significant variations are observed in Fig. 4.15 for the Nernst potential as well as the concentration, activation, and ohmic overpotentials. This result is mainly caused by the variation of temperature distribution in IT-SOFCs due to different cell length. The cell temperature with

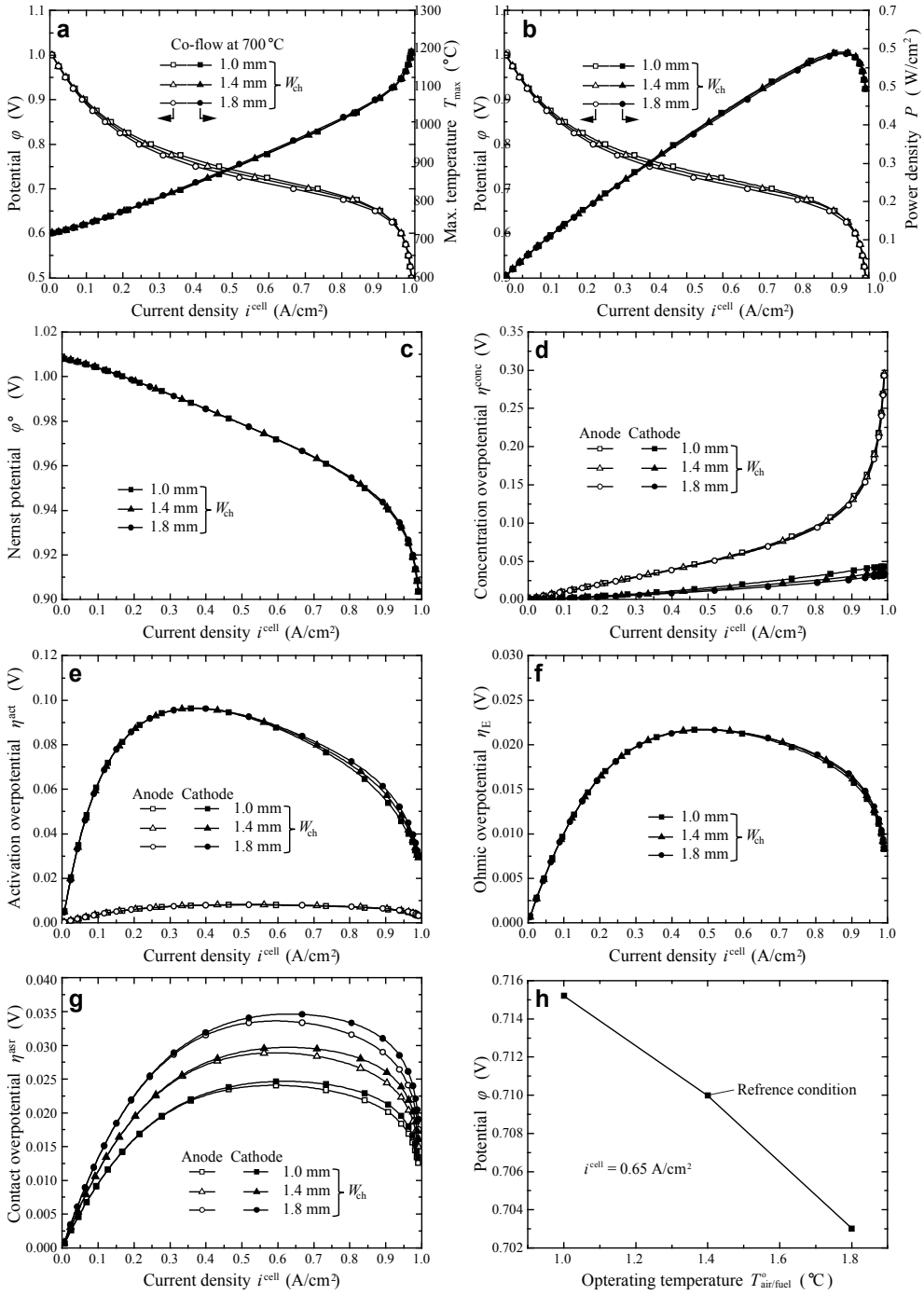

Fig. 4.14 Effect of channel width on (a) $I-V$ characteristics, (b) power density, (c) Nernst potential, (d) concentration overpotential, (e) activation overpotential, (f) ohmic overpotential, (g) contact overpotential, and (h) cell potential at 0.65 A/cm^2.

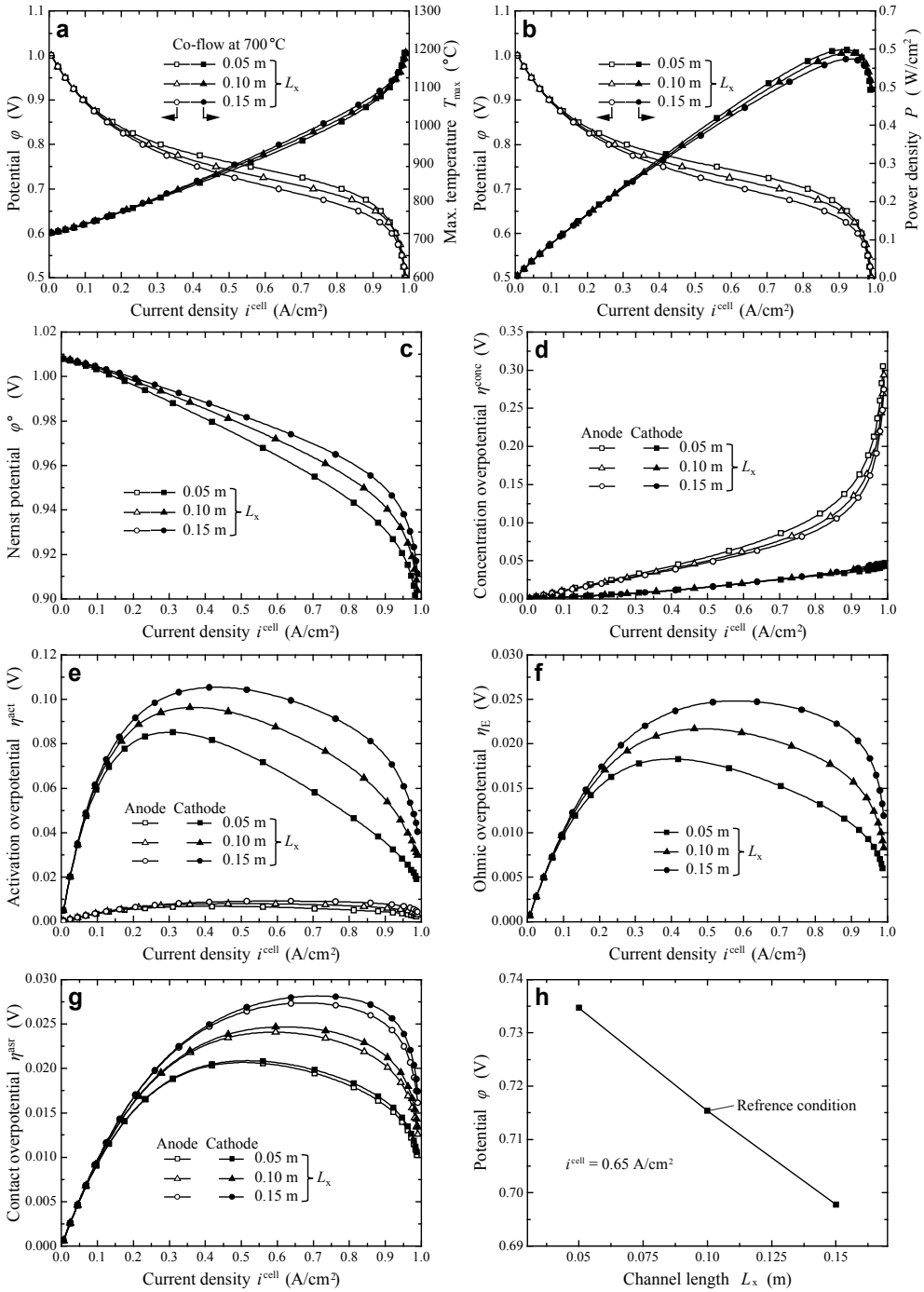

Fig. 4.15 Effect of cell length on (a) $I-V$ characteristics, (b) power density, (c) Nernst potential, (d) concentration overpotential, (e) activation overpotential, (f) ohmic overpotential, (g) contact overpotential, and (h) cell potential at 0.65 A/cm^2.

larger L_x tends to be more non-uniform and have a lower average value. By reducing the cell length, the heat transfer in the axial direction (through the interconnect plates) is facilitated, thereby enabling more uniform temperature distribution as well as higher average temperature. The effects of uniformly high temperature with larger L_x can be easily observed by the reduced Nernst potential in Fig. 4.15(c), the increased concentration overpotentials in Fig. 4.15(d), the reduced activation, ohmic, and contact overpotentials from Fig. 4.15(e) to Fig. 4.15(g).

In Fig. 4.15(h), the sensitivity of the cell potential at 0.65 A/cm^2 current density to the cell length, L_x, is investigated. Fig. 4.15(h) indicates that the cell potential is improved by about 2.5% (from 0.715V to 0.735V) during L_x is reduced from 10 cm to 5 cm. The cell potential is found to be a linearly decreasing function with respect to L_x for the cell length range considered in this study.

4.3.4 Distribution of current and temperature

In this section, the effects of the key parameters on the current and temperature distributions at the standard fuel utilization ($\zeta_{\text{fuel}} = 0.65$) are briefly investigated. In the previous sections, four key parameters have been identified to significantly influence the performance of IT-SOFCs. These include the inlet temperature and pressure (the operational parameters), the particle diameter in the CFL (the microstructural parameter), and the cell length (the dimensional parameter). From Figs. 4.16 to 4.19, the variation of current density and temperature along the channel is inspected with the change in these key parameters. Note that the axial current distribution is obtained by averaging (in the y-direction) the ionic current that crosses the electrolyte. Similarly, the temperature inside the electrolyte is used to obtain the averaged temperature distribution.

Fig. 4.16(a) shows the axial distribution of the current density in IT-SOFCs at different inlet gas temperatures. In the co-flow configuration, the fuel and air inlets are at $x = 0$ m and the outlets are at $x = 0.1$ m. In 4.16(a), the location of the maximum current density is found to move towards the inlet region. This result may be easily explained by examining the axial temperature distribution shown in Fig.

4.16(b). The cell temperature in IT-SOFCs is observed to increase proportional to the increment in the inlet gas temperature from 600°C to 800°C. Higher temperature can significantly improve the electrochemical reactions by reducing the activation overpotentials. Close inspection of Figs. 4.16(a) and 4.16(b) points out that the fast electrochemical reactions are obtained when temperature becomes higher than 825~850°C.

Fig. 4.17 shows the axial distribution of the current density and temperature in IT-SOFCs with different operating pressures. It is observed in 4.17(a) that the current density distribution is relatively uniform (ranging from 0.55 A/cm^2 to 0.72 A/cm^2) and also is not much influenced by the operating pressure. However, the temperature distribution is observed to decrease as the operating pressure increases in Fig. 4.17(b). As discussed before, higher gas pressure in IT-SOFCs is expected to improve the Nernst potential and also reduce the concentration and activation potential losses. Thus, smaller reaction heat is released when the operating pressure is increased, resulting in lower temperature distribution. Note that the ohmic and contact overpotentials are believed to slightly increase due to the reduction of cell temperature.

Fig. 4.18 presents the effects of the particle diameter in the CFL on the axial distribution of the current density and temperature. The particle diameter in the CFL determines the amount of active TPBL for the oxygen reduction reaction (ORR), the most limiting electrochemical process in IT-SOFCs. Reducing particle diameter in the CFL by half will result in four times larger TPBL, which greatly enhances the activity of the electrochemical reactions in the cathode. The maximum current density is obtained at the region of lower temperature in Fig. 4.18(a), when smaller the particle diameter is used for the CFL. The lower temperature distribution shown in Fig. 4.18(b) is the consequence of the reduced reaction heat due to the performance enhancement with smaller diameter in the CFL.

Finally, the effects of the cell length on the spatial distribution of the current density and temperature are investigated in Fig. 4.19. In Fig. 4.19(b), temperature distribution inside IT-SOFCs is observed to become more uniform and have a higher average temperature as the cell length decreases. Heat transfer through the

interconnect plate (in the axial x-direction) can be significantly enhanced at smaller cell length, and this increases the cell temperature near the inlets of fuel and air streams. Then, the current generation near the inlets is also enhanced as shown in Fig. 4.19(a), leading to further increase of cell temperature there. These two effects cooperatively help to make the temperature distribution with smaller cell length more uniform around higher average temperatures. Note that the location of the maximum current density roughly corresponds to the region where temperature increases higher than 825~850°C from the inlets.

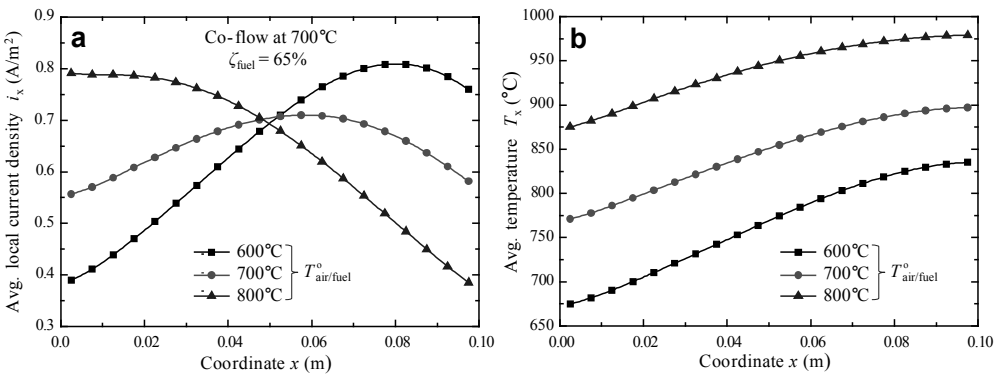

Fig. 4.16 Effect of operating temperature on the distribution of (a) current and (b) temperature along the flow channel of IT-SOFCs at 65% fuel utilization factor.

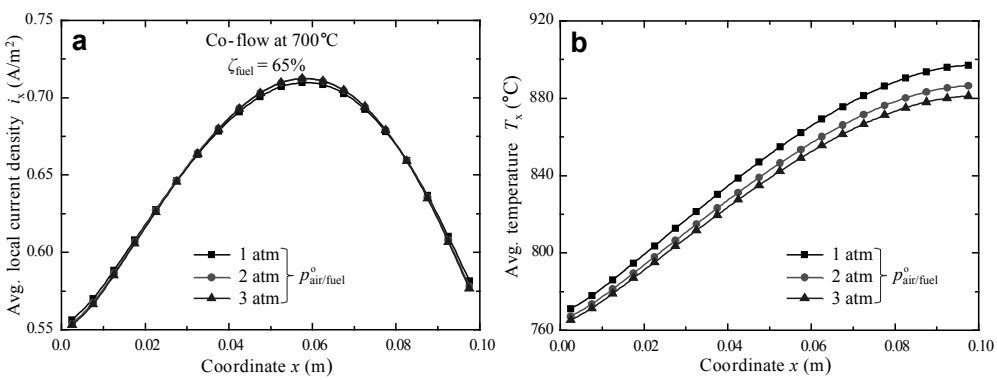

Fig. 4.17 Effect of operating pressure on the distribution of (a) current and (b) temperature along the flow channel of IT-SOFCs at 65% fuel utilization factor.

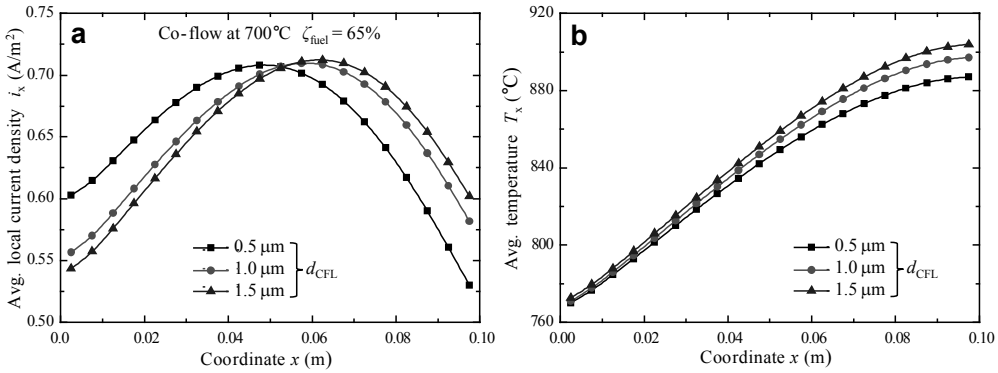

Fig. 4.18 Effect of particle diameter in CFL on the distribution of (a) current and (b) temperature along the flow channel of IT-SOFCs at 65% fuel utilization factor.

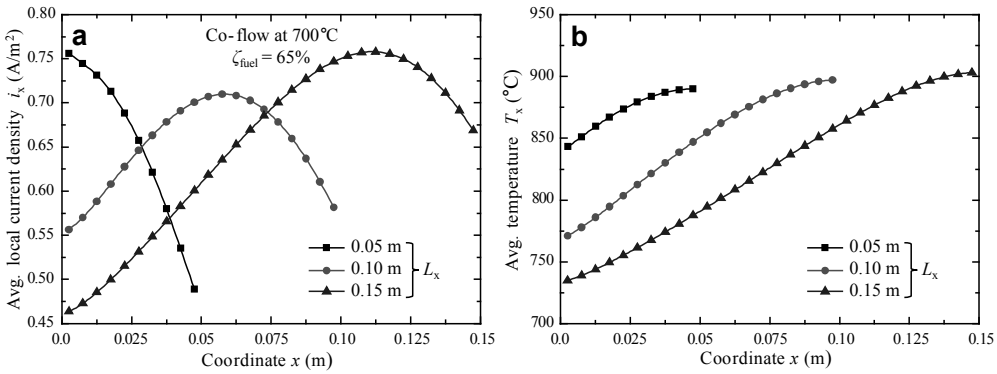

Fig. 4.19 Effect of cell length on the distribution of (a) current and (b) temperature along the flow channel of IT-SOFCs at 65% fuel utilization factor.

4.4 Summary

The parametric analysis is conducted in this chapter to investigate the effects of the operating conditions, electrode microstructures, and cell dimensions on the performance of planar, anode-supported IT-SOFCs operated with hydrogen fuel. The required calculations are performed by using the 3D micro/macroscale model developed and used in chapter 2 and chapter 3. The co-flow configuration is assumed to be the flow configuration of IT-SOFCs. A total of 14 parameters are selected, which are the inlet temperature and pressure as the operational parameters,

the particle diameter in the ASL, CCCL, AFL, and CFL and the porosity of the ASL and CCCL as the microstructural parameters, and the layer thickness of the ASL, CCCL, AFL, and CFL, the channel width, and the cell length as the dimensional parameters. The effects of each parameter on the current–voltage performance characteristics are investigated, along with the decomposed contribution of the Nernst potential as well as the concentration, activation, ohmic (and contact) overpotentials.

The parametric study clearly demonstrates that higher operating temperature and pressure are advantageous for the performance of IT-SOFCs. Increasing the operating temperature is found to decrease the activation, cathode concentration, ohmic and contact overpotentials (positive effects) while it decreases the Nernst potential and increases the anode concentration overpotential (negative effects). The positive effects due to higher operating temperature are more dominant than the negative effects, leading to higher cell potential. Likewise, increasing the operating pressure is observed to mainly increase the Nernst potential and decrease the concentration overpotential, thereby resulting in enhanced performance of IT-SOFCs.

The simulations for the microstructural parameters show that increasing particle diameter and porosity of the ASL and CCCL improves the cell potential of IT-SOFCs by facilitating mass transport in the bulk transport layers. On the other hand, smaller particle diameter in the AFL and CFL is found to be more desirable for the cell performance since smaller particle diameter can reduce the activation overpotential. This result is explained by the fact that the TPBs in the functional layers are greatly increased by reducing the particle diameter. In particular, reducing the particle diameter in the CFL is observed to lead to more noticeable enhancement in the performance of IT-SOFCs, compared with reducing the particle diameter in the AFL. This is because that the oxygen reduction reaction (ORR) in the CFL is slower electrochemical reaction than the hydrogen oxidation reaction (HOR) in the AFL.

Finally, the simulations are conducted to investigate the effects of the dimensional parameters, which show that cell performance can be improved by

decreasing the thickness of the ASL (due to the reduction of cross-plane mass diffusion length) or by increasing the thickness of CCCL (due to the enhanced uniformity of oxygen concentration under the channel and the rib). Increasing the thickness of the functional layers (AFL and CFL) is found to result in higher cell performance due to the increase of TPBL for electrochemical reactions. The simulations also point out that smaller channel width is more desirable for the performance due to the rapid increase of the contact overpotential at wider channel designs. In addition, smaller cell length is observed to result in improved performance due to more uniform temperature distribution and higher average temperature.

CHAPTER 5
METHANE-FUELED IT-SOFC

In this chapter, a 3D micro/macroscale model is proposed to predict the performance and detailed operation characteristics of for planar, anode-supported IT-SOFCs fueled with partially reformed methane fuels. The new micro/macroscale model for methane-fueled IT-SOFCs is an extended version of the model for hydrogen-fueled IT-SOFCs presented in chapter 2. Thus, the present model includes additional consideration on the chemical reactions for steam reforming of methane inside the anode as well as the multicomponent transport of mixture gases. A total of five gas species should be considered for methane reformate, which are methane (CH_4), water vapor (H_2O), hydrogen (H_2), carbon monoxide (CO), and carbon dioxide (CO_2). Accordingly, the thermo-physical properties (binary diffusivity, viscosity, thermal conductivity, and specific heat) for these species should also be accurately considered.

However, the new micro/macroscale model largely retains the overall numerical frameworks of the predecessor, such as the 3D calculation domain composed of a PEN and two channel/interconnect plate structures, the assumption of full-developed channel flow with negligible pressure drop, the boundary conditions for top/bottom (periodic), side (symmetric), and inlet/outlet boundaries, not to mention the core calculation procedures for the charge, mass, and energy conservations. Then, the three-step global reaction kinetics proposed by Xu and Froment (1989a) are adopted to determine the rate of direct internal reforming (DIR) of methane inside the anode (particularly, in ASL). The global reaction kinetics considers the steam methane reforming reaction (SMR), the water-gas shift reaction (WGS), and the reverse methanation reaction (RM). In addition, the Wilke's formula is utilized to obtain the effective diffusivity of gas species in the multicomponent system of the reformate gas.

The simulations are conducted with the base case operating condition at 750°C and 1 bar and with 30% pre-reformed steam/methane mixture gas as fuel. The effects of the co- and counter-flow configurations are considered. From the

simulation, the basic current–voltage performance characteristics of IT-SOFCs operated with reformed fuel are investigated along with the behaviors of the activation, concentration, and ohmic potential losses. The spatial distribution of temperature, concentration, and current production is also studied in detail. In addition, we carefully investigate the characteristics of DIR reactions inside the anode and their effects on the cell performance and the local variation of the conditions.

5.1 Model Description

The fuel flexibility is one of important advantages of IT-SOFCs in that relatively less costly hydrocarbon fuels, including methane, methanol, gasoline, diesel, bio gas, coal gas, etc. can be used (Meusinger et al., 1998; Brett et al, 2005). Hydrogen is an expensive fuel since it is currently obtained by industrial steam reforming process (Armor, 1999). While much research efforts are taken to lower the production cost for hydrogen, the price of hydrogen is not expected to drop dramatically in near future. The operating temperature of IT-SOFCs around 600~800°C provides sufficient high temperature for steam reforming of methane (CH_4) inside the anode. This is called the direct internal reforming (DIR) because the conversion of methane into hydrogen occurs inside the IT-SOFCs using the high temperature and water vapor-rich environment in the anode. The DIR process can simplify the methane-fueled IT-SOFC system by using simpler fuel processing units.

In methane-fueled IT-SOFCs, hydrogen is still the primary fuel for the electrochemical reactions that occurs inside the AFL. Although methane (CH_4) can participate in the direct electrochemical reaction on Ni catalyst surface, its reaction rate is found to be negligible. The carbon monoxide (CO) produced during the DIR process participates in the direct electrochemical oxidation in the AFL as

$$\mathrm{CO} + \mathrm{O}^{2-} \rightarrow \mathrm{CO}_2 + 2e^- . \tag{5.1}$$

The rate of the carbon monoxide oxidation reaction (COR) has been found to be considerable. However, the concentration of carbon monoxide is generally smaller than the concentration of hydrogen inside the anode, especially when IT-SOFCs are operated at low fuel utilization factors less than 50%.

Thus, the direct electrochemical oxidation of CO in the AFL is neglected in the present model according to its small contribution. In facts, previous studies demonstrated that the current–voltage performance curves are similar for 100% hydrogen fuel and 86% H_2/14% CO mixture fuel (Jiang and Virkar, 2003). The models and theories used for the extension of the micro/macroscale models towards methane-fueled IT-SOFCs are explained in the following section. The performance and operating characteristics of methane-fueled IT-SOFCs are then investigated in detail using the extended 3D micro/macroscale model.

5.1.1 Structure of methane-fueled IT-SOFC

Fig. 5.1(a) illustrates the structure of planar, anode-supported IT-SOFCs with two-layer electrodes, which coincides with the calculation domain consisting of a PEN and two gas channels and interconnects plates. The cell structure shown in shown in Fig. 5.1(a) is exactly the same as that in Fig. 2.1(a) considered for simulating hydrogen-fueled IT-SOFCs. The only difference is that pre-reformed methane fuel composed of CH_4, H_2O, H_2, CO, and CO_2 is introduced at the inlet of

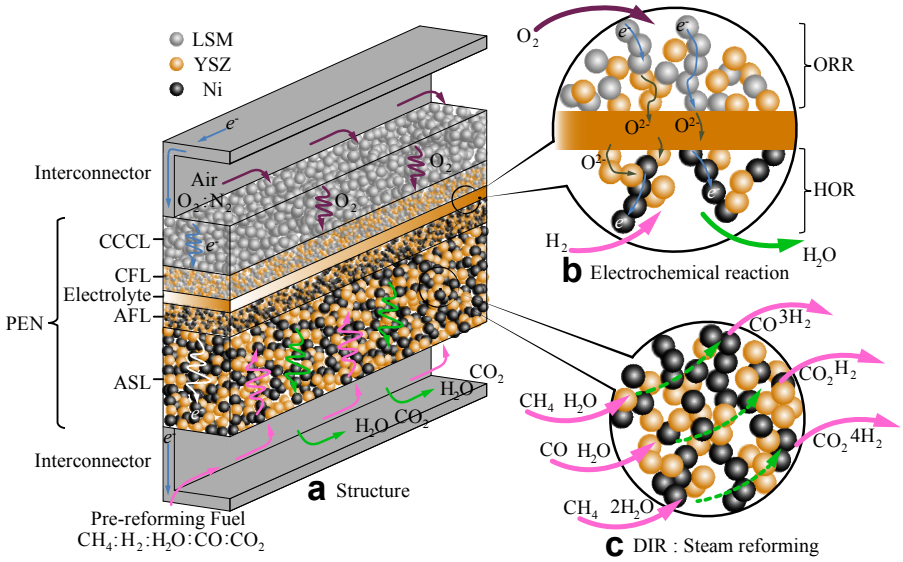

Fig. 5.1 Physical process in an anode-supported IT-SOFC with two-layer electrodes, operated with methane and air: (a) structure, (b) electrochemical reactions, and (c) steam reforming reactions.

the fuel gas stream. The boundary conditions for top/bottom (periodic), side (symmetric), and inlet/outlet boundaries of the calculation domain are also the same as those in the previous model.

5.1.2 Fuel cell process

The electrochemical reactions occurring inside methane-fueled IT-SOFCs are explained in Fig. 5.1(b) with the detailed transport of participating elements such as the gas molecules, oxygen ions, and electrons. It should be noted that the electrochemical oxidation of carbon monoxide (CO) on the anode three-phase boundaries (TPBs) is not considered in the present model. As discussed above, the contribution of the carbon monoxide oxidation to the overall current density is believed to be small due to relatively low carbon monoxide in the reformate gas stream. In other words, carbon monoxide is assumed to participate in the electrochemical reaction in the anode only by producing hydrogen through water-gas shift (WGS) reaction. Thus, the electrochemical reactions in the methane-fueled IT-SOFCs are assumed equal to those occurring in the hydrogen-fueled IT-SOFCs.

The overall electrochemical reaction can be written as Eq. (5.4), by combining the cathode and anode half reactions.

Cathode reaction: $$\frac{1}{2}\mathrm{O_2} + 2e^- \rightarrow \mathrm{O^{2-}} \tag{5.2}$$

Anode reaction: $$\mathrm{H_2} + \mathrm{O^{2-}} \rightarrow \mathrm{H_2O} + 2e^- \tag{5.3}$$

Overall reaction: $$\mathrm{H_2} + \frac{1}{2}\mathrm{O_2} \rightarrow \mathrm{H_2O} + (\mathrm{Power}) + (\mathrm{Heat}) \tag{5.4}$$

In Fig. 5.1(b), oxygen molecules (O_2) diffuse into the cathode current collector layer (CCCL) during air flows through the cathode flow channel and finally reach the TPBs in the cathode functional layer (CFL). The TPBs are electrochemically active sites because electrons, ions, and gas molecules that participate in the electrochemical reaction co-exist according to the presence of electronic, ionic, and gas phase materials. Electrons (e^-) are transported from the cathode interconnect

plate to the CFL. Then, oxygen molecules and electrons are combined to produce oxygen ions (O^{2-}) at the cathode TPBs according to the oxygen reduction reaction (ORR) provided in Eq. (5.2). These oxygen ions are then transported towards the anode through the ion-conducting electrolyte.

At the anode, hydrogen molecules (H_2) diffuse from the anode flow channel into the anode substrate layer (ASL) and finally arrive at the active TPBs in the anode functional layer (AFL). There these hydrogen molecules and oxygen ions are combined to produce water vapor (H_2O) according to the hydrogen oxidation reaction (HOR) provided in Eq. (5.3). The electrons separated from the oxygen ions move out of the anode along the electronic phase in the AFL and ASL, and finally flow to the interconnect plate completing the fuel cell processes.

In general, partially reformed steam/methane mixture gas is supplied at the fuel inlet of methane-fueled IT-SOFCs. This methane pre-reforming is done using the waste heat from the SOFCs. Five species are assumed to be introduced at the inlet of the anode gas channel, which are methane (CH_4), water vapor (H_2O), hydrogen (H_2), carbon monoxide (CO), and carbon dioxide (CO_2). The nickel (Ni) present in the anode acts as the catalyst for the steam reforming. The present model assumes that the reforming reactions are assumed to occur only in the ASL, not in the AFL. This assumption helps the numerical stability of the solution while the accuracy is not much degraded due to the small thickness of the AFL. The global three-step reaction mechanism proposed by Xu and Froment (1989a) is considered for the direct internal reforming (DIR) of methane in the anode, which are

I. Steam methane reforming (SMR):

$$\mathrm{CH_4 + H_2O \leftrightarrow CO + 3H_2}, \quad \Delta\tilde{h}_{298.15\mathrm{K}} = +206 \text{ kJ/mol}, \tag{5.5}$$

II. Water-gas shift (WGS):

$$\mathrm{CO + H_2O \leftrightarrow CO_2 + H_2}, \quad \Delta\tilde{h}_{298.15\mathrm{K}} = -41 \text{ kJ/mol}, \tag{5.6}$$

III. Reverse methanation (RM):

$$\mathrm{CH_4 + 2H_2O \leftrightarrow CO_2 + 4H_2}, \quad \Delta\tilde{h}_{298.15\mathrm{K}} = +165 \text{ kJ/mol}. \tag{5.7}$$

The three reactions listed in Eqs. (5.5)~(5.7) are reversible. The SMR reaction (reaction I) explains that methane reacts with steam on Ni catalyst surface to produce carbon monoxide and hydrogen. This reaction is a strongly endothermic reaction occurring at relatively high temperature (700~1000°C), as can be implied by the positive reaction enthalpy shown in Eq. (5.5). The WGS reaction (reaction II) explains the conversion between carbon monoxide and carbon dioxide, and this is slightly exothermic. The RM reaction (reaction III) explains that methane reacts with steam to yield hydrogen and carbon dioxide while absorbing large reaction heat (strongly endothermic). Note that the RM reaction is the same as the overall steam reforming reaction of methane into hydrogen; one unit of CH_4 produces four units of H_2 by reacting with two units of H_2O with the stoichiometric steam-to-carbon ratio of two ($S/C = 2$). Hydrogen molecules (H_2) produced by methane reforming diffuse to the active TPBs in the AFL where it participate in the electrochemical reaction.

In general, the temperature in IT-SOFCs is expected to increase along the flow direction of air stream because overall electrochemical reaction in Eq. (5.4) is exothermic. However, near the inlet of reformate fuel gas, the cell temperature is expected to drop rapidly due to the strong endothermic methane reforming reactions.

5.1.3 Model configuration

The 3D micro/macroscale model for methane-fueled IT-SOFCs is developed by extending the previous model for hydrogen-fueled IT-SOFCs explained in chapter 2. Thus, the present model inherit from the predecessor the essential numerical frameworks including the microstructural characterization of composite electrodes, the continuum models for detailed electrode processes, and the macroscale models for heat and mass transport in the PEN, flow channels, and interconnect plates. In addition, the chemical model is newly included to consider the reforming reaction of methane and the accompanying heat and mass sources inside the ASL. The configuration of the micro/macroscale model for methane-fueled IT-SOFCs is summarized in Fig. 5.2.

The multicomponent gas mixture of CH_4, H_2O, H_2, CO, and CO_2 in the anode

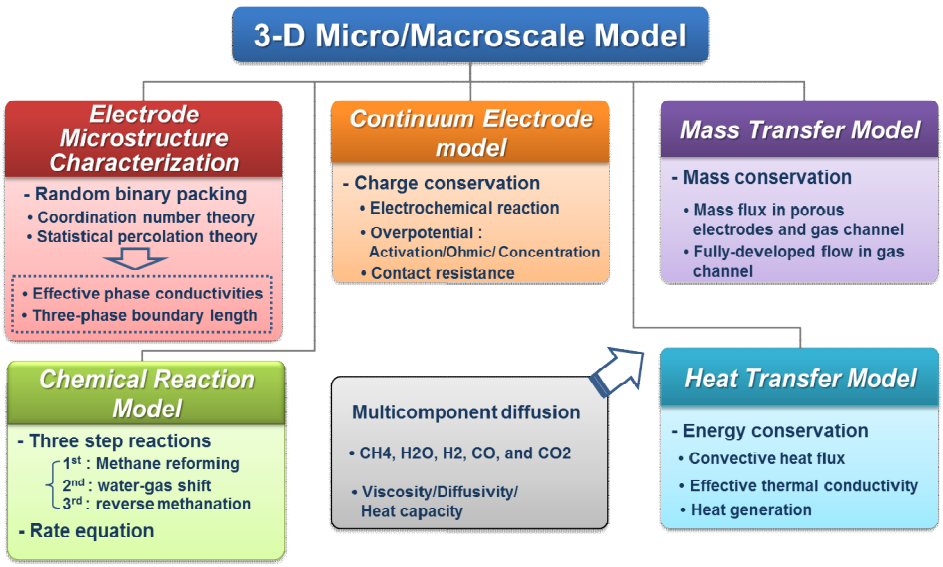

Fig. 5.2 Overall configuration of the present 3D micro/macroscale model for IT-SOFCs operated with methane and air.

requires the modification of the heat and mass transfer model. That is, the ordinary diffusivity is calculated based on the Wilke's formula and this is combined with species Knudsen diffusivity to determine the effective diffusivity (including the effect of porosity and tortuosity factor) for the multicomponent reformate gas. This approach is somewhat different from using the Maxwell-Stefan equations to calculate the effective species diffusivities for binary H_2/H_2O system in hydrogen fuel or O_2/N_2 system in air. However, Wilke's formula is generally accepted as a proper approximation for effective diffusivities of the multicomponent systems. In addition, the viscous permeation is still included in the mass transport calculation to follow the dusty-gas model (DGM) framework. The thermophysical properties of each species in the methane reformate are fully considered to accurate simulate the operation of IT-SOFCs with DIR.

5.1.4 Chemical reaction model (DIR)

In the present micro/macroscale model, three major reactions are considered for the steam reforming of methane inside the ASL, which are the SMR, WGS, and

RM reactions shown in Eqs. (5.5)~(5.7). The intrinsic reaction kinetics proposed by Xu and Froment (1989a) are used to determine the rates of these reactions as

$$r_{\mathrm{I}}^{\mathrm{o}} = \frac{1}{33480}\frac{k_{\mathrm{I}}}{p_{\mathrm{H_2}}^{2.5}}\left(p_{\mathrm{CH_4}}p_{\mathrm{H_2O}} - \frac{p_{\mathrm{H_2}}^{3}p_{\mathrm{CO}}}{K_{\mathrm{eq,I}}}\right)/DEN^2 \quad \mathrm{mol/m^2_{cat}\text{-}s}, \tag{5.8}$$

$$r_{\mathrm{II}}^{\mathrm{o}} = \frac{1}{33480}\frac{k_{\mathrm{II}}}{p_{\mathrm{H_2}}}\left(p_{\mathrm{CO}}p_{\mathrm{H_2O}} - \frac{p_{\mathrm{H_2}}p_{\mathrm{CO_2}}}{K_{\mathrm{eq,II}}}\right)/DEN^2 \quad \mathrm{mol/m^2_{cat}\text{-}s}, \tag{5.9}$$

$$r_{\mathrm{III}}^{\mathrm{o}} = \frac{1}{33480}\frac{k_{\mathrm{III}}}{p_{\mathrm{H_2}}^{3.5}}\left(p_{\mathrm{CH_4}}p_{\mathrm{H_2O}}^{2} - \frac{p_{\mathrm{H_2}}^{4}p_{\mathrm{CO_2}}}{K_{\mathrm{eq,III}}}\right)/DEN^2 \quad \mathrm{mol/m^2_{cat}\text{-}s}, \tag{5.10}$$

$$DEN = 1 + K_{\mathrm{CO}}p_{\mathrm{CO}} + K_{\mathrm{H_2}}p_{\mathrm{H_2}} + K_{\mathrm{CH_4}}p_{\mathrm{CH_4}} + K_{\mathrm{H_2O}}\frac{p_{\mathrm{H_2O}}}{p_{\mathrm{H_2}}}, \tag{5.11}$$

where k_{I}, k_{II}, and k_{II} are the reaction rate constants for each reaction, $K_{\mathrm{eq,I}}$, $K_{\mathrm{eq,II}}$, and $K_{\mathrm{eq,III}}$ are the equilibrium constants, K_{j} ($\mathrm{j} = \mathrm{CO}$, H_2, CH_4, H_2O) is the adsorption constants for species j, and p_{j} is the partial pressure of species j in the unit of bar.

It should be noted that the intrinsic reaction rates, $r_{\mathrm{I}}^{\mathrm{o}}$, $r_{\mathrm{II}}^{\mathrm{o}}$, and $r_{\mathrm{III}}^{\mathrm{o}}$, in Eqs. (5.8)~(5.10) are defined per unit catalyst surface area (as $\mathrm{mol/m^2_{cat}\text{-}s}$), different from the original reaction rates of Xu and Froment (1989a) defined per unit catalyst mass including the support mass (as $\mathrm{kmol/kg_{cat}\text{-}h}$). Xu and Froment (1989a) used commercial catalyst pellets that contain 15.2% nickel (Ni) supported on magnesium spinel ($MgAl_2O_4$). They also showed that the surface area of nickel in the catalyst is 9.3 $\mathrm{m^2/g_{cat}}$ from the BET measurement (total surface area was 58 $\mathrm{m^2/g_{cat}}$). Based on this information, the unit of the intrinsic reaction rate can be converted from $\mathrm{kmol/kg_{cat}\text{-}s}$ to $\mathrm{mol/m^2_{cat}\text{-}s}$ using the conversion factor of 1/33480 (=1000 mol/kmol × 1/9300 $\mathrm{kg_{cat}/m^2_{cat}}$ × 1/3600 h/s). The Ni catalyst pellets used for steam reforming have much larger catalyst area compared with the electrodes in IT-SOFCs, because the pore diameter is much smaller as about 20 nm in the catalyst pellets than about 0.1~0.5 μm in the electrodes.

The reaction rate constant, k_{i} ($\mathrm{i} = \mathrm{I}$, II, III), and the adsorption coefficient, K_{j} ($\mathrm{j} = \mathrm{CO}$, H_2, CH_4, H_2O), are given by Arrhenius equations as

$$k_{\mathrm{i}} = k_{0,\mathrm{i}} \exp\left[-\frac{E_{\mathrm{i}}}{R_{\mathrm{g}}T}\right], \tag{5.12}$$

$$K_{\mathrm{j}} = K_{0,\mathrm{j}} \exp\left[-\frac{\Delta H_{\mathrm{j}}}{R_{\mathrm{g}}T}\right]. \tag{5.13}$$

Here, $k_{0,\mathrm{i}}$ is the pre-exponential factor and E_{i} is the activation energy for the reaction rate constants. Likewise, $K_{0,\mathrm{j}}$ is the pre-exponential factor and ΔH_{j} is the adsorption enthalpy required to calculate the adsorption coefficient, K_{j}. The parameters are summarized in Table 5.1. And, the equilibrium constants are given as (Xu and Froment, 1989a)

$$K_{\mathrm{eq,I}} = \exp\left[-\frac{26{,}830}{T} + 30.114\right] \ \mathrm{bar}^2, \tag{5.14}$$

$$K_{\mathrm{eq,II}} = \exp\left[\frac{4{,}400}{T} - 4.036\right], \tag{5.15}$$

$$K_{\mathrm{eq,III}} = K_{\mathrm{eq,I}} K_{\mathrm{eq,II}} = \exp\left[-\frac{22{,}430}{T} + 26.078\right] \ \mathrm{bar}^2. \tag{5.16}$$

Since the intrinsic reaction rates, $r_{\mathrm{I}}^{\mathrm{o}}$, $r_{\mathrm{II}}^{\mathrm{o}}$, and $r_{\mathrm{III}}^{\mathrm{o}}$, are defined per unit

Table 5.1 Pre-exponential factors and activation energies (heats of adsorption) for reaction rate constants and adsorption coefficients, from Xu and Froment (1989a).

Constants	Unit	Pre-exponential factor $k_{0,\mathrm{i}}$, $K_{0,\mathrm{i}}$	Activation energy E_{i}, $-\Delta H_{\mathrm{i}}$ (kJ/mol)
k_{I}	kmol·bar$^{0.5}$/kg$_{\mathrm{cat}}$·h	4.225×10^{15}	240.1
k_{II}	kmol/bar·kg$_{\mathrm{cat}}$·h	1.955×10^{6}	67.13
k_{III}	kmol·bar$^{0.5}$/kg$_{\mathrm{cat}}$·h	1.020×10^{15}	243.9
K_{CO}	bar^{-1}	8.23×10^{-5}	70.65
$K_{\mathrm{H_2}}$	bar^{-1}	6.12×10^{-9}	82.9
$K_{\mathrm{CH_4}}$	bar^{-1}	6.65×10^{-4}	38.28
$K_{\mathrm{H_2O}}$		1.77×10^{5}	–88.68

catalyst area in Eqs. (5.8)~(5.10), it is essential to determine the surface area of Ni. The volumetric Ni surface area, $\lambda_{\mathrm{Ni}}^{\mathrm{V}}$, inside the ASL can be calculated as

$$\lambda_{\mathrm{Ni}}^{\mathrm{V}} = N_{\mathrm{t}} n_{\mathrm{el}} \pi d_{\mathrm{el}}^2 \times \eta_{\mathrm{Ni}}^{\mathrm{eff}} = \frac{6(1-\varepsilon)\phi_{\mathrm{el}}}{d_{\mathrm{el}}} \times \eta_{\mathrm{Ni}}^{\mathrm{eff}}, \tag{5.17}$$

where N_{t} is the total number density of all particles, n_{el} is the number fraction of electronic nickel particles in the ASL, d_{el} is the diameter (the surface area of Ni particle is πd_{el}^2), ε is the porosity, and ϕ_{el} is the electronic phase volume fraction among solid volume. In Eq. (5.17), the nickel surface efficiency, $\eta_{\mathrm{Ni}}^{\mathrm{eff}}$, is introduced to consider the reduction of nickel catalyst surface area due to the sintering, intimate contact of particles, and other reasons. In the present model, $\eta_{\mathrm{Ni}}^{\mathrm{eff}}$ is assumed to be 0.5.

Then, the volumetric reaction rates, r_{I}, r_{II}, and r_{III}, in the ASL is calculated by multiplying the intrinsic reaction rates, $r_{\mathrm{I}}^{\mathrm{o}}$, $r_{\mathrm{II}}^{\mathrm{o}}$, and $r_{\mathrm{III}}^{\mathrm{o}}$, with the volumetric Ni surface are, $\lambda_{\mathrm{Ni}}^{\mathrm{V}}$, as

$$r_{\mathrm{I}} = \lambda_{\mathrm{Ni}}^{\mathrm{V}} \times r_{\mathrm{I}}^{\mathrm{o}}, \quad r_{\mathrm{II}} = \lambda_{\mathrm{Ni}}^{\mathrm{V}} \times r_{\mathrm{II}}^{\mathrm{o}}, \quad r_{\mathrm{III}} = \lambda_{\mathrm{Ni}}^{\mathrm{V}} \times r_{\mathrm{III}}^{\mathrm{o}}. \tag{5.18}$$

5.1.5 Properties of multicomponent gas mixtures

Five gas species participate in the steam reforming of methane, such as methane (CH_4), water vapor (H_2O), hydrogen (H_2), carbon monoxide (CO), and carbon dioxide (CO_2). In the micro/macroscale model, accurate experimental correlations are utilized to determine the thermophysical properties of gas species including the dynamic viscosity, binary diffusivities, Knudsen diffusivity, and sensible enthalpy. The dynamic viscosity of mixtures gas, μ, is calculated by averaging the species viscosities, μ_{i}, weighted by mole fraction as

$$\mu = \sum_{\mathrm{i}=5}^{5} x_{\mathrm{i}} \mu_{\mathrm{i}}, \tag{5.19}$$

where x_{i} is the mole fraction of species i. The dynamic viscosity of species i, μ_{i}, can be determined by the polynomial correlation from Todd and Young (2002) as

$$\mu_{\mathrm{i}} = 10^{-7} \sum_{\mathrm{k}=0}^{6} b_{\mathrm{i,k}} \tau^{\mathrm{k}} , \tag{5.20}$$

where $\tau = T/1000$ and b_{k} are the correlation coefficients provided in Table 5.2.

Table 5.2 Dynamic viscosity coefficients for reformate gas species, adopted from Todd and Young (2002).

Species	b_0	b_1	b_2	b_3	b_4	b_5	b_6
CH_4	–9.9989	529.37	–543.82	548.11	–367.06	140.48	–22.920
H_2O	–6.7541	244.93	419.50	–522.38	348.12	–126.96	19.591
H_2	15.533	299.78	–244.34	249.41	–167.51	62.966	–9.9892
CO	–4.9137	793.65	875.90	883.75	–572.14	208.42	–32.298
CO_2	–20.434	680.07	–432.49	244.22	–85.929	14.450	–0.4564

For calculating the mass transport for multicomponent reformate gas in the porous anode, the effective ordinary diffusivity of gas species i, $D_{\mathrm{m,i}}^{\mathrm{eff}}$, is first calculated based on the Wilke's formula as

$$D_{\mathrm{m,i}}^{\mathrm{eff}} = \frac{\varepsilon}{\tau} D_{\mathrm{m,i}} = \frac{\varepsilon}{\tau} \frac{1 - x_{\mathrm{i}}}{\sum_{\substack{\mathrm{j}=1 \\ \mathrm{j} \neq \mathrm{i}}}^{5} \frac{x_{\mathrm{j}}}{D_{\mathrm{ij}}}} , \tag{5.21}$$

where ε is the porosity, τ is the tortuosity, and D_{ij} is the binary diffusivity for $\mathrm{i} - \mathrm{j}$ species pair. The term ε / τ accounts for the reduction of diffusion volume and the elongation of diffusion length in porous media. Note that Wilke's formula is derived from the Maxwell-Stefan equation with the assumption that species i diffuses through other stagnant species. The binary diffusivity for $\mathrm{i} - \mathrm{j}$ species pair, D_{ij}, is determined based on the empirical correlation written as

$$D_{\mathrm{ij}} = \frac{0.0143 T^{1.75}}{p_{\mathrm{t}} M_{\mathrm{ij}}^{1/2} \left(V_{\mathrm{i}}^{1/3} + V_{\mathrm{j}}^{1/3} \right)^2} , \tag{5.22}$$

where M_{ij} is the mean molar mass defined as $M_{\mathrm{ij}} = 2(1/M_{\mathrm{i}} + 1/M_{\mathrm{j}})^{-1}$ and V_{i} is

the diffusion volume. The diffusion properties are listed in Table 5.3.

Table 5.3 Molecular mass and diffusion volume for reformate gas species, adopted from Todd and Young (2002).

Species	CH_4	H_2O	H_2	CO	CO_2
Molecular mass, M_k	16.043	18.015	2.016	28.01	44.01
Diffusion volume, V_k	25.14	13.1	6.12	18.0	26.7

Then, the effective diffusivity of gas species i, $D_{\mathrm{i}}^{\mathrm{eff}}$, is determined by combining the ordinary diffusivity, $D_{\mathrm{m,i}}^{\mathrm{eff}}$, and the effective Knudsen diffusivity, $D_{\mathrm{iK}}^{\mathrm{eff}}$, following the Bonsanquet relation (Mason and Malinauskas, 1983) as

$$D_{\mathrm{i}}^{\mathrm{eff}} = \frac{1}{\dfrac{1}{D_{\mathrm{m,i}}^{\mathrm{eff}}} + \dfrac{1}{D_{\mathrm{iK}}^{\mathrm{eff}}}} . \tag{5.23}$$

The the effective Knudsen diffusivity, $D_{\mathrm{iK}}^{\mathrm{eff}}$, is easily determined as

$$D_{\mathrm{iK}}^{\mathrm{eff}} = \frac{\varepsilon}{\tau}\frac{97}{2} d_{\mathrm{p}} \sqrt{\frac{T}{M_{\mathrm{i}}}} , \tag{5.24}$$

where d_{p} is the pore diameter in the anode. The molar flux of species i, $\mathbf{n}_{\mathrm{i}}$, can be obtained by combining the diffusive flux and viscous flux as

$$\mathbf{n}_{\mathrm{i}} = \mathbf{n}_{\mathrm{i}}^{\mathrm{d}} + \mathbf{n}_{\mathrm{i}}^{\mathrm{v}} = -\frac{1}{RT} D_{\mathrm{i}}^{\mathrm{eff}} \nabla p_{\mathrm{i}} - \frac{p_{\mathrm{i}}}{RT}\frac{K}{\mu}\nabla p_{\mathrm{t}} \tag{5.25}$$

where K denotes the flow permeability. For the anode flow channel, the effective diffusivity, $D_{\mathrm{i}}^{\mathrm{eff}}$, is equal to the $D_{\mathrm{m,i}}$ for plain medium in Eq. (5.21). Note that Knudsen diffusion needs not to be considered in the channel. And the channel permeability, K_{CH}, has been set to $200 D_{\mathrm{m,i}} / p_{\mathrm{t}}$ for solution convergence.

In the micro/macroscale model for methane-fueled IT-SOFCs, the convective heat transfer in the anode is accurate accounted for, by using the polynomial correlations suggested by Todd and Young (2002) for evaluating the molar specific heats of CH_4, H_2O, H_2, CO, and CO_2. The molar specific heat of species i, $\tilde{c}_{\mathrm{p,i}}$

(J/mol-K), is determined as

$$\tilde{c}_{\mathrm{p,i}} = \sum_{\mathrm{k}=0}^{6} a_{\mathrm{i,k}} \tau^{\mathrm{k}} \ , \tag{5.26}$$

where $\tau = T/1000$ and a_{k} are the required correlation coefficients provided in Table 5.4. Then, $\tilde{h}_{\mathrm{sen,i}}(T)$ denotes the sensible enthalpy of species i at a certain temperature T higher than the reference temperature, T_{ref}, and is calculated by integrating $\tilde{c}_{\mathrm{p,i}}$ as

$$\tilde{h}_{\mathrm{sen,i}}(T) = \int_{T_{\mathrm{ref}}}^{T} \tilde{c}_{\mathrm{p,i}}(T^*) dT^* \ . \tag{5.27}$$

The reference temperature, T_{ref}, is set to $T_{\mathrm{ref}} \equiv T_{\mathrm{fuel}}^{\mathrm{o}} - 200$ by noting the temperature drop in methane-fueled IT-SOFCs due to direct internal reforming (DIR). Note that $T_{\mathrm{ref}} \equiv T_{\mathrm{fuel}}^{\mathrm{o}}$ for hydrogen-fueled IT-SOFCs.

Table 5.4 Molar heat capacity coefficients for reformate gas species, adopted from Todd and Young (2002).

Species	a_0	a_1	a_2	a_3	a_4	a_5	a_6
CH_4	47.964	-178.59	712.55	-1068.7	856.93	-358.75	61.321
H_2O	37.373	-41.205	146.01	-217.08	181.54	-79.409	14.015
H_2	21.157	56.036	-150.55	199.29	-136.15	46.903	-6.4725
CO	30.429	-8.1781	5.2062	41.974	-66.346	37.756	-7.6538
CO_2	4.3669	204.60	-471.33	657.88	-519.90	214.58	-35.992

In the micro/macroscale model, heat convection is calculated by tracking the transport of sensible enthalpy, $\tilde{h}_{\mathrm{sen,i}}(T)$, due to the mass transfer between finite volume cells. However, the total enthalpy of species i, $\tilde{h}_{\mathrm{tot,i}}(T)$, is easily obtained as

$$\tilde{h}_{\mathrm{tot,i}}(T) = \Delta h_{\mathrm{f,i}}(T_{\mathrm{ref}}) + \tilde{h}_{\mathrm{sen,i}}(T) \ , \tag{5.28}$$

where $\Delta h_{\mathrm{f,i}}(T_{\mathrm{ref}})$ is the enthalpy of formation of species i at the reference temperature. The formation enthalpy of hydrogen, $\Delta h_{\mathrm{f,H_2}}(T_{\mathrm{ref}})$, is zero by the

definition, while those for other gas species are adopted from Hernandez-Pacheco and Mann (2004) as provided in Table 5.5. The total enthalpy is utilized to check the balance between the chemical, thermal, and electrical energies during iterative calculations. The error range less than 0.0001% can be achieved for the total energy balance after sufficiently large iteration count.

Table 5.5 Correlations for the molar enthalpy of formation for reformate gas species, adopted from Hernandez-Pacheco and Mann (2004).

Species	Enthalpy of formation, $\Delta h_{\mathrm{f,i}}(T)$, of reformate gas species (kJ/mol)
CH_4	$\dfrac{-68.31657-0.02244517T-0.0001987408T^2}{1+0.0002184224T+1.917568\times10^{-6}T^2+8.629875\times10^{-11}T^3}$
H_2O	$\dfrac{-238.0392-0.07369004T+2.072838\times10^{-6}T^2}{1+0.0002495145T}$
CO	$\dfrac{-114.8079-0.1803191T-2.255532\times10^{-5}T^2+1.685088\times10^{-9}T^3}{1+0.001822827T}$
CO_2	$\dfrac{-393.5301}{1+2.955723\times10^{-6}T-9.660127\times10^{-9}T^2+4.875419\times10^{-12}T^3-9.033876\times10^{-16}T^4}$

The reaction enthalpies for the SMR, WGS, and RM reactions for DIR are denoted as $\Delta h_{\mathrm{I}}(T_{\mathrm{ref}})$, $\Delta h_{\mathrm{II}}(T_{\mathrm{ref}})$, and $\Delta h_{\mathrm{III}}(T_{\mathrm{ref}})$, which can be determined using the formation enthalpies of reactants and products at the reference temperature, $\Delta h_{\mathrm{f,i}}(T_{\mathrm{ref}})$, as

$$\Delta h_{\mathrm{I}}(T_{\mathrm{ref}}) = \Delta h_{\mathrm{f,CO}}(T_{\mathrm{ref}}) - \Delta h_{\mathrm{f,CH_4}}(T_{\mathrm{ref}}) - \Delta h_{\mathrm{f,H_2O}}(T_{\mathrm{ref}}), \tag{5.29}$$

$$\Delta h_{\mathrm{II}}(T_{\mathrm{ref}}) = \Delta h_{\mathrm{f,CO_2}}(T_{\mathrm{ref}}) - \Delta h_{\mathrm{f,CO}}(T_{\mathrm{ref}}) - \Delta h_{\mathrm{f,H_2O}}(T_{\mathrm{ref}}), \tag{5.30}$$

$$\Delta h_{\mathrm{III}}(T_{\mathrm{ref}}) = \Delta h_{\mathrm{f,CO_2}}(T_{\mathrm{ref}}) - \Delta h_{\mathrm{f,CH_4}}(T_{\mathrm{ref}}) - 2\Delta h_{\mathrm{f,H_2O}}(T_{\mathrm{ref}}). \tag{5.31}$$

Finally, the thermal conductivity of reformate mixtures gas, k_{eff}, is calculated

by averaging the species thermal conductivity, k_{i}, weighted by mole fraction as

$$k_{\mathrm{eff}} = \sum_{\mathrm{i}=5}^{5} x_{\mathrm{i}} k_{\mathrm{i}} \ . \tag{5.32}$$

Table 5.6 provides the correlations for the thermal conductivities of reformate gas spicies, which are valid over the temperature range of 273~1473K.

Table 5.6 Thermal conductivity of reformate gas species, adopted from Todd and Young (2002).

Species	Thermal conductivity [W/m-K]
CH_4	$k_{\mathrm{CH_4}} = 0.01 \times (0.4796 + 1.8732\tau + 37.413\tau^2 - 47.440\tau^3 + 38.251\tau^4 - 17.283\tau^5 + 3.2774\tau^6)$ [a]
H_2O	$k_{\mathrm{H_2O}} = 0.01 \times (2.0103 - 7.9139\tau + 35.922\tau^2 - 41.390\tau^3 + 35.993\tau^4 - 18.974\tau^5 + 4.1531\tau^6)$
H_2	$k_{\mathrm{H_2}} = 0.01 \times (1.5040 + 62.892\tau - 47.190\tau^2 + 47.763\tau^3 - 31.939\tau^4 + 11.972\tau^5 - 1.8954\tau^6)$
CO	$k_{\mathrm{CO}} = 0.01 \times (-0.2815 + 13.999\tau - 23.186\tau^2 + 36.018\tau^3 - 30.818\tau^4 + 13.379\tau^5 - 2.3224\tau^6)$
CO_2	$k_{\mathrm{CO_2}} = 0.01 \times (2.8888 - 27.018\tau + 129.65\tau^2 - 233.29\tau^3 + 216.83\tau^4 - 101.12\tau^5 + 18.698\tau^6)$

[a] $\tau = T/1000$

5.1.6 Governing equations

The governing equations for the conversation of charge, mass, and energy in methane-fueled IT-SOFCs are similar to those for hydrogen-fueled IT-SOFCs presented in chapter 2. First, the governing equations for the conservation of the electronic and ionic charges are expressed as

$$\nabla \cdot \mathbf{i}_{\mathrm{el}} \equiv \nabla \cdot \left(-\sigma_{\mathrm{el}}^{\mathrm{eff}} \nabla \varphi_{\mathrm{el}} \right) = +i_{\mathrm{tr}} \equiv +i_{\mathrm{tpb}} \lambda_{\mathrm{tpb}} \ , \tag{5.33}$$

$$\nabla \cdot \mathbf{i}_{\mathrm{io}} \equiv \nabla \cdot \left(-\sigma_{\mathrm{io}}^{\mathrm{eff}} \nabla \varphi_{\mathrm{io}} \right) = -i_{\mathrm{tr}} \equiv -i_{\mathrm{tpb}} \lambda_{\mathrm{tpb}} , \tag{5.34}$$

where $\mathbf{i}_{\mathrm{el}}$ and $\mathbf{i}_{\mathrm{io}}$ are the electronic and ionic current densities. The positive value of the transfer current density, i_{tr}, indicates that electronic charges are created while ionic charges are consumed in the functional layers. The domain for the electronic potential calculation includes the ASL, AFL, CFL, CCCL, and interconnect plates, while that for the ionic potential calculation includes the AFL, electrolyte, and CFL.

For methane reformate gas in the anode, the five gas species of CH_4, H_2O, H_2, CO, and CO_2 should be considered. Thus, the governing equation for the conservation of gas species i can be expressed as

$$\nabla \cdot \mathbf{n}_{\mathrm{i}} = i_{\mathrm{tr}} \beta_{\mathrm{i}} + s_i , \tag{5.35}$$

where $\mathbf{n}_{\mathrm{i}}$ is the molar flux (mol/m^2-s) of species i, $i_{\mathrm{tr}}\beta_{\mathrm{i}}$ (mol/m^3-s) is the volumetric species source due to electrochemical reactions, and s_{i} is the volumetric species source due to methane reforming reactions. β_{i} has different values for different domains, such as $1/2F$ for H_2 and $-1/2F$ for H_2O in the AFL, and $-1/4F$ for O_2 and zero for N_2 in the CFL (see Table 2.5).

The volumetric mass source for species i, s_{i} can be directly determined from the rates of the SMR, WGS, and RM reactions determined by Eq. (5.18) and Eqs. (5.8)~(5.10) as

$$s_{\mathrm{CH_4}} = (-r_{\mathrm{I}} - r_{\mathrm{III}}) \ \ \mathrm{mol/m^3\text{-}s}, \tag{5.36}$$

$$s_{\mathrm{H_2O}} = (-r_{\mathrm{I}} - r_{\mathrm{II}} - 2r_{\mathrm{III}}) \ \ \mathrm{mol/m^3\text{-}s}, \tag{5.37}$$

$$s_{\mathrm{H_2}} = (+3r_{\mathrm{I}} + r_{\mathrm{II}} + 4r_{\mathrm{III}}) \ \ \mathrm{mol/m^3\text{-}s}, \tag{5.38}$$

$$s_{\mathrm{CO}} = (+r_{\mathrm{I}} - r_{\mathrm{II}}) \ \ \mathrm{mol/m^3\text{-}s}, \tag{5.39}$$

$$s_{\mathrm{CO_2}} = (+r_{\mathrm{II}} + r_{\mathrm{III}}) \ \ \mathrm{mol/m^3\text{-}s}. \tag{5.40}$$

These mass conservation equations are solved for the domain of the ASL, AFL, CFL, CCCL, and gas channels.

The governing equation for the conservation of energy is written as

$$\nabla \cdot \left(\sum_{\mathrm{i}} \mathbf{n}_{\mathrm{i}} h_{\mathrm{sen,i}}(T) - k_{\mathrm{eff}} \nabla T \right) = \dot{q}_{\mathrm{gen}} , \tag{5.41}$$

where $h_{\mathrm{sen,i}}(T)$ is the molar sensible enthalpy of gas species i. Then, the term inside the parenthesis in the left-hand-side (LHS) of Eq. (5.41) denotes the total heat flux composed of the convective flux, $\Sigma_{\mathrm{i}}\mathbf{n}_{\mathrm{i}}h_{\mathrm{sen,i}}(T)$, and the conductive flux, $-k_{\mathrm{eff}}\nabla T$. The right-hand-side (RHS) term, $\dot{q}_{\mathrm{gen}}$, denotes the volumetric heat generation rate (W/m^3) due to the electrochemical reactions, Joule heating, and the DIR reactions. The heat generation rates are summarized in Table 5.6 for relevant calculation regions.

Table 5.7 Heat sources for regions in methane-fueled IT-SOFCs.

Region	Heat source	
	Reaction heat, $\dot{q}_{\mathrm{re}}$	Joule heat, $\dot{q}_{\mathrm{joule}}$
Interconnect plate		$i_{\mathrm{el}}^2 r_{\mathrm{el}}$ [a]
ASL/Interconnect		$i_{\mathrm{el}}^2 r_{\mathrm{asr}}$ [b]
ASL		$i_{\mathrm{el}}^2 r_{\mathrm{el}}$
AFL	$-i_{\mathrm{tr}}(-\frac{\Delta h_{\mathrm{f,H_2O}}(T_{\mathrm{ref}})}{2F}+\varphi_{\mathrm{el}}-\varphi_{\mathrm{io}})$	$i_{\mathrm{el}}^2 r_{\mathrm{el}}+i_{\mathrm{io}}^2 r_{\mathrm{io}}$
Electrolyte		$i_{\mathrm{io}}^2 r_{\mathrm{io}}$
CFL	$+i_{\mathrm{tr}}(\varphi_{\mathrm{io}}-\varphi_{\mathrm{el}})$	$i_{\mathrm{el}}^2 r_{\mathrm{el}}+i_{\mathrm{io}}^2 r_{\mathrm{io}}$
CCCL	$-\sum_{\mathrm{k=I,II,III}} r_{\mathrm{k}}\Delta h_{\mathrm{k}}(T_{\mathrm{ref}})$	$i_{\mathrm{el}}^2 r_{\mathrm{el}}$
CCCL/Interconnect		$i_{\mathrm{el}}^2 r_{\mathrm{asr}}$
Interconnect plate		$i_{\mathrm{el}}^2 r_{\mathrm{el}}$

[a] For volume domains, the current density i [A/m^2] multiplied by $r=1/\sigma$ [Ω-m] results in volumetric heat source $i^2 r$ [W/m^3].

[b] For interface domains, the current density i [A/m^2] multiplied by r_{asr} [Ω-m^2] results in area heat source $i^2 r_{\mathrm{asl}}$ [W/m^2].

5.1.7 Boundary and operating conditions

The simulations for methane-fueled IT-SOFCs are performed based on the cell

geometries that have been considered for hydrogen-fueled IT-SOFCs in the previous chapter 3 and chapter 4. And also, the same boundary conditions are employed as the periodic condition for the top/bottom boundaries and the symmetric condition for the side boundaries. Thus, only the inlet conditions for the fuel stream need to be changed to consider the steam/methane reformate fuel. The operation conditions considered for methane-fueled IT-SOFCs are summarized in Table 5.8, where the inlet temperature is slightly increased from 700°C for hydrogen fuel in chapter 2 to 750°C for methane reformate fuel. This is because the strong endothermic nature of the SMR and RM reactions.

The mixture gas at the fuel inlet is assumed to be the methane reformate with 30% pre-reforming degree (methane conversion ratio, $\beta_{\mathrm{CH_4}}$, of 0.3) at the steam-to-carbon (S/C) ratio of 2.0 (stoichiometric ratio). The mole fractions of CH_4, H_2O, H_2, CO, and CO_2 are fully provided in Table 5.8. Note that pre-reforming is commonly used to reduce the thermal shock due to high endothermic reforming reactions. In addition, the S/C ratio higher than 2.0 is also used to avoid the risk of carbon deposition. The composition of 30% pre-reformed steam/methane mixture is 19.4% methane, 43.8% water vapor, 28.5% hydrogen, 5.0% carbon monoxide, and 3.4% carbon dioxide in volume.

The flow rate of methane reformate fuel is defined by setting the limiting current density of fuel supply, $i_{\mathrm{fuel}}^{\mathrm{lim}}$, as 1 A/cm^2. Based on the prescribed $i_{\mathrm{fuel}}^{\mathrm{lim}}$, the total molar flow rate that enters through the anode channel inlet, $N_{\mathrm{x,tot,A}}^{\mathrm{o}}$, can be calculated as

$$N_{\mathrm{x,tot,A}}^{\mathrm{o}} = \frac{i_{\mathrm{fuel}}^{\mathrm{lim}} \times L_{\mathrm{x}}(W_{\mathrm{CH}} + W_{\mathrm{Rib}})}{2Fx_{\mathrm{fuel}}^{\mathrm{o}}} = \frac{i_{\mathrm{fuel}}^{\mathrm{lim}} \times 2L_{\mathrm{x}}L_{\mathrm{y}}}{2F(4x_{\mathrm{CH_4}}^{\mathrm{o}} + x_{\mathrm{H_2}}^{\mathrm{o}} + x_{\mathrm{CO}}^{\mathrm{o}})}, \tag{5.42}$$

where L_{x} is the cell length (0.1 m), W_{CH} and W_{Rib} are the channel and rib width, $x_{\mathrm{fuel}}^{\mathrm{o}}$ is the mole fraction of fuel species (CH_4, H_2, and CO) calculated as $x_{\mathrm{fuel}}^{\mathrm{o}} = 4x_{\mathrm{CH_4}}^{\mathrm{o}} + x_{\mathrm{H_2}}^{\mathrm{o}} + x_{\mathrm{CO}}^{\mathrm{o}}$. Since the half channel and half rib width are included in the calculation domain, $(W_{\mathrm{CH}} + W_{\mathrm{Rib}})$ equals to double the transverse domain size as $2L_{\mathrm{y}} = (W_{\mathrm{CH}} + W_{\mathrm{Rib}})$. Then, $i_{\mathrm{fuel}}^{\mathrm{lim}} = 1$ A/cm^2 is equivalent to $N_{\mathrm{x,tot,A}}^{\mathrm{o}} = 9.33\times10^{-6}$ mol/s.

The mean fluid velocity at the fuel inlet, $u_{\mathrm{m,A}}^{\mathrm{o}}$, is calculated as

$$u_{\mathrm{m,A}}^{\mathrm{o}} = \frac{N_{\mathrm{x,tot,A}}^{\mathrm{o}}}{c_{\mathrm{fuel}}^{\mathrm{o}} W_{\mathrm{CH}} H_{\mathrm{CH}}} = \frac{RT_{\mathrm{fuel}}^{\mathrm{o}} N_{\mathrm{x,tot,A}}^{\mathrm{o}}}{p_{\mathrm{fuel}}^{\mathrm{o}} W_{\mathrm{CH}} H_{\mathrm{CH}}}, \tag{5.43}$$

where $c_{\mathrm{fuel}}^{\mathrm{o}}$ denotes the molar density at the fuel inlet ($c_{\mathrm{fuel}}^{\mathrm{o}} = p_{\mathrm{fuel}}^{\mathrm{o}} / RT_{\mathrm{fuel}}^{\mathrm{o}}$) and H_{CH} denotes the channel height (1 mm). In Table 5.8, $i_{\mathrm{fuel}}^{\mathrm{lim}}$ of 1 A/cm^2 results in $u_{\mathrm{m,A}}^{\mathrm{o}}$ of 0.783 m/s. For air flow rate, the limiting current density, $i_{\mathrm{air}}^{\mathrm{lim}}$, is set to 4 A/cm^2 as before, which corresponds to the fluid velocity, $u_{\mathrm{m,C}}^{\mathrm{o}}$,of 8.287 m/s at the cathode channel inlet.

Fig. 5.3 show the variation of the standard composition of steam/methane reformate gas according to the methane conversion ratio, $\beta_{\mathrm{CH_4}}$, defined as

$$\beta_{\mathrm{CH_4}} = 1 - \frac{N_{\mathrm{CH_4}}}{N_{\mathrm{CH_4}}^{\mathrm{o}}}, \tag{5.44}$$

where $N_{\mathrm{CH_4}}^{\mathrm{o}}$ denotes the methane flow rate at the inlet of a reformer while $N_{\mathrm{CH_4}}$ denotes the remaining methane flow rate after some distance from the inlet. The methane reforming reactions are calculated at 750°C and 1 bar using the reforming kinetics proposed by Xu and Froment (1989a). Note that the S/C ratio is varied as 1.5, 2.0, and 2.5, which are believed to fall between the operating ranges of pre-reformer for methane-fueled IT-SOFCs. In Fig. 5.3, the mole fractions of CH_4 and H_2O are observed to decrease with $\beta_{\mathrm{CH_4}}$ while those of H_2, CO, and CO_2 generally increase. Note that the mole fraction of methane, $x_{\mathrm{CH_4}}$, does not show linear relationship with $\beta_{\mathrm{CH_4}}$. This is because more gas molecules are produced than consumed during the reforming reactions; for example, three reactant molecules are combined to generate five product molecules in the RM reaction. In Fig. 5.3, higher S/C ratio is observed to shift the equilibrium point towards higher conversion ratio according to the presence of more reactant molecules (H_2O).

Using the data for each species shown in Fig. 5.3, third-order polynomial correlations are determined to help evaluate the composition of partially reformed methane fuels. These correlations are found to well predict the composition variation as indicated by the coefficient of determination, R^2, near 1. The coefficients for the polynomial correlations are summarized in Table 5.9. In addition, the composition of methane reformate gas is also provided for several discrete methane conversion ratios, for easier evaluation of the

Table 5.8 Standard operating conditions for IT-SOFCs operated with pre-reformed methane fuel and air.

Parameters		Values
Air: O_2/N_2 mixture		
Inlet temperature, T^{o}_{air}		750°C
Pressure, p^{o}_{air}		1 atm
Air composition	Oxygen, $x^{o}_{O_2}$	0.21
	Nitrogen, $x^{o}_{N_2}$	0.79
Flow rate (limiting current density), i^{lim}_{air}		4 A/cm^2 equivalent
⟍ Molar flow rate in channel, $N^{o}_{x,tot,C}$		9.87×10^{-5} mol/s
⟍ Mean fluid velocity, $u^{o}_{m,C}$		8.287 m/s
Fuel: $CH_4/H_2O/H_2/CO_2/CO$ mixture		
Inlet temperature, T^{o}_{fuel}		750 °C
Pressure, p^{o}_{fuel}		1 atm
Steam-to-carbon ratio, S/C		2.0
Pre-reforming degree		30%
Fuel composition	Methane, $x^{o}_{CH_4}$	0.1941
	Water vapor, $x^{o}_{H_2O}$	0.4377
	Hydrogen, $x^{o}_{H_2}$	0.2846
	Carbon monoxide, x^{o}_{CO}	0.0496
	Carbon dioxide, $x^{o}_{CO_2}$	0.0340
Flow rate (limiting current density), i^{lim}_{fuel}		1 A/cm^2 equivalent
⟍ Molar flow rate in channel, $N^{o}_{x,tot,A}$		9.33×10^{-6} mol/s
⟍ Mean fluid velocity, $u^{o}_{m,A}$		0.783 m/s

5.1.8 Numerical artifacts

Some numerical artifacts are utilized to enhance the solution convergence of the present model. The first is the turn-off switch for electrochemical reactions and this artifact is inherited from the micro/macroscale model for hydrogen-fueled IT-SOFCs. When a finite volume cell in the functional layers runs short of reactant

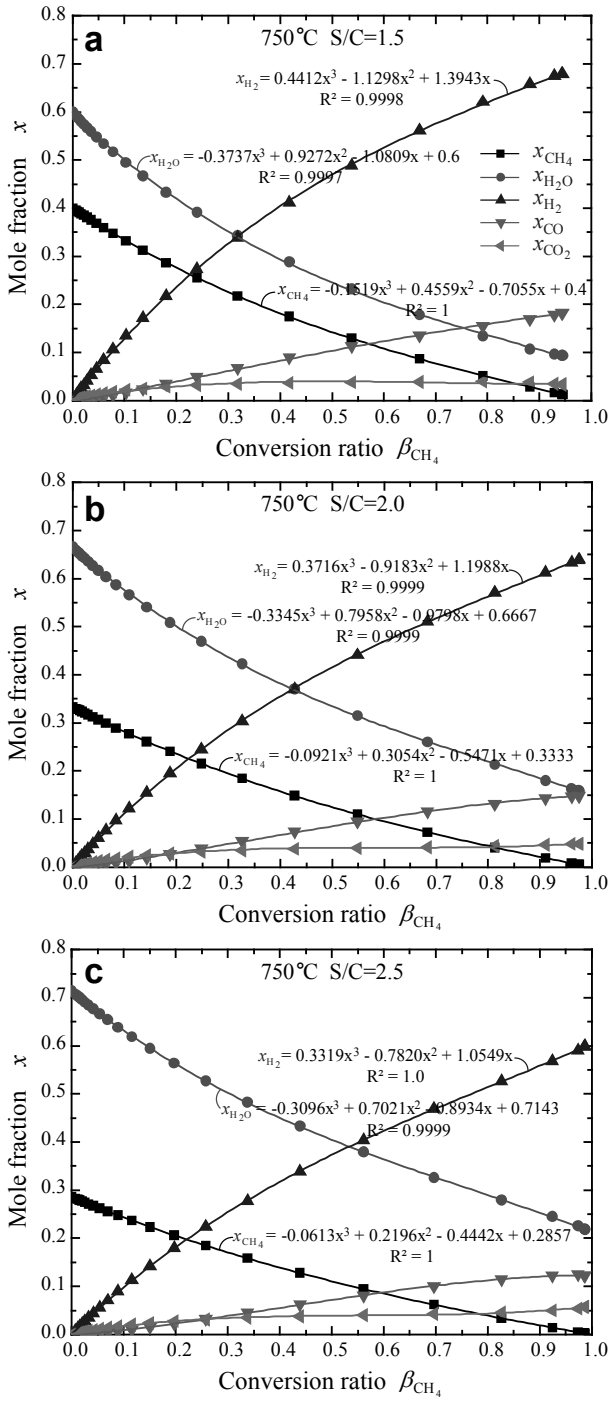

Fig. 5.3 The standard composition of steam/methane reformate gas with respect to the conversion ratio, β_{CH_4}, at 750°C and 1 bar, calculated based on the reforming kinetics proposed by Xu and Froment (1989a).

Table 5.9 The coefficients for the standard composition of steam/methane reformate gas at 750°C and 1 bar, according to the reforming kinetics proposed by Xu and Froment (1989a).

S/C	Coefficients	CH_4	H_2O	H_2	CO	CO_2
	a_0 [a]	0.4000	0.6000	0	0	0
	a_1	−0.7055	−1.0807	1.3943	0.1735	0.2185
1.5	a_2	0.4559	0.9272	−1.1298	0.1167	−0.3700
	a_3	−0.1519	−0.3737	0.4412	−0.1037	0.1881
	R^2 [b]	1.0000	0.9997	0.9998	0.9987	0.9534
	a_0	0.3333	0.6667	0	0	0
	a_1	−0.5471	−0.9798	1.1988	0.1151	0.2134
2.0	a_2	0.3054	0.7958	−0.9183	0.1833	−0.3670
	a_3	−0.0921	−0.3345	0.3716	−0.1494	0.2050
	R^2	1.0000	0.9999	0.9999	0.9992	0.9885
	a_0	0.2857	0.7143	0	0	0
	a_1	−0.4442	−0.8934	1.0549	0.0758	0.2069
2.5	a_2	0.2196	0.7021	−0.7820	0.2230	−0.3627
	a_3	−0.0613	−0.3096	0.3319	−0.1758	0.2148
	R^2	1.0000	0.9999	1.0000	0.9994	0.9959

[a] The mole fraction of species k, x_k, is calculated from the third-order polynomial correlation, $x_k = a_0 + a_1\beta_{CH_4} + a_2\beta_{CH_4}^2 + a_3\beta_{CH_4}^3$, for the range of $\beta_{CH_4} < 0.95$.
[b] R^2 denotes the coefficient of determination for the polynomial correlations.

(hydrogen in the AFL or oxygen in the CFL), this is manifested by negative partial pressure of the corresponding species. Then, the transfer current density in the finite volume cell is reset to zero, while increasing the depletion count, $n_{H_2,dep}$ or $n_{O_2,dep}$, for the cell. If the depletion of reactant recurrently occurs in the finite volume cell, the depletion count will increase over the preset margin (such as 10 in the present model) and the electrochemical reaction in that finite volume cell is turned off. Because reactant depletion is expected to first occur near the electrolyte, the electrochemical reaction is immediately turned off when n_{dep} becomes larger

Table 5.10 The standard composition of partially reformed steam/methane gas at 750°C and 1 bar, according to the reforming kinetics proposed by Xu and Froment (1989a).

S/C	Conversion ratio, β_{CH_4}	CH_4	H_2O	H_2	CO	CO_2
1.5	10%	0.3335	0.4971	0.1325	0.0154	0.0216
	30%	0.2255	0.3530	0.3245	0.0632	0.0337
	50%	0.1427	0.2486	0.4658	0.1059	0.0370
	70%	0.0765	0.1658	0.5780	0.1408	0.0389
2.0	10%	0.2814	0.5738	0.1136	0.0111	0.0201
	30%	0.1941	0.4377	0.2846	0.0496	0.0340
	50%	0.1247	0.3359	0.4143	0.0865	0.0387
	70%	0.0681	0.2536	0.5191	0.1175	0.0417
2.5	10%	0.2433	0.6301	0.0996	0.0084	0.0186
	30%	0.1709	0.5036	0.2524	0.0398	0.0333
	50%	0.1109	0.4051	0.3728	0.0721	0.0391
	70%	0.0613	0.3248	0.4711	0.1002	0.0426

than 10 for finite volume cells at the AFL/electrolyte or CFL/electrolyte interface. However, for finite volume cells inside the AFL or the CFL, the electrochemical reactions are turned off on the condition that n_{dep} is larger than 10 and also the electrochemical reaction at the neighboring finite volume cell nearer to the electrolyte is previously turned off.

Another numerical artifact used in the present micro/macroscale model is the turn-off switch for the SMR and RM reactions. The reforming of methane is usually completed within a short distance from the fuel inlet, which results in negligible methane concentration (or partial pressure) in the remaining part of the anode. Then, calculating the SMR and RM reactions in such methane-depleted regions can delay the numerical convergence by requiring very low under relaxation factors. Thus, the occurrence of methane (CH_4) depletion is also counted for finite volume cells in the ASL during iterative calculations. When the methane depletion count, $n_{CH_4,dep}$, for

a finite volume cell exceeds the preset number (10 in the model), the SMR and RM reactions at that cell are turned off permanently. It should be noted that the steam reforming of methane in the thin AFL is ignored due to negligible contribution. This also helps the solution to converge faster.

5.2 Results and Discussions

The performance characteristics of methane-fueled IT-SOFCs are studied for the standard operating conditions presented in Table 5.8. The cell geometry and electrode microstructure have been set the same as those for hydrogen-fueled IT-SOFCs, by employing the microstructural and geometrical parameters provided in Table 2.6. The standard fuel utilization factor, ζ_{fuel}, is set to be 50% ($\zeta_{\text{fuel}} = 0.5$), which is lower than $\zeta_{\text{fuel}} = 0.65$ assumed for studying hydrogen-fueled IT-SOFCs. From the inlet flow rate of methane reformate fuel derived in Eqs. (5.41), ζ_{fuel} can be easily evaluated as (Campanari, 2001)

$$\zeta_{\text{fuel}} = \frac{i^{\text{cell}} \times 2L_{\text{x}}L_{\text{y}}}{2F(4x^{\text{o}}_{\text{CH}_4} + x^{\text{o}}_{\text{H}_2} + x^{\text{o}}_{\text{CO}})N^{\text{o}}_{\text{x,tot,A}}} = \frac{i^{\text{cell}}}{i^{\text{lim}}_{\text{fuel}}}. \tag{5.45}$$

Note that $\zeta_{\text{fuel}} = 0.5$ corresponds to $i^{\text{cell}} = 0.5$ A/cm^2 at the standard operating conditions ($i^{\text{lim}}_{\text{fuel}} = 1$ A/cm^2).

5.2.1 Current–voltage characteristics

The simulated current–voltage ($I - V$) and the maximum temperature results are presented in Fig. 5.4 for methane-fueled IT-SOFCs with co- and counter-flow configurations. In Fig. 5.4, the counter-flow configuration is observed to result in higher cell potential, φ^{cell}, than the co-flow configuration when the inlet temperature is fixed at 750°C for both fuel and air streams. For example, φ^{cell} at 50% fuel utilization is about 0.699 V for the co-flow configuration and about 0.762 V for the counter-flow configuration. The observed better performance is related with the maximum temperature inside the methane-fueled IT-SOFCs, T_{max}. The maximum temperature is higher for the counter-flow configuration than for the co-flow configuration, e.g., by about 27°C at 50% fuel utilization, which is believed to results in higher ionic conductivity in the electrolyte and faster electrochemical

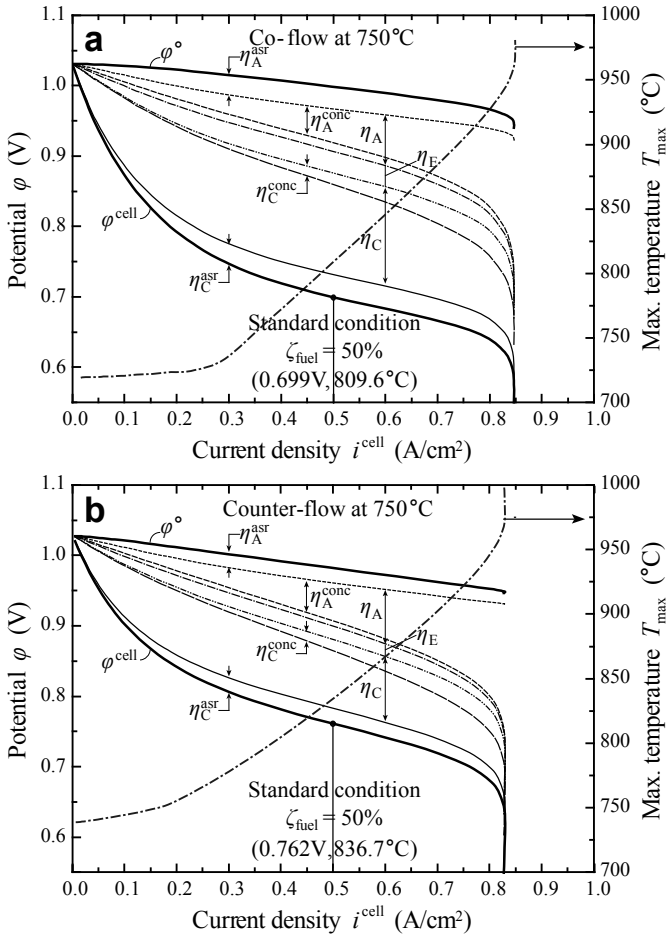

Fig. 5.4 The current–voltage ($I-V$) performance characteristics of methane-fueled IT-SOFCs with (a) co-flow configuration and (b) counter-flow configuration.

reactions in the electrodes.

Note that T_{max} is obtained by auditing the temperature of all finite volume cells in the calculation domain (including the PEN, flow channels, and interconnect plates while excluding the inlet and outlet boundaries). Thus, T_{max} may be lower than the prescribed inlet temperature (700°C) for low fuel utilization factors (below 0.2~0.3 A/cm^2) as shown in Fig. 5.4, because of the endothermic methane reforming reactions. However, with higher fuel utilization factors, T_{max} increases over the inlet temperature due to the reaction heat from the electrochemical reactions as well

as Joule heat. In Fig. 5.4, the concentration-limited behaviors, such as rapid drop of φ^{cell} and steep increase of $T_{\max}$, are observed at the current density, i^{cell}, of about 0.85 A/cm^2. This result indicates that the maximum achievable fuel utilization is about 85%, pointing out that about 15% of methane reformate fuel cannot be utilized by methane-fueled IT-SOFCs. On the contrary, the limiting behaviors are observed at near 1 A/cm^2 current density in hydrogen-fueled IT-SOFCs (see Fig. 3.2 in chapter 3), indicating almost full utilization of hydrogen fuel.

The present micro/macroscale model ignores the participation of carbon monoxide (CO) in the electrochemical reaction. Instead, carbon monoxide and water should be converted to hydrogen and carbon dioxide according to the WGS reaction, and then this hydrogen can participate in the electrochemical reaction. Neglecting the electrochemical oxidation of CO in the AFL may have resulted in the observed low maximum achievable fuel utilization in methane-fueled IT-SOFCs. However, considerable amount of CO always exists inside the anode according to the near-equilibrium WGS reaction and the concentration of CO at equilibrium generally increases as temperature increases. Thus, the exhaust of CO molecules through the outlet of the fuel channel directly decreases the maximum achievable fuel utilization, and this becomes more noticeable as temperature increases.

Fig. 5.4 also shows the contribution of each overpotential to the total potential loss (the difference between the Nernst potential, φ°, and the cell potential, φ^{cell}). The Nernst potential curves are observed to decrease rather linearly with respect o the current density, i^{cell}, which is believed to be the direct consequence of the cell temperature increase according to i^{cell}. In Fig. 5.4, the cell potential curves clearly show three distinctive regions; the so-called activation-loss-dominant region at low i^{cell}, and the ohmic-loss-dominant region at moderate i^{cell}, and the concentration-loss-dominant region near the limiting current density. Note that the concentration limited behaviors are observed at current densities lower than the prescribed feed rate of methane reformate fuel (equivalent to 1 A/cm^2), which is primarily due to the considerable amount of CO exhaust at the fuel outlet.

Fig. 5.4(a) indicates that the sum of the activation and ohmic overpotentials in the cathode (calculated as $\eta_{\text{C}} - \eta_{\text{C}}^{\text{conc}}$) is the most significant potential loss for

methane-fueled IT-SOFCs with the co-flow configuration. Only after the current density, i^{cell}, increases over 0.8 A/cm^2, the concentration overpotential in the anode, $\eta_{\text{A}}^{\text{conc}}$, becomes dominant. For methane-fueled IT-SOFCs with the counter-flow configuration shows similar but slightly different trends in the overpotentials. In Fig. 5.4(b) for the counter-flow configuration, $\eta_{\text{C}} - \eta_{\text{C}}^{\text{conc}}$ is dominant at low current densities below 0.5 A/cm^2 but its magnitude is much smaller than that with the co-flow configuration. Instead, $\eta_{\text{A}}^{\text{conc}}$ with the counter-flow configuration becomes dominant for $i^{\text{cell}} > 0.6$ A/cm^2 and its magnitude is larger than that with the co-flow configuration. Therefore, the observed higher cell potential with the counter-flow configuration is largely attributed to the reduced overpotential in the cathode, η_{C}.

Higher cell temperature in IT-SOFCs significantly reduces the activation overpotentials, $\eta_{\text{A}}^{\text{act}}$ and $\eta_{\text{C}}^{\text{act}}$, by enhancing the activities of the electrochemical reactions in the AFL and CFL. Higher temperature moderately decreases the ohmic overpotential in the electrolyte, η_{E}, by increasing the ionic conductivity. Similarly, the contact potential losses at the electrode/interconnect interfaces, $\eta_{\text{A}}^{\text{asr}}$ and $\eta_{\text{C}}^{\text{asr}}$, are moderately reduced due to the enhanced electronic conductivity of corrosion-resistant film on the interconnect plates. Finally, higher cell temperature slightly decreases the concentration polarization in the cathode, $\eta_{\text{C}}^{\text{conc}}$, while increases that in the anode, $\eta_{\text{A}}^{\text{conc}}$. These trends of various overpotentials are well observed by comparing the cell potential curves with the co- and counter-flow configurations shown in Figs. 5.4(a) and 5.4(b).

5.2.2 Overpotential distribution

Fig 5.5 presents the spatial distribution of electrical potentials, φ_{avg}, and electrolyte temperature, T_{avg}, along the flow channel (x-direction) of methane fueled IT-SOFCs. The results are for the standard operating condition with 50% fuel utilization ($\zeta_{\text{fuel}} = 0.5$ and $i^{\text{cell}} =$ 0.5 A/cm^2). Note that the results at the standard conditions are denoted by points in Fig. 5.4. Because of the 3D computational domain, φ_{avg} has to be calculated by averaging the electronic or ionic potentials at relevant locations in the transverse y-direction. Similarly, T_{avg} is also obtained by

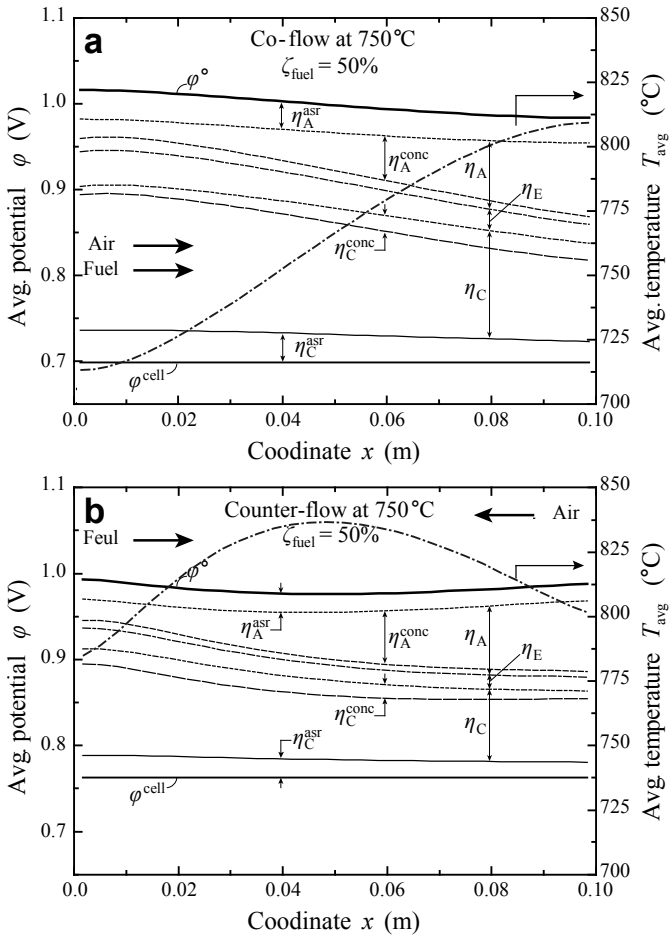

Fig. 5.5 The distribution of potential and temperature along the flow direction (x-direction) of methane-fueled IT-SOFCs with (a) co-flow configuration and (b) counter-flow configuration, operated at 50% fuel utilization ($\zeta_{fuel} = 0.5$).

averaging the temperature in electrolyte. The activation, concentration, ohmic, and contact polarizations that contribute to the drop of the cell potential, φ^{cell}, from the Nernst potential, $\varphi°$, can be investigated in detail with Fig. 5.5.

Temperature distribution is one of the most important environmental variables that govern the fuel cell processes inside IT-SOFCs. It is believed that T_{avg} can accurately represent the temperature distribution in the PEN since it is obtained based on the temperature at the electrolyte. The observe trends of cell temperature distribution are widely different for the co-flow configuration and the counter-flow configuration. In Fig. 5.5(a), the cell temperature with the co-flow configuration

monotonically increases along the flow direction of parallel fuel and air streams (x-direction). The cell temperature near the air and fuel inlets ($x = 0$) is lower than the prescribed inlet temperature (750°C) due to the heat absorption by the endothermic reforming reactions. Then, the cell temperature steadily increases due to the heat release by the exothermic electrochemical reactions (also including Joule heating) and finally reaches the maximum temperature at the air and fuel outlets ($x = 0.1$ m).

However, the cell temperature with the counter-flow configuration is observed to have a local maximum near the center of the cell length, as shown in Fig. 5.5(b). Since the flow rate of air is much larger than that of fuel at the standard operating condition, we choose to explain the temperature variation along the direction of air flow. In Fig. 5.5(b), cell temperature near the air inlet ($x = 0.1$ m) is much higher than the inlet temperature (750°C) and also the cell temperature increases along the flow direction of air until it reaches it maximum near the center of the cell ($x = 0.05$ m). This behavior is a natural outcome of the electrochemical reaction heat and Joule heat. Then, the cell temperature starts to decreases as air flow moves towards the air outlet ($x = 0$), which is caused by the endothermic reforming reactions that occurs actively near the inlet of partially reformed methane fuel. Thus, local minimum temperature is observed at the fuel inlet ($x = 0$).

If we calculate the average temperature for the whole cell length of methane-fueled IT-SOFCs, the average temperature at the standard condition is much higher for the counter-flow configuration by about 50°C than for the co-flow configuration. The better performance of IT-SOFCs with counter-flow configuration observed in Fig. 5.4 is then easily explained by the temperature distribution. In addition, the uniformity of the cell temperature is also much higher with the counter-flow configuration than the co-flow configuration. This also leads to smaller temperature gradient along the x-direction, which is favorable for reducing the thermal stress. This result clearly indicates that more uniformly higher temperature distribution can be achieved in methane-fueled IT-SOFCs by utilizing the endothermic reforming reactions with proper flow configuration and air flow rate.

Fig. 5.5 clearly explains why the output cell potential, φ^{cell}, is higher with the

co-flow configuration than the counter-flow configuration at the standard operating condition considered in this study. The Nernst potential, $\varphi°$, is observed to be inversely proportional to the temperature, which leads to slightly higher Nernst potential with the co-flow configuration than with the counter-flow configuration. However, the total potential loss, η_{tot}, is found to be much larger with the co-flow configuration, which results in better performance with the counter-flow configuration.

In Fig. 5.5, the variation of individual overpotentials along the channel (x-direction) is presented. Note that temperature and hydrogen concentration are the two most important variables that govern the spatial distribution of overpotentials shown in Fig. 5.5. Higher temperature IT-SOFCs improves the electrochemical and charge transport properties, while higher hydrogen concentration reduces the concentration polarization. The cathode activation overpotential, $\eta_{\mathrm{C}}^{\mathrm{act}}$ ($\equiv \eta_{\mathrm{C}} - \eta_{\mathrm{C}}^{\mathrm{conc}}$), is observed to be the largest among various overpotentials, followed by the anode concentration overpotential, $\eta_{\mathrm{A}}^{\mathrm{conc}}$. Fig. 5.5 clearly shows that smaller $\eta_{\mathrm{C}}^{\mathrm{act}}$ is obtained where the cell temperature is higher (near the maximum temperature region) and smaller $\eta_{\mathrm{A}}^{\mathrm{conc}}$ where hydrogen concentration is higher (near the fuel outlet). Other overpotentials also exhibit similar dependencies on temperature and concentration; $\eta_{\mathrm{A}}^{\mathrm{act}}$, η_{E}, $\eta_{\mathrm{A}}^{\mathrm{asr}}$, and $\eta_{\mathrm{C}}^{\mathrm{asr}}$ are smaller where temperature is higher and $\eta_{\mathrm{C}}^{\mathrm{conc}}$ is smaller where oxygen concentration is higher (near the air inlet).

5.2.3 Current density distribution

The local current density along the axial flow direction (x-direction) inside the methane-fueled IT-SOFCs is presented in Fig. 5.6, where the local temperature is also shown for easier reference. Again, the local current density is obtained by averaging (in the transverse y-direction) the ionic current densities that cross the electrolyte. The results are for the standard fuel utilization factor, ζ_{fuel}, of 50%.

In Fig. 5.6(a), the average local current density, i_{x}, for the co-flow configuration is observed to have a local maximum near the outlet of the fuel channel. This result can be explained by the temperature distribution in the electrolyte; starting from about 710°C at the fuel inlet ($x = 0$), the electrolyte

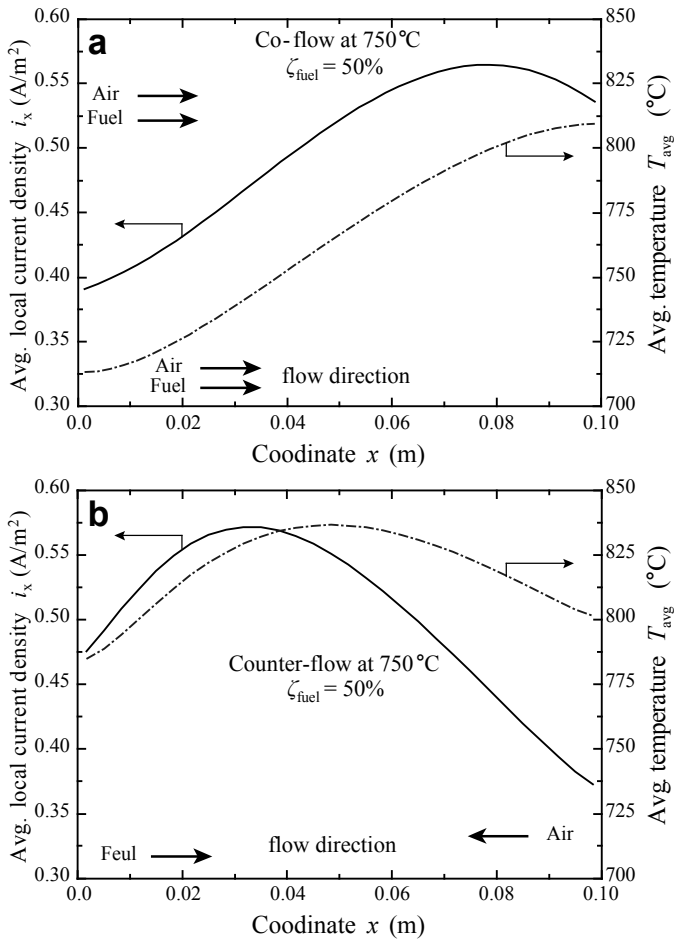

Fig. 5.6 The distribution of current density along the flow direction (x-direction) of methane-fueled IT-SOFCs with (a) co-flow configuration and (b) counter-flow configuration, operated at 50% fuel utilization ($\zeta_{fuel} = 0.5$).

temperature gradually increases along the channel and finally reaches the highest temperature of about 810°C at the fuel outlet ($x = 0.1$ m). The existence of the local current maximum may be explained as follows. Near the fuel inlet, the hydrogen concentration is higher but the cell temperature is lower, which results in large activation overpotentials, η^{act}. On the contrary, the cell temperature is higher near the fuel outlet but hydrogen concentration is lower, which results in large concentration overpotentials, η^{act}. Thus, local maximum current density is obtained in between the fuel inlet and the outlet. The range of the local current

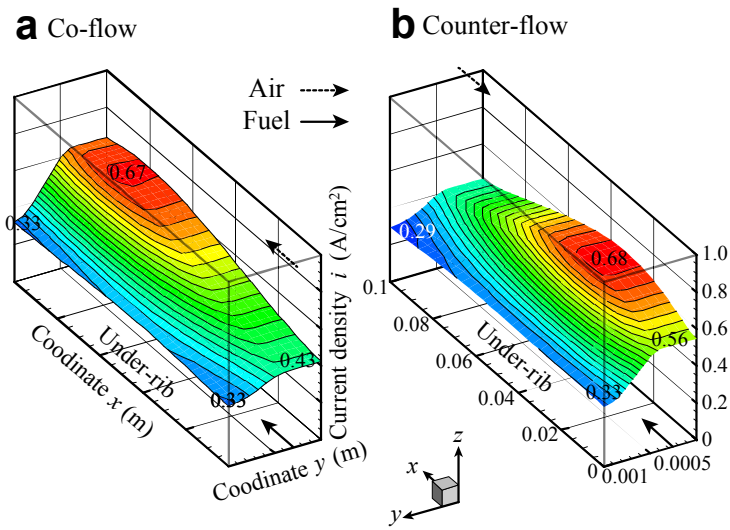

Fig. 5.7 The 2D distribution of local current density in methane-fueled IT-SOFCs with (a) co-flow configuration and (b) counter-flow configuration, operated at 50% fuel utilization ($\zeta_{\text{fuel}} = 0.5$).

density, i_x, is observed to be about 0.39~0.57 A/cm^2 in Fig. 5.6(a) for the co-flow configuration.

The average local current density, i_x, for the counter-flow configuration is presented in Fig. 5.6(a). A local maximum current density is also observed for the counter-flow configuration but its location is near to the fuel inlet compared with the co-flow configuration. This result is also explained by the cell temperature distribution in the electrolyte which also has a local maximum. Near the fuel inlet ($x = 0$), the electrochemical reactions direct follow the cell temperature variation, since the variation in the anode concentration overpotential, $\eta_{\text{A}}^{\text{conc}}$, is negligible due to high hydrogen concentration. Thus, the current density generally follows the trend of temperature distribution as observed in Fig. 5.6(b). Note that the general trend of i_x along the channel is quite similar to that of temperature in Figs. 5.6(a) and 5.6(b), except for the more noticeable drop in the magnitude near the fuel outlet ($\eta_{\text{A}}^{\text{conc}}$ becomes significant). The range of the local current density for the counter-flow configuration is found to be about 0.37~0.57 A/cm^2 in Fig. 5.6(b).

The distribution of local current density in the 2D electrolyte plane is shown in

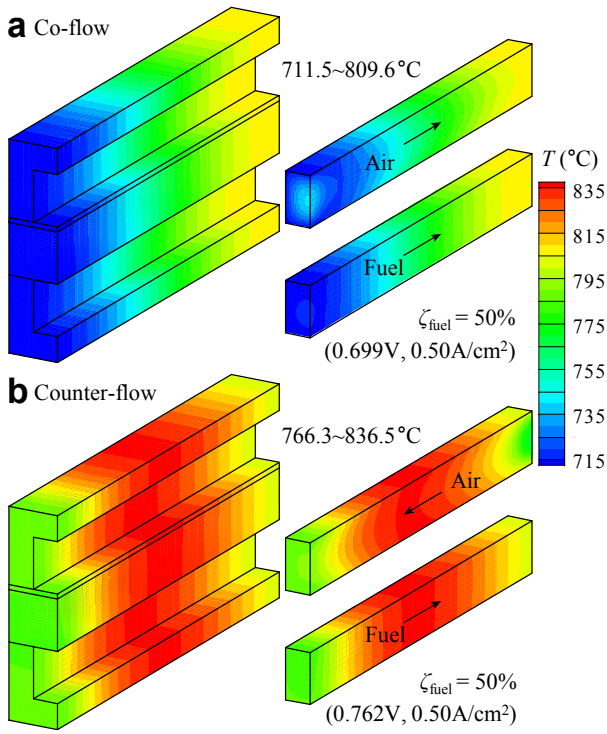

Fig. 5.8 The temperature distribution inside methane-fueled IT-SOFCs with (a) co-flow configuration and (b) counter-flow configuration, operated at 50% fuel utilization ($\zeta_{\text{fuel}} = 0.5$).

Fig. 5.7. Due to the presence of interconnect ribs which obstruct mass transport, the current density under the interconnect rib (under-rib region) is generally lower than that under the flow channel (under-channel region). In Fig. 5.7, the extent of y-axis includes the half channel width (½$W_{\text{CH}} = 0.5$ mm) and half rib width (½$W_{\text{Rib}} = 0.5$ mm). For the co-flow configuration, the maximum current density is about 0.67 A/cm^2 while the minimum is about 0.33 A/cm^2. For the co-flow configuration, the maximum current density is about 0.68 A/cm^2 while the minimum is about 0.29 A/cm^2. The uniformity of current density is found to be slightly better for the co-flow configuration than counter-flow configuration.

5.2.4 Temperature distribution

The temperature distribution inside IT-SOFCs is intimately related with the

mechanical failure of the PEN structure due to large thermal stress and the long-term performance loss due to the physical and chemical degradation of electrode materials. Thus, the temperature distribution is one of the most important results that any prediction model should provide for better design and optimization of IT-SOFCs. Fig. 5.8 shows the distribution of temperature inside the whole calculation domain of methane-fueled IT-SOFCs with co- and counter-flow configurations. The results are obtained with the standard operating condition with the fuel utilization factor of 50% and the inlet temperature of 750°C.

Fig. 5.8 indicates that the temperature mainly varies along the flow direction (x-direction) while it is rather uniform in the transverse directions (y- and z-directions). In addition, the temperature in the air channel shows more noticeable variation in the transverse directions than that in the fuel channel, according to the magnitude of their heat capacity rates as $(\dot{m}c_{\mathrm{p}})_{\mathrm{air}} > (\dot{m}c_{\mathrm{p}})_{\mathrm{fuel}}$. Near the fuel inlet, the temperature in the PEN (and interconnect plates) is generally lower than that in the flow channels and this indicates heat transfer from the flow channels to the PEN. This result is believed to be caused by the active endothermic reforming reactions in the anode. For regions other than the fuel inlet, temperature is higher in the PEN than the flow channels, indicating heat transfer from the PEN to the flow channels. This is because the electrochemical reaction heat and Joule heat is exhausted by the air and fuel gas flow.

In Fig. 5.8, the range of the temperature distribution in the whole calculation domain with the co-flow configuration is from 711.5 to 809.6°C. This range is larger than the temperature range with the counter-flow configuration from 766.3 to 836.5°C. In Fig. 5.8(a), the lowest temperature for the co-flow configuration is found in the ASL near the fuel inlet while the highest is found in the CFL near the fuel outlet. In Fig. 5.8(b) for the counter-flow configuration, the lowest temperature is observed in the flow channel near the air inlet while the highest is found in the CFL near the maximum current location.

The temperature distribution in the electrolyte is an important design parameter to be considered since thin electrolyte layers in planar, anode-supported IT-SOFCs are vulnerable to mechanical failures. In addition, the electrolyte temperature is the

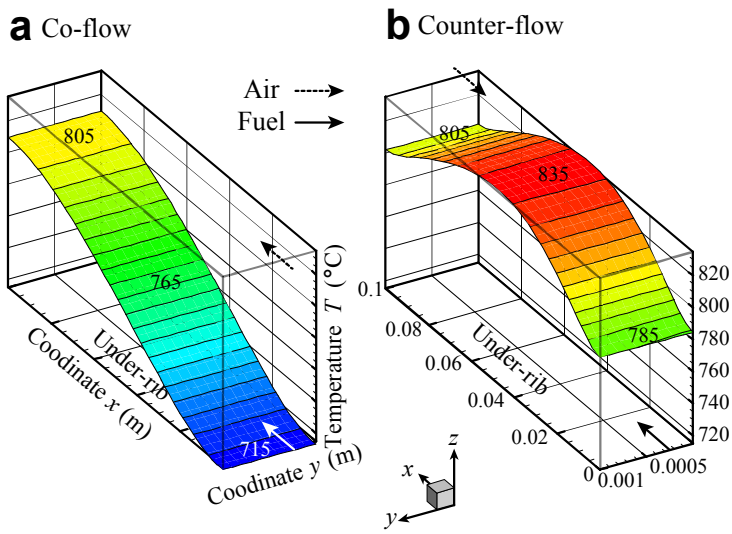

Fig. 5.9 The 2D distribution of local temperature at the electrolyte in methane-fueled IT-SOFCs with (a) co-flow configuration and (b) counter-flow configuration, operated at 50% fuel utilization ($\zeta_{\text{fuel}} = 0.5$).

most representative temperature for investigating the fuel cell processes that are concentrated in the thin regions of the AFL, electrolyte, and CFL. The 2D distribution of local temperature inside the electrolyte is shown in Fig. 5.9, where the temperature variation is observed to mainly occur in the direction of gas flow (x-direction). However, the temperature distribution in the electrolyte is observed to be almost insensitive to the presence of interconnect ribs, showing no noticeable temperature variation in the y-direction. The temperature range in the electrolyte is about 715~805°C (90°C difference) for the co-flow configuration and 785~835°C (50°C difference) for the counter-flow configuration. Therefore, the counter-flow configuration is found to results in more uniform temperature in the PEN when operated at the standard conditions.

5.2.5 Concentration distribution

Fig. 5.4 presents the variation of reformate gas composition along the fuel channel of methane-fueled IT-SOFCs. The concentration of methane (CH_4) in the partially reformed gas decreases along the channel according to the consumption of

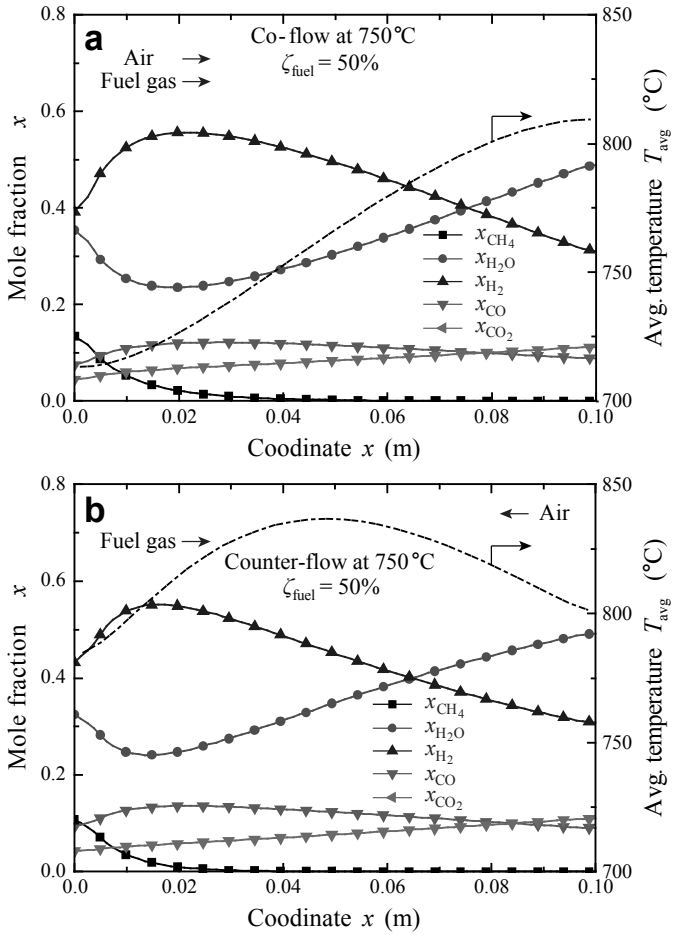

Fig. 5.10 The variation of reformate gas composition inside the fuel channel of methane-fueled IT-SOFCs with (a) co-flow configuration and (b) counter-flow configuration, operated at 50% fuel utilization ($\zeta_{fuel} = 0.5$).

CH_4 on Ni catalyst surface by the SMR and RM reactions. Thus, the mole fraction of methane, x_{CH_4}, becomes negligibly small in the downstream region after the active reforming zone (short distance from the inlet where methane is present). The active reforming zone is longer as about 4 cm for the co-flow configuration in Fig. 5.4(a) than about 3 cm for the counter-flow configuration in Fig. 5.4(b). The higher temperature near the fuel inlet is believed to be the main reason for the shorter active reforming zone with the counter-flow configuration. Because methane reforming reactions are strongly endothermic in overall, higher temperature enables faster conversion of methane into hydrogen.

The concentration of water vapor (H_2O) initially decreases in the active reforming zone near the fuel inlet since water vapor is consumed by the reforming reactions. Then, the mole fraction of water, x_{H_2O}, starts to increase along the channel due to the production of H_2O by the hydrogen oxidation reaction (HOR) in the anode. The concentration of hydrogen (H_2) shows the exactly opposite trend of that of H_2O. That is, the mole fraction of hydrogen, x_{H_2}, increases along the channel in the active reforming zone according to fast hydrogen production by methane reforming, and then starts to decrease according to hydrogen consumption by HOR. The concentration of carbon monoxide (CO) slightly increases due to the SMR reaction in the active reforming zone near the fuel inlet and then slowly decreases proportional to the increase of the concentration of carbon dioxide (CO_2) by the WGS reaction. Note that the WGS reaction is a near equilibrium reaction and the equilibrium concentration of CO generally increases with the ambient temperature.

The molar composition of fuel gas at the outlet of the fuel channel is found to be 0% CH_4, 48.9% H_2O, 31.1% H_2, 8.8% CO, and 11.2% CO_2 for the co-flow configuration and 0% CH_4, 49.2% H_2O, 30.8% H2, 9.0% CO, and 11.0% CO_2 for the counter-flow configuration. The mole fraction of CO, x_{CO}, and that of CO2, x_{CO_2}, at the fuel outlet are believed to close to the equilibrium composition corresponding to the condition with the temperature and the hydrogen and water vapor concentrations. Note that the anode gas at the fuel outlet is still rich in hydrogen and carbon monoxide since the fuel utilization is fixed at 50%. In general, many methane-fueled IT-SOFCs are operated with relatively low fuel utilization factors, ζ_{fuel}, which enables higher output potentials and also helps to reduce the cell temperature. The hydrogen-rich exhaust gas from IT-SOFCs can be used for operating turbines after combustion in hybrid systems.

It should be noted that the gas concentrations inside the channel shown in Fig. 5.10 is different from those inside the electrodes, primarily due to the consumption and generation of gas species by the chemical and electrochemical reactions as well as the concentration gradient required for mass transport. The 3D distribution of species concentrations inside methane-fueled IT-SOFCs is shown in Fig. 5.11, vapor,

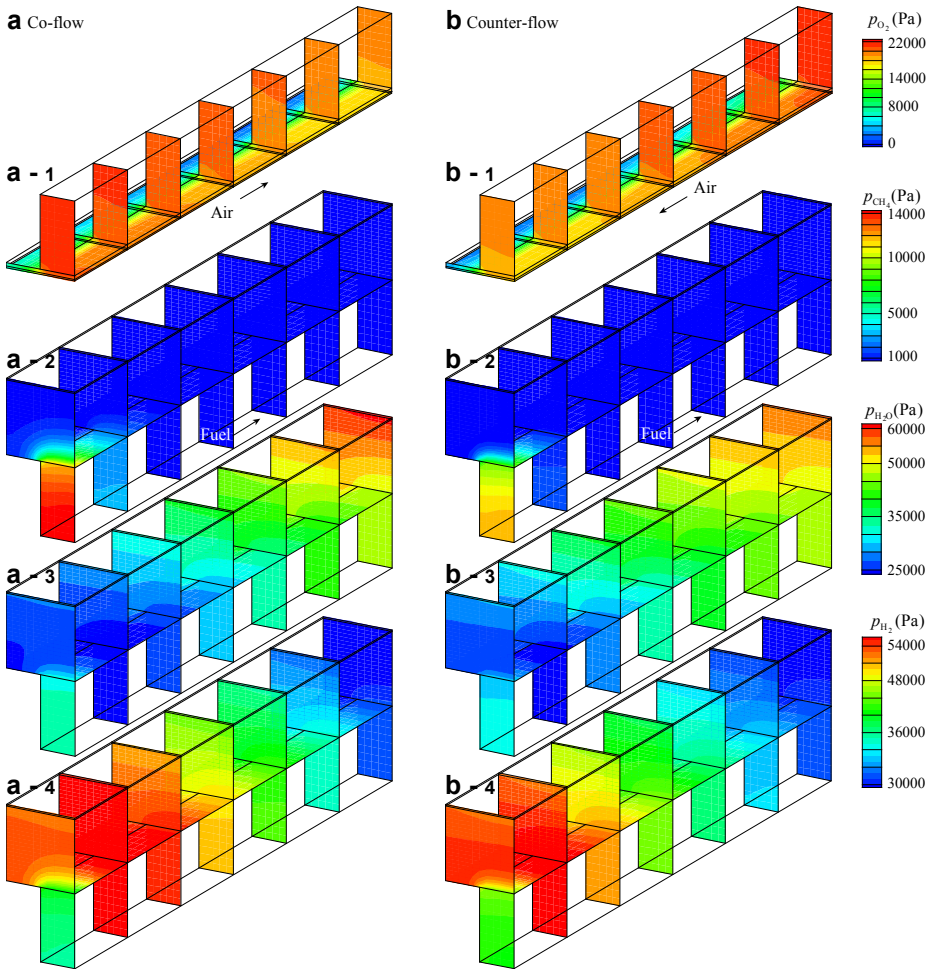

Fig. 5.11 The 3D distribution of gas concentrations in methane-fueled IT-SOFCs with (a) co-flow configuration and (b) counter-flow configuration, operated at fuel utilization factor of 50% ($\zeta_{\text{fuel}} = 0.5$): oxygen (1), methane (2), water vapor (3), and hydrogen (4).

and hydrogen in the anode are plotted. The results are for the inlet gas temperature of 750°C and the fuel utilization factor of 50%. The oxygen partial pressure, p_{O_2}, in Figs. 5.11(a-1) and 5.11(b-1) clearly indicates the mass block effect of the interconnect plates. The oxygen concentration under the interconnect rib is much lower than that under the flow channel, due to the small thickness of the cathode (20 μm for the CFL and 50 μm for the CCCL) as well as the relatively low diffusivity of oxygen. Note that the depletion of O_2 occurs preferentially in the under-rib regions

due to this reason.

The partial pressure of methane, p_{CH_4}, is presented in Figs. 5.11(a-2) and 5.11(b-2), which indicates that methane exists only in the anode channel and the ASL near the fuel inlet. This clearly points out that CH_4 is completely consumed by the reforming reactions inside the ASL within short distance from the fuel inlet. Accordingly, the partial pressure of water vapor, p_{H_2O}, also decreases in this short distance due to the consumption by the reforming reactions. However, p_{H_2O} gradually increases along the fuel channel since water vapor is produced by electrochemical reaction in the AFL. Hydrogen is produced by methane reforming reactions and consumed by the electrochemical reaction in the anode. Thus, the partial pressure of hydrogen, p_{H_2}, increases rapidly near the fuel inlet, reaches a local maximum at around 2 cm from the inlet, and then continuously decreases until the fuel gas stream arrives at the fuel outlet.

5.3 Summary

In this chapter, the 3D micro/macroscale model developed for hydrogen-fueled IT-SOFCs in chapter 2 is extended to consider of methane-fueled IT-SOFCs with direct internal reforming (DIR) process. The conversion of methane into hydrogen is considered using the global three-step reaction models composed of the steam methane reforming (SMR), water-gas shift (WGS), and reverse methanation (RM) reactions. The reaction kinetics are accurately calculated based on the volumetric nickel (Ni) surface area inside the ASL. The mass transport model is modified to account for the multicomponent gas mixtures (CH_4, H_2O, H_2, CO, and CO_2) in the anode. The heat and mass sources due to the methane reforming reactions are also included in the heat and mass transfer models.

The simulations are performed to investigate the effects of the co- and counter-flow configurations on the performance and operating characteristics of methane-fueled IT-SOFCs as well as on the spatial distribution of temperature, current density, and gas composition. The fuel composition is assumed to follow that in the 30% pre-reformed steam/methane mixture with the steam-to-methane (S/C) ratio of 2.0. The simulation results indicate that the endothermic reforming reactions

significantly alter the temperature distribution and the resultant cell performance.

For the co-flow configuration, the cooling effects due to air introduction and endothermic reforming reactions are concentrated in the inlet regions of the fuel and air; a monotonically increasing temperature distribution along the fuel channel is obtained. However, for the counter-flow configuration, the cooling effect due to endothermic reforming reactions is present near the fuel inlet while that due to air introduction is present near the fuel outlet (air inlet); an increasing then decreasing temperature distribution along the fuel channel is observed. Thus, the counter-flow configuration is found to leads to uniformly higher temperature distribution inside methane-fueled IT-SOFCs, compared with the con-flow configuration. With this higher and more uniform temperature distribution, the cell performance becomes much better with the counter-flow configuration than with the co-flow configuration. These results clearly suggest that better performance and durability of methane-fueled IT-SOFCs can be achieved by carefully arranging the flow direction and optimizing operating conditions.

CHAPTER 6
CONCLUSIONS, CONTRIBUTIONS, AND FUTURE WORKS

This dissertation presents three-dimensional micro/macroscale models for planar, anode-supported IT-SOFCs operated with hydrogen and methane fuels and the results obtained by the models for various situations due to different operating conditions, different electrode microstructures, and different cell geometries. The main outcome of this study is the development of comprehensive prediction models for the design and optimization of planar IT-SOFCs by fully considering the microscale processes in the PEN as well as the three-dimensional macroscale processes in the flow channels and interconnect plates. This chapter summarizes the main points from this dissertation and contributions, along with the suggestion for the future works for developing more advanced models.

6.1 Conclusions

In this dissertation, three-dimensional micro/macroscale models are developed as an efficient simulation and design tool to evaluate the effects of various operational, microstructural, and dimensional parameters on the performance of IT-SOFCs operated with hydrogen and methane. These micro/macroscale models are constructed to consider the complete three-dimensional calculation domain of planar IT-SOFCs, comprising of a PEN, two interconnect plates, and two gas channels.

In chapter 2, fundamental theories, governing equations, and constitutive models employed in the three-dimensional micro/macroscale model for planar hydrogen-fueled IT-SOFCs are presented in detail. These include the models for charactering of the electrode microstructure, those for calculating the electrode processes, and those for considering the heat and mass transport processes. Based on the statistical theories for randomly packed mixtures of binary spherical particles, the electrode microstructure characterization determines microscale

electrode properties such as the three-phase boundary length (TPBL), effective conductivities, and effective diffusivities. Then, the continuum electrode model predicts the transport and electrochemical reactions inside the porous electrodes, based on the conservation of electronic and ionic charges and using the experimental electrochemical reaction kinetics for TPBs in the electrode.

The heat and mass transfer models determines temperature and species concentration due to the macroscale transport processes in the electrolyte, porous electrodes, gas channels, and interconnect plates. In the present model, the axial fluid velocity in the gas channels is prescribed by assuming fully-developed laminar flow, with the validity of this assumption fully explained. Thus, this approach is expected to significantly save the computational cost without severe loss of accuracy. Finally, the validity of the micro/macroscale model is demonstrated by comparing the performance curves from the one-dimensional simulation and those from single-cell experiments.

In chapter 3, the basic performance and operating characteristics of planar, anode-supported IT-SOFCs fueled with hydrogen are investigated using the three-dimensional micro/macroscale model developed in this dissertation. The operation of IT-SOFCs with co-flow and counter-flow configurations is simulated, from which the current–voltage performance curves are determined along with the contribution of activation, concentration, and ohmic overpotentials to total potential loss. The spatial distribution of temperature, current density, and concentrations is also investigated in detail. The results generally indicate that the counter-flow configuration results in higher efficiencies than the co-flow configuration. However, the co-flow configuration is found to have more uniform distribution of temperature and current density compared with the counter-flow configuration, which is believed advantageous for long-term stability of the performance as well as mechanical durability of IT-SOFCs.

It is found that temperature and hydrogen concentration is the primary cause for the current density variation along the channel (x-directional variation). On the contrary, oxygen concentration is observed to be the primary cause for the current density variation under the channel and interconnect rib (y-directional variation).

The distribution of temperature gradient inside the electrolyte and the functional layers are also studied since it is closely related with the thermal stress buildup. The results point out that the co-flow configuration has lower temperature gradient than the counter-flow configuration. Finally, fluid velocity distribution in the gas channels is presented.

In chapter 4, parametric studies are conducted using the three-dimensional micro/macroscale model to clarify the effects of operational, microstructural, and dimensional parameters on the performance of the IT-SOFCs with the co-flow configuration. The effects of each parameter on the Nernst potential and the activation, concentration, and ohmic potential losses are investigated. From the sensitivity analysis, key parameters which strongly influence the performance are identified. These parameters include the operating temperature and pressure, the particle size in the cathode functional layer (CFL), and the cell length. It is found that higher operating temperature reduces the activation overpotential in the cathode and higher operating pressure increases the Nernst potential and decreases the concentration overpotential by enhancing mass diffusivities. Smaller particle size in the CFL is observed to greatly reduce the activation overpotential in the cathode by increasing the active TPB sites for electrochemical reactions. Shorter cell length leads to more uniform temperature at higher level, resulting in better cell performance. Other parameters are found to have less noticeable effect on the performance of IT-SOFCs with the co-flow configuration.

In chapter 5, the micro/macroscale model for IT-SOFCs with hydrogen fuel is extended to simulate the operation of IT-SOFCs with methane fuel. For this purpose, three-step global reaction model consisting of the steam reforming reaction, water-gas shift reaction, and reverse methanation reaction is employed to consider the direct internal reforming process. In addition, the mass transfer model is modified to consider the multicomponent gas mixtures in the anode (CH_4, H_2O, H_2, CO, and CO_2), and the reaction heat due to the reforming reactions are also included in the heat transfer model. The operation of methane-fueled IT-SOFCs with co-flow and counter-flow configurations is simulated, from which the current–voltage performance characteristics as well as the spatial distribution of

temperature, current density, and concentration are investigated.

The steam reforming reactions are endothermic, whereas the electrochemical reactions are exothermic. Thus, temperature decreases near the inlet of methane fuel where reforming reactions are active. In IT-SOFCs with the co-flow configuration, temperature drops lower than the inlet temperature near the air inlet (fuel inlet) due to the endothermic reforming reactions in the anode, and then steadily increases along the channel due to exothermic electrochemical reactions. However, in IT-SOFCs with the counter-flow configuration, temperature increases from the air inlet (fuel outlet) and then decreases approaching the air outlet (fuel inlet). In other words, temperature in the electrolyte exhibit monotonically increasing behavior along the direction of air flow in the co-flow configuration but increasing then decreasing behavior in the counter-flow configuration. The temperature level is found to be much higher in the counter-flow configuration than in the co-flow configuration, which is the main reason for the observed higher performance with the counter-flow configuration. Because higher temperature also enhances the endothermic reforming reactions, the conversion of methane to hydrogen is also much faster for the counter-flow configuration than for the co-flow configuration.

Finally, the results presented in chapter 3 to chapter 5 clearly demonstrate the capabilities of the present three-dimensional micro/macroscale model as an efficient tool for detailed investigation of the electrochemical and transport processes occurring in planar, anode-supported IT-SOFCs.

6.2 Contributions

From the academic point of view, the main contribution of this dissertation is the development of the micro/macroscale models that take into full account the three-dimensional geometries of planar IT-SOFCs. In general, many microscale models for SOFCs were developed previously to consider only a PEN structure in one-dimension or a PEN and flow channels in two-dimension. Thus, these models could provide only the qualitative results for the effects of various parameters and conditions on the performance of IT-SOFCs. It is believed to be indispensible to consider the interconnect plate/channel geometries to obtain quantitative results for

IT-SOFCs. However, there have been few three-dimensional micro/macroscale models developed.

In the present micro/macroscale model, the three-dimensional region of a PEN, two gas channels, and two interconnect plates is set as the calculation domain with proper boundary conditions. In addition, the axial fluid velocity in the gas channel is prescribed by assuming the fully-developed laminar flow in the channel. Then, the present micro/macroscale models can accurately calculate the variation of reactant and product concentrations and temperature along the flow channel. In addition, the present models fully consider the main impacts due to the presence of interconnect plates, i.e., the contact resistances for electron and heat conduction, obstructed mass transport for the part of electrode surface, and enhanced axial heat transfer through interconnect plates. Therefore, the models presented in this dissertation are able to produce the most typical and quantitative performance and operating characteristics of planar IT-SOFCs. The performance curves presented in this dissertation can be used as the reference for other studies.

From the practical point of view, the main contribution of this dissertation is that the three-dimensional micro/macroscale models offer fast and efficient design tools for predicting and optimizing planar IT-SOFCs. This becomes possible for complex fluid dynamics calculation is eliminated from the models. With these tools, engineers designing electrodes and stacks can experiment many different options, such as electrode microstructures, materials, dimensions, and operating conditions, numerically. In addition, the results presented in this dissertation can also be used as the guidelines in designing planar, anode-supported IT-SOFCs.

6.3 Future works

The micro/macroscale models developed in this dissertation have several limitations, from which suggestions for future works can be derived. First, the present models consider only the physical properties of rather standard materials, such as Ni/YSZ cermet for the anode, YSZ for the electrolyte, LSM/YSZ for the cathode, and LSM-coated SUS 430 for the interconnect plates. However, new materials with better properties are continuously being developed and employed in

the fabrication of IT-SOFCs. Thus, the inclusion of these new material properties in the micro/macroscale models will be required to predict the performance of IT-SOFCs employing new electrode and electrolyte materials.

Second, the present models derive the electrode properties from the microstructural parameters, such as porosity, particle diameter, phase composition, etc., based on the statistical correlations for randomly packed binary spherical particles. However, recent studies showed that three-dimensional microstructures of the electrodes in IT-SOFCs can be reconstructed utilizing the X-ray tomography or the focused ion beam/scanning electron microscopy (FIB/SEM) techniques. Then, the electrode properties, such as the volume-specific three-phase boundary length, effective electrical conductivities, and effective mass diffusivities, can be directly determined from the phase distribution in the reconstructed electrodes. Thus, using these properties in the present micro/macroscale models will provide more accurate linkage between the electrode microstructure and the performance of IT-SOFCs.

Third, the present micro/macroscale model for methane-fueled IT-SOFCs disregards the electrochemical oxidation reaction of CO into CO_2 in the anode. This may be justified because the methane-fueled IT-SOFCs are generally operated at low fuel utilization factors, at which conditions the contribution of the CO oxidation reaction to the total current density is known to relatively small. However, the current density due to the oxidation of CO should be included in the present model for the completeness of calculation. In addition, new experimental data are available for the hydrogen oxidation reaction in nickel pattern anodes, which can be used to update the electrochemical reaction model for the three-phase boundaries in the anode.

Finally, the most critical limitation of the three-dimensional micro/macroscale model is that only planar IT-SOFCs with straight, rectangular channel geometries can be simulated. Eliminating the fluid dynamics calculation based on fully-developed channel flow assumption helps to reduce the computational cost and thus enable fast and efficient solution procedure; however, this also disables the simulation of IT-SOFCs with other interconnect/channel geometries. Thus, the present micro/macroscale model should be extended to include the fluid dynamics

calculation, possibly using the computational fluid dynamics (CFD) tools such as Fluent or OpenFOAM. In general, the CFD tools provide by default the solution for mass, momentum, energy, and species conservation, as well as the capability for handling complex grid. To extend the present models to CFD models, a method should be devised to reduce the number of grids in the PEN while preserving the accuracy of the detailed calculation in the electrodes.

Although suggestions are mentioned above for possible direction of future works, there are still many problems that can be clarified by the micro/macroscale models in the present forms. Therefore, the present models can be used in detailed investigation of planar, anode-supported IT-SOFCs fueled with hydrogen or methane for various purposes.

References

Minh, N.Q., 1993, Ceramic fuel cells, *Journal of American Ceramics Society*, **76**(3), 563−588.

Larminie, J. and Dicks, A., 2000, *Fuel Cell Systems Explained*, John Wiley & Sons, Chichester.

Achenbach, E. and Riensche, E., 1994, Methane/steam reforming kinetics for solid oxide fuel cells, *Journal of Power Sources*, 52(2), 283–288.

Su, C., Ran, R., Wang, W., Shao, Z.P., 2011, Coke formation and performance of an intermediate-temperature solid oxide fuel cell operating on dimethyl ether fuel, *Journal of Power Sources*, 196(4), 1967–1974.

Liu, M.F., Peng, R.R., Dong, D.H., Gao, J.F., Liu, X.Q. and Meng, G.Y., 2008, Direct liquid methanol-fueled solid oxide fuel cell, *Journal of Power Sources*, 185(1), 188–192.

Ma, Q.L., Peng, R.R., Lin, Y.J., Gao, J.F. and Meng, G.Y., 2006, A high-performance ammonia-fueled solid oxide fuel cell *Journal of Power Sources*, 161(1), 95–98.

Zhao, F. and Virkar, A.V., 2005, Dependence of polarization in anode supported solid oxide fuel cells on various cell parameters, *Journal of Power Sources*, 141(1), 79−95.

Haanappel, V.A.C., Mertens, J., Rutenbeck, D., Tropartz, C., Herzhof, W., Sebold, D. and Tietz, F., 2005, Optimisation of processing and microstructural parameters of LSM cathodes to improve the electrochemical performance of anode-supported SOFCs, *Journal of Power Sources*, 141(2), 16−226.

Ormerod, R.M., 2003, Solid oxide fuel cells, *Chemical Society Reviews*, 32(1), 17–28.

Singhal, S.C. and Kendall, K., 2003, *High-Temperature Solid Oxide Fuel Cells: Fundamentals, Design and Applications*, Elsevier, New York.

Kenjo, T. and Nishiya, M., 1992, $LaMnO_3$ air cathodes containing ZrO_2 electrolyte for high temperature solid oxide fuel cells, *Solid State Ionics*, 57(3−4), 295−302.

Fergus, J.W, 2007, Materials challenges for solid-oxide fuel cells, *JOM Journal of the Minerals, Metals and Materials Society*, 59(12), 56–62.

Steele, B.C.H., 2000, Materials for IT-SOFC stacks: 35 years R&D: the inevitability of gradualness?, *Solid State Ionics*, 134(1–2), 3–20.

Fergus, J.W., 2005, Metallic interconnects for solid oxide fuel cells, *Materials Science and Engineering: A*, 397(1–2), 271–283.

Costamagna, P., Costa, P. and Antonucci, V., 1998, Micro-modelling of solid oxide fuel cell electrodes, *Electrochimica Acta*, 43(3−4), 375−394.

Chan, S.H. and Xia, Z.T., 2001, Anode micro model of solid oxide fuel cell, *Journal of The Electrochemical Society*, 148(4), A388−394.

Chen, X.J., Chan, S.H. and Khor, K.A., 2004, Simulation of a composite cathode in solid oxide fuel cells, *Electrochimica Acta*, 49(11), 1851−1861.

Janardhanan, V.M., Heuveline, V. and Deutschmann, O., 2008, Three-phase boundary length in solid-oxide fuel cells: A mathematical model, *Journal of Power Sources*, 178(1), 368−372.

Chen, D., Lina, Z., Zhu, H. and Kee, R.J., 2009, Percolation theory to predict effective properties of solid oxide fuel-cell composite electrodes, *Journal of Power Sources*, 191(2), 240−252.

Hussain, M.M., Li, X. and Dincer, I., 2009, A numerical investigation of modeling an SOFC electrode as two finite layers, *International Journal of Hydrogen Energy*, 34(7), 3134−3144.

Xu J.G. and Froment, G.F., 1989, Methane steam reforming, methanation and water-gas shift: I. Intrinsic kinetics, *AIChE Journal*, 35(1), 88−96.

Xu J.G. and Froment, G.F., 1989, Methane Steam Reforming: II. Diffusional limitations and reactor simulation, *AIChE Journal*, 5(1), 97−103.

Suzuki, M. and Oshima, T., 1983, Estimation of the co-ordination number in a multi-component mixture of spheres, *Powder Technology*, 35(2),159−166.

Bouvard, D. and Lange, F.F., 1991, Relation between percolation and particle coordination in binary powder mixtures, *Acta Metallurgica et Materialia*, 39(12) 3083−3090.

Kuo, C.H. and Gupta P.K., 1995, Rigidity and conductivity percolation thresholds in particulate composites, *Acta Metallurgica et Materialia*, 43(1), 397−403.

Kirkpatrick, S., 1973, Percolation and Conduction, *Reviews of Modern Physics*, 45(4), 574−588.

Nam, J.H., Jeon, D.H., 2006, A comprehensive micro-scale model for transport and reaction in intermediate temperature solid oxide fuel cells, *Electrochimica Acta*, 51(17), 3446−360.

Jeon, D.H., Nam, J.H. and Kim, C.-J., 2006, Microstructural optimization of anode-supported solid oxide fuel cells by comprehensive microscale model, *Journal of The Electrochemical Society*, 153(2), A406−417.

Ni, M., Leung, M.K.H. and Leung, D.Y.C., 2007, Micro-scale modelling of solid oxide fuel cells with micro-structurally graded electrodes, *Journal of Power Sources*, 168(2), 369−378.

Zhu, H., and Kee, R.J., 2008, Modeling distributed charge-transfer processes in SOFC membrane electrode assemblies, *Journal of The Electrochemical Society*, 155(7), B715−729.

Sohn, S., Nam, J.H., Jeon D.H. and Kim, C.-J., 2010, A micro/macroscale model for intermediate temperature solid oxide fuel cells with prescribed fully-developed flow in gas channels, *International Journal of Hydrogen Energy*, 35(21), 11890~11907.

Ferguson, J.R., Fiard, J.M. and Herbin, R., 1996, Three-dimensional numerical simulation for various geometries of solid oxide fuel cells, *Journal of Power Sources*, 58(2), 109−122.

Anselmi-Tamburini, U., Chiodelli, G., Arimondi, M., Maglia, F., Spinolo, G. and Munir, Z.A., 1998, Electrical properties of Ni/YSZ cermets obtained through combustion synthesis, *Solid State Ionics*, 110(1−2), 35−43.

Kiatkittipong, W., Tagawa, T., Goto, S., Assabumrungrat, S. and Praserthdam, P., 2005, Oxygen transport through LSM/YSZ/LaAlO system for use of fuel cell type reactor, *Chemical Engineering Journal*, 106(1), 35−42.

Chu, T.K. and Ho, C.Y., 1978, Thermal conductivity and electrical resistivity of eight selected AISI stainless steels, in: V.V. Mirkovich (Ed.), *Thermal Conductivity 15*, Plenum Press, New York, 79–104

Sunde, S., 2000, Simulations of Composite Electrodes in Fuel Cells, *Journal of Electroceramics*, 5(2), 153-182.

Bieberle, A., Meier, L.P. and L. J. Gauckler, 2001, The electrochemistry of Ni pattern anodes used as solid oxide fuel cell model electrodes, *Journal of The Electrochemical Society*, 148(6), A646−656.

Radhakrishnan, R., Virkar, A.V. and Singhal, S.C., 2005, Estimation of charge-transfer resistivity of $La_{0.8}Sr_{0.2}MnO_3$ cathode on $Y_{0.16}Zr_{0.84}O_2$ electrolyte using patterned electrodes, *Journal of The Electrochemical Society*, 152(1), A210−218.

Jiang, S.P., Love, J.G., and Apateanu L., 2003, Effect of contact between electrode and current collector on the performance of solid oxide fuel cells, *Solid State Ionics*, 160(1−2), 15−26.

Kim, J.H., Song, R.H. and Hyun, S.H., 2004, Effect of slurry-coated $LaSrMnO_3$ on the electrical property of Fe−Cr alloy for metallic interconnect of SOFC, *Solid State Ionics*, 174(1−4), 185−191.

Mason, E.A. and Malinauskas A.P., 1983, *Gas Transport in Porous Media: The Dusty Gas Model*, Elsevier, New York.

Krishna, R. and Wesselingh J.A., 1997, The Maxwell-Stefan approach to mass transfer, *Chemical Engineering Science*, 52(6), 861−911.

Bird, R.B., Stewart, W.E. and Lightfoot, E.N., 2002, *Transport Phenomena, 2nd edition*, John Wiley & Sons, New York.

Fuller, E.N., Schettler, P.D. and Giddings, J.C., 1966, New method for prediction of binary gas-phase diffusion coefficients, *Industrial & Engineering Chemistry*, 58(5), 18−27.

Williford, R.E., Chick, L.A., Maupin, G.D., Simner, S.P. and Stevenson, J.W., 2003, Diffusion limitations in the porous anodes of SOFCs, *Journal of The Electrochemical Society*, 150(8), A1067−1072.

Kaviany, M., 1999, *Principles of Heat Transfer in Porous Media, 2nd edition*, Springer, New York.

Purday, H.F.P., 1949, *An Introduction to the Mechanics of Viscous Flow*, Dover, New York.

Natarajan, N.M. and Lakshmanan, S.M., 1972, Laminar flow in rectangular ducts: Prediction of the velocity profiles and fraction factors, *Indian Journal of Technology*, 10, 435−438.

Todd, B. and Young, J.B., 2002, Thermodynamic and transport properties of gases for use in solid oxide fuel cell modeling, *Journal of Power Sources*, 110(1), 186−200.

Hernandez-Pacheco, E., and Mann, M.D., 2004, The rational approximation method in the prediction of thermodynamic properties for SOFCs. *Journal of Power Sources*, 128(1), 25−33.

Iwaa, M., Hikosaka, T., Morita, M., Iwanari, T., Ito, K., Onda, K., Esaki, Y., Sakaki, Y. and Nagata, S., 2000, Performance analysis of planar-type unit SOFC considering current and temperature distributions, *Solid State Ionics*, 132(3–4), 297–308.

Iora, P., Aguiar, P., Adjiman, C.S. and Brandon, N.P., 2005, Comparison of two IT DIR-SOFC models: Impact of variable thermodynamic, physical, and flow

properties. Steady-state and dynamic analysis, *Chemical Engineering Science*, 60(11), 2963–2975.

Singhal, S.C., 2000, Advances in solid oxide fuel cell technology, *Solid State Ion*, 135(1–4), 305–313.

Atkinson, A., Barnett, S., Gorte, R.J., Irvine, J.T.S, Mcevoy, A.J., Mogensen, M., Singhal, S.C. and Vohs, J., 2004, Advanced anodes for high-temperature fuel cells. Nat Mater 3(1), 17–27.

Nakajo, A., Stiller, C., Harkegard, G. and Bolland, O., 2006, Modeling of thermal stresses and probability of survival of tubular SOFC, *Journal of Power Sources*, vol. 158(1), 287-294

Aguiar, P., Adjiman, C. and Brandon, N., 2005, Anode-supported intermediate-temperature direct internal reforming solid oxide fuel cell: II. Model-based dynamic performance and control, *Journal of Power Sources*, 147 (1–2), 136–147.

Radovic, M., and Lara-Curzio, E., 2004, Mechanical properties of tape cast nickel-based anode materials for solid oxide fuel cells before and after reduction in Hydrogen, *Acta Materialia*, 52(20), 5747–5756.

Selcuk, A., Merere, G., and Atkinson, A., 2001, The Influence of Electrodes on the Strength of Planar Zirconia Solid Oxide Fuel Cells, *Journal of Materials Science*, 36(5), 1173–1182.

Brett, D.J.L., Atkinson, A., Cumming, D., Ramirez-Cabrera, E., Rudkin, R. and P. Brandon, N., 2005, Methanol as a direct fuel in intermediate temperature (500–600°C) solid oxide fuel cells with copper based anodes. *Chemical Engineering Science*, 60(21), 5649–5662.

Meusinger, J., Riensche, E., and Stimming, U., 1998, Reforming of natural gas in solid oxide fuel cell systems, *Journal of Power Sources*, 71(1–2), 315–320.

Armor, J.N., 1999, The multiple roles for catalysis in the production of H_2, *Applied Catalysis A: General*, 176(2), 159–176.

Jiang, Y. and Virkar, A.V., 2003 Fuel composition and diluent effect on gas transport and performance of anode-supported SOFCs, *Journal of The Electrochemical Society*, 150 (7), A942–A951.

Campanari S., 2001, Thermodynamic model and parametric analysis of a tubular SOFC module, *Journal of Power Sources*, 92(1–2), 26–34.

요 약 문

수소 및 메탄 연료로 운전되는 중온 평판형 고체 산화물 연료전지의 마이크로/매크로 시뮬레이션

중온형 고체 산화물 연료전지는 고온 작동 조건에 의한 재료선택의 제한, 미세전극의 가속 열화, 열 사이클의 한계, 긴 작동 시간의 요구 등과 같은 문제점들을 해결 할 수 있는 기술로 주목 받고 있다. 이러한 제약 및 제한의 대부분은 1000도 근처의 작동 온도 조건의 고온형 고체 산화물 연료전지로부터 기인한다. 중온형 고체 산화물 연료전지는 상대적으로 낮은 600~800도의 작동 온도 범위를 가지므로, 보다 저렴한 재료 구성을 바탕으로 연료전지의 장기간 안정성을 확보할 수 있다. 게다가, 고체산화물 연료전지는 비백금 촉매의 사용, 탄화수소 연료의 직접 내부 개질, 그리고 양질의 폐열 생산 등과 같은 장점을 보유하고 있다.

본 논문은 수소 및 메탄 연료로 운전되는 음극 지지 중온 평판형 고체 산화물 연료전지의 설계, 평가 그리고 최적화를 위한 포괄적인 3차원 마이크로/매크로 모델 개발을 제시한다. 마이크로/매크로 모델은 랜덤 바이너리 팩킹 기반의 전극 미세구조 특성에 대한 모델, 전극 내 삼상계면에서의 전기 화학 반응 과정을 위한 모델, 인터커넥터를 포함한 3차원 기체 유로 내 완전 발달 유동 가정을 기반으로 한 열 및 물질 전달 모델, 그리고 증기 개질 반응, 수성-가스 전환 반응 및 역 메탄 반응으로 이루어진 음극 내의 직접 내부 개질을 위한 모델 등 다수의 구성 모델로 이루어져 있다. 개발된 3차원 마이크로/매크로 모델을 기반으로 니켈, YSZ, LSM 그리고 스테인리스 스틸과 같은 중온형 고체 산화물 연료전지의 표준 재료 물성치와 공기 (O_2 and N_2) 및 연료 (H_2, H_2O, CH_4, CO, and CO_2)의 정확한 열역학적 물성치를 이용하여 시뮬레이션을 수행하였다.

3차원 마이크로/매크로 모델은 병류 및 향류와 같은 유로 내 유동 조건과 수소 혹은 메탄을 연료로 운전되는 음극 지지 중온 평판형 고체 산화물 연료전지의 성능 및 작동조건의 특성을 평가하기 위해 이용되었

다. 전류-전압 성능 곡선 안에 전체 전압 손실에 영향을 미치는 활성화 과전압, 농도 과전압, 저항 및 접촉 과전압을 세분화 하여 제시하였다. 또한, 온도, 전류 밀도, 그리고 농도에 대한 3차원 분포를 자세히 살펴보았다. 해석 결과는 병류 유동 조건 보다 향류 유동 조건의 수소 연료로 운전되는 중온형 연료전지의 효율이 높게 나타났다. 그리나 향류 유동 조건 보다 병류 유동 조건일 경우 온도와 전류 밀도에서 고른 분포를 나타내었다. 따라서 병류 유동 조건은 중온형 고체 산화물 연료전지의 장기간 전지 성능의 안정성뿐만 아니라 기계적 내구성 면에서 더 유리한 것으로 결론 내릴 수 있다. 또한, 작동 조건, 전극의 미세 구조 그리고 전지 형상의 매개변수들에 대한 영향을 명확히 파악하기 위하여 광범위한 매개 변수 연구를 수행하였다. 메탄을 연료로 사용하는 고체 산화물 연료전지 해석 결과에서는 향류 유동 조건이 병류 유동 조건에 비해 높은 효율과 균일한 온도 분포를 나타내는 것을 확인하였다. 이러한 결과는 흡열성 증기 개질 반응에 의한 영향 때문이다.

개발된 3 차원 마이크로/매크로 모델를 통해 제시한 결과들로부터 음극 지지 중온 평판형 고체 산화물 연료전지의 작동 조건, 전극의 미세 구조 조건 그리고 전지 형상 조건의 최적 설계 도출뿐만 아니라 화학적, 전기화학적, 그리고 열 및 물질 전달 과정에 대한 정량적 평가를 위해 정확하고 효율적인 설계 도구란 것을 명확히 검증하였다.

주요어 : 중온형 고체 산화물 연료전지;음극 지지형, 직접 내부 개질; 수증기 개질; 병류 및 향류; 마이크로/매크로 모델
학 번 : 2008-30856